Brain-Machine Interface for Reaching:
Accounting for Target Size, Multiple Motor Plans, and Bimanual Coordination

by

Peter J. Ifft

Department of Biomedical Engineering
Duke University

Date: _____
Approved:

_____
Miguel A. L. Nicolelis, Supervisor

_____
Craig Henriquez

_____
Marc Sommer

_____
Michael Platt

_____
Richard Bedlack

Dissertation submitted in partial fulfillment of
the requirements for the degree of Doctor
of Philosophy in the Department of
Biomedical Engineering in the Graduate School
of Duke University

2014

ABSTRACT

Brain-Machine Interface for Reaching:
Accounting for Target Size, Multiple Motor Plans, and Bimanual Coordination

by

Peter J. Ifft

Department of Biomedical Engineering
Duke University

Date: _____

Approved:

_____
Miguel A. L. Nicolelis, Supervisor

_____
Craig Henriquez

_____
Marc Sommer

_____
Michael Platt

_____
Richard Bedlack

An abstract of a dissertation submitted in partial fulfillment of
the requirements for the degree of Doctor
of Philosophy in the Department of
Biomedical Engineering in the Graduate School
of Duke University

2014

Abstract

Brain-machine interfaces (BMIs) offer the potential to assist millions of people worldwide suffering from immobility due to loss of limbs, paralysis, and neurodegenerative diseases. BMIs function by decoding neural activity from intact cortical brain regions in order to control external devices in real-time. While there has been exciting progress in the field over the past 15 years, the vast majority of the work has focused on restoring of motor function of a single limb. In the work presented in this thesis, I first investigate the expanded role of primary sensory (S1) and motor (M1) cortex during reaching movements. By varying target size during reaching movements, I discovered the cortical correlates of the speed-accuracy tradeoff known as Fitts' law. Similarly, I analyzed cortical motor processing during tasks where the motor plan is quickly reprogrammed. In each study, I found that parameters relevant to the reach, such as target size or alternative movement plans, could be extracted by neural decoders in addition to simple kinematic parameters such as velocity and position. As such, future BMI functionality could expand to account for relevant sensory information and reliably decode intended reach trajectories, even amidst transiently considered alternatives.

The second portion of my thesis work was the successful development of the first bimanual brain-machine interface. To reach this goal, I expanded the neural recordings system to enable bilateral, multi-site recordings from approximately 500 neurons

simultaneously. In addition, I upgraded the experiment to feature a realistic virtual reality end effector, customized primate chair, and eye tracking system. Thirdly, I modified the tuning function of the unscented Kalman filter (UKF) to conjointly represent both arms in a single 4D model. As a result of widespread cortical plasticity in M1, S1, supplementary motor area (SMA), and posterior parietal cortex (PPC), the bimanual BMI enabled rhesus monkeys to simultaneously control two virtual limbs without any movement of their own body. I demonstrate the efficacy of the bimanual BMI in both a subject with prior task training using joysticks and a subject naïve to the task altogether, which simulates a common clinical scenario. The neural decoding algorithm was selected as a result of a methodical comparison between various neural decoders and decoder settings. I lastly introduce a two-stage switching model with a classify step and predict step which was designed and tested to generalize decoding strategies to include both unimanual and bimanual movements.

Contents

List of Tables

List of Figures

Acknowledgements

I first and foremost want to thank my family of Mark, Michelle and Andrea for their endless support and love. I couldn't ask for better role models for life, work, and faith. Second, I could not have reached this point without the support of my fiancé Ellen, who brings happiness and balance to my life, as well as helping to keep my perspective broader than simply the work I was pursuing in lab.

Secondly, I am grateful for my thesis advisor Miguel Nicolelis and his scientific expertise, ceaseless passion, and steadfast optimism about the field he played a major role in creating. Together with Mikhail Lebedev, I was challenged to think about problems in a new way which helped shape the researcher I've become. In addition, I thank committee members Marc Sommer, Michael Platt, Craig Henriquez, and Richard Bedlack for their valuable critiques and comments. The lab staff of Susan Halkiotis, Laura Oliveira, Terry Jones, and Tamara Phillips has been endlessly valuable as well.

I also express special gratitude to former roommate and "lab spouse" Solaiman Shokur, who was equal parts clever, hardworking, and a great friend. In addition, the research team in the Nicolelis lab has been an honor and pleasure to work with, most notably Gary Lehew, Jim Meloy, Joseph O'Doherty, Katie Zhuang, Zheng Li, Arjun Ramakrishnan, David Schwarz, Tim Hanson, Olga Mutter, Leo Medina, and Andrew Tate. This group been incredible in so many ways – soccer teammates, Chipotle lunchers, late-night lab buddies, and of course a brilliant research team to work with.

Outside of lab, I want to thank my great friends Pete, Devin, Tyler, Vrad, and so many other outstanding people I've gotten to know here at Duke.

1. Neuronal control of reaching movements

The ability to generate movements in a coordinated and efficient way underlies some of the most interesting and complex phenomena of primate behavior. It enables both the essential movements for survival as well as a diverse repertoire that enriches our daily lives. The behavioral evidence of this is striking, simply by observing the precision and mastery of a concert pianist or the requisite dexterity, athleticism, and strength of professional athletes. The body's motor machinery enables a fusion between the innate and the unimaginable. We grow and learn and adapt our behaviors throughout our lifespan because our brain maintains the ability to do so. Evident from the enlargement and specialization of the brain itself throughout primate evolution [1] there was a clear connection between the complexity of the motor system and the complexity of the resultant movements.

For these, and many other reasons, I focus my investigation on rehabilitative solutions for subjects with severe motor deficits. Loss or absence of healthy motor function can be devastating and very often the paralysis is irreversible. The most common cause is spinal cord injury which is estimated to have an incidence of 22 people/million population in the western and developing world and nearly twice this rate in the US for a total of nearly 3 million people worldwide [2]. Other causes of lost motor function include limb amputation and neurodegenerative diseases such as amyotrophic lateral sclerosis (ALS). These conditions are devastating not only because of the acute reduction in quality of life, but also due to the currently bleak outlook on

viable and affordable rehabilitation therapies. In my research, I embark on the development of a technology, called a brain-machine interface (BMI), which can bypass the nonfunctional structures which sustained injury or pathology to enable the brain to act directly on the world. This is possible because the brain is often still fully intact post-injury and the signaling within the brain is rich with motor, sensory, and cognitive information which can be extracted to re-establish a functional motor pathway. Although still in the early stages of development, BMIs offer tremendous potential in the coming years. BMIs themselves are a broad class of neural engineering tools which will be outlined more completely in Chapter 2. I will begin the background discussion by introducing what is known about the anatomy and physiology of the brain with respect to creating and executing movements.

A great deal of research has embarked on understanding motor physiology, ranging from the origins [1], various pathologies [3, 4], and the underlying principles [5-8]. Taking advantage of the widespread similarities of our most recent ancestors - apes and monkey species – the research conducted in many laboratories such as ours looks at the mechanisms related to movements in *non-human* primates. The following section introduces a literature-driven review of fundamentals of neuronal control of movements in a limited context that relates specifically to development of BMI technology in the subsequent studies of this thesis.

1.1 Cortical neuroanatomy and physiology

Execution of volitional motor plans is the result of signaling amongst a network

of regions ranging from the cortex (the outermost layers near the surface) to subcortical areas of the brain, as well as in spinal and peripheral nerves. The anatomy of the primate motor system is extensive and to review all such components with their respective contributions would be unnecessary for the content of this work. The focus will be primarily motor neurophysiology at the cortical level. The localization of a cortical area related to movement control was facilitated by late 19th century advancements in surgical and experimental techniques. A series of experiments by Fritsch and Hitzig in 1870 [9, 10] used electrical stimuli on the cortical surface and laid the foundation for much of today's motor cortical research. First, the electrical stimuli evoked movements which suggested a critical link between brain and periphery. Secondly, there was a topographic organization of the primate body in cortex – what would eventually be known as the homunculus or the motor map. Axial and lower limb regions were identified most medial, with upper limb, hand, and face most lateral. What these scientists discovered was the central cortical structure in voluntary movement: the primary motor cortex, or M1.

The nature of the neural representation of movements in M1 is today still not yet completely understood [11-13]. Enacting even a simple reaching movement involves many other cortical regions [14]. More specifically, the areas involved include the premotor cortex [15], supplementary motor area (SMA) [16], posterior parietal cortex (PPC) [17], and more indirectly, association areas like prefrontal cortex [18]. The relative contribution of each area has been the subject of many studies in motor

neurophysiology. M1 has remained the central figure among this network, commonly thought of as downstream of these other cortical areas [19]. M1 is thus considered to be the location of the output signal from the cortex to subcortical structures. Anatomically, this is supported by the unique existence of huge cell bodies in the output layer V in primary motor cortex, termed Betz cells, which project to the specific level of the spinal cord appropriate for the intended movement. Although most Betz cells project to spinal interneurons, a fraction of these cells directly synapse on lower motor neurons [19]. In addition, not all of M1 output projects to the spinal cord. M1 output also engages striatal [20], thalamic [21] and brainstem circuits [22]. The various output targets suggest both a direct and indirect function in movement execution.

Premotor cortex, most often dorsal portions (PMd), has been found to encode higher order components of movements, such as spatial attention [23], visual perception [24], planning [25-27], and execution [25, 28]. In a more general sense, premotor cortex has been characterized as serving an intermediate role between higher order cognitive function and pure motor representation [29-31]. A similar role is reported for SMA in motor sequence planning [32], movement initiation [33], and kinematics of movement [34]. Both premotor cortex and SMA have dense inputs to M1 as well as corticospinal projections [19, 35]. A third major sources of input to M1 is somatotopically organized input from primary sensory cortex (S1) [19]. The topographic organization of S1 mirrors that of M1 on the precentral gyrus. The high interconnectivity between M1 and S1 provides a high-level feedback of proprioceptive and tactile information from the body

area being controlled by M1. The final major input to M1 comes from PPC. Located caudal to M1, this region synthesizes relevant spatial information via the dorsal visual processing stream [19]. Studies have shown a several subregions of PPC, the parietal reach region and area 5b, to be related to spatial, goal-directed actions [36, 37].

1.2 Neurophysiological representation of movements

The anatomy and subsequent neurophysiological characterization of these motor-related cortical areas has laid the groundwork for the next question to be asked: How does the brain use this machinery to enact multi-joint movements? There are two prevailing theories on the mechanism of control enacted by motor-related cortex during movements. The first is termed force-control [38] and in the strictest sense claims that voluntary movements are carried out by a series of coordinate transformations. This is a hierarchical model that was in part influenced by robotic controller studies [8, 39]. The first step would be identify the goal of the movement in space with respect to the end effector (e.g. the hand), termed the extrinsic kinematics. Second, the motor system would compute the requisite joint rotations and muscle lengths to accomplish this movement, referred to as the intrinsic kinematics. Lastly, the intrinsic dynamics of the movement - the forces generated by muscle activation - must be specified. The support for this theory is provided by electrophysiological studies of neurons in motor cortex. Reach kinematics such as direction and velocity are well known to modulate firing rate in M1 [5, 8]. Similarly, studies have shown a tuning of M1 neurons to muscle contractile forces, measures as EMG [7, 40], c.f. [41]. These results have a strong basis

experimentally and serve as the foundation by which many intracortical BMIs operate.

The criticism of the force-control model is that a vast amount of information must be specified at the cortical level and updated constantly. For example, in a simple reaching movement, the first computation is the three-dimensional trajectory of the hand, then the precise joint rotations through a series of coordinate transformations, and lastly the magnitude of contractile forces of all involved shoulder, arm, and hand muscles. Despite the complexity, the cerebral cortex seems to be highly capable of making these transformations. A series of studies by the Kalaska and Andersen groups describe a mechanism in PPC that generates multiple simultaneous spatial representations based on differing reference frames (eye, hand, head, etc.) [8, 42]. In the most basic sense, the required coordinate transformation for a reaching movement is to identify the end location in hand-centric coordinates and convert this into patterns of muscle activation. The force-control model attempts to establish a causal relationship between cortical activation and very specific components of a movement. The many calculations suggested by the force-control theory, although based on strong evidence experimentally, have given rise to a second theory of motor control of reaching movements.

The second prevalent model for motor control is the equilibrium point model. Rather than specify explicit kinematic and kinetic parameters of movements, this model proposes that the motor system signals the desired final equilibrium state [43]. An important difference with this model is that the properties of the muscles dictate the

precise joint rotations and movements rather than commands from the cerebral cortex. Early models proposed by Feldman propose that the length-force relationship of muscles and the stretch reflex determine the various equilibrium states, which provides the basis for voluntary motor control [43-45]. More recently, two new hypotheses have emerged from this model: motor synergies and the uncontrolled manifold hypothesis (UCM) [46, 47]. The muscle synergy hypothesis proposes that small groups of muscles (synergies) become activated or inactivated collectively [46, 48]. Doing so greatly reduces the degrees of freedom of motor output and could provide a parsimonious solution which minimizes the number of computations performed in higher order structures of the CNS [49]. EMG recordings during realistic, multi-joint movements show activations in discrete, modular combinations, which supports this hypothesis [50, 51]. The UCM hypothesis differs from the motor synergy hypothesis in several key areas. Rather than reduce the dimensionality of the output space, synergies of elemental variables (e.g. the rotations shared by the shoulder, elbow, and wrist joints) are used to stabilize the performance variable (e.g. the endpoint coordinates of the hand) [52]. The manifold is the set of these elemental variable points that are organized according to some imposed physical criteria. Higher level motor circuits in spinal cord and CNS, would act in the space of the elemental variables and organize covariation of these points within the UCM [52, 53]. This framework suggests that the controller (higher level circuits) exerts minimal control over elemental variables when within the UCM, and act to return these variables to the UCM when deviation occurs.

A cortical role that lies somewhere between the force-control model and equilibrium point model could be termed end effector control. The force-control model would identify this reference frame as the extrinsic kinematics. A purely end effector neural representation, however, points to a higher level control by cortex. Rather than supposing that movements are generated by complex joint angle and muscle kinematic and kinetic computations at multiple reference frames, the theory suggests that motor cortical networks delegate this responsibility to downstream systems. The predominant parameters being encoded would be related to how the end effector moves. The work by Georgopoulos et al [6, 54] showed impressive modulations in M1 neurons with respect to end effector movement direction. Single M1 neurons exhibited cosine-tuned directional preferences (discussed more in Chapter 2) and the population represented enacted movements as the vector sum of the individual units, termed a population vector. Additional work by this group introduced further evidence of a largely end effector-centric neural representation. The activity within motor cortical populations, even of a single neuron, can encode multiple parameters including hand movement direction in 2D space, velocity, and acceleration [55, 56]. In addition, the representation of these can vary on a moment-to-moment basis throughout a task [5]. These results do not act to fully disprove either force-control or equilibrium point models. The results from the Georgopoulos studies, together with the evidence from the previous models demonstrate the diversity of parameters which M1 may represent. Higher-level cortical commands could very well be one of the several parameters represented by motor

cortical neurons.

1.3 Cognitive functions of motor-related cortex

Further evidence for higher-order cognitive functions of motor-related cortex comes from decision making studies. The initiation of a movement is often thought of as the surpassing of a decision threshold. Within single or populations of neurons, multiple possibilities are considered in terms of the activity of the neuron(s). Support for the various choices could come either internally or from accumulated sensory information. Many of the same regions with motor-related modulations such as PPC [57, 58] and PMd [28, 59] have been found to encode sensory evidence in sensorimotor transformation tasks. This suggests a tremendous overlap between motor and cognitive areas of the brain. An example of this comes from the work by Shadlen and colleagues in a two-alternative forced choice paradigm [57]. The average firing rate from a population of 54 LIP neurons (located within PPC) reflected the coherence of the random-dot motion visual stimuli. The onset of neuronal firing rate across the population was less steep when the evidence was less clear. LIP receives many inputs from visual cortex and accumulates visual evidence for motor decisions [60, 61]. Although shown in a saccade study, work by Cisek and Kalaska showed that reaching decisions were represented in PMd [28]. PMd provides dense inputs into M1, analogous to LIP inputs into frontal eye field for saccades. More recent work has identified a decision circuit between PPC and PMd [62].

The multilayered information content of the motor-related cortical areas may be

inconvenient for the purpose of clear functional segregation, however this may underlie how intertwined motor and decision circuits are in the motor system. The ability to evaluate alternative outcomes and provide motor output commands within the same cortical area could be advantageous biologically. Furthermore – and to consider from the perspective of brain-machine interface development – this expands the quantity and type of information that can potentially be extracted from the brain using intracortical multielectrode arrays. Cognitive neural prosthetics (CNP) have been proposed to extract the cognitive state of the subject rather than strictly motor commands [63-65]. This will be further discussed within the context of BMI development.

1.4 Neural representations of bimanual movements

A phenomenon almost entirely unique to upper limb movements is the ability to coordinate the two limbs with high spatiotemporal precision, termed bimanual coordination. There are several different definitions of bimanual coordination throughout experimental and clinical studies. In the most general sense, a movement has been considered bimanual when the two arms are coordinated either simultaneously [66] or sequentially [67]. The two limbs are often coupled temporally such that the in-phase or out-of-phase movements can be reliably performed with high synchrony. A strong preference for temporal coordination suggests that a bimanual action is not simply the linear superposition of two distinct motor plans. It has been shown through lesion studies that interhemispheric connections play a major role in establishing bimanual motor routines [68, 69]. Spatial coordination in split brain patients is greatly

reduced, however the temporal coordination remains intact [70]. It has been proposed that the temporal coordination is localized within central pattern generator (CPG) circuits of the spinal cord, strengthened by findings that rhythmic, bilateral movements that could be produced following high spinal transections [71]. Because CPG circuits are modulated by cortical and subcortical efferent projections, the motor structures of the brain may enact an indirect role of temporal coordination.

To study bimanual neurophysiology and the single cell level, the most common experimental model has been rhesus macaques. Despite some behavioral differences such as less lateralization/handedness compared with humans [72], rhesus monkeys naturally couple and decouple two arms in a spatiotemporally precise way, similar to bimanual movements in humans. One of the earliest studies of specialized bimanual function in primate cortex was by Tanji et al during a key-press task [73]. This study found that 28% of SMA neurons and 16% of premotor neurons exhibited limb-specific (only left/right/both) activity before movement initiation. Brain imaging [74] and EEG [75] studies have shown increased SMA activation that is specific to bimanual movements. Later work by the Vaadia group found an even larger percentage of SMA neurons with bimanual task-related activity [76]. These two groups both investigated whether this bimanual-specific activity also occurred in M1, but their results differed. Tanji et al found almost no M1 cells with bimanual modulation [73], but the Vaadia group reported 69% of M1 neurons with activity specific to bimanual movements compared to 64% of SMA neurons in a bimanual center-out reaching task [77].

The different results could be a byproduct of testing reaching movements (Vaadia) instead of tapping movements (Tanji). Furthermore, the Vaadia results were found in a series of additional studies [78-80]. SMA seems an especially likely candidate for bimanual coordination when considering the location along the sagittal sulcus as well as anatomical evidence. A study in macaques found dense callosal projections from the hand representations of SMA to the same area in the opposite hemisphere [81, 82]. These studies found callosal M1 projections to be much more diffuse.

The phenomenon of bimanual-related (BR) activity is a multi-layered question. The existence of BR-type M1 and SMA neurons is typically identified by looking at peri-event time histograms (PETHs). BR neurons will show strong bursts of firing in a particular direction during exclusively bimanual or unimanual movements. The Georgopoulos cosine-tuning model has been well-established to describe unimanual reaches in contralateral motor cortical neurons [6]. It was initially unclear how neuronal tuning would change, if at all, when the enacted movement was bimanual. It has also been shown that M1 and SMA neurons have both contralateral and ipsilateral arm directional tuning [73, 83]. Furthermore, the preferred directions (PDs) of tuning curves for the contralateral and ipsilateral arm of M1, SMA, and PMd neurons were highly correlated [80].

If single neurons in motor-related cortex represent movements of each arm individually, how could a neuron encode both movement directions simultaneously, as in a bimanual movement? A linear model would suppose that the neural representation

of bimanual movements would be simply the linear combination of the contralateral and ipsilateral commands. A comprehensive study by Donchin et al [76] refuted the claim that BR neural activity could be explained by linear combinations of unimanual activity. In addition, the study showed that it could not be explained by differences in kinematics or EMG activity. With these alternative explanations rejected, the neural activity in M1, SMA, and PMd must reflect some specialized cortical processing associated with bimanual coordination. Further work has shown that during bimanual movements, the PDs of these neurons shift from the unimanual contralateral and ipsilateral PDs [78]. The contralateral PD, on average, is shifted much less than the ipsilateral PD. The directional tuning of neurons to each arms' movements is combined in a nonlinear mechanism which has been proposed to be a byproduct of callosal inhibition [78]. The network/corticocortical mechanisms which establish bimanual modulation properties M1, SMA, and PMd remain largely unknown. Further discussion of intercellular mechanisms would distract from the focus of the present project, however an understanding of this component in the future may play a key role in understanding the cortical role in bimanual motor control.

2. Brain-machine interface development

Brain-machine interfaces (BMIs) are technologies designed to facilitate mobility and limb function for millions of people suffering from paralysis, neurological injuries, neurodegenerative diseases, and limb loss [84]. Among these people, the spinal cord or peripheral areas often suffer severe trauma which have few viable treatment options and the patients suffer from poor quality of life [85, 86]. Fortunately, the regions of the brain which output motor commands and receive sensory information, such as M1 and S1, are often entirely intact. BMIs are a subfield of neuroprosthetics with a goal to extract the user's motor commands from cortical neuronal activity to control an external device, such as a prosthetic limb. As discussed previously, motor-associated cortical areas encode a wide variety of information related to motor execution, motor planning, and cognitive function. Research related to BMIs has grown immensely over the past twenty years [87-89]. The impressive progress has resulted from three major areas of advancement:

(1) Improved understanding of neurophysiology

(2) Technological improvements

(3) Improved strategies for decoding motor commands

The first of these provides the biological foundation for BMIs and was discussed in the previous chapter. Important work in the latter two areas will be discussed in the present section. These three areas will again be discussed with respect to the findings of this thesis work.

2.1 Technological advancements in brain-machine interfaces

2.1.1 Electrodes and neural signal acquisition

Neural signals can be acquired for a BMI using a variety of techniques. This ranges from noninvasively with scalp/electroencephalogram (EEG) electrodes [90], slightly more invasively with electrocorticogram (ECoG) electrodes [91], to most invasively using intracortical multielectrode arrays (MEA) [92]. Although the research in the present project uses exclusively invasive MEA recordings, it is worth discussing the differences and advantages of each approach. EEG systems require no surgical implantation and have been successful in human studies for communication [93], target-selection [94], and 2-D cursor control [94, 95]. The EEG signal is low bandwidth and thus has limited ability to extract complex kinematic parameters. The most successful EEG BMI implementation has been the P300-based BMI which has enabled locked-in or ALS patients to communicate with the outside world [93, 96]. The P300 evoked potential is represents the parietal cortex response to a preferred versus nonpreferred stimulus [97]. The recorded EEG signal is typically less that 30 Hz and represents field potentials of large populations of neurons across several brain regions. The spatial resolution of the signal is poor, and is further deteriorated by passing through brain tissue, bone, and skin before reaching the scalp electrode.

ECoG systems record higher frequency 30-100Hz signals which have been shown to be correlated with single unit action potentials in the surrounding tissue [98]. ECoG electrodes are placed below the dura and typically over cortical gyri to record from

neurons perpendicular with the plane of the electrode. Similar to EEG systems, ECoG-based BMIs have achieved success in human studies to control a 2D computer cursor [99]. Researchers see ECoG as a unique opportunity to obtain an accurate representation of single-unit activity from large populations of neurons with improved long-term stability and reduced invasiveness compared to intracortical MEAs [100].

The earliest and still most direct method to record activity from cortical neurons is with intracortical electrode arrays. The fundamental unit of communication in the brain is the action potential, or spike, which can be detected by a microelectrode when located within 50-100 μm of the neuron [101, 102]. An intracortical electrode-based BMI would detect and decode the spiking pattern of populations of neurons for the purpose of controlling some external device. A series of studies by Fetz and colleagues found that single-unit cortical activity could be volitionally modulated in monkeys [103-106]. This direct user control over the activity pattern of a single neuron, dissociated from the related muscle movement, provided the first proof-of-concept for volitional control of cortical neurons. This was an important early step towards cortically controlled BMIs. Later work by Schmidt further demonstrated an even finer level of volitional control such that the firing rate of a single neuron could be modulated to as many as eight different frequency gradations [107]. Quantifying this result in terms of bits of information per second, the volitional control of even a single neuron gave a 2.45 bits/sec information output rate compared to 4.48 bits/sec with wrist flexion/extension (normal motor output). Schmidt proposed that neural signals may be sufficient to control an

external device given advances in electrode stability and signal processing.

Much of the modern success of BMIs is owed to the technological development related to MEA improvements in the approximately thirty years that followed. The Utah Intracortical Electrode Array was developed in the early 1990's using a silicon-based penetrating electrode array with 100 needle-type electrodes, specifically designed for implantation in the cerebral cortex [108, 109]. The 96 channel Utah array (now a product of Blackrock Microsystems) has remained a critical component of intracortical BMI systems even to this day [110, 111]. By 2000, Nicolelis and colleagues pioneered a large-scale multi-site neural recording paradigm capable of recording from hundreds of neurons throughout sensory and motor cortices [92, 112]. With large neuronal populations of task-related M1 and ventrolateral neurons, Chapin and colleagues demonstrated for the first time the real-time brain control of a robotic arm in in rats [113]. As the number of recorded neurons increased, it was shown by several research groups that primate reaching and grasping could be driven by an intracortical BMI [114-116].

MEAs implanted within the cortex have clear advantages for BMI engineering purposes, but the potential danger of chronic implants often overshadows the tremendous potential. Most commonly, MEAs are lowered into the cortical tissue at an angle orthogonal to the plane of the cortical surface to a depth of 0.5 to 1.5 mm [117, 118]. Upon insertion, the electrodes must penetrate the brain parenchyma which causes acute local neural and vascular damage, increasing the risk for CNS infections [119]. In

the days and weeks that follow, a cascade of tissue responses to the implant occur which act to isolate the foreign MEA materials and protect the brain (review by Polikov et al. [120]). This immunological process is referred to as the foreign-body response. Astrocytes in the brain proliferate and become reactive causing increased extracellular matrix production and gliosis. After several weeks a glial scar forms around the electrodes to encapsulate the foreign body and reestablish the blood-brain barrier [121]. Once encapsulated, the electrode becomes nearly electrically isolated from the brain due to the high impedance of the glial scar. In BMIs, this can contribute to the loss of quality recorded units over time. Efforts to limit the injury and improve the viability of chronic implants have prompted new electrode designs. This research has focused on electrode geometry and spacing [92, 117, 122], electrode coating materials [92, 123], or use of bioactive molecules to promote positive tissue integration [124]. Proof of the safety and long term efficacy of chronically implanted MEAs is a key step in the clinical translation of BMIs in the coming years.

2.1.2 End effectors for BMIs

Other technological advancements have centered on the end effector of the BMI. The motor goal of BMIs is to enact highly realistic walking or upper limb movements in the absence of healthy limbs. Limb kinematic are often characterized by the degrees of freedom (dof) – a term common in robotics to specify the number of ways that a limb (or artificial limb) can move. The human arm (excluding hand) is considered to have seven degrees of freedom [125]. Early BMI work in rats demonstrated a single dof to position

a robot arm [113]. Within four years, monkeys in several labs learned to control a three dof robotic arm for reaching and grasping [116, 126]. A self-feeding prosthetic arm for rhesus monkeys was developed by the Schwartz lab using five dof [127]. The DEKA prosthetic limb was developed shortly thereafter offering a highly realistic six arm dof and four hand dof (DARPA's Revolutionizing Prosthetics program, 2006). Although some dof were removed by wrist angle fixation, the DEKA arm was utilized most recently in a human study where tetraplegic patients with M1 implants were able to reach and grasp objects using modulations of cortical activity [111]. The rapid progression of research has resulted in prosthetic limbs approaching the complexity of natural limbs, but intuitive enough such that they can be controlled with a BMI. Psychologically it is important for the subject (monkey or human) to feel a sense that the prosthetic limb is an extension of their own body.

Ongoing work in the Nicolelis lab is exploring the use of realistic virtual reality avatar body representations for BMI applications [128, 129]. The sense of being ability to control the movements of an object such as a limb is known as agency [130]. In virtual reality studies, users have reported a sense of agency for external devices, such as virtual hands [131]. The agency of the virtual hands was manifested both perceptually and in oxygenation changes in the brain detected by fMRI. If the external device not only feels under the user's control, but actually feels like an extension of one's body, this is known as incorporation. Full incorporation of an external device has been demonstrated using experiments such as the rubber hand illusion. In this experiment, the tactile sensations

from one's own hidden hands conflict with visual information from the touching of a visible rubber hand [132]. This is an example of creating incongruence between visual and sensory input to the external device. Detectability of the incongruent sensory information is a key marker for body incorporation. Incorporation is a stronger phenomenon than agency, in which the user not only feels control over the object's movements but possesses a sense of ownership of the object [130]. It has yet to be demonstrated how BMI control of artificial limbs effects the user's agency or incorporation of the external device.

2.2 Decoding movements from neural activity for BMIs

The third area of research which has greatly contributed to intracortical BMI success has been improved neural decoding methods. It should be noted that neuroscientists are still far from understanding the complex rate encoding, temporal encoding, and population encoding of motor neuronal populations in the brain. Certain aspects of neural encoding have been understood through carefully designed experimental paradigms and trial-averaged spike histograms. Even in the cleanest analysis, however, there is biological "noise" in virtually all central neurons with a poorly understood function [133]. Fortunately, a comprehensive understanding of single cell and motor network computations does not preclude a clinically relevant BMI system. Variance in the neuronal discharge can be largely accounted for by changes in several parameters of movements – often simply the kinematics or kinetics. This correlation is strong enough to be exploited in fairly straightforward neural decoding

algorithms.

Regardless of which algorithm is used, the first step is to characterize each recorded neuron so that modulations in its activity can be predictive of a motor parameter. This is typically accomplished by fitting a set of parameters to the activity according to a mathematical model. The method of fitting movement parameters to neuronal modulation is a question of major clinical relevance. Experimentally it is common to train the model on several minutes of the task when the arms are moving naturally [116, 126]. With this being impossible to obtain clinically from patients lacking upper limb mobility, there is a need for efficacious training paradigms that do not require one's own arm movements. A co-adaptive framework was proposed by Taylor et al [116], where the movements would be enacted by cortical control from the beginning. Over the course of trials which showed both the cursor and the target, the tuning properties were iteratively refined. Furthermore, this technique resulted in improvement from one session to the next. Other studies have requested the subjects to imagine movements during model training [111, 134] or had the subjects passively observe end effector movements [135, 136]. This remains an actively researched topic and is a subject which will be discussed further in later sections.

2.2.1 Early approaches: Population vector and the Wiener Filter

The basis for the theory that neural activity can be modeled as a simple function of motor parameters (or in actuality, the inverse) stems from the work of Georgopoulos et al. [6, 54]. Recordings from M1 neurons revealed directional preferences –

mathematically described by a simple linear relationship as shown in Eq. 1 (from [6]):

$$\mathrm{d}(\mathbf{M}) = b_0 + b_1 \cos\theta_{PM} \qquad (1)$$

where d is the discharge rate of an M1 neuron, θ_{PM} is the angle between the neuron's preferred direction and the direction of movement, with b_0 and b_1 are coefficients determined for each neuron. Substituting $\theta_P - \theta_M = \theta_{PM}$ and solving for θ_M:

$$\theta_M = \theta_P - \cos^{-1}\left(\frac{d(\boldsymbol{M}) - b_0}{b_1}\right) \qquad (2)$$

it becomes more clear how the single-neuron pointing vectors are computed. Knowing the discharge rate of the neuron, the optimal coefficients, and the preferred direction θ_P, the direction of movement θ_M could be computed. The single-neuron pointing vector was therefore a vector in the direction of θ_M with a magnitude scaled by the firing rate of the neuron. The vector sum of all single neuron vectors was termed the population vector [6]. Several research groups have utilized a population vector-based algorithm to compute 3D upper limb kinematics in non-human primates [116, 135] and 2D cursor control in humans [137].

The discrete-time Wiener filter is an optimal linear finite impulse response filtering method which has also been successfully applied to BMI systems. The algorithm is based on the time-series signal processing algorithm pioneered by Wiener and Kolmogorov [138, 139]. The Wiener filter is commonly used to reduce the noise of a signal or estimate a desired signal in a way that minimizes the expected mean-square

error. With motor command signals being embedded within noisy neural activity, this relatively simple approach was a good starting point for neural decoders. BMIs using a Wiener filter have been successful in predicting arm movement trajectories that correlate with actual trajectories with correlation coefficients of around 0.8 [114, 115]. It may initially seem surprising that the high dimensionality of the input space (hundreds of millions of motor cortical neurons) can project to a low dimensional output trajectory using a linear model. The projection is performed on a set of bases that are continuously following the input signal (the past input samples) [140]. That is, using a short history of the neural activity, it is possible to reliably extract the most relevant two or three motor parameters from the activity of large populations of neurons. In the most common implementation of the Wiener filter, the neural input $\boldsymbol{x}$ and kinematic output $\boldsymbol{y}$ are related as in Eq. 3 (from [140]):

$$y^c(n) = \sum_{l=0}^{L-1} \sum_{i=1}^{M} x_i(n-l) w_{il}^c + b^c \qquad (3)$$

where c is the output dimension, n is the time instance, L is the number of taps, and M is the number of neurons. In Eq. 3, w_{il}^c is the weight for neuron i, during tap l, for output dimension c. The bias term b for each dimension is typically removed by zeroing the mean of input and output. L is commonly set such that the previous 1 s of neural activity is sampled [83, 114, 126]. Given a sampling rate of 10 Hz, L= 10. Despite its simplicity and relative success in low dof BMI studies (2 dof: [134] or 3 dof: [114, 116]), predictions made with the Wiener filter show substantial jitter and noise. Additionally,

the non-probabilistic nature of the decoder makes integration into more sophisticated decoding system difficult.

2.2.2 More sophisticated solutions for neural decoding

The challenge of neural decoding in BMI research has spurred the use of increasingly complex algorithms that have shown improved performance in certain applications (see review by Bashashati [141]). The different methods that can be used generally falls into two groups: linear and non-linear. Linear methods are generally less computationally demanding, yet ascribe a linear mapping between neural activity and limb movements. A probabilistic linear method, with marked advantages over the Wiener filter, is the Kalman filter. The Kalman filter [142] applies recursive Bayesian inference to compute an *a posteriori* probability of hand kinematics based on an observed sequence of firing rates [140, 143]. The posterior probabilities are the product of a likelihood term and an *a priori* probability as in Eq. 4 (from [143]):

$$p(\boldsymbol{x}_k|\boldsymbol{z}_k) = \kappa \; p(\boldsymbol{z}_k|\boldsymbol{x}_k) \int p(\boldsymbol{x}_k|\boldsymbol{x}_{k-1}) p(\boldsymbol{x}_{k-1}|\boldsymbol{z}_{k-1}) d\boldsymbol{x}_{k-1} \tag{4}$$

where $p(\boldsymbol{z}_k|\boldsymbol{x}_k)$ is the likelihood term - an estimate of the probability of the firing rates given hand kinematics. This likelihood is multiplied by the integral term, called the prior. In a reaching experiment, the $p(\boldsymbol{x}_k|\boldsymbol{x}_{k-1})$ prior term models how the hand moves and the $p(\boldsymbol{x}_{k-1}|\boldsymbol{z}_{k-1})$ term represents the kinematics at the previous time instant [143]. When both the likelihood and prior models are linear and Gaussian, the recursive update algorithm within the Kalman filter provides the optimal and exact estimate of

the posterior probability.

The Kalman filter implementation for neural decoding purposes is described fully by Wu et al. [143]. There are two steps to the algorithm: predict and update. In the predict step, the mean and the covariance values for the kinematics from the previous iteration are used to predict the kinematics in the current iteration. The results of this prediction serve as the prior for the current step. In the update step, the posterior mean and covariance matrix of the kinematics are computed using the priors, as in Eq. 4.

The main difference of the Kalman filter from the Wiener filter is the probabilistic approach. At every time point, an estimate of uncertainty is computed in terms of an error-covariance matrix. The drawback from this model (and the cause of its simplicity) is the assumption of linearity in the models describing neural activity and kinematic evolution. Despite the weakness of this assumption, the Kalman filter has been successfully implemented into real-time BMI systems [110, 111, 143, 144]. Some BMI groups argue that the linearity assumption affects algorithm performance during real-time control in a much more subtle way than previously thought [145].

Much of the decoding algorithm development in the past decade has focused on non-linear models [146-150]. A quadratic tuning model was implemented by Li et al [150] and was much more predictive of neural firing rate than a linear model. The linear model, Eq. 5:

$$\#\ spikes = A \cdot vel_x + B \cdot vel_y + C \qquad (5)$$

was modified to add velocity squared terms as in Eq. 6:

$$\#\ spikes = A \cdot vel_x + B \cdot vel_y + C \cdot \sqrt{vel_x^2 + vel_y^2} \qquad (6)$$

This change increased accuracy of offline kinematic reconstructions over standard linear models (Kalman and Wiener filters). Another nonlinear approach, called a particle filter or sequential Monte-Carlo, is a decoding algorithm being researched by several groups for BMI applications [146, 147, 151]. The particle filter is a recursive Bayesian estimator based on non-parametric probability distribution representations and stochastic simulation [152]. The major disadvantage of the particle filter is heavy computational cost, which makes it more difficult to implement into real-time BMIs.

Another approach is to decode from individual neuron spike times, rather than instantaneous firing rates. These decoders are called point process filters and they use models of spike trains as discrete events, or point processes. Work within the Donoghue group has focused on developing a point process filter, analogous to the Kalman filter, which used a Gaussian representation for uncertainty in state estimates and an inhomogeneous Poisson model for neural activity [153-155]. Although this has shown promising results offline [155, 156], point process filters have yet to be implemented in an online BMI.

A different nonlinear technique which has been successful in both offline and online BMIs is artificial neural networks (ANN) [149, 157, 158]. Most recently, the Shenoy group has implemented dynamical variations of these, known as recurrent

neural networks (RNN), to control a virtual cursor in a 2D point-to-point reaching task in a real-time BMI [158]. This model emphasizes the recurrent nature of neuronal dynamics, where the activity of a neuron is a function of its own past firing in addition to desired movements. In the study, the researchers overcame a previous challenge of training an RNN model by using an echostate network [159] – a randomly initialized RNN. Using a constrained learning paradigm, the echostate network output (a linear readout of the recurrent, nonlinear units) easily trained the RNN to enable online control [158]. Furthermore, the RNN decoder outperformed the Kalman filter algorithm. Although presented as one piece of the BMI puzzle, neuronal decoding algorithm development and parameter optimization is a field unto itself.

Similar to the work being done for development for decoding algorithms, there are innovations in decoding *strategies* which are important for BMI efficacy as well. These often utilize well-established neural decoders but make modifications to the way is it applied to neural data. Such studies often focus on neuron selection procedures [160, 161], nonstationarities in neuronal properties [162, 163], or parameter optimization [164]. There are countless other studies with novel approaches and modifications which could be discussed. For the purposes of the present review – and to focus this discussion – the remainder of this section will focus on the algorithm most important to the work in the present thesis project. The work within the Nicolelis lab within the past five years has developed a nonlinear decoding algorithm which has shown to be a strong improvement over the three of the most commonly used BMI models: the

population vector model, the Wiener filter and Kalman filter [150].

2.2.3 The unscented Kalman filter for BMI decoding

Improvements to the Kalman algorithm were accomplished by using an unscented Kalman filter (UKF). The most important advance was transitioning to a nonlinear, quadratic tuning model (see Eq. 6) while remaining computationally light. The latter part is not a trivial consideration, even with the rapid improvement of computing power. Future BMIs will be highly mobile systems. The power consumption and weight must be minimized. Similarly, the algorithms must be able to decode signals from large populations of neurons and control prosthetic limbs in real-time. Many of the previous nonlinear models, such as the point process filter and the particle filter have yet to be realized in real-time BMI systems for these and other reasons. The modification to the Kalman filter algorithm which enables nonlinear modeling is termed the unscented transform [165]. It uses a deterministic sampling method to approximate non-linear function evaluation on random variables. Using the unscented transform, a set of simulation points (rather than a single value), called sigma points, are selected around the mean. These points are then propagated through the non-linear model, resulting in a mean and covariance estimate for the effect of the non-linear model on the distribution. The decoding result is more accurate than the Kalman filters [150, 165, 166]. This approach also eliminates the need to compute Jacobian matrices as in the extended Kalman filter, which is not as accurate of an approximation.

A second important feature of the UKF described by Li et al. [150] is that it takes

advantage of patterns of movements that are found within a given task. Taking advantage of these patterns has been shown to improve accuracy of BMI-enacted movements. The state variables were extended to keep a history (n offsets) of the desired hand movements. This allowed an autoregressive (AR) movement model and tuning model for each of the n time offsets. Using an n-th order UKF, position and velocity are computed using the quadratic tuning model (Eq. 6) using n taps of position and velocity. The standard Kalman filter used in previous BMI studies [110, 111, 143, 144] uses only a single tap to predict the future parameters. The optimal number of past and future taps was found to be task dependent. In a smoother movement with slow, predictable trajectories, adding more taps resulted in improved predictions offline [150]. More variable reach trajectories and speeds, such as the center-out movements used in this project, were best predicted using fewer (3-6) taps.

The algorithm [150, 165] follows the same general two-step predict and update structure as the standard Kalman filter. The predict step is very similar. The prior term models how the hand moves and is computed using the conditional probability $p(\boldsymbol{x}_k|\boldsymbol{x}_{k-1})$. Evaluating the non-linear tuning model on the sigma points ($\chi_0 \dots \chi_{2d}$) (in a state space of dimension d) produces an estimate of the neural firing:

$$\hat{Z}_0 \dots \hat{Z}_{2d} = f(\chi_0 \dots \chi_{2d}) \qquad (7)$$

The mean and covariance of the predicted neural firing are then computed using the weighted sigma points:

$$\hat{z}_t = \sum_{i=0\ldots2d} w_i Z_i \quad (8)$$

$$P_{zz,t} = w_0(Z_0 - \hat{z}_t)(Z_0 - \hat{z}_t)^T + \sum_{i=1\ldots2d} w_i(Z_i - Z_0)(Z_i - Z_0)^T + Q \quad (9)$$

where Q is the observational noise fit during training. From the predicted neural firing covariance matrix, the optimal Kalman gain K can be computed. In the final step, the state mean and covariance are updated using the previous state and the predicted neural firing $\hat{z}_t$ and $P_{zz,t}$:

$$\hat{x}_t = \hat{x}_{t'} + K(y_t - \hat{z}_t) \quad (10)$$

$$P_{xx,t} = P_{xx,t'} - P_{xz,t}({P_{xx,t}^{-1}}^T)P_{xz,t}^T \quad (11)$$

where y_t is the spike data and $P_{xz,t}$ is the cross covariance of state and observation. The unscented transform avoids costly numerical calculations while yielding an accurate approximation of the posterior distribution under the non-linear model.

The nth order UKF presented by Li et al has become the standard decoding model used in the Nicolelis lab since its development. Certain properties of the model even suggest that it may be applied to training paradigms in the absence of arm movements. The UKF could be trained during passively observed movements, when the user is attending to the task and neural activity is simultaneously recorded [129]. UKF decoded neural activity during passively observed realistic avatar limb movements could reconstruct the movement trajectories with very high fidelity offline [129]. This passive observation phenomenon has been observed in previous work within PMd and M1 [129, 167, 168], although it has only recently been exploited for BMI applications. Recent

work in the Nicolelis lab has shown that the UKF can function in an adaptive manner, updating parameters using Bayesian regression [169]. This approach is further advantageous because it would require no information about the user actions and can update in the background without explicit recalibration. Notwithstanding the improvements made by our lab and elsewhere, there remain several key questions. First, it is unknown how well these models can generalize as experiments beyond oversimplified, lab-setting movements towards real-life applications. Second, all previous models aim to control a single limb and prior to my work, it was unknown how to model multiple limbs simultaneously. Lastly, there remains the challenge of utilizing the right model in the right context. For example, a certain model might be optimal in one behavioral state (left arm movement), but not for another (bimanual movement). The ability to identify differences in differing "states" to guide model selection is another key area for improvements. I address these opportunities to advance the UKF decoding strategies for bimanual BMIs within Chapter 9.

3. Cortical correlates of Fitts' Law

In the effort to advance the sophistication and naturalism of BMIs, it is beneficial to take a brief step back to understand the processing steps that go into even very basic reaching movements. In goal-directed reaching movements, there exists a known or estimated endpoint. The properties of the endpoint can often be just as important as the location. In daily life, we encounter a wide range of endpoints: push-open doors, a can on a grocery store shelf, or simply reaching out for self-protection from incoming threats. Fortunately, we adapt the arm movements in a context-dependent way which benefits whatever motor parameters that we favor. For the examples given, the emphasis could be spatial precision (picking the right can from a shelf), reach speed (safety concerns), or crude movements that optimize force generation (opening a heavy door). Notably, the first two these are tightly related. Careful, spatially precise movements are generally slower in order to preserve the accuracy of the reach. The act of processing sensory information and converting this into action is termed sensorimotor transformation (see Section 1.3). In the present context, the size of the target is the sensory input affecting the action, which is a reaching movement. This intuitive and well-known behavioral phenomenon is quantified in Fitts' law [170-172]. Fitts hypothesized that this tradeoff existed due to a limitation of information capacity in the motor system. The law derived by Fitts [170] and Shannon [172] states that there exists a relationship between the target properties (size, distance from reach origin) and

the speed that a person moves their arm towards a target. This is quantified as shown in Eq. 12 and Eq. 13:

$$ID = log_2 \frac{2D}{W} \qquad (12)$$

$$T = a + b \cdot ID \qquad (13)$$

where ID is the index of difficulty for a reach which is simply a function of the distance to target D and the width of the target W. The time to reach (or inversely, the velocity) was proposed to be a linear function of ID and b is the information capacity of the system. More simply, b quantifies the degree that target difficulty influences the motor system's decision to reduce velocity. This law has held for a wide variety of movements and suggests underlying machinery of the motor system. In other words, Fitts used behavior to make conclusions about how the nervous system generates movements. In this study, I look from the reverse perspective – looking at the motor cortical firing to understand which parameters are being represented by neurons when issuing motor commands to create behaviors.

Fitts' law considerations have been critical for computer interface design in the past 20 years [173], resulting in improved pointing devices, screen layouts, and menu designs. Recently, the BMI field has used Fitts' law as a tool to measure performance of neuroprosthetic systems [174]. As BMIs continue to develop, interfacing with computers will need to be improved in much the same way as traditional computer interaction. Rather than gaining the user intentions directly, I hypothesize that a BMI

system would be able to extract both the movement trajectories and goals (e.g. speed vs. accuracy) from neural signals. This study [175] was the first to identify the cortical correlates of Fitts' law and demonstrate that both kinematics and target-related properties can be extracted using a simple BMI decoding approach.

3.1 Electrode implantation and experimental design

To conduct this study, one male and one female rhesus monkey (M and N, respectively) were chronically implanted with multielectrode arrays in M1 and S1 of right and left hemispheres using established surgical methods [92]. Within each hemisphere, two 96 channel arrays were placed in cortical areas corresponding to the leg and arm representations in S1 and M1 (Fig. 1B). Each array consisted of two 4x4 grids of independently movable electrode triplets. Each of the triplets was comprised of electrodes of different lengths in 300 μm intervals which allowed us to sample neuronal activity from different depths of cortical tissue. For the purpose of this study, neural activity was recorded from depths of 1.2-2.0 mm into the arm representation of the right hemisphere M1 (both monkeys) and S1 (only monkey M) (Fig. 1B). Recorded signals were amplified, digitized, and filtered by a multichannel recording system (Plexon Inc., Dallas, TX, USA). Neuronal spikes were sorted on-line using waveform template matching and threshold features built into the spike sorting software.

We developed a variation of the original Fitts experiment by training each monkey to perform two dimensional center-out reaching movements towards peripheral targets. The monkey placed its working hand on a hand-held joystick located

at waist level in front of the monkey (Fig. 1A). For both monkeys, the working hand was chosen to be the left hand because the quality of the neural recordings was better in the right hemisphere than the left. Movements of the joystick in the X (left-right) direction and Y (forward-backward) directions were translated to X (left-right) and Y (up-down) movements of a computer cursor on the display screen. Trials were initiated by holding the joystick within a central target for a random interval between 800 and 1500 ms. After this hold period, the central target would disappear and a peripheral target would appear on the screen. The monkey was required to move the cursor radially toward the peripheral target to complete a correct trial and receive a juice reward (Fig. 1D,F). To simulate a range of ID values from the Fitts' law formulation (Eq. 12 and 13), the peripheral target was designed to be an arc of variable width: either 8, 15, or 22° aligned on the center of the screen (Fig. 1E). The target arc appeared as a thickened arc along the perimeter of a grey boundary circle. There were four potential target locations: 45, 135, 225, 315° relative to the center of the screen (Fig. 1C). A correct trial required the monkey to move the cursor through the specified arc without first leaving the boundary circle. Trials where the monkey made errant reaches resulted in a 500-ms timeout period and no juice reward. The trial sequence is illustrated in Fig. 1D.

3.2 Results

3.2.1 Fitts' Law in reaching movements of rhesus monkeys

The first analysis was to determine if Fitts' law existed in rhesus monkeys. Trials were divided up both by target location and by target size (TS). Mean reach trajectories

for each trial category were computed offline (Fig. 1F, 3A-B). Several components of these reaches reflect TS-related differences. Reaction time (RT) was defined as the time elapsed between target onset and initiation of movement. I developed an algorithm which identifies specific patterns in joystick velocity and acceleration to identify the movement onset (See Appendix B). This algorithm was validated by visual inspection of correct movement onset identification on greater than 95% of tested trials. I found that RT was elongated for smaller targets ($p<0.05$, Kruskal-Wallis test; Table 1). This effect held true in both monkeys for each of the four reach directions (Fig. 2). One observation was that the most difficult target size (8°) was handled very differently than the two easier target sizes. This could have been the result of center-out overtraining which had made all except the very small targets very easy to perform for the monkey. Nevertheless, there were consistent trends of longer RT ($p<0.05$; Fig. 2; Table 1) and slower movements ($p<0.05$, Kruskal-Wallis test; Fig. 3; Table 1) as a result of smaller target sizes. Fitting Eq. 13 with parameters from both monkeys, the estimate of information capacity was within a similar range as that of humans from Fitts' original work (10-20 bits/s, Fig. 2D). Thus, Fitts' law held in rhesus monkeys and TS caused similar behavioral changes as were found in previous human studies [176]. I next pursued the identification of the neural correlates of this behavioral phenomenon.

3.2.2 Neural representation of Fitts' law in M1 and S1 populations

Activity of M1 and S1 neurons during center-out reaches follows a characteristic profile each trial. After target onset, activity across the population rises quickly,

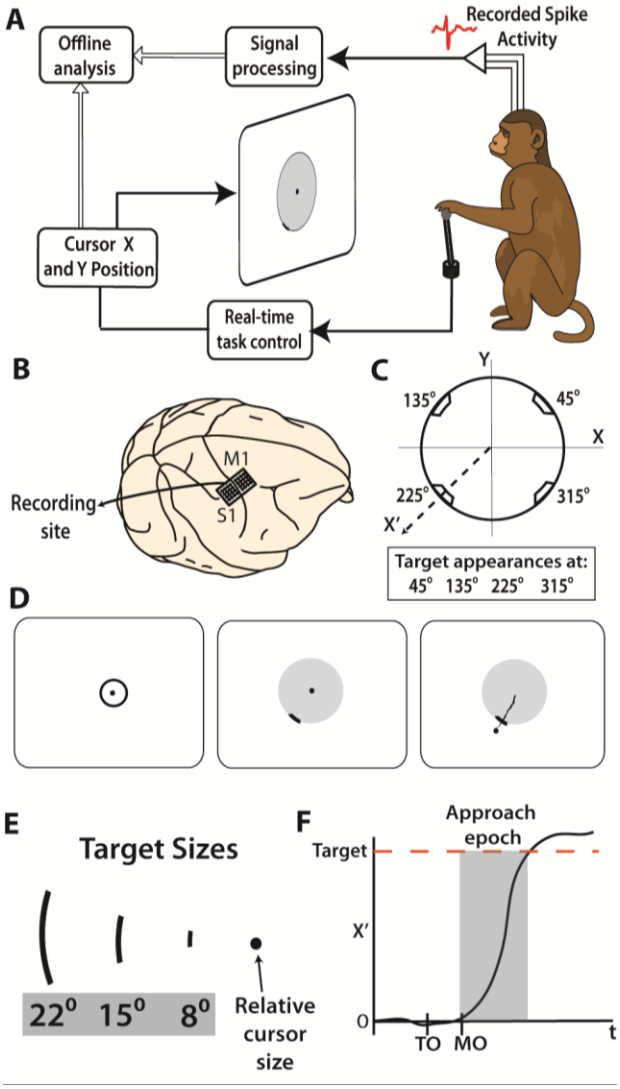

Figure 1: Implantation and experimental protocol. (A) Rhesus monkeys controlled the location of a cursor on a display screen by moving a joystick with their left hand. Joystick kinematics as well as the neural activity were recorded and analyzed offline. (B) 4×4 Grids of 16 electrode triplets were implanted bilaterally in M1 and S1arm and leg regions, however only the right hemisphere arm region of M1 and S1 was recorded from in this study. (C) For each trial, the cursor was to move along the radial origin-to-target axis (X') toward one of four potential target locations. (D) Left to right-typical trial begins with cursor moved within the target at center of screen. After hold period, penalty ring and target arc appear. The cursor is then moved radially through the target arc to receive a reward. (E) Three potential target sizes are shown with respect to the cursor, for size reference. (F) An example of a single trial movement trace is shown. Target onset (TO) and movement onset (MO) are denoted on time axis. The approach epoch that was used in later analysis spanned from movement onset to target acquisition.

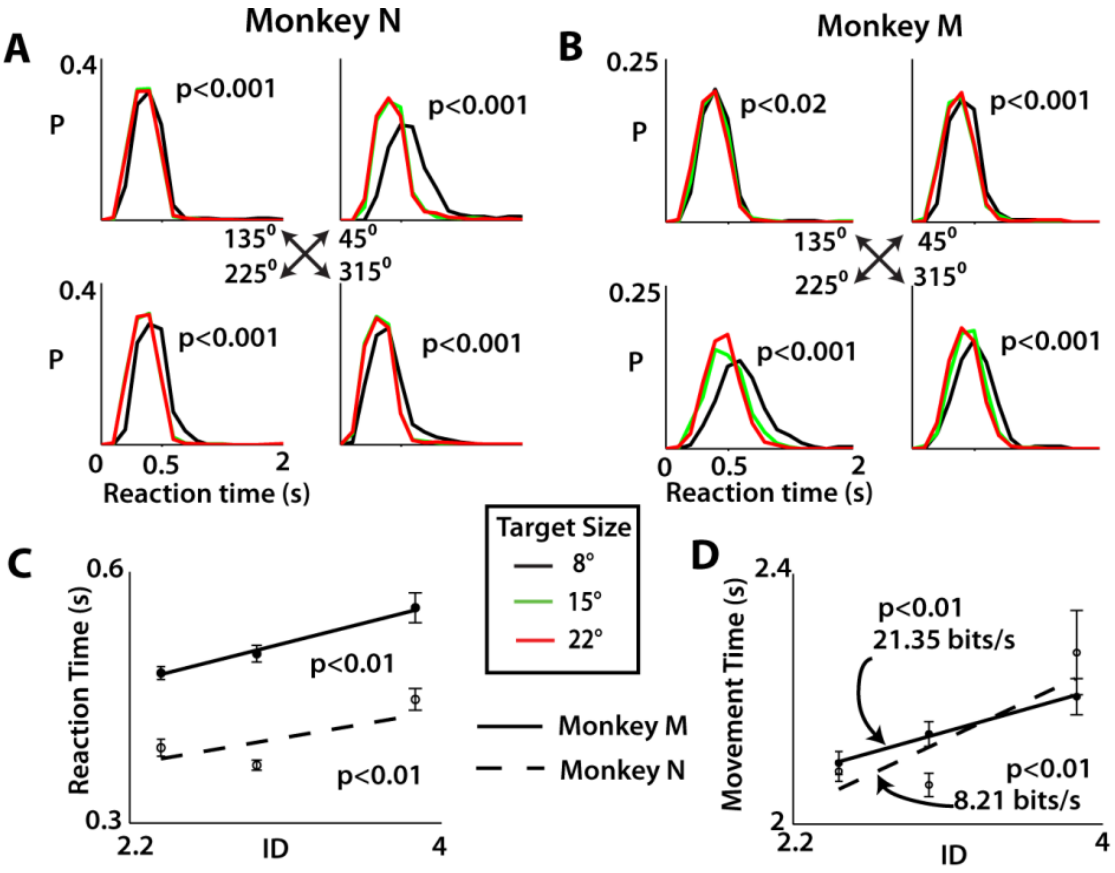

Figure 2: Effect of target size on movements. Distribution of reaction times was computed for each movement direction by monkey N (A) and monkey M (B) with probability "P" shown as a function of RT. A Kruskal-Wallis test was performed for each direction to determine significance of target size on distribution of reaction times (see Table 1). C, Reaction time for trials of the three different indices of difficulty (ID) was fit with linear function and tested for significance using F test. Means for each ID plotted as filled circles (monkey M) and open circles (monkey N). The target size of the trial is denoted by colors specified below panels A and B. D, Movement time for the three ID conditions. A regression line was used to fit all trials and the subsequent inverse of slope yields Index of Performance (IP) in bits/s. Significance was tested in same way as in C. All error bars indicate standard error.

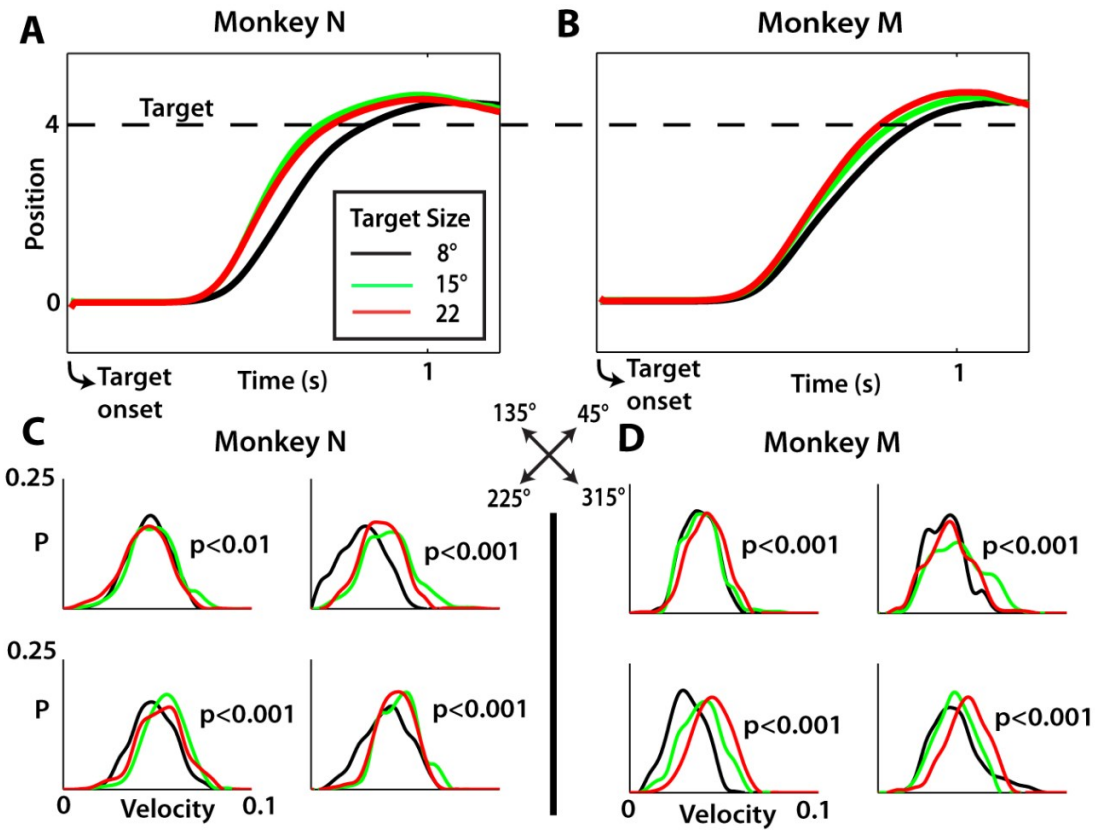

Figure 3: Reach kinematics reflect differences in target size. A,B, Averaged position traces of monkey N and monkey M along the X′ axis from 0 (the origin) to 4 (the target, denoted by dashed line). The target size of the trial is denoted by colors specified in panel A. C,D, Distribution of mean approach velocity for each of the four movement directions with probability (P) shown as a function of mean approach velocity. For each direction, Kruskal-Wallis test performed to evaluate the effect of target size; p-values shown for each separately (see Table 1).

Table 1: Effect of target size on reaction time and target approach time

Direction	Monkey N		Monkey M	
	Target Size x Reaction Time	Target Size x Velocity, TAT	Target Size x Reaction Time	Target Size x Velocity, TAT
45°	p<0.001	p<0.001	p<0.001	p<0.001
135°	p<0.001	p<0.001	p<0.02	p<0.01
225°	p<0.001	p<0.001	p<0.001	p<0.001
315°	p<0.001	p<0.001	p<0.001	p<0.001

Table 2: Effect of reaction time and target size on firing rate slope preceding movement onset

	Monkey N, M1 cells		Monkey M, M1 cells		Monkey M, S1 cells	
	Pref	Least	Pref	Least	Pref	Least
Long RT	0.114±0.01	0.085±0.01	0.232±0.01	0.202±0.01	0.092±0.01	0.096±0.01
Short RT	0.266±0.01 (0.53)**	0.257±0.01 (0.57)**	0.345±0.01 (0.69)**	0.278±0.01 (0.56)**	0.143±0.01 (0.58)**	0.112±0.01 (0.53)†
Small	0.058±0.01	0.077±0.01	0.260±0.01	0.192±0.01	0.058±0.01	0.077±0.01
Medium	0.153±0.01 (0.64)***	0.104±0.01 (0.57)*	0.297±0.01 (0.57)***	0.263±0.01 (0.60)***	0.152±0.01 (0.64)***	0.104±0.01 (0.57)*
Large	0.143±0.01 (0.65)***	0.132±0.01 (0.61)***	0.313±0.01 (0.61)***	0.265±0.01 (0.62)***	0.143±0.01 (0.65)***	0.132±0.01 (0.61)***

*p<0.05, ** p<0.001 short RT vs. long RT, ***p<0.001 medium or large target vs. small target, †not significant.

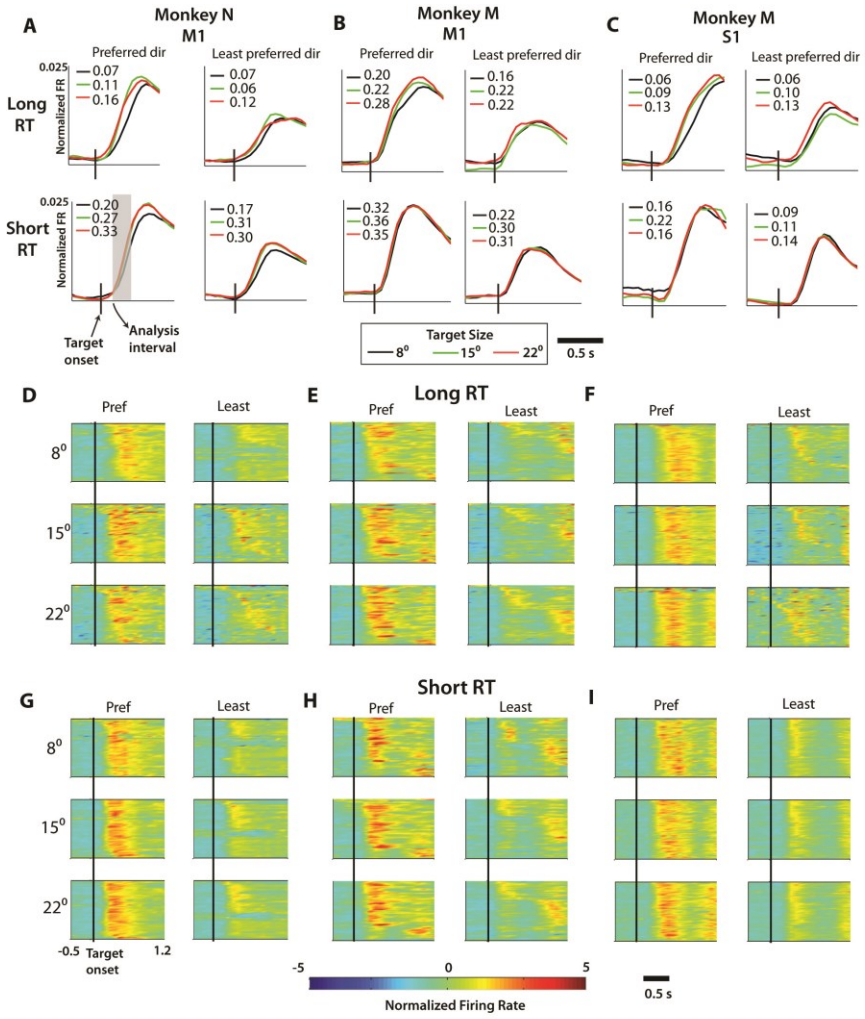

Figure 4: Effect of reaction time on firing rate profiles. A-C, Averaged and normalized firing rate of all recorded M1 cells in monkey N, M1 cells in monkey M, and S1 cells in monkey M. For each four-axis panel, the left column denotes movements in preferred direction of each neuron and right column shows the least preferred direction. The upper and lower rows represent the averaged and normalized PSTH across long and short reaction time trials, respectively. Target size specified by line color (see legend below B). Slopes in spk/s2 computed from regression of normalized firing rate during analysis interval (gray box, see methods). D-F, Population PSTH showing normalized firing rate profiles on long reaction time trials for all cells (ordinate) over time (abscissa) relative to target onset (denoted by vertical black bar) from M1 of monkey N (D), M1 of monkey M (E), and S1 of monkey M (F). For each, the most preferred (left) and least preferred direction (right) are compared. G-I, Same as D-F with PSTH showing firing rate profiles during the short reaction time trials. Color of pixel represents normalized firing rate (z-score. Scale of axis in A-C narrower than in D-I due to averaging across M1 or S1 populations reducing the amplitude of PSTH profile compared to single cell activity levels.

reaching a maximum level approximately near movement onset. After this, the activity returns to baseline levels. The firing rate amplitude of a motor-tuned neuron is a function of velocity and directional preference of the specific neuron, among other parameters. To establish the neural correlates of target representation independent of these two kinematic parameters, I compared the firing rate (FR) profiles between trials with different size targets. Peri-event time histograms (PETHs, Appendix A.1.1) [177] were generated to visualize the activity of neurons temporally aligned to the onset of the peripheral target.

The first major result was that TS affected the slope of the FR ascent following target appearance (Fig 4). TS had a significant effect on FR slope ($p<0.05$, 1-way ANOVA, Table 2), with larger targets related to steeper slopes. This effect persisted when looking only at short RT trials ($p<0.05$) and only long RT trials ($p<0.05$). Furthermore, the TS – FR slope effect was observed both in the preferred and least preferred direction of M1 neurons ($p<0.05$). Among S1 neurons, the TS-FR slope effect was only significant in the preferred direction ($p<0.05$). Analysis of the FR slope is complicated by the clear effect that RT has on slope. Trials with elongated RTs (greater than the median) had a significantly lower FR slope than short RT trials ($p<0.05$). Multiple linear regression was used for each recorded neuron to quantify the fraction of the population which exhibited each of these effects. To do this, single trial FR slopes were computed and fit as a function of both RT and TS (Eq. 14):

$$Slope = a \cdot RT + b \cdot TS + c \qquad (14)$$

Regression of each neuron individually yielded 95% confident intervals (from *t* statistic) for the coefficients. If the confidence interval did not contain zero, it was deemed significant (Table 2). From monkey N, 40% of M1 neurons had significant regression coefficients for the TS term, compared to 18% for the RT term. For monkey M, the results from M1 were 11% for TS and 31% for RT and in S1 the results were 20% for TS and 32% for RT. To summarize, both the reaction time and the target size had a significant effect on the FR slope. Differences in reach velocity were also reflected in modulation in M1 and S1 activity. A similar analysis to Fig. 4 was performed where trials were separated into low and high velocity trials (Fig. 5). Amongst these two

Table 3: Effect of trial velocity and target size on mean firing rate in peri-movement epoch

	Monkey N, M1 cells		**Monkey M, M1 cells**		**Monkey M, S1 cells**	
	Pref	Least	Pref	Least	Pref	Least
Slow	1.29±0.02	0.41±0.02	1.31±0.02	0.19±0.02	0.73±0.02	0.57±0.01
Fast	1.44±0.03 (0.67)*	0.53±0.03 (0.62)*	1.53±0.03 (0.59)*	0.31±0.03 (0.55)*	1.25±0.02 (0.82)*	0.74±0.02 (0.53)*
Small	1.04±0.03	0.35±0.03	1.34±0.04	0.24±0.03	0.20±0.03	0.56±0.03
Medium	1.54±0.03 (0.75)***	0.54±0.03 (0.64)***	1.44±0.04 (0.56)**	0.27±0.03 (0.51)†	1.03±0.03 (0.93)***	0.59±0.03 (0.53)†
Large	1.50±0.02 (0.73)***	0.50±0.03 (0.62)***	1.48±0.03 (0.56)***	0.23±.0.03 (0.48)†	0.97±0.01 (0.92)***	0.58±0.03 (0.61)†
ANOVA overall	P<0.001	P<0.001	P<0.02	n/s	P<0.001	n/s
ANOVA fast only	P<0.001	n/s	n/s	n/s	P<0.001	n/s
ANOVA slow only	P<0.001	P<0.001	P<0.001	n/s	P<0.001	n/s

* p<0.001 difference from slow trial MFR, ** p<0.05 difference from small target MFR, *** p<0.001 difference from small target MFR.

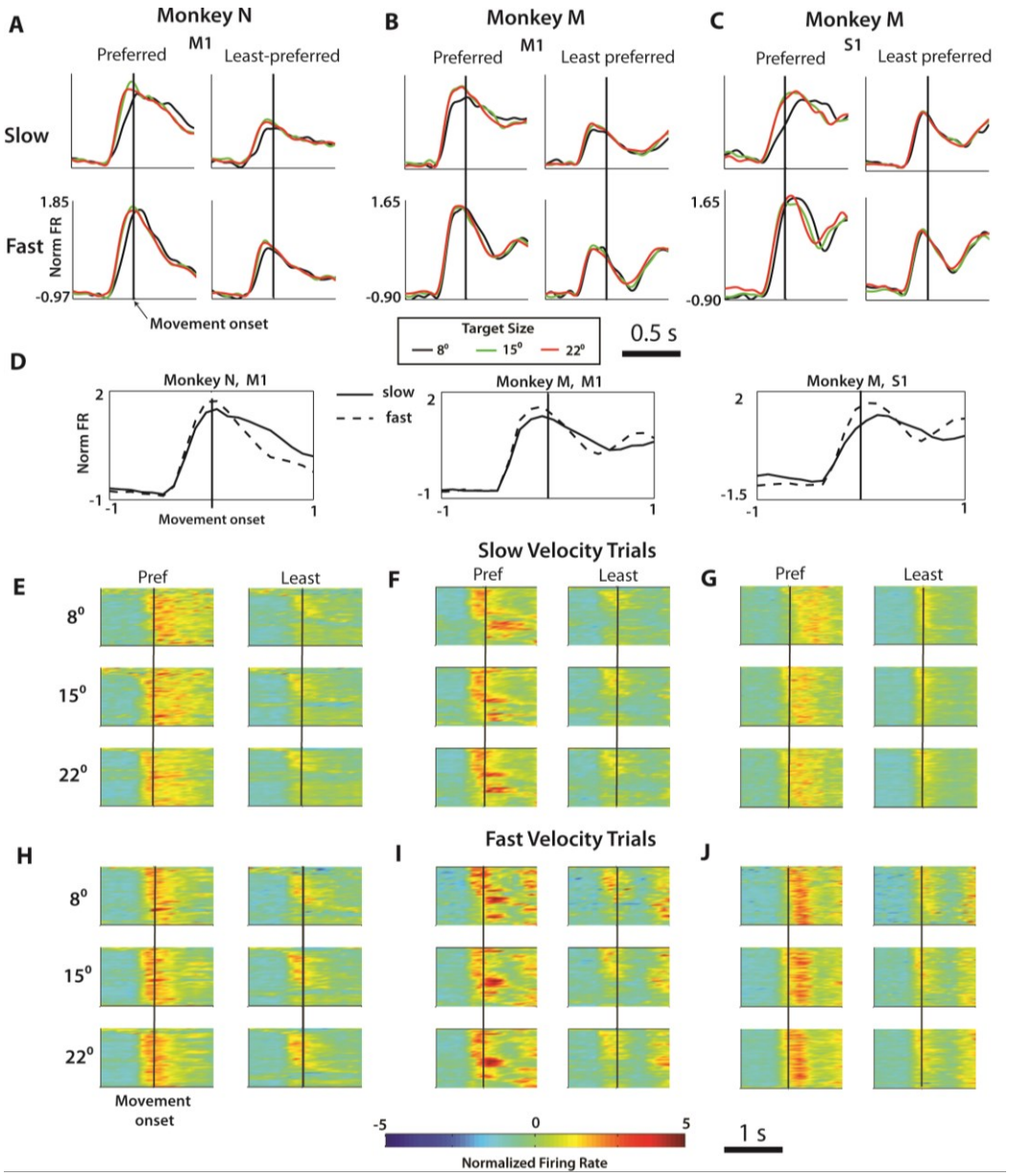

Figure 5: Effect of velocity on firing rate profiles. The normalized firing rate was computed during the one second interval surrounding movement onset from three subpopulations of neurons: (A) M1 neurons in monkey N, (B) M1 neurons in Monkey M, (C) S1 neurons in Monkey M. In each panel, the left column represents averaged, normalized FR for movements in each cell's preferred direction, right column the least preferred direction. The top row is averaged over all trials slower than the median approach epoch velocity and the bottom row shows only fast trials. Target size specified by line color (see legend below B). D, Same data from A-C collapsed into simply a comparison of slow vs. fast trial average PSTH for each of the three cell groups. Population PSTH for slow (E-G) and fast (H-J) trial averages. In each panel: y-axis contains all neurons, x-axis represents time aligned on movement onset (black bar). Color of pixel represents normalized firing rate (z-score).

groups, trials were further separated into three target size groups. PETH analysis was once again performed, with data now aligned on movement onset. The clearest effect was an increase in firing rate amplitude across both M1 and S1 populations during high velocity trials relative to low velocity trials during the peri-movement epoch ($p<0.001$, paired t- test; Table 3). In addition to velocity, TS had a small effect on the amplitude of this activity as well. Mean FR during the peri-movement epoch increased with larger TS ($p<0.02$, 1-way ANOVA; Table 3) among all three cell populations. Also among all three populations, the TS effect on mean FR was prominent in the preferred direction ($p<0.05$, 1-way ANOVA) but less clear or absent in the least preferred direction.

Next, I performed a linear regression of velocity and target size using single trial data following Eq. 15:

$$MFR = a \cdot Vel + b \cdot TS + c \qquad (15)$$

where *MFR* is computed during the peri-movement epoch and *Vel* is the mean velocity during the 500 ms following movement onset. Neurons were fit individually and the coefficients were deemed significant if the 95% confidence interval (from *t* statistic) for its value did not include zero. I found that during this epoch, FR amplitude is more strongly modulated by velocity than TS in monkey N M1 (44.5% *Vel*, 10.9% TS; Table 3), monkey M M1 (38% *Vel*, 18.9% TS), and monkey M S1 (55.1% *Vel*, 14.7% TS).

The next step was to more clearly isolate the different neural representations (reaction time, target size, velocity) and determine when during a typical trial the neuron encodes certain parameters. I used multiple linear regression analysis (Fig. 6) to

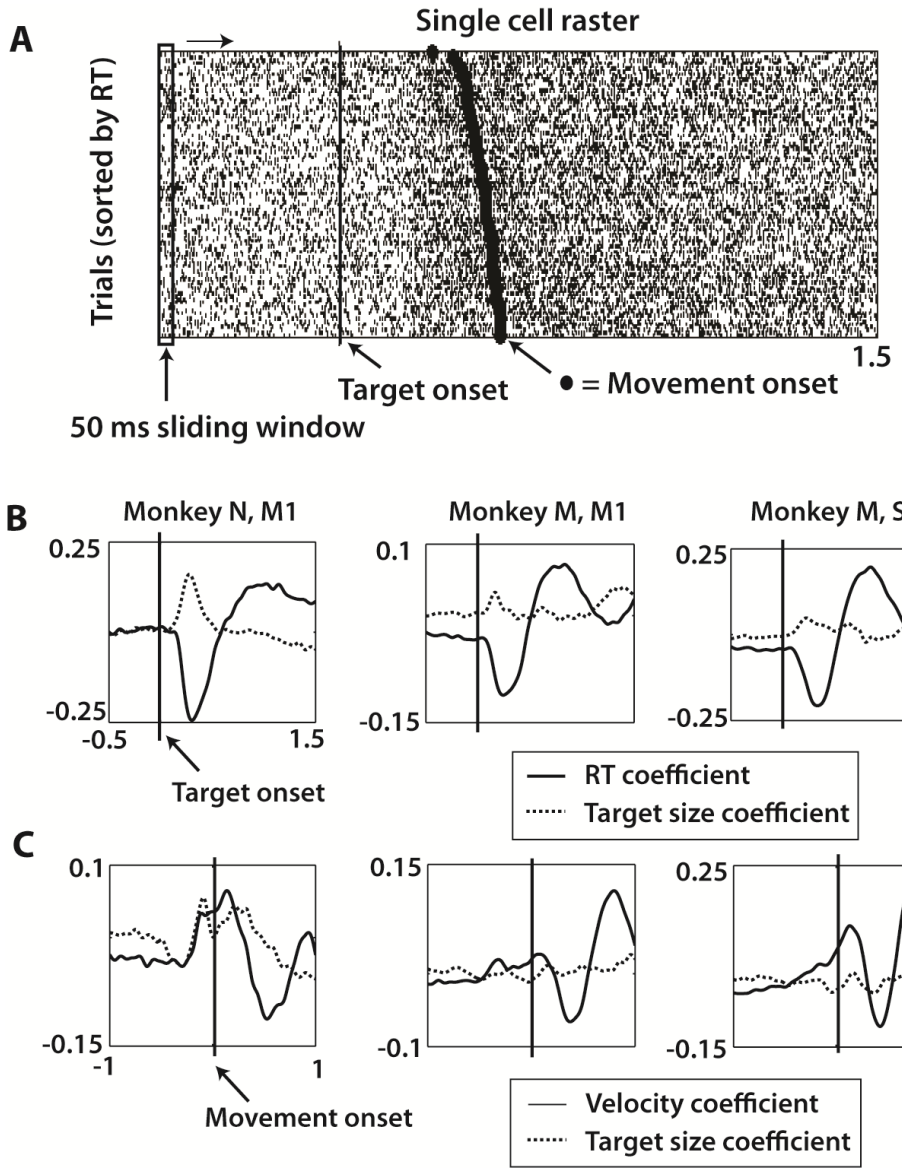

Figure 6: Multiple linear regression analysis of target size, reaction time, and velocity with firing rate over task interval. A, Firing rates were estimated using a 50 ms sliding window slid with 50 ms time steps in the interval from 0.5 s before target onset until 1.5 s after target onset. The firing rate of a single cell in the window was fit with a linear function of the corresponding trial RT and target size and then averaged across all cells (see eq. 16). B, Data showing the coefficient for RT and target size of eq. 16 as a function of location of sliding window right-most bound in monkey N M1, monkey M M1, and monkey M S1 (left to right). Dashed line represents target onset. C, Firing rates were fit with linear function of mean approach velocity and target size of each trial (eq. 15). Methods for C same as shown in A, except data realigned on movement onset (dashed line) and sliding window range from 1 s before to 1 s after movement onset.

fit mean FR during a sliding 50 ms window as the sum of RT and TS (Eq. 16):

$$MFR = a \cdot RT + b \cdot TS + c \qquad (16)$$

Regression was performed by fitting MFR as a function of reach velocity and TS, once again using a sliding window regression approach using Eq. 15. The sliding window was incremented at 25 ms steps from 0.5 s before to 1.5 s after target onset. MFR and TS had a positive correlation very early in the trial, during or slightly before RT neural representations (Fig. 6B). RT was inversely correlated with FR as would be expected from Fig. 4. Both the TS and RT coefficient trends were observed in both M1 and S1 populations. A similar regression was performed by fitting MFR as a function of reach velocity and TS, once again using a sliding window regression approach using Eq. 15. With this analysis, data was realigned on the movement onset. The velocity coefficient correlated with FR near movement onset then falls to a negative correlation during the movement, before returning to positive correlation 600-800 ms after movement onset (Fig 6C). From these analyses, I conclude that reaction time, target size, and velocity all contribute to activity levels in M1 and S1 neurons. If MFR during the reaction time period could be completely explained by RT modulation, then the mean TS coefficient would be zero. This is consistent with the results from the earlier analyses (Fig. 4). For these results to be applicable BMI applications, I demonstrated that these same parameters could be extracted from neural activity with common neural decoders. Linear discriminant analysis (LDA) was used to make discrete/categorical predictions

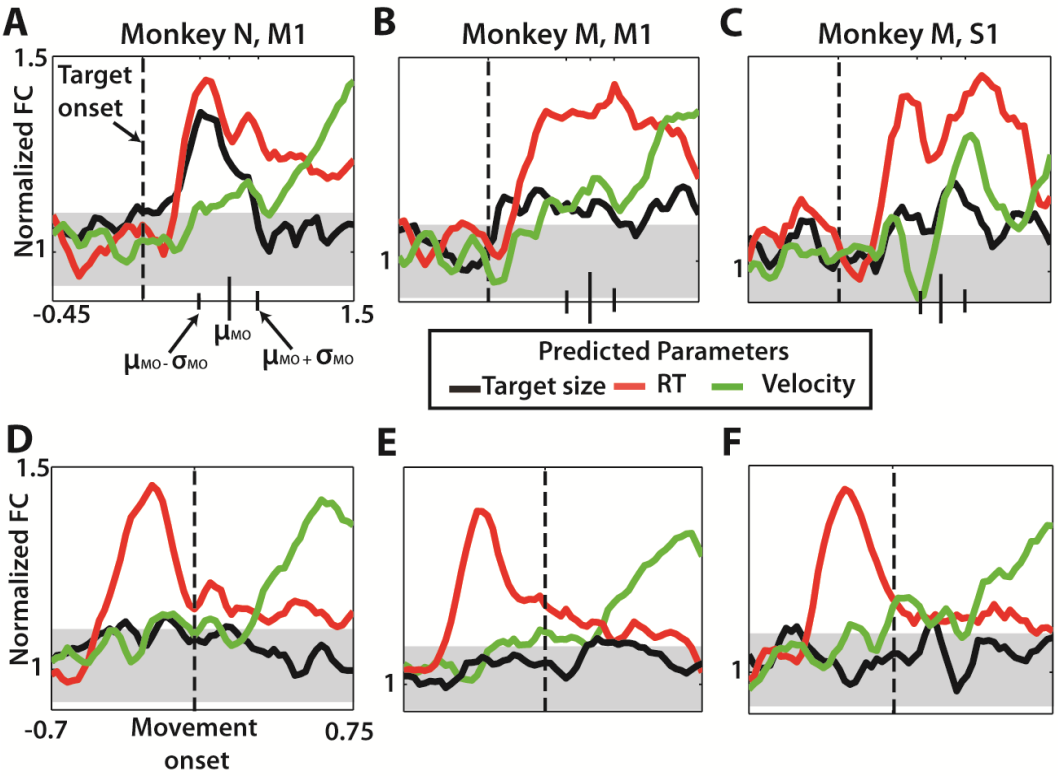

Figure 7: Velocity, target size, and reaction time predicted using linear discriminant analysis. Each parameter was divided into three groups for analysis. Data for each prediction collected from a single bin, 100 ms sliding window of neuronal data incremented at 25 ms through the specified interval. Data denote normalized fraction correct by dividing the fraction correct prediction by the chance level performance (see methods). A-C, Prediction of the three parameters aligned on target onset (dashed vertical line) for monkey N M1 (A), monkey M M1 (B), and monkey M S1 (C). Noted on each is the mean time of movement onset (μMO) with the mean±standard deviations denoted by smaller black vertical bars on time axis. D-F, Prediction of the three parameters now aligned on movement onset (dashed vertical line). Each panel shown with 95% confidence interval for expected LDA classification performance (grey horizontal band).

and the Wiener filter was used to make continuous predictions. For LDA predictions, a 100 ms sliding window was incremented every 25 ms across the task interval from 0.5 s before to 1 s after target onset (Appendix A.1.2). At each shift, a prediction was made for all three parameters. To make RT and velocity categorical parameters, trial RTs and

mean reach velocities were calculated for all trials, then divided into lower 1/3, middle 1/3, and upper 1/3. When data was aligned on target onset, both RT and TS were represented by neurons during the reaction time period in M1 and S1 populations (Fig. 7A-C). The epoch of the trials that neurons encode velocity encoding is typically around 650-725 ms after movement onset (Fig. 7D-F), which is most clearly seen when the data is realigned on movement onset. The target size representation is clearly aligned on the target presentation, as the representation is almost entirely lost when the data is centered on the movement itself. This is an example of the difference between RT and TS neural encoding, as RT remains well decoded when aligned on the movement event. Continuous predictions were made with a Wiener filter using six 100 ms taps of neural data and ridge regression for regularization (Fig. 8A,B) [178]. The Wiener filter weights for each neuron were fit using the first 50% of the session and used to make predictions of cursor X and Y positions at 10 Hz for the latter 50% of the session. Overall, the X and Y positions were predicted very accurately, with $r = 0.80$ and 0.82 respectively. These predictions contained no time information about the trial, such as aligning data to specific events. This is a major difference from LDA and is much more applicable to real-time BMIs.

To further evaluate performance, the predicted kinematics were aligned on movement onset (Fig. 8C) or target onset (Fig.8E,F) and then averaged to obtain mean predicted trajectories. Comparing the mean predicted trajectories with actual trajectories, there is overall very strong agreement. More specifically, the difference in

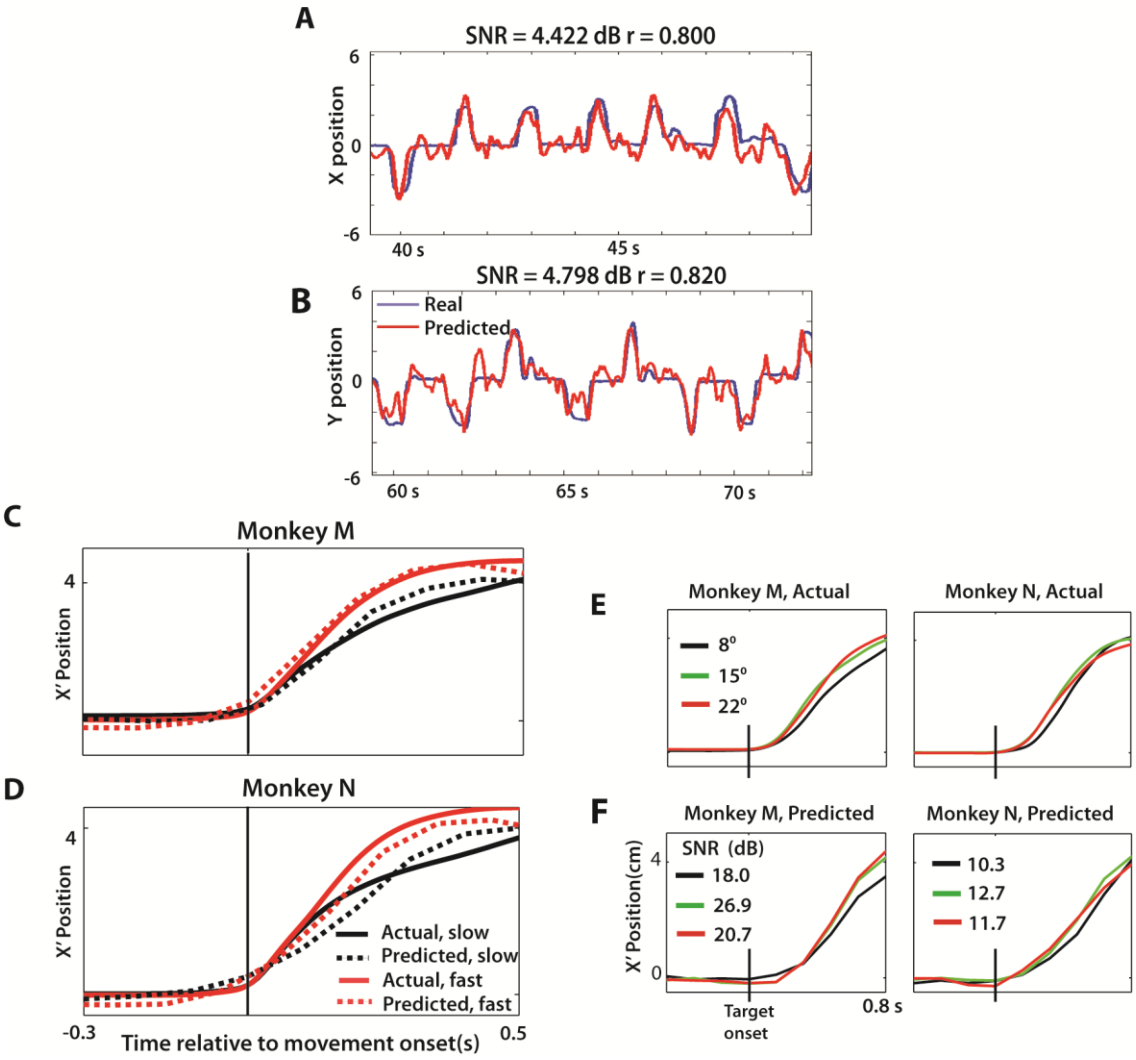

Figure 8: Movement kinematics can be decoded from neural activity with Wiener filter. A,B, Movements along the X axis and Y axis decoded offline and shown with the actual traces. C,D, Average X′ vs. time profile for the two velocity groups, both real (solid lines) and predicted (dashed lines). E,F, Actual X′ position vs. time for each target size, in both monkeys (E) compared with predicted X′ trace for each target size (F). Shown separately for clarity, however SNR computed by comparing actual and predicted for a given target size. In all predicted X′ trajectories, the single trial kinematics were predicted then averaged across the session to generate the traces in panels C-F.

trajectories between slow and fast trials are similarly reflected in the predicted traces (dashed lines, Fig. 8C,D). Even the subtle kinematic differences related to target size

could be extracted from neural activity to accurately reconstruct reaches. The correlations between the mean actual and predicted trajectories were very high for all three target sizes (SNR> 10dB; $r > 0.97$). The Wiener filter and LDA results show that target size information can be extracted from neural activity in much the similar way as reaction time or kinematics.

3.3 Discussion

In this study, I elucidated the neural correlates underlying the changes in the parameters of arm reaching movements with different target sizes. At the behavioral level, I found a strong TS-dependency (ID-dependency) for three parameters of arm reaches performed by rhesus monkeys: total movement time, reaction time, and mean approach velocity. At the neuronal level, analysis across the recorded neuronal populations in M1 and S1 revealed changes in modulations that depended on TS as well. These neuronal modulations could not be explained by changes in movement parameters – the effect that would be expected if M1 and S1 represented only motor aspects of behavior. Rather, sensorimotor cortical activity represented both characteristics of movement and TS. During the RT period, the slopes of neuronal rates depended on TS and reach velocity. Likewise, RT, TS, and cursor trajectories were each individually decoded from cortical activity using both LDA and Wiener filter predictions. These results indicate that M1 and S1 ensembles do encode TS during motor preparation and execution.

3.3.1 Fitts' Law in Monkeys

There are clear similarities between the behavioral data obtained in the present study and those obtained from previous work in humans. I found a positive, linear relationship between ID and MT, confirming the canonical Fitts' law relation [170, 179]. From regression of this data, the IP was computed for the two monkeys to be 8.21 b/s (monkey N) and 21.35 b/s (monkey M). These compare to similar values shown for human motor systems which Fitts found to be around 10-12 b/s [170]. Monkey behavior also matched previous human work with respect to target-dependent shifts in RT [180, 181] and velocity [180, 182].

When comparing monkey data to previous human findings, several key differences were discovered. I found that monkeys treat different movement directions unequally. For each monkey, one out of four directions was the most difficult and resulted in longer RTs and clearer Fitts' law dependency compared to other reach directions. For other directions the monkey moved in a ballistic fashion, showing less clear features of Fitts' law. I propose that ballistic movements can at least partially explain loss of Fitts' law-type behavior, in agreement with previous work on Fitts' law in humans [183].

3.3.2 Neural correlates of Fitts' Law

The cortical correlates of Fitts' law were observed in M1 and S1 during both motor preparation (RT period) and movement execution (movement period). During motor preparation, populations of M1 and S1 neurons exhibited clear modulations of FR

that were characterized as FR slopes. The slopes increased in steepness with shorter RT and larger TS. FR slopes have been shown to be involved prominently in decision making, as demonstrated by evidence-accumulation models [57, 184]. These models are based mostly on the data from eye-movement studies that required selecting a saccade direction in response to complex visual clues [185, 186]. Thus, it has been shown that neural activity recorded in middle temporal (MT) and lateral intraparietal (LIP) areas rises more gradually when the task is perceived to be more difficult, thus lengthening the pre-movement period [57, 58]. Such dependency is similar to the behavioral and neurophysiological results of our study: I also observed elongated RTs for smaller TS, and the changes of neuronal rats developed slower. My findings correspond to a previous study in the Nicolelis lab where we observed lower FR slopes in M1 and PMd neurons for longer self-timed intervals [187]. Thus, gradual changes of FR during behavioral epochs preceding movements appear to be a general phenomenon in the cortex during tasks that involve sensorimotor transformation and decision making. Notably, I did not observe a clear segregation between motor (M1) and sensory (S1) areas which both showed modulations during the RT period. This adds to previous reports of premotor activity in S1 [188, 189]. The exact role of M1 and S1 circuitry in the sensorimotor transformation that involves TS processing is not clear. One possibility is that M1 and S1 modulations reflect the processing performed mostly from associative areas [190] and basal ganglia [191]. Alternatively, M1 and S1 may be involved in the sensorimotor transformation as an essential part of a distributed network where there is

no clear-cut segregation of processing modules [192-194]. While my results cannot distinguish between these two possibilities, the presence of TS information in M1 and S1 indicates that these areas are not involved in merely movement production, but reflect sensory components of the visuo-motor transformation, as well.

The second feature of movements clearly reflected by cortical activity was velocity. Approach velocity was found to shift as a function of TS (Fig. 3C,D). Neural activity at the time of movement initiation paralleled this shift via FR amplitude. Higher velocity trials correlated with higher FR during and slightly after movement onset (Fig. 5D). This results was expected, as numerous previous studies have strongly linked motor cortical activity with velocity [56, 150, 195, 196]. Additionally, a large percentage of M1 neurons were found to encode both target-centric (reach distance) and motor (direction, position) parameters during movements, often in a serial manner [5]. My findings also indicate that S1 neurons exhibit velocity tuning, consistent with previous studies that have described S1 neurons with kinematic modulations [126, 189, 195, 197]. In this study, S1 representation of velocity was somewhat weaker than M1, however the maximum modulation epoch was similar (300-700 ms after movement onset).

Target size has not previously been identified to modulate FR profiles in M1 or S1. Using both linear regression and LDA, I found that in both M1 and S1, the neural representation of TS first becomes prominent during the RT period, coinciding with the rise of RT encoding (Fig. 7A-C). This, again, expands the role of M1 beyond simply motor execution [192, 193]. The data showed a second, more subtle effect in both

monkeys, where TS was again represented 100-300 ms after movement onset (Fig. 7D-F) near the onset of velocity representation. Thus, my results suggest that M1 is one of the loci of evidence-accumulation, since it seems to integrate TS information with motor parameters during the pre-movement period (affecting RT) and near movement onset (affecting velocity).

Somewhat surprisingly, I did not observe clear-cut difference between M1 and S1 modulations during the execution of center-out reaching movements. During the pre-movement period, I found S1 neurons to modulate very similarly to M1. RT and TS were both encoded in S1 during this period, although the onset of this representation was no sooner than 200 ms after target onset, compared to an earlier 50-100 ms post-stimulus representation in M1 (Fig. 6B-C). Pre-movement activity has been previously reported in S1 [188, 189, 198]. Moreover, visual information has been reported to affect pre-movement activity patterns in S1 [199]. My findings of TS representation in M1 provide additional evidence of the representation of visual information in M1. In addition to cortical visual streams [200], the basal ganglia appear a likely candidate for a structure that mediates transmission and processing of this information [191, 201, 202].

3.3.3 Implications for BMIs

Much of current BMI research focuses on improving movement predictions by either technical improvement (electrode type/number) or algorithm optimization. The motor goal for cortically controlled neuroprosthetics is to recreate biologically relevant movements in an efficient way using only the neural activity from the patient.

Notwithstanding strong early work towards this goal [126, 127, 195, 203], there are still many milestone to accomplish [88, 204, 205]. A recent human BMI study using EEG (P300) driven BMIs confirmed Fitts' law in movements controlled by neural signals, thus supporting the idea that Fitts' law parameters can be incorporated into BMI cursor control [174]. Because Fitts' law is widely seen in naturally enacted movements, Felton and others [206, 207] suggest that Fitts' law would be an effective tool for comparing BMI subjects, modalities, and tasks. With the results from the present study, I suggest that TS, in addition to motor parameters, could be decoded from neural activity in order to improve neuroprosthetics control and approximate naturalistic movements. The present understanding of Fitts' law has drastically influenced the ergonomics field, especially in the streamlining of human-computer interaction. Computer interface designs heavily favor rapid point-and-select layouts, prompting the prevalence of pop-up and pie menus, corner icon locations, and appropriate sizing of buttons and GUI controls [208, 209]. Pointing devices such as a mouse or joystick were demonstrated to follow Fitts' law in a similar manner as manual pointing [179]. As brain-computer interfacing develops in coming years, it will be increasingly important to understand the underlying neural mechanisms behind this behavioral property. With BMIs, the subject's thoughts replace the mouse or joystick as the input device. Being able to decode the size of the desired target, for example, enables a forward model to enhance performance in terms of accurate on-line kinematic predictions, indices of performance, and decreased error rates – the current standards used by the International Organization

of Standards uses for input devices such as a mouse and joystick. Such a forward model could extract the TS from the neural activity during the RT period, as was demonstrated in this study's results, and use this parameter to guide more accurate brain-controlled movements. This result would greatly impact the field of neuroprosthetics and make headway toward realizing the goal of enacting naturalistic movements in humans.

The results from this study demonstrate for the first time the existence of Fitts' law in two rhesus macaques and provide strong indications of the underlying neural correlates. The changes at the behavioral level were paralleled by the modulation of M1 and S1 neurons during the pre- and peri-movement epochs. TS-dependent modulation existed in addition to kinematic tuning thus suggesting a potential encoding that could be exploited in the design of future BMIs. Improved movement predictors that incorporate reach information such as TS will enhance the ability of cortically driven neuroprosthetics in terms of both accuracy and similarity to naturalistic movements.

4. Identification of the neural correlates of motor plan transitions in primary motor and sensory cortex

The second phase of experimentation focused on the behavior and underlying neural correlates of a switch in motor plans [210]. The ability to select an appropriate motor plan and inhibit unwanted movements is essential for the behaviors of advanced organisms. Similarly, BMIs must account for the moment to moment changes in movement goals to ensure the intended movement is performed. An example of the importance motor plan cancellation is safety. A movement may be selected initially, but sensory information updates inform the motor system that a safer or more optimal alternative movement should be executed instead. With this being a known and important property of the motor system, I sought to understand its neural basis such that it could be implemented into a real-time BMI system. Previous work by other research groups have identified populations of neurons which encode multiple potential motor plans in PMd [28], SMA [211], and elsewhere, however the role of M1 and S1 neurons is unclear. Furthermore, this study was important for demonstrating an expanded role of M1. Neurons which encode information about alternative motor plans and movement cancellation provide valuable higher order control, rather than (or in addition to) simple motor output commands.

4.1 Center-out task and behavioral results

The same two rhesus monkeys were used for this project as were used in the Fitts' law project from Chapter 3. Once again, activity was recorded from right

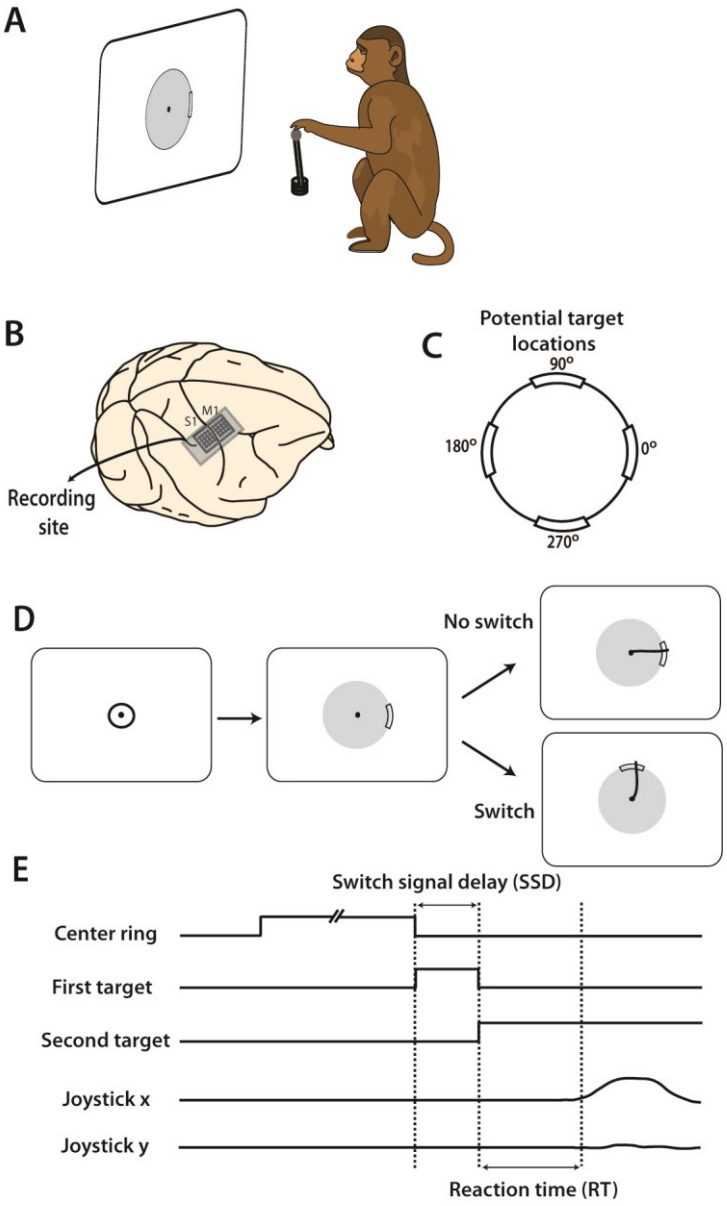

Figure 9: Experiment and location of neural recordings. (A) Rhesus monkey controlled joystick with left hand which translated to movements on computer screen. (B) Electrode arrays in arm representation regions of M1 and S1 cortex were implanted prior to data collection. (C) During task, peripheral targets appeared at one of four potential locations on the screen: 0, 90, 180, 270°. (D) Typical task sequence begins with cursor inside central target. After a random hold time, the target appears an as an arc on the gray boundary circle. On 25% of trials, this target persists and the cursor must be move through the target for reward. On the remaining trials, the target moves after a brief delay and the cursor must be move towards the new target to obtain a reward. (E) Shown are timelines of the presence of each target. SSD is defined to be the time between when the first target appears and when the target is switched to the second location.

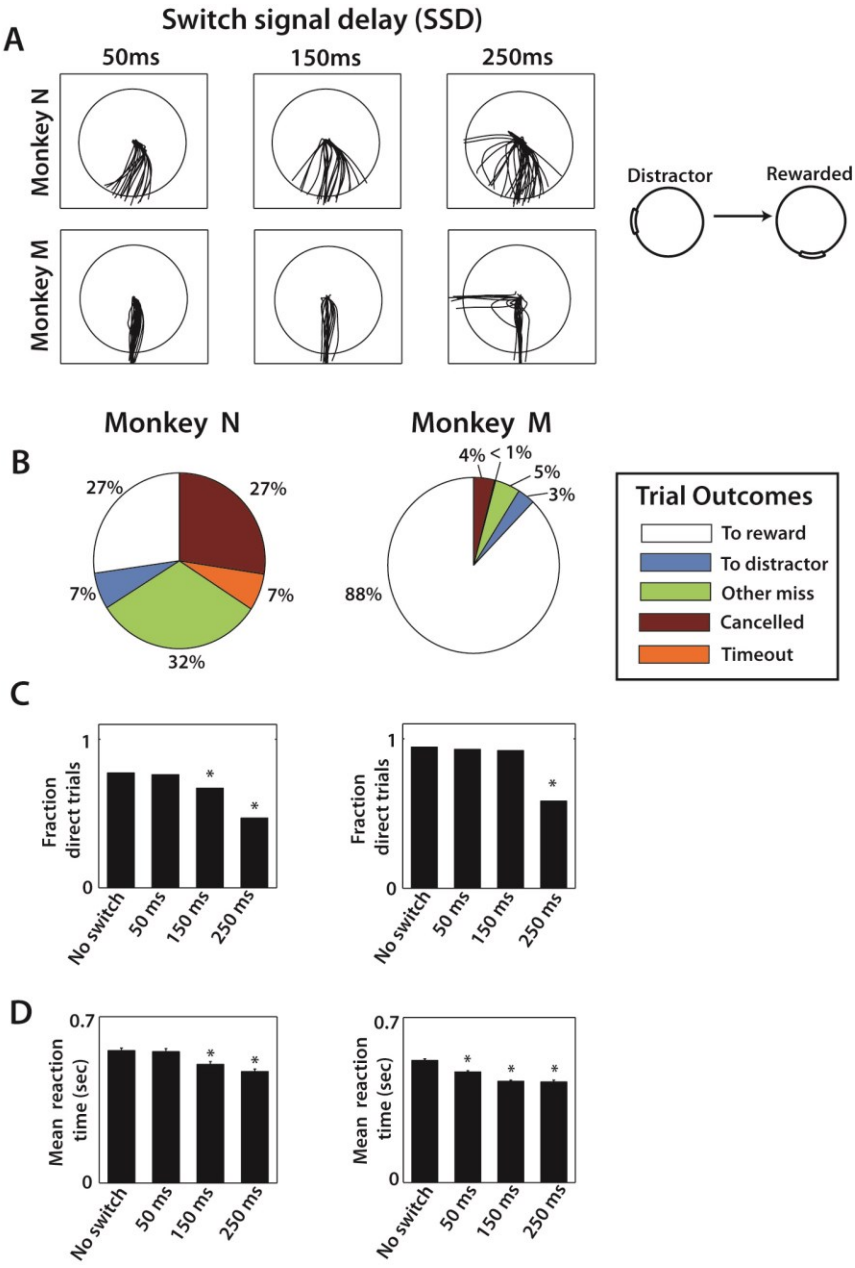

Figure 10: Behavioral results from both monkeys. (A) Typical movement traces from one combination of first and second target locations. The columns show different cursor trajectories on trials with different SSDs. The first row is data from monkey N and the second row from monkey M. (B) Pie chart shows the breakdown in trial outcomes by monkey. (C) The fraction of direct trials shown for each SSD group in both monkey M (left) and N (right). 1-way Kruskal-Wallis test followed by post-hoc Wilcoxon signed rank tests were performed. * denotes $p<0.001$ relative to no-switch group. (D) Mean reaction time shown for both monkeys for each SSD group with error bars that represent standard error. Reaction time is defined as the time from true target appearance to movement onset. Same statistical procedure as (C).

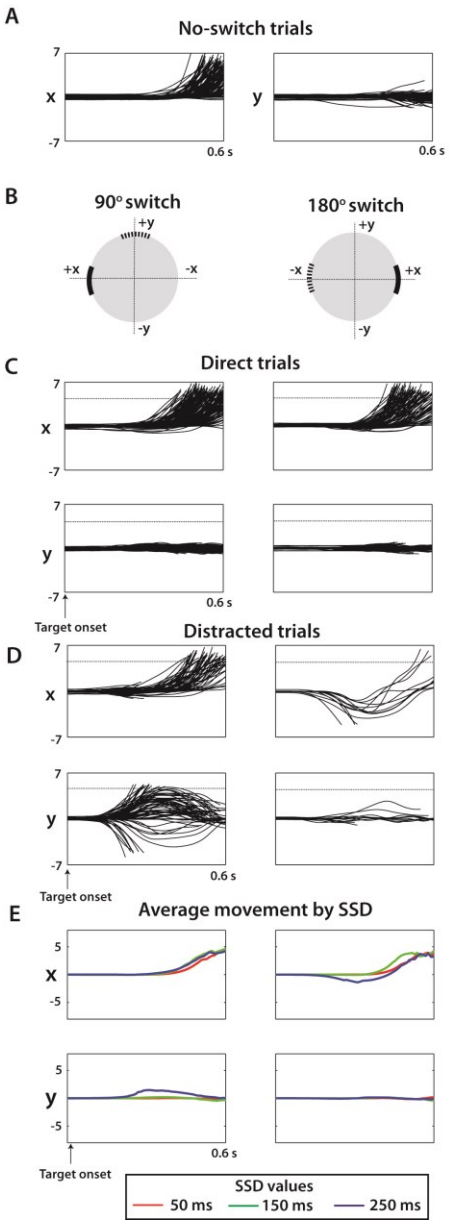

Figure 11: Raw cursor trajectories for 2 sessions (1018 total trials) from monkey M. (A) X and Y position of cursor versus time during no-switch trials. Offline, all targets were moved to (X,Y) position (5,0) and the associated coordinate transform was made to all kinematic data. Y indicates movement orthogonal to the ideal trajectory. (B) For switch trials, two categories of trials shown separately for clarity: Trials with a 90° switch (left) and trials with a 180° switch. The coordinate systems for a given trial were rotated such that the true target was in the positive X direction and the Y direction was orthogonal to this axis. (C) X and Y cursor positions versus time for direct trials among 90° switch (left column) column and 180° switch trials. (D) Same as (C) except looking at only distracted trials. (E) Average X and Y trajectory of cursor separated by SSD (see legend) and by switch angle (columns same as C-D).

hemisphere M1 (both monkeys) and S1 (monkey M only) (Fig. 9B). The task was set up similar to the Fitts' law task (Fig. 9A). The major difference was that a distractor target would briefly appear at one of the four potential target locations before disappearing and a true target would appear at the same or a different location (Fig. 9C-E). The target would appear to switch locations on 75% of trials (25% to each of remaining three locations) and would persist at the original location on 25% of trials, which termed no-switch trials (Fig. 9D). The two targets are referred to as the "distractor" and "true target". On switch trials, the distractor was visible for a short time, called the switch signal delay (SSD), which was less than the typical reaction time. In this experiment, SSD values of 50, 150, and 250 ms were used and each was equally likely to occur.

The behavioral results varied somewhat between the two monkeys but followed the same general trend (Fig. 10). Monkey N performed movements with less overall accuracy (27% of trials rewarded) than monkey M (88% rewarded) but for both monkeys the longer SSD times yielded more distracted trials (Fig. 10C, 11E) and shorter reaction time relative to true target onset (Fig. 10D). I categorized trials as either direct or distracted based on fixed criteria related to the trajectory of the reach either moving directly toward the target or moving in a path which deviated toward the distractor a small amount. An example of the differing reach behaviors for the two monkeys is shown in Fig. 10A and more detailed examples from monkey M are shown in Fig. 11.

4.2 Neural representation of distractor and true target

The difference in the two monkeys' behavior enabled a unique opportunity to

study the neural correlates of two differing strategies: a more thoughtful and accurate approach compared with an easily distracted and less precise approach. PETHs aligned on distractor onset were utilized to study the sequential M1/S1 neural representation of switch and no-switch trials. An example of the results at the single cell level can be seen in Fig. 12. A single neuron has a clear preference for the true target to be located at 90° and somewhat less at 180° (rows 2 and 3 of Fig. 12A-B, Fig. 13A). When the distractor is located in the preferred location (column 2), the cell transiently responds with increased activity (Fig. 12B, 13B). This initial modulation makes way for the true target tuning which occurs after a short delay. The sequential representation of both directions is most clear in the second column and third row up in Fig. 12B, when the both the distractor and true target are at preferred locations (also, see Fig. 13B, bottom row). This dual encoding, within the same cell, was shown to exist both during direct and distracted trials (not shown) but not when SSD is very short (50 ms, Fig. 12A).

The analyses then expanded to the population level, where hundreds of M1 and S1 neurons were analyzed in a similar method (Fig. 14). I found that the firing rate of neurons across the population was a function of both the distractor and true target locations. For each neuron, the four target locations were ranked from most preferred to least preferred. Firing rate (shown as pixel color in Fig. 14A) decreases both up the columns and down the rows. This is even more clearly shown in Fig. 15. In the first 200 ms after the target switch has been made, the distractor is still more prominently encoded by M1 neurons than the true target. The time when neurons shift to represent

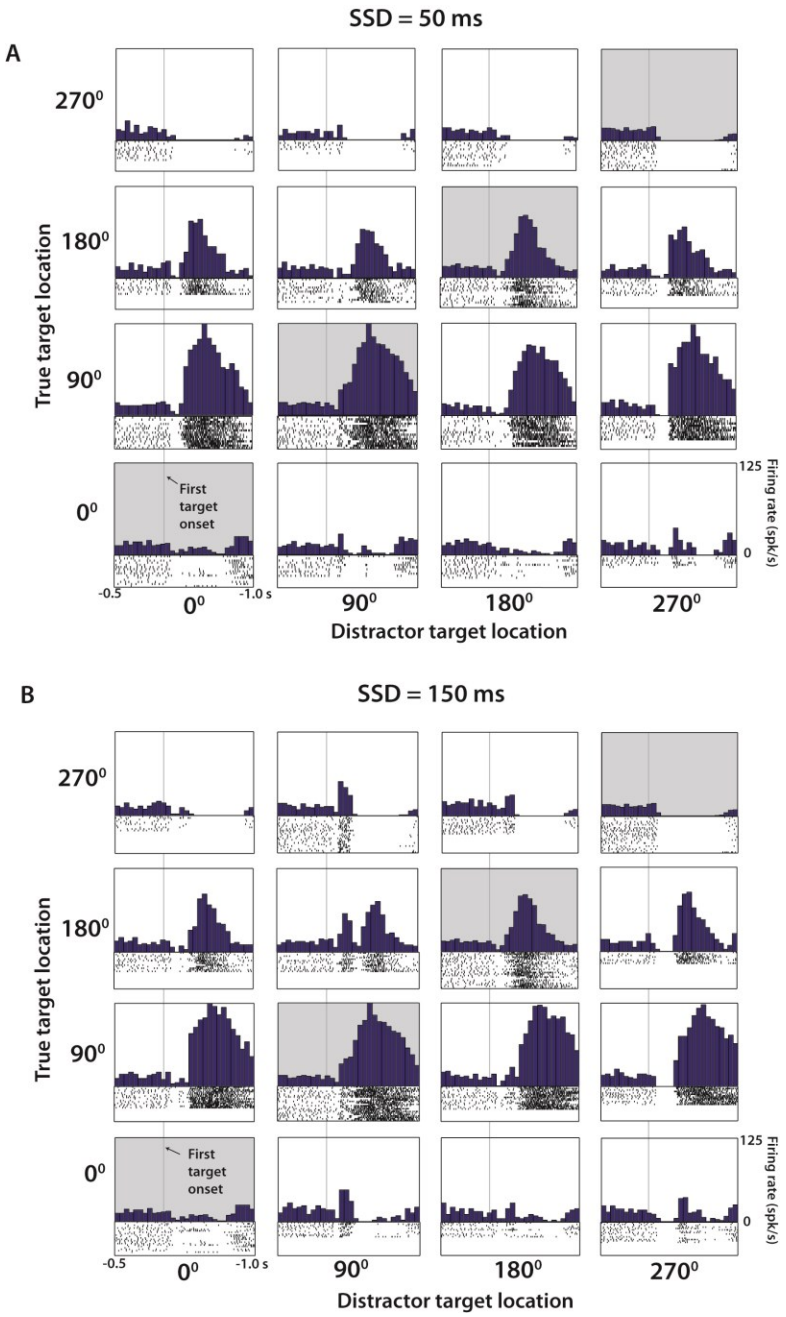

Figure 12: Representative M1 neuron from Monkey M. (A) PETH aligned on distractor target onset from trials with SSD of 50 ms. Position within the 4x4 grid determined by the position of the distractor and true target. Along the diagonal (shaded), these PETHs are generated from no-switch trials. Units are in terms of firing rate, where the bin count is divided by the bin width (50 ms in each case). Spike rasters below each histogram indicate time stamps of spikes from six randomly chosen trials of this particular combination. (B) Same cell and analysis as (A), with only difference being that data collected from trials with SSD of 150 ms.

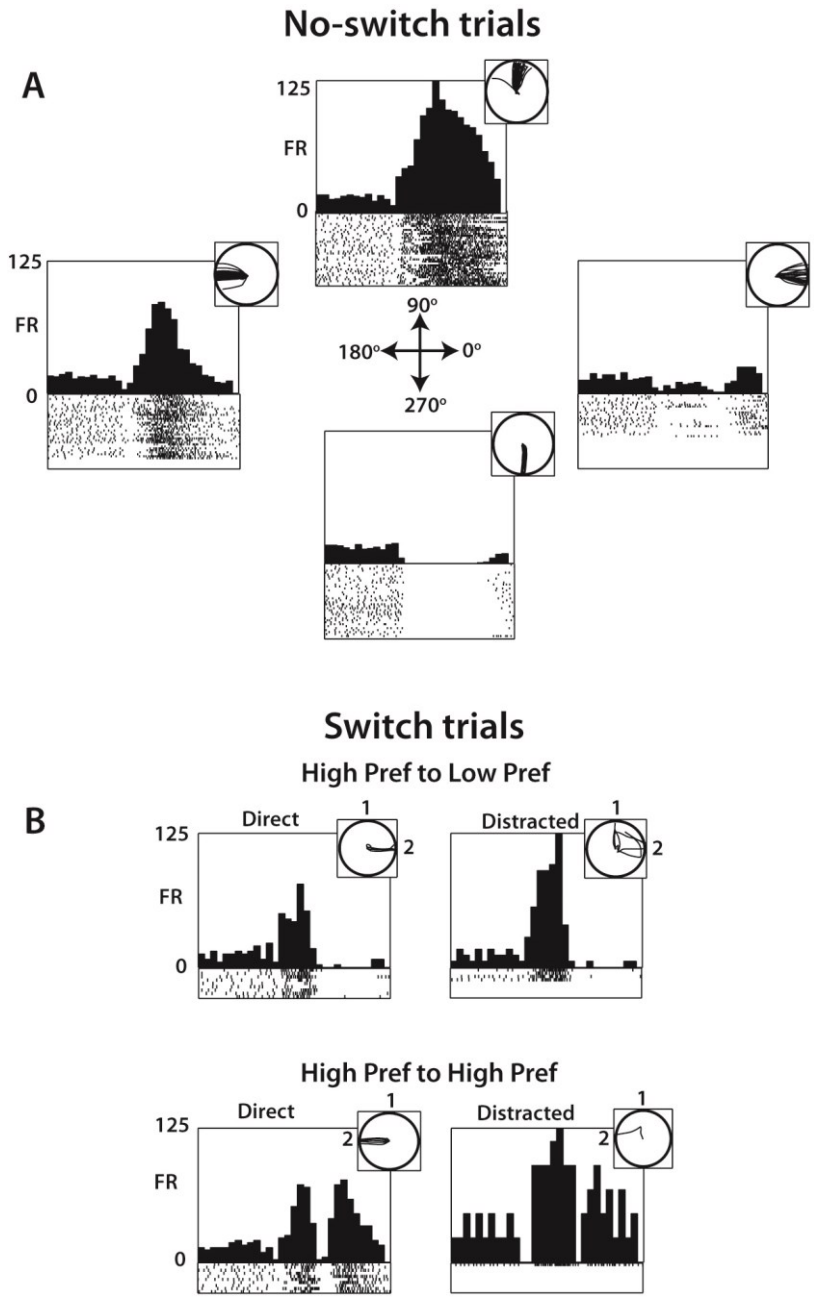

Figure 13: PETH of a single M1 neuron during specific transitions. (A) Neural activity from no-switch trials separated by target location shows directional preferences with PETH and single-trial raster plots (below PETH) aligned on distractor target onset. Inset shows cursor trajectory from trials to the specified target. (B) Among switch trials, PETH and raster plots generated from trials with distractor in one of the neuron's preferred direction (90°) and the true target in a nonpreferred direction (0°). Data from both direct (left) and distracted (right) shown, with inset showing cursor traces. (C) Same as (B) except data drawn from trials where both the distractor and true target are in preferred directions (90° and 180° respectively).

the true target is dependent on SSD time. For the 250 ms SSD, the transition occurs between 300-400 ms, although by 500 ms, both target locations are influencing firing rate (note the lower left triangle in the last panel of Fig. 15C). Data in Fig. 15 is solely derived from direct trials to assure that the cause for this dual representation was not simply movement to the distractor. An interesting side observation from this analysis was the difference in neural response profiles between trials where the monkey correctly switched to the true target and when they did not (not shown). The mean normalized population firing rate was higher at the time of target switch on trials where the monkey failed to correct switch to the true target than on correctly switched trials. This suggests that some threshold had been crossed and a change-of-decision could not be made. This threshold-crossing concept is consistent with change-of-decision models such as the bounded form of the accumulator model [212], a drift-diffusion model, or race model with criterion boundaries for both initial and change of decision events [186]. This is further discussed with my article published on this study [210].

Among rewarded trials, I analyzed neuronal representation of the target switch (Fig. 16). To do this, the trial-averaged PETH for switch trials was directly compared with the PETH of the no-switch trials. As the metric for the neuronal representation of the switch, I used RMS differences between PETHs for the trials with no target switches (diagonal data in Fig. 12 and 14) and the trials with target switches. Fig. 16A shows RMS differences averaged across all possible location of the distractor and true targets for each individual neuron, and Fig. 16B shows the result of additional averaging across

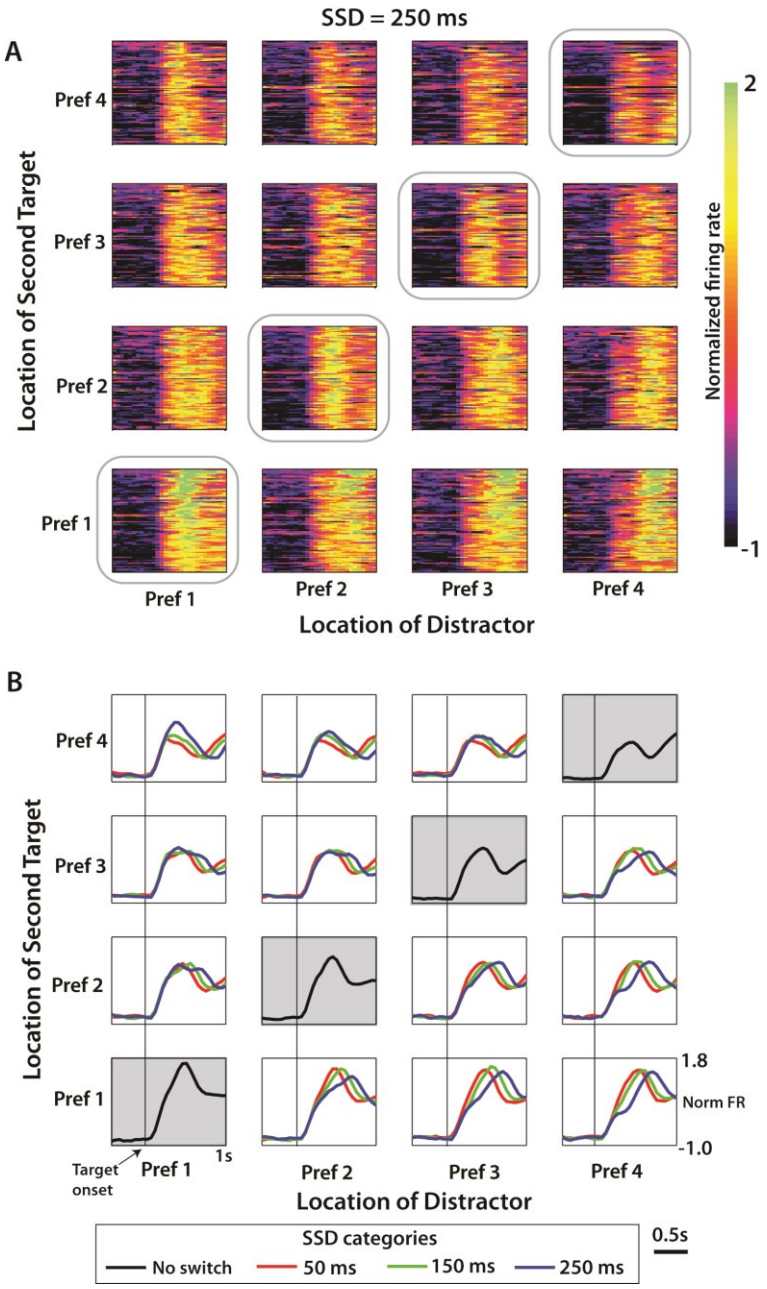

Figure 14: Population activity from M1 neurons in Monkey M aligned on distractor target onset. (A) Normalized firing rate for each cell and each pairwise combination of distractor and true targets shown for the SSD of 250 condition. Amplitude of firing shown by color scale (on right) interpreted as the z-score. Position within the 4x4 grid for each cell determined separately according to directional preference order. Data along the diagonal is from no-switch trials. (B) Population mean PETH for each of the three SSD conditions. Data averaged within a specific condition (within one box on the 4x4 grid) organized by cell directional preference ranking. Along the diagonal is mean population PETH for no-switch trials.

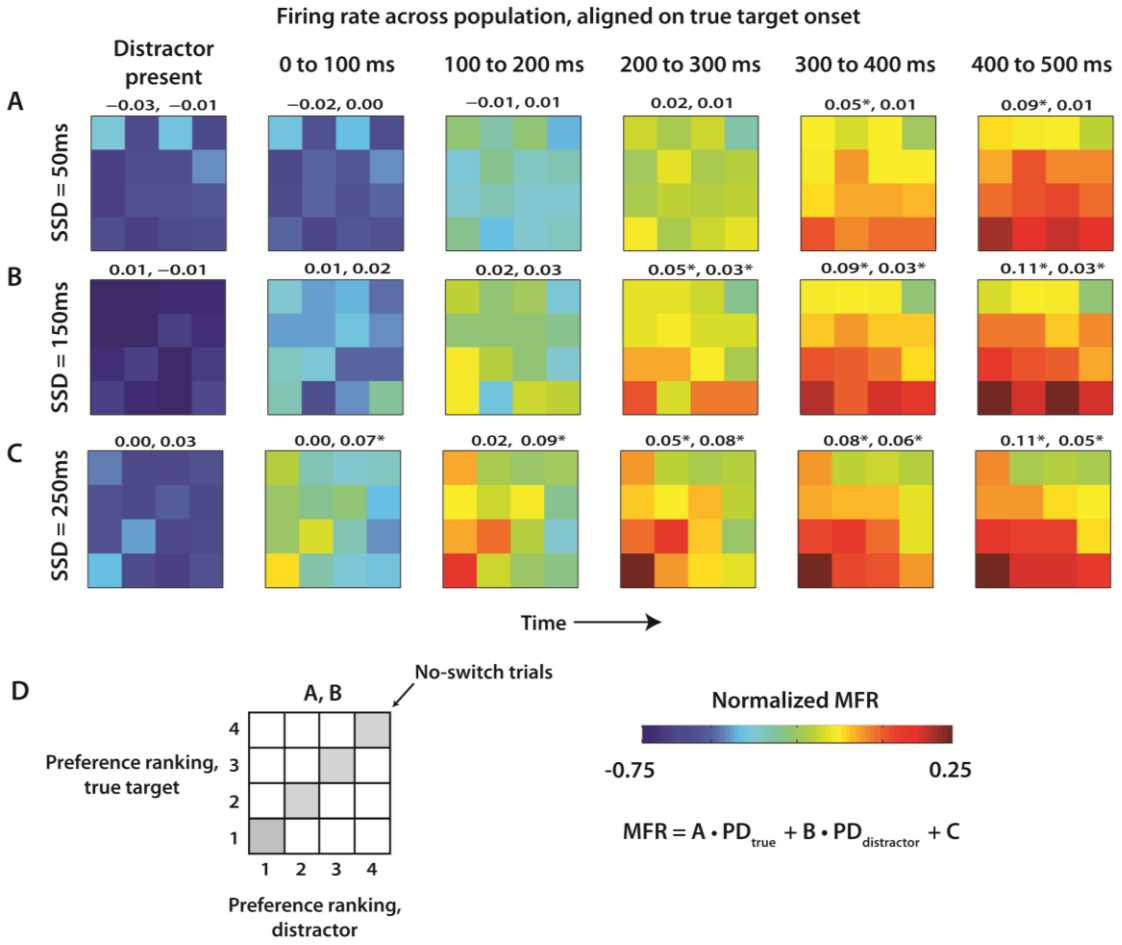

Figure 15: Mean population firing rate as a function of distractor and true target locations. 4x4 grids showing population MFR for each target combination. Target for each cell were ranked in terms of preferred direction as shown in Fig. 14. 4x4 grids are computed for epochs throughout the trial, beginning with presence of the distractor. Six epochs are reflected by six time columns proceeding from left to right. Data from each of the SSD conditions was shown separately for 50 ms (A), 100 ms (B), and 150 ms (C). MFR within each 4x4 grid was fit by a linear function of true and distractor preference ranking. Coefficients for true target and distractor target, respectively, are shown above each panel. (D) Layout of 4xe grid, color scale, and linear regression equation.

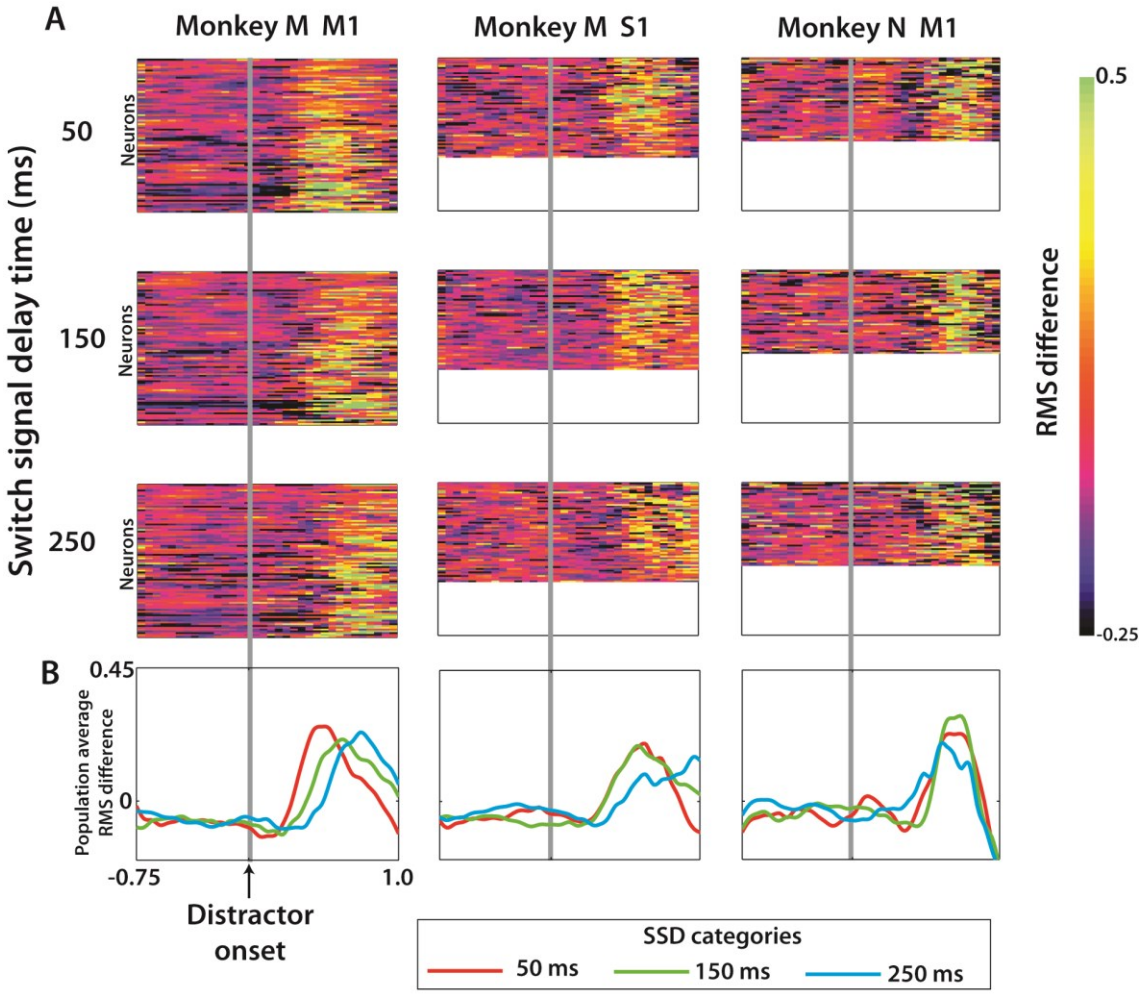

Figure 16: Effect of a target switch on the firing rate in each of the three neuronal populations. (A) RMS difference computed for each cell at each time step from 0.75 s before to 1.0 s after distractor target onset. Data shown separately for three SSD groups, with rows 1-3 the cell RMS difference for trials SSD of 50 ms, 150 ms, and 250 ms respectively. Within each panel, the rows of the color plot indicate one single cell and the row height was fixed in all three cell groups (the three columns). The panel size is thus a reflection of the number of neurons in this population. (B) The population average RMS difference was computed from each panel in (A).

neurons in particular cortical areas. These averages reflect the target switch from its initial position. It is clear from Figs. 16A and B that neurons represented the target switch in M1 and S1 of both monkeys. Monkey M M1 population represented the timing of target switch for all tested SSDs, as evident from the latencies of the average curves (Fig. 16B, left). The S1 population of monkey M resolved the timing of the switch at 250 ms from the switches at 50 and 150 ms. The differences in switch timing were less clear in monkey N. Because of these representations of distracting and true targets by M1 and S1 neurons, I was able to extract target information from neuronal population activity.

4.3 Extraction of target position with LDA classifier

The results from Figs. 14-16 are important for providing a neurophysiological basis for the goal of this study, which is to evaluate how neural decoders handle rapid changes in motor plans. The distracting target was encoded by M1 neurons, even in the absence of movement towards the distractor target. This is a potential problem from BMIs which could falsely generate movements from these unwanted motor plans. The second half of this project was to assess how well linear discriminant analysis (LDA) and Wiener filter decoding algorithms could extract both distractor and true target location. Data from 70% of trials was used to train the LDA model and the remainder was test data. The sliding window evaluated how well LDA could predict first and second target locations as a function of when during the task interval the data was sampled, from 0.5 s before to 1.0 s after distractor onset. I found that both M1 and S1 populations could

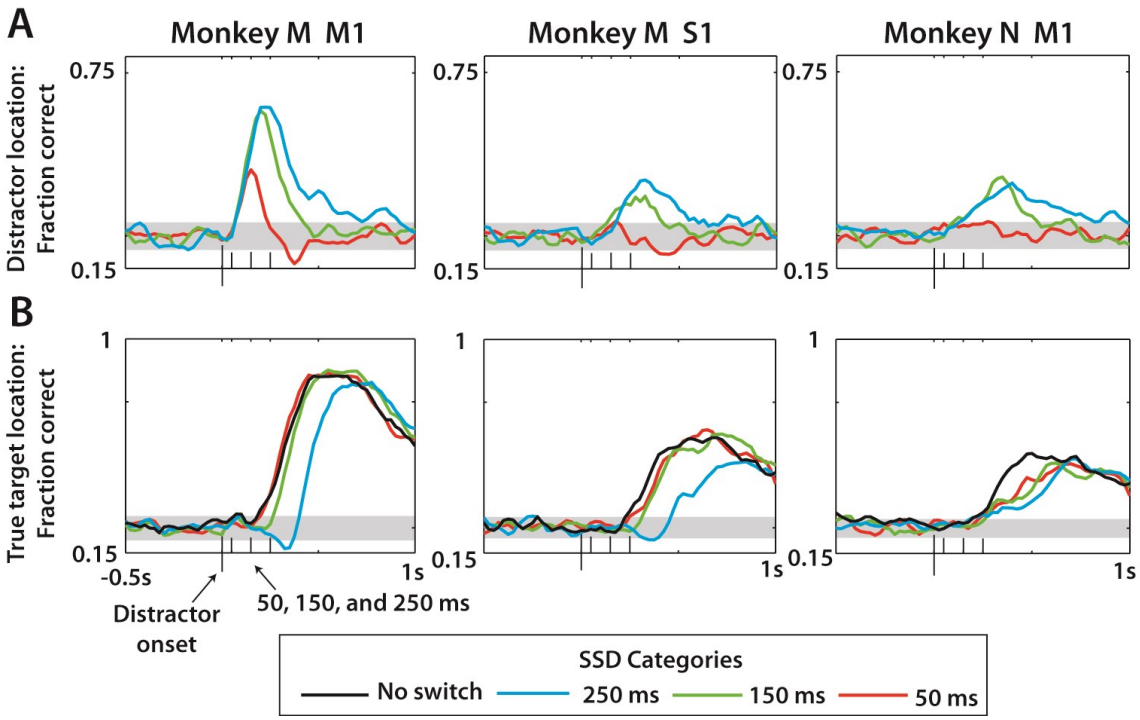

Figure 17: Prediction of distractor and true target locations using neural activity and LDA classification over all trials. (A) Prediction of distractor location for each of the three cell groups (columns). Within each panel, the fraction correct predicted at each time step of the sliding window is reported. (B) Prediction of true target location, which is the second target in the case of switch trials but the first on no-switch trials. In addition to three SSD groups, the no-switch prediction is shown for comparison. The horizontal grey band in each panel indicates the chance level performance (0.25±95%CI). On x-axis are four ticks representing the first target onset (largest tick) and the three SSDs (50, 150, 250 ms).

extract the true target with high accuracy - up to 90% in monkey M M1 (Fig. 17B). The distractor target location could also be decoded at above-chance levels in both M1 and S1 (Fig. 17A). The short 50 ms SSD distractors were decoded at a much lower rate than longer SSD trials, although still at statistically significant rates. Confidence intervals were computed using a 1-proportion z-test with chance performance at 25% (4 target

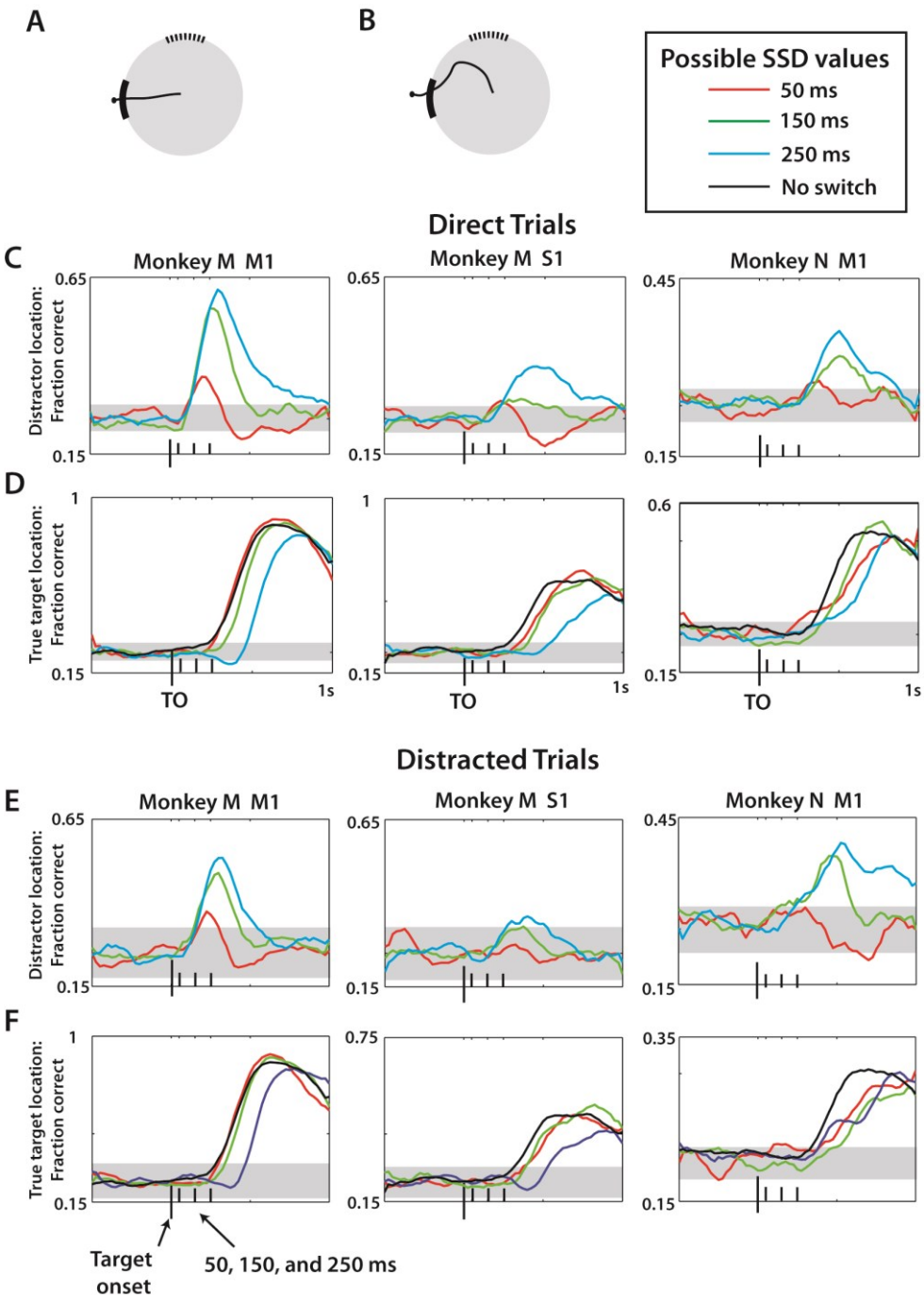

Figure 18: LDA prediction of first and second target separated by movement type. (A) Example of a direct trial. (B) Example of a distracted trial – see Methods for more details. For (C-F), the prediction methods and display are the same as Fig. 17. (C-D) Predictions of distractor (C) and true (D) target location made using data only drawn from direct trials for monkey M M1, monkey M S1, and monkey N M1 (left to right). Different SSD groups denoted by colors, see Legend. (E-F) Same as (C-D) except data reflects on predictions made for distracted trials. Chance level prediction shown by horizontal grey band line at 0.25±95%CI.

locations) and sample size n was the number of test trials (30% of total trials). Because the target representation in Fig. 17A could simple indicate the distracted trials, a more in depth analysis of the result in Fig. 17 was performed in Fig. 18 where direct and distracted trials were separated. Importantly, the neural representation of the distractor target persisted, even for trials where the distractor was wholly ignored (direct trials). In monkey M M1 and S1, the representation was even stronger for direct trials (Fig. 18C,E). The prediction of the true target in both direct and distracted trials was similar (Fig. 18 D,F).

4.4 Decoding of cursor and target position using Wiener Filter

The Wiener filter was used to decode neural data offline to most closely mimic real-time conditions where time information (e.g. target onset) is unknown *a priori*. Wiener filter predictions were made using a similar method as for the Fitts' law analysis in the previous chapter, with six 100 ms taps of neural activity. Cursor X and Y position were decoded with high accuracy (Fig. 19A, $r > 0.84$) and the true target location was decoded very reliably (Fig. 19C). To further quantify this decoding performance, I set a radial distance threshold at 5 cm, such that when the cursor (X,Y) position exceeded this radius, a prediction of the target location was made (Fig. 19B). The time of threshold crossing relative to target onset is shown in Fig. 19D-E. The Wiener filter was able to extract not only the target onset event but also the location at a high rate (inset). The same decoding strategy was unable to decode the distracting target at a significant level (not shown).

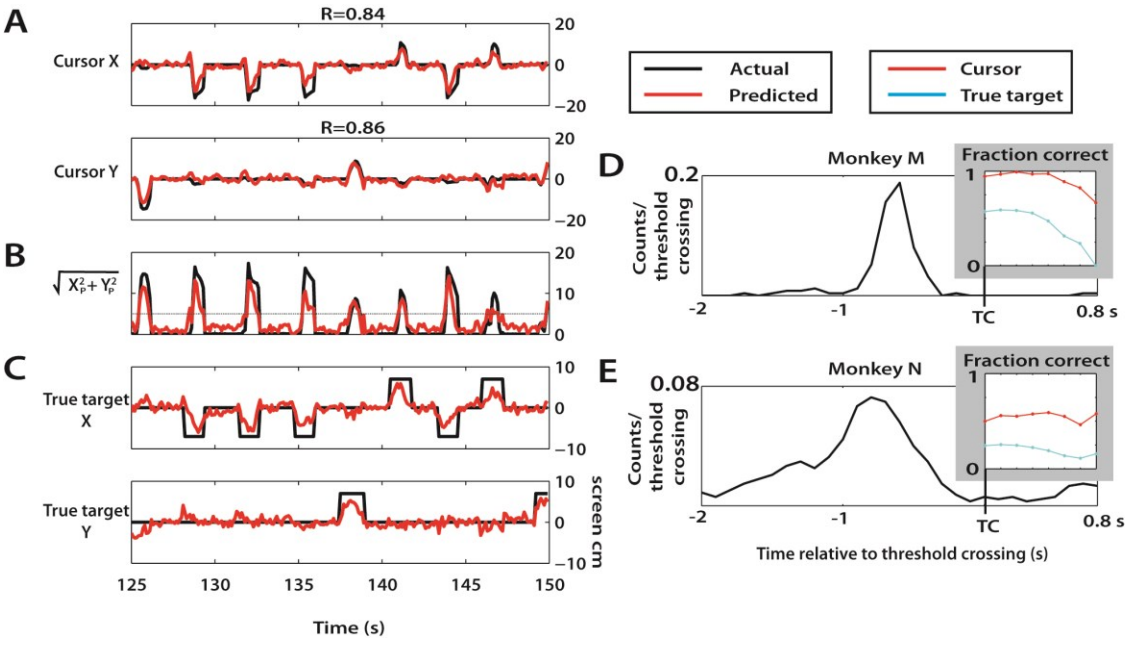

Figure 19: Offline Wiener filter predictions of cursor and target locations. (A-D) 25 s epoch of trials during a session with monkey M. (A) Cursor X and Y positions (black) and corresponding Wiener predictions (red) during selected epoch. (B) The radial distance of the predicted cursor location was computed and plotted versus time. Reach threshold level of 5 cm is shown as horizontal gray line. (C) True target X and Y position during selected epoch (black) and Wiener predictions (red). (D-E) Probability distribution of the time of the true target onset relative to threshold crossings from monkey M (D) and monkey N (E). Inset: fraction correct predictions of cursor and true target location during the 0 to 0.8 s epoch beginning with threshold crossing.

4.5 Discussion

In this study I examined M1 and S1 ensemble activity recorded in a motor task that required reprogramming of center-out reaching movements to visual targets. This was achieved by changing the target location in the midst of the RT period [213, 214]. I hypothesized that BMI decoding algorithms could dissociate representations of potential and selected motor targets from the activity of sensorimotor cortex ensembles. I found that locations of distracting targets presented shortly before the true targets of movements were indeed represented by M1 and S1 ensembles and could be extracted by

an LDA classifier. The LDA results were recapitulated using a continuous Wiener filter which extracted cursor and target location. These results suggest that real-time BMI decoders could be implemented in the future to decode motor programming and decision making parameters under the conditions of multiple potential choices.

Despite the behavioral differences between the two monkeys in this study, as is common in primate studies, both helped to elucidate behavioral responses and the neural basis for transient distractors. In the previous study [175] discussed in Chapter 3, these monkeys were overtrained to perform center-out movements with high accuracy when no distractor was used. For monkey N, the distractor induced marked changes to movement trajectories. Thus both the overt behavior and cortical modulations contributed to the neural representation of distractor and true target locations. Monkey M was less distracted, yet the change in motor plan was still manifested in sensorimotor cortex, even when movements to the distractor target were wholly absent.

4.5.1. Sensorimotor cortex and reprogramming movements

Neural processes of motor program selection and cancellation has received much attention during the last two decades of research. The summary of this body of work suggests that different aspects of sensorimotor transformations that motor plan selection are processed by multiple cortical and subcortical areas [15, 191, 192]. Here I recorded ensemble activity in M1 and S1. These areas most closely reflect the final motor output from the brain and act to carry out whatever movements were decided upon by decision making circuits. Consistent with previous work [201] I observed M1 activity that

represented potential motor targets even when no movement was initiated toward those targets. This representation persisted well beyond distractor disappearance and the termination of this encoding coincided with the onset of the robust second (true) target representation. Somewhat surprisingly, I observed moderate movement and pre-movement modulation in S1—an area whose primary function is commonly assumed to be related with sensory processing, but also known to be activated in advance of movements [188, 189, 198] and encode information about potential reach targets [175].

From my results, I cannot resolve whether representation of potential targets that I observed in M1 and S1 merely reflected inputs from associative areas that were the primary players in target selection [190] or M1 and S1 constituted an integral part of a distributed network with less clearly defined hierarchy [192, 194]. Visuomotor information has been shown to be encoded by cortical visual processing networks in parietal [200, 215, 216], premotor [15, 217, 218], and prefrontal [195, 219] areas. These associative areas could act as filters of sensory information that is subsequently signaled to M1 output areas. The exact mechanisms of interactions between primary and non-primary areas will have to be elucidated by future investigations.

My previous unpublished observations indicated that certain initial stages of target selection for a movement goal have to take place for target information to start to be represented in M1 and S1. In that experiment, animals had to deal with two targets that appeared on the screen simultaneously instead of in rapid succession. One of the targets was large, and the other was small. The monkeys would be rewarded for

reaching to either of the targets, but they typically selected the larger target because it was easier to hit with the cursor. In contrast to the results from the distractor experiments reported here, in the unpublished study M1 and S1 neurons represented the non-chosen target in a much more subtle way, with less than 10% of recorded cells exhibiting any significant directional tuning to its location. This observation, in the context of the results of the present study, suggests that M1 and S1 representation of movement direction is much stronger when the motor goal is chosen, even if only for several hundred milliseconds.

Serial activation of M1 during motor sequences has been well-studied [5, 220] and my results suggest that the manifestation of change-of-decision in the motor cortex is a sequential, but somewhat overlapped representation of distinct motor plans. In other words, sensorimotor cortex represents selected motor targets, but movements to those targets can still be canceled. Such movement cannot be canceled if M1 activity is already elevated and has reached a certain motor initiation threshold [221, 222].

A prominent model to describe the change-of-decision is a bounded form of the accumulator model [212], drift-diffusion model, or race model with criterion boundaries for both initial decision and change of decision events [186]. Applying this model to neurophysiology of sensorimotor neurons, one hypothesis would be that the firing rate of a single neuron or entire neuronal populations would encode the degree of commitment to the specific motor plan. Lower levels of activity would elongate the decision window while additional evidence is accumulated, even if a different

movement had been initiated. To address this hypothesis, my study compared population activity between a subset of trials where the true target was successfully reached versus trials where an error in behavioral outcome was caused by the transient distractor presence. Whether this lower population activity is causal to the behavioral differences is beyond the scope of this study. However, the results reinforce this model by showing lower initial population activity and more gradual FR slope between distractor target presentation and movement initiation on trials where the switch was successfully made.

4.5.2 Decoding motor reprogramming

Here I used a rather simple LDA decoder that extracted target and target switch information from both cortical activity and the timing of the distractor target onset. This decoder was useful to describe the representation of targets by neuronal activity as a function of time. A practical decoder will have to extract target onset, as well. Using a BMI approach also adds an interesting twist to experiments because information extracted from different parts of sensorimotor hierarchy could be used to retrain brain circuitry. For instance, learning a BMI task that involves extraction of target information may result in an enhanced representation of such information in M1. Additionally, non-primary areas should be considered as sources of information about multiple potentials targets [28, 218, 223] for a practical real-time decoder. With the current approach, I was able to extract the location of distractor targets from the primary sensorimotor cortical activity even if those targets were presented for a brief period of time (as short as 50 ms)

and if no movement was initiated to that target. It is important to emphasize that under this same condition, the true target to which the monkeys moved was also decoded very accurately.

As the BMI field advances, practical and versatile neuroprosthetics based on BMI technology are becoming a real possibility [88, 204-206, 224]. The need for practical clinical applications that provide higher degree of freedom control [127] and expanded decoding strategies [225] will drive BMI research to expand into more complex motor programs. Naturally enacted movements require the flexibility to rapidly modify upcoming motor plans. Such a behavior capability was reflected in the neuronal data I collected in the present study. The ability to decode such changes has critical implications for not only accuracy but also safety in the execution of everyday movements by a prosthetic device controlled by brain activity.

Our present experimental approach, based on a discrete rather than continuous decoder, adds to previous literature where similar ideas were evaluated under the framework of a potential cognitive neuroprosthetic [64, 226]. A cognitive neuroprosthetic extracts from brain activity information that is different from motor execution signals and utilizes it to improve the performance. For example, a high-performance BMI proposed by Santhanam et al. [227] extracted target location from delay-period activity recorded in dorsal premotor cortex and thereby obtained information transfer rate of up to 6.5 bits per second. Additional improvements may come from hybrid BMI designs that utilize both single-unit recordings and local field

potentials (LFPs). Thus, Hwang and Andersen [228] decoded movement onset from LFPs while decoding movement direction from single-unit activity.

Hasegawa et al. [229, 230] implemented decoding algorithms that served a similar purpose that I describe here. They decoded go/no go decisions from the activity of 2–5 neurons recorded in monkey superior colliculus and were able to extract multidimensional decisions (e.g., go/no go for two potential movement directions). The information was accessed approximately 150 ms after cue onset, which is consistent with the present results and the results of Santhanam et al. [227]. Given a high interest to neurophysiological mechanisms of response inhibition [211, 231-234], it is reasonable to expect that BMIs that extract response inhibition and response reprogramming information will continue to develop.

4.5.3 Versatile BMIs of the future

The original conception of BMI systems was to strive to mimic normal functions of the brain as closely as possible [235]. The approach that I propose here can be generally characterized as a BMI with impulsivity control. Impulsivity is a person's inability to inhibit unwanted or harmful actions [236, 237]. Prefrontal mechanisms are normally responsible for such inhibition in primates [237-239]. It is conceivable that practical BMIs of the future will need an inhibition control module to operate properly. Moreover, such a module may become one of the essential elements of the design. It may not only examine potential actions and select those that fit the context and are wanted by the user, but also set the limits to volitional control. In the past, we have

already proposed that such an optimal design may be based on a shared-control BMI, i.e., one that gives the user control over higher-order goals and delegates lower-order controls to the robotic controller [140]. A prominent role of prefrontal cortex is executive function, such as the one required for inhibition of potential actions. Future work could seek to exploit the multiple levels of control within the brain to not only recreate naturalistic movements, but at the same time streamline the transitions and selections from the many possible behavioral outcomes. Certainly this goal is challenging, but I remain optimistic in light of recent developments in the fast growing field of neuroprosthetics.

5. Advances in surgical, experimental, and technical components in preparation for a bimanual brain-machine interface

Moving forward from the established single-arm paradigm to a first-of-its-kind bimanual experiment requires a great deal of foresight, innovation, and engineering. Neural recordings during bimanual arm movements had previously been accomplished in monkeys [76, 77, 80] and provided a good background understanding of how the certain areas of the brain represent such movements. The methods of these initial studies were not transferrable to my proposed experiments – only 1 to 8 electrodes were inserted into only a single area of the brain at a given time. Our lab has repeatedly demonstrated that large ensembles of neurons must be recorded to effectively sample the functional modulations of the motor cortical areas [126, 195, 240]. Furthermore, we were embarking upon a level of sophistication of a BMI system that had yet to be developed by anyone in the field. This chapter will provide an in-depth explanation of the large-scale recording system using the bimanual BMI experiments.

Secondly, the experiment itself needed to be advanced to keep with recent virtual reality (VR) advances in our lab and a more rigorous experimental apparatus for rhesus monkey experiments. These improvements provided a critical piece that established not only a viable animal-experiment model, but laid the groundwork for a potential clinical training paradigm for paralyzed patients. The inclusion of these experimental, technical, and engineering accomplishments should not be overshadowed by the key results of the

bimanual BMI study, but rather, they stand on their own as important steps.

5.1 Large-scale, multi-site cortical recording system

Over the past 25 years, microelectrode array technology has advanced such that tens or even several hundred neurons can be simultaneously recorded [129, 241, 242]. This was not always the case. Classical neurophysiologists would insert a single microwire and record units serially to gain an understanding about neuronal activity and function [6, 103]. Through a combination of smaller wires, more biocompatible systems, and new manufacturing techniques, (see Section 2.1) this norm is rapidly trending towards very large scale brain activity (VLSBA) [204, 243]. The precise definition of VLSBA is itself changing year-by-year, but the theory behind such large recordings pushes for 10^3 to 10^4 neuronal counts.

Furthermore, the neuronal ensemble should be derived from brain areas that are well-established to encode the reaching movements of the task and contain sufficient information to drive a BMI. The cortical areas involved in reaching, but more specifically bimanual reaching extend beyond simply primary motor cortex (see Sections 1.2, 1.4). An understanding of the previous literature guided our design of the multielectrode implantation procedure. In January 2012, monkey C was implanted with electrode arrays in bilateral SMA, PMd, M1, S1, and PPC (Fig. 20A-B). I worked with the lab engineer to arrange the electrode layout with considerations for space limitations within the headcap, electrode design, surgical difficulty, and the goals of this project. The surgery was successfully performed by a clinical neurosurgeon who has performed

rhesus monkey cortical implantations for our lab for the past 15 years. Eight 96 channels arrays (Fig. 20C) were implanted for a total of 768 electrode channels. Cortical locations were identified both with stereotaxic coordinates and cortical surface landmarks, such as the central sulcus and prominent vasculature. Each shaft of the 4x10 array grid contained up to three electrode microwires (42 micron diameter each) which were offset by 400 microns to different depths (Fig. 20D). This enabled neural activity to be sample from different layers of cortical tissue. The microwires were stainless steel 304 with polyimide insulation. The ends were clipped to expose the conductive material to the tissue. The bundle of 2 or 3 wires on each cannula could be moved vertically in the tissue by a microdrive system. Final assembly of all electrode arrays was conducted at the Duke University Center for Neuroengineering by lab engineer Gary Lehew.

On the day of surgery, the electrode array structure (Fig. 20C) was lowered into exposed craniotomy sites across the skull. Because the dura was removed, the arrays were lowered until the cannula reached but did not enter the cortical surface (Fig. 20C). At this point, the microwire bundles were still up within the cannulae. The electrode array structure was wider than just the grid of cannulae and the green housing extended over the intact skull. As was used in previous surgeries, dental cement fixed the electrode array housing to the skull. Furthermore, I decided to add Cerasorb to the implant site, which is a synthetic powder used to promote bone regeneration and strong integration with the implant (Fig. 20C, bottom right). A headcap was fastened to the skull in 6 locations with T-bolt screws. The headcap enclosed the surgical sites and the

newly implanted electrode arrays, allowing recovery to occur while restricting access to the monkey. Three days after the initial surgery, Omnetics output connectors (Omnetics Connector Corporation, Minneapolis, MN) were fixed within the headcap with dental cement. It is these connectors which are routinely plugged into during daily experiments. This connector layout remains intact for current experiments (Fig. 20B). One week after surgery, we used the microdrive system to slowly insert the microwire bundles into the cortical tissue such that the deepest electrodes were 2 mm below the cortical surface. The microdrives were driven by a screw located on the top of the electrode array (grey part of Fig. 20C). The monkey fully recovered and stable neural units are still found at many of the electrode sites, 25 months post-surgery.

The next step in scaling to high channel-count neural recordings is in the signal processing hardware. The recording capability of the experimental setup was expanded from 128 to 384 channels, meaning that signals on up to 384 electrodes could be recorded simultaneously. All neural data was amplified 8X by headstages and 1000X by 64-channel preamplifiers. Three 128-channel Plexon Multichannel Acquisition Processors (MAP) received input from preamplifiers and digitized the signals. Each MAP then sent data to the spike sorting software of its corresponding computer. To temporally synchronize the data across three recording systems (and allow channel count to increase beyond 128), an external sync feature was added such that offline data would be precisely aligned. Recorded activity was displayed using Plexon Sortclient software. Multiple cells on each channel could be sorted using a combination of built-in features

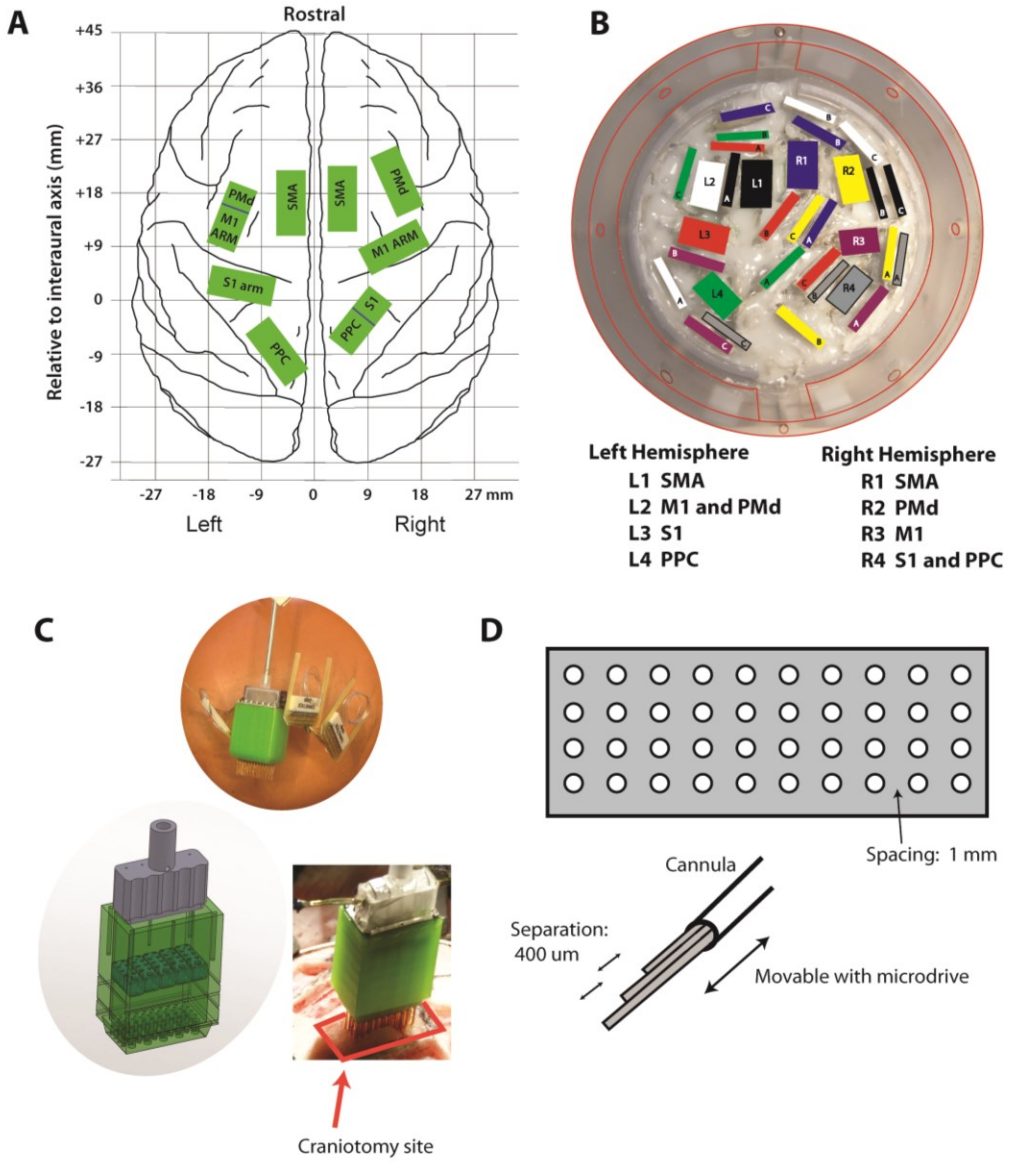

Figure 20: Electrode array cortical layout and design. (A) Monkey C was implanted with eight 96 channel arrays (green rectangles) across both cerebral hemispheres and eight cortical areas. (B) A top-down photo after array implantation showing array location (large rectangles) and the output connectors (thin rectangles). Color indicates the output connectors corresponding to specific arrays. Array location denoted below (B). (C) Photo of a single 96 channel array with the three output connectors (top), a CAD rendering of the array (bottom left), and a photo of the array during implantation after it was lowered to the cortical surface (bottom right). (D) Each array was comprised of a 4x10 grid of cannulas, and each cannula had up to 3 microwires offset at different depths. Lateral spacing was 1 mm cannula to cannula and vertical spacing was 0.4 mm between microwires on same cannula.

and visual/auditory inspection. During recording sessions, on-line waveform template matching and thresholding features recorded timestamps of spike events.

5.2 Experimental apparatus

Several modifications were made to the experimental setup to facilitate the types of experiments proposed in this study. Both changes discussed here were essential for the passive observation and brain-control experiments of this study. Although previous studies may not have included such features, I saw this as an opportunity to raise the standard for rigorous experimentation in movement-free BMI experiments.

5.2.1 Eye tracking system

Among the many challenges of using rhesus monkeys for a brain control task, a primary concern was accounting for shifts in attention. Once the joystick is removed, it is often difficult to know exactly when the monkey is attending to the screen and when they are not. This simple piece of information provides important context for task performance and neural activity recorded in non-joystick sessions. In a typical experiment, the first 10 minutes would feature nearly 100% attention to the screen. This includes 5-7 minutes of passive observation when receiving "free" juice when the hand enters the targets. During the next 20-30 minutes of brain control, the monkey would typically attend to trials for long, contiguous segments of time with periods interspersed when they would lose attention from the screen. At the end of the session, typically starting 35-45 minutes after the beginning of the experiment, the monkey would lose all

interest in engaging in the task. This became very clear when the monkey would attempt to twist their body/neck such as to not face the screen or close their eyes for extended periods of time.

My solution was to add an eye tracking system to the experiment room. The level of sophistication did not to be as advanced as the scleral-embedded search coil commonly used in saccade studies [244], but we simply needed a reliable way to gauge monkey attention to the display screen. The precise gaze of the monkey was not important to this study. We decided against a commercially available optical tracking system due to the high cost ($10,000-$30,000). The eye tracking system I used for experiments was a combination of open source software, a single camera, electronics equipment available in our laboratory, and UDP communication with the BMI suite. The camera was a DMK 21BF04 monochrome firewire camera by Imaging Source with a 180 mm lens that was mounted on a motorized pan-tilt support (Fig. 21A). The different components of the system were assembled and tested by both myself and fellow graduate student prior to first passive observation experiment.

The open source tracking software was based on the TLD (Tracking-Learning-Detection) algorithm for tracking unknown objects in real-time video streams [245]. The algorithm works by simultaneously detecting, learning, and updating its tracking with additional training data. The algorithm had four blocks: a classifier, a collection of labeled training examples, a training method, and a function that generates positive (attending to screen) and negative (looking away, eyes closed, etc.) training examples

during learning. During the first few minutes of a typical experiment, the monkey would be highly attentive to the screen. I used this period to train the algorithm. This ensured that the database of positive and negative data would have sufficient positive data for better object tracking sensitivity. Additionally, this obviated the need for predefined databases with large data sets of potential monkey eye positions that generalized across animals. Rather, training an animal on its own eye tracking was a better solution for this project.

The method for using the TLD algorithm during an experiment was very simple. Running the Matlab code prompted a frame from the video stream to open in a figure window. The user then empirically defined the outermost boundaries needed for discriminating whether the monkey was watching the screen (Fig. 21B). This was typically a rectangle slightly larger than the boundary of the monkey's left eye (only one eye needed to be tracked). I considered the monkey to be watching the screen when the eye was tracked inside the defined boundary. If the eye was tracked outside the defined area or not at all (head turned completely sideways or eyes closed, Fig. 21B, lower panel), the state was considered "not watching." An additional feature was added that allowed the user to discontinue the learning phase while continuing to detect. Typically, the real-time algorithm could be trained within 1-2 minutes of the onset of the experiment.

The final step of eye tracking was the interface with the BMI software, which dictated task control and decoded neural activity from the monkey. The eye tracking

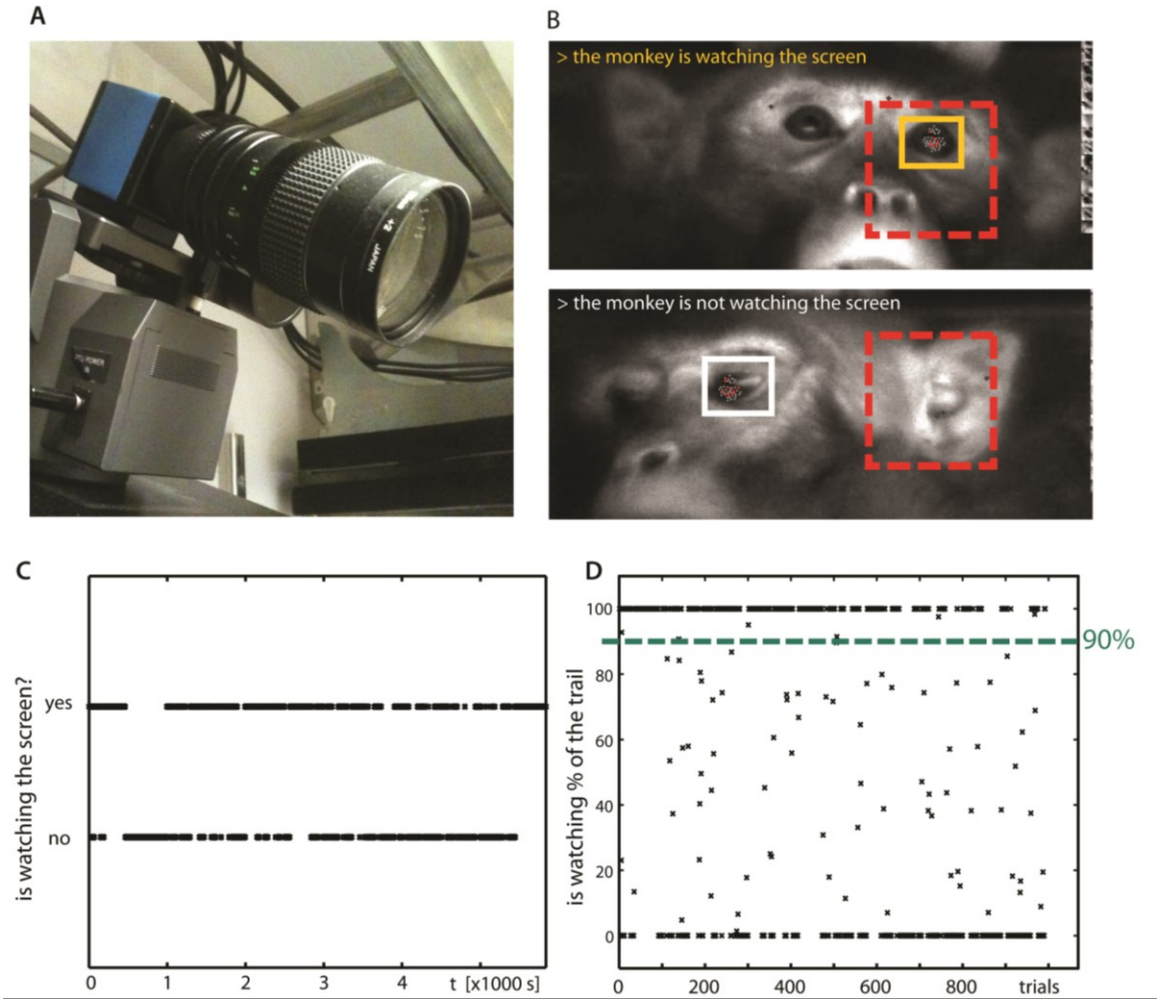

Figure 21: Eye tracking system used during experiments. (A) The firewire monochrome camera was mounted on a pan-tilt support near the ceiling on the wall facing the monkey. (B) Snapshots of the tracking window. Dashed square is the predefined "watching" area. Top: the eye is tracked and is inside of the "watching" area. Bottom: the eye is tracked but is outside of the "watching" area. (C) Value of "is watching" logged in the BMI throughout the session. Tracking data downsampled to 1Hz and shown for full 80 minute session. (D) Percentage of each trial that the monkey was watching the screen. If the monkey attended to the screen for less than 90% of the trial, it was considered a "not watching" trial.

data was sampled at 10Hz in Matlab and send over UDP to the BMI. The reasoning for this was twofold. First, I sought to use the watching/not watching state to control whether the monkey received juice reward. If the eye tracker determined a "not watching" state for greater than 5 seconds continuously, the reward would be withheld until the state was returned to "watching" for at least 1 second continuously. This prevented the monkey from looking away from the screen during the task and only turning to receive their reward when they heard the juice being dispensed. More importantly, this reinforced the correct forward-facing, eyes-engaged behavior that was needed for the experiments of this study. Secondly, sending the watching/not watching state to the BMI was important because the BMI logged this data synchronous with behavioral data. This allowed the watching state to be logged at 10Hz for the entirety of the experiment (Fig. 21C). Offline, a trial was considered to be attended if the eye tracking state was "watching" for greater than 90% of the duration of the trial (Fig. 21D).

5.2.2 Customized primate chair for experiments

The primate chairs used in bimanual BMI experiments featured a removable piece to allow full arm restraint during brain control experiments (Fig. 22). There were several important design considerations. First, the restraints must be safe and comfortable for the rhesus monkey during the course of the 45-60 minute experiments. Second, both arms must be securely immobilized in a natural position. Third, the design must be adaptable for monkeys of different arm lengths and torso sizes.

To ensure comfort and safety, the restraint was foam-padded at all points of

contact with the monkey – the torso, the dorsal side of forearm, and the ventral side of forearm (Fig. 22D). The restraint slid into the waist plate slot of the chair and could be inserted to different degrees in order to allow both large and small monkeys to be comfortable in this restraint. This was important because the two rhesus monkeys used for these experiments were a large male (10.6±0.3 kg) and a small female (6.4±0.2 kg). The restraint was inserted at waist level until the foam pad made light contact with the mid-torso, but without any constant pressure.

The arms were comfortably secured by placing the elbows just over the torso padding and resting the pronated arms at a natural upward angle in front of the monkey. The angle of elbow bend was enforced by setting an adjustable shelf to a fixed angle (Fig. 22D). To be consistent, I adjusted the angle such that the middle of the hands was approximately the same height as the base of their neck, regardless of the size of the monkey. First, a Velcro strap attached to the restraint was looped around the biceps and tightened. Next, a foam pad was laid on top of the pronated forearms (in addition to the foam-padded shelf beneath both arms). The forelimbs were secured to the shelf by looping a cable tie around each forearm and into pairs of holes in the shelf itself. This method assured that the arms could not be moved and there was no pinching due to the cable tie being in contact with the skin. There was always a foam pad between the cable tie and the monkey's arm. The design was successfully utilized in all passive observation and brain control without arm movement experiments. I observed that the monkeys became accustomed to the restraint within 1 week of experiments. The initial

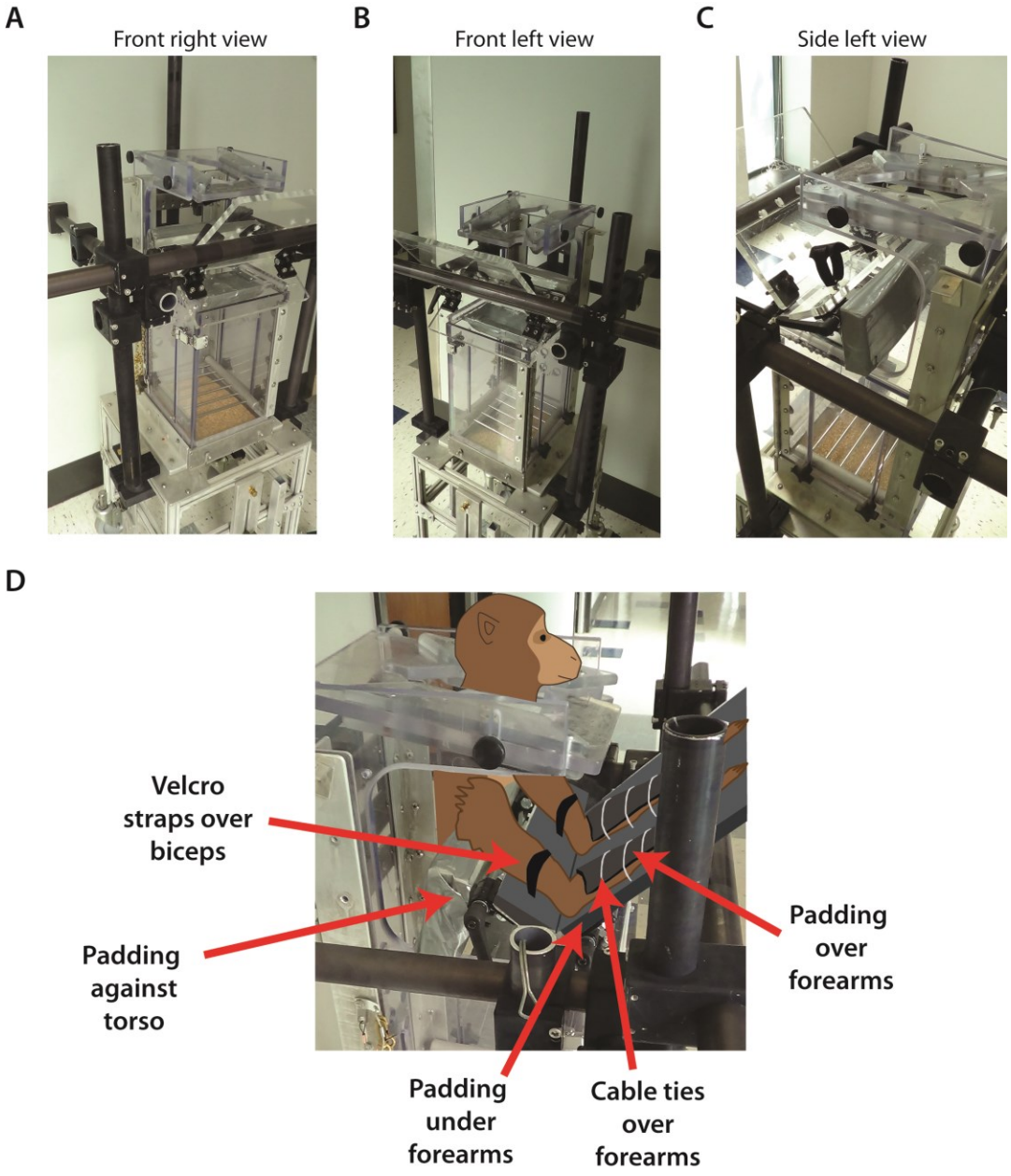

Figure 22: Custom primate chair for experiments. (A-C) Photo images of the primate chair with attachments to adequately restrain both arms of the monkey. In images, the restraint is inserted at waist level and includes both the torso pad and the forearm shelf. Black rods in the images are for additional support for the shelf so it could not be pushed downwards. Different views are front right (A), front left (B), and side left (C). (D) Image of custom primate chair with drawing of monkey superimposed to show full setup. As shown, the Velcro straps, foam padding, and cable ties are in place as described in text.

goal of movement restriction was confirmed by recording with electromyography (EMG) electrodes on left and right arm muscles. Although the results will be shown more extensively with the BMI results, I largely observed that the monkeys did not move their arms while the restraint was in place. Occasional arm movements did occur, but they were not related to the movements on the screen.

5.3 Virtual reality rhesus monkey avatar

The need to advance to more sophisticated, realistic artificial limbs becomes even more pronounced during bimanual movements. My solution to this challenge was to enhance the realism of the end effector. The term end effector is commonly used in robotics to describe the distal end of a robotic limb, designed to interact with the environment. In neural prosthetics, the end effector is controlled in real-time through some form of actuation system. There have been different actuation/end effector solutions proposed in past studies. Most provide some form of visual feedback, although this can be highly simplistic such as a cursor circle on a computer screen [116, 195]. Others attempt to recreate the arm itself with complex, high degree-of-freedom (dof) prosthetic limbs that can give the user full or partial control [111, 241]. As discussed in the literature review (Section. 2.1), all have their advantages and drawbacks. A highly customizable, inexpensive solution which exploits several key advantages is an end effector within a virtual environment. For reaching movements, this end effector would be the arms of an avatar body in virtual space. Although some work in our lab had pursued using a single avatar arm in a subset of experiments in

parallel with cursor-only experiments [129], the bimanual BMI study was the first to exclusively use a virtual environment throughout all paradigms: joystick control, passive observation, and brain control experiments [242]. The scientific advantages of using an avatar compared with a cursor or other actuators will be more thoroughly discussed in later sections on the bimanual BMI and passive observation experiments. Here, I will present some details on the design and control of the rhesus monkey avatar

5.3.1. Important considerations

1) **Intuitive end effector control:** The user should be able to easily infer the relationship between planning/executing a movement and the ability to control the end effector.

2) **Fast rendering and control:** The rendering and control needs to be very fast and without any apparent delays. Real-time control must be possible with <10 ms delays.

3) **Customizable, experiment-specific paradigms:** Different experiments need different perspectives (first vs. third person), different tasks (single arm vs. two arm reach), or different interactions with their virtual environment.

4) **Inverse kinematics**: By controlling the endpoint of the reach, the avatar should enact biomechanically realistic joint rotations to accomplish the desired movement.

5) **Simple to interface with BMI**: The control module for movements is fully dependent on the neural decoder from the BMI. There should be a straightforward way to communicate between the BMI software and the virtual environment.

5.3.2 Motionbuilder and other viable alternatives

The solution which our lab has pursued, given the aforementioned list of considerations, was a commercially available character animation software program called Autodesk Motionbuilder™ (Autodesk, Inc., San Rafael, CA). The rhesus monkey avatar graphic artwork was designed previously by a fellow member of the Nicolelis lab and a professional 3D designer in Autodesk 3ds Max™. Motionbuilder is software commonly used in film and gaming industries and offers a real-time 3D game engine. As such, Motionbuilder fully meets the requirements for rapid rendering, built-in inverse kinematics, and customizability. Alternatives such as a fully customized (from the ground up) C++/openGL/python development or a gaming engine (e.g. Unreal Engine) could fully satisfy all considerations as well, yet the learning curve was unnecessarily steeper for the typical paradigms in our lab's research. Character controls are built-in for Motionbuilder and the position of up to 20 points on the rhesus monkey skeleton can be controlled. Advances by others in the lab prior to my project included several iterations through increasingly realistic monkey avatars as well as a richer set of facial expressions which could be animated (Fig. 23).

5.3.3 BMI communication with Motionbuilder

For Motionbuilder to animate movements of the avatar in real-time, there must be fast communication between the task control software (the BMI) and Motionbuilder. Two open source Motionbuilder plugins were modified by myself and graduate student Solaiman Shokur in order to receive the input sent from the BMI and send information back to the BMI, respectively. In the BMI suite, kinematic data was updated and logged

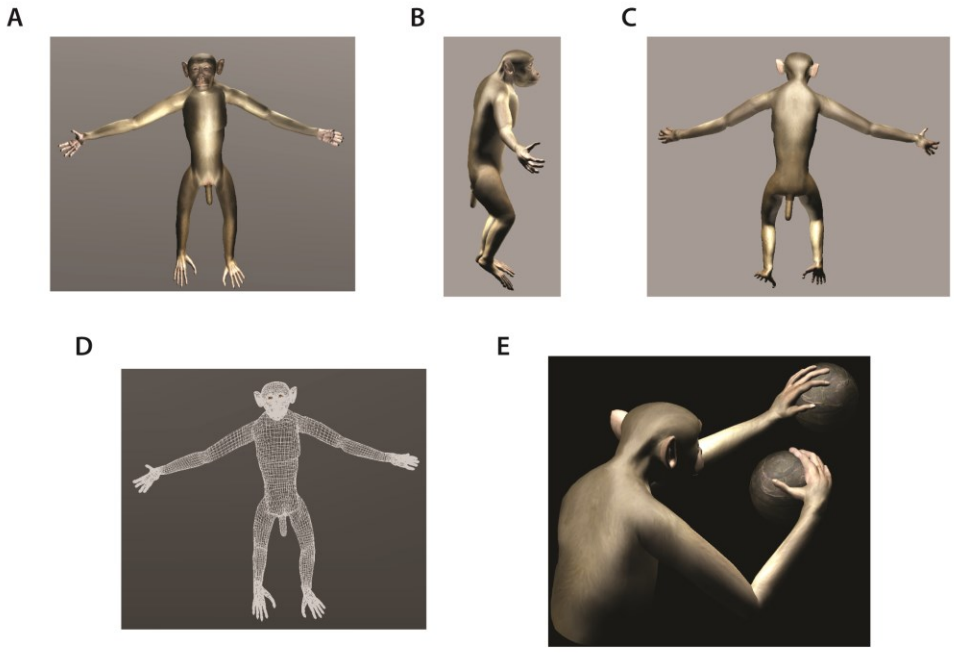

Figure 23: Rhesus monkey avatar in Motionbuilder. (A-C) Screenshots of the rhesus monkey avatar body in an upright posture with all limbs outstretched from front (A), side (B), and rear (C) angles. (D) Same as (A) but in wireframe view. (E) Avatar during bimanual reaching – note the detail and realism of the hands and arms.

at 100 Hz during experiments. I added an additional function that was called during the main update function that sent appropriately formatted data over UDP to the computer running Motionbuilder. To reduce CPU usage on the computer performing real-time neural decoding, Motionbuilder was run on a separate computer.

The plugin was customized such that all task-relevant information could be sent to the virtual reality environment. For example, the (x,y) position of the right and left arms was important and constantly varied during bimanual movements, but the z position of both was fixed for 2D reaching. In addition, task parameters like target

location and size were also sent by way of the UDP stream. Within Motionbuilder, the peripheral targets appeared as white spheres and the center targets as white cubes. All state updates during task performance (e.g. in/out of target, hold times) were judged by the task state machine in the BMI. The only function of Motionbuilder was to display the virtual representation of the arm movements and the reach targets. Although Motionbuilder has capability of object interaction physics, such complexity was not essential for the experiments in this study.

During the experiment, the arms were viewed from a first person perspective. The hands reached towards 2D projections of spheres (circles) and cubes (squares). Instead of actually touching these objects – an action that would require collision detection physics – the movements were all made in a 2D (x,y) plane above the targets, so the hands never would pass into the spheres or cubes.

5.4 Discussion

With every new scientific study, it is essential to consider technological and experimental advances that could augment the significance of the results. Pursuing an ambitious goal such as bimanual BMI control was a great example of this. One alternative would be to employ small microelectrode arrays in single cortical areas. Similarly, I could have omitted the custom primate chair and eye tracking system. These had not been used previously. Despite this option, I believed that the additional time spent improving the electrodes, experimental apparatus, and VR system was critical for the proposed experiments. A first-of-its-kind experiment required first-of-its-kind

technology. I have discussed several different ways to achieve these technical advances, but the solutions I pursued were selected both because of the best mix of function, customizability, and quick implementation.

At the time of surgical implantation, the 768 electrodes implanted into monkey C (Fig. 20) was the largest documented implantation of microwire electrodes in any subject. This monkey was the first subject to surpass 500 neurons recorded simultaneously. Even more, these neurons were sampled from multiple areas in both cortical hemispheres. Our lab considers this alone to be a significant achievement, as we consistently report the great value of larger ensembles of neurons for BMIs. The large numbers of healthy, recorded, single units in monkey C persist even to this day, approximately 25 months after surgery. We have since implanted a monkey with even larger arrays but the 768 channel surgery was a key demonstration of efficacy for the electrode geometry, material, and surgical techniques.

Improvements to the experimental apparatus were also critical for the success of the study for the purpose of scientific rigor. BMI systems often do not track attention to the screen, however I felt that knowing this information was highly relevant to understanding what are task-related modulations and what are not. Restraining the arms may also seem unorthodox, but it is a straightforward way of preventing own-body movements such that cortical modulations only represent virtual-body movements. Many studies outside of the Nicolelis lab omit such sessions, leaving open the possibility that arm movements are still occurring during BMI control [115, 116, 246].

The arm restraint continues to be used in experiments performed since the bimanual BMI study. The restrain works very well for monkeys of different sizes and the subjects quickly become accustomed to the fit.

Lastly, the rhesus monkey avatar was an improvement to the BMI paradigm that I feel will become even more important as the clinical stage is approached. The potential impact for using VR is enormous and I am only making a small, but important first step in this study. Fully immersive virtual environments evoke an even stronger experience for the user and could be the focus of human studies in the future. Preliminary results which will be discussed in later chapters show that even rhesus monkeys respond better to the avatar arm end effector than to a cursor circle on the screen. Virtual arms have some advantages and disadvantages compared with robotic limbs. The interface we developed in this study between the BMI and Motionbuilder allows for what we believe is a simpler way to adapt avatar arms visualization and control from day to day or experiment to experiment. An easier learning curve was valuable for lab members with varied programming backgrounds. Virtual reaches, however realistic and immersive, fail to provide the same user satisfaction as reaching and interacting with the world around them (e.g. robotic prosthetic limbs). The ability for a patient to see themselves move and manipulate real objects is important for basic quality of life and should not be overlooked. Despite this consideration, utilizing VR in BMI paradigms is highly advantageous at this stage of development. In the next series of experiments, I promote how using a virtual environment can be extremely valuable as a tool clinically for

patients to experience limb movements who may be paralyzed or without a limb. I will discuss this further in the context of the results in Chapters 6-8.

6. Cortical neurophysiology of unimanual and bimanual movements

The ability to simultaneously record from large ensembles of 500 or more neurons with a new scalable recording system paved the way for innovative and important experiments in both basic neurophysiology and neural prosthetics research. The first step, however, was to carry out relatively simple experiments requiring joystick movements to better understand the neural representation of upper limb reaching movements. I decided to start here rather than immediately begin with bimanual BMI experiments for several reasons. First, no experiments have ever looked at distributed, large-scale cortical recordings during bimanual movements. Although comparisons between unimanual and bimanual movements at the cortical level have been made previously, these studies all had small recorded populations and could only observe single or few neurons simultaneously [76, 77]. Beyond simply the neuronal mass, looking at neuronal modulations in primary motor, sensory, supplementary motor, and posterior parietal areas simultaneously enables a unique perspective on pre- and peri-movement neural processing. Such a perspective reveals not only relationships between neural activity and movement but spatiotemporal relationships between area A and area B at the single neuron and population levels. These rich data sets can be mined for meaningful patterns and themselves could identify key findings which could fill the remainder of this thesis. Maintaining the focus on building towards a bimanual BMI, I used this initial phase of experiments to collect data for offline analysis and testing of

decoding algorithms prior to real-time implementation (Chapter 9). To reach this point, the rhesus monkeys needed to be methodically trained to perform accurate one and two arm reaches. I will begin by outlining the training steps which introduce the behavioral tasks and experimental designs.

6.1 Methods

6.1.1 Behavioral training and joystick control task

Prior to surgical implantation (Section 5.1), monkey C was trained over the course of 18 months to accurately and simultaneously manipulate two joysticks in goal-directed reaching movements. The training began when the monkey had no previous experience in any task with a joystick or juice reward. Monkey C was first introduced to the primate chair and the juice lixit which delivered the liquid reward (typically this was fruit flavored Hawaiian Punch) through a straw to a monkey who was when seated and facing forward. Next, a single spring-loaded joystick was placed in front of the working arm of the monkey, with the knob at waist level approximately 20 cm in front of the monkey. The single joystick denotes a one arm ("unimanual") experiment. Tasks where the joystick must be manually moved by the monkey will be referred to as "joystick control" tasks. During initial training, the monkey received juice anytime they touched the top part of the joystick. After the monkey learned to associate the joystick with the juice reward, I changed to a task called "center-out" and the monkey learned to associate movements of the joystick with movements of a cursor on the screen. The center-out task (Fig. 24A, left to right) proceeds in the following steps:

(1) Cursor is moved inside an 8 cm diameter circle at the center of the screen ("center target")

(2) Cursor remains inside the center target for a random hold time (400-1000 ms)

(3) Center target disappears and a new 8 cm diameter circle ("peripheral target") appears near the edge of the screen at either 0, 90, 180, or 270° relative to the center of the screen

(4) The cursor must move into the peripheral target and stay within this target for 100 ms

(5) If steps (1)-(4) are completed within 10 seconds, the monkey receives a small juice reward. If the steps are not completed in 10 seconds, the trial times out and the next trial begins at (1)

Monkey C learned and mastered center-out first with her left arm and later with her right arm. To advance to the next paradigm, the monkey had to achieve consistent daily performance of greater than 95% correct trials. These steps took approximately 6 months to complete.

Next, a second joystick was introduced such that two identical joysticks were positioned in front of the monkey – both at waist level as with the unimanual experiments. The monkey then learned a new type of center-out which required movements of both arms toward a single target (Fig. 24B, left to right). This experiment was a transition between unimanual and bimanual center-out. In the single-target bimanual task, two cursors appeared on the screen. The left joystick cursor was white

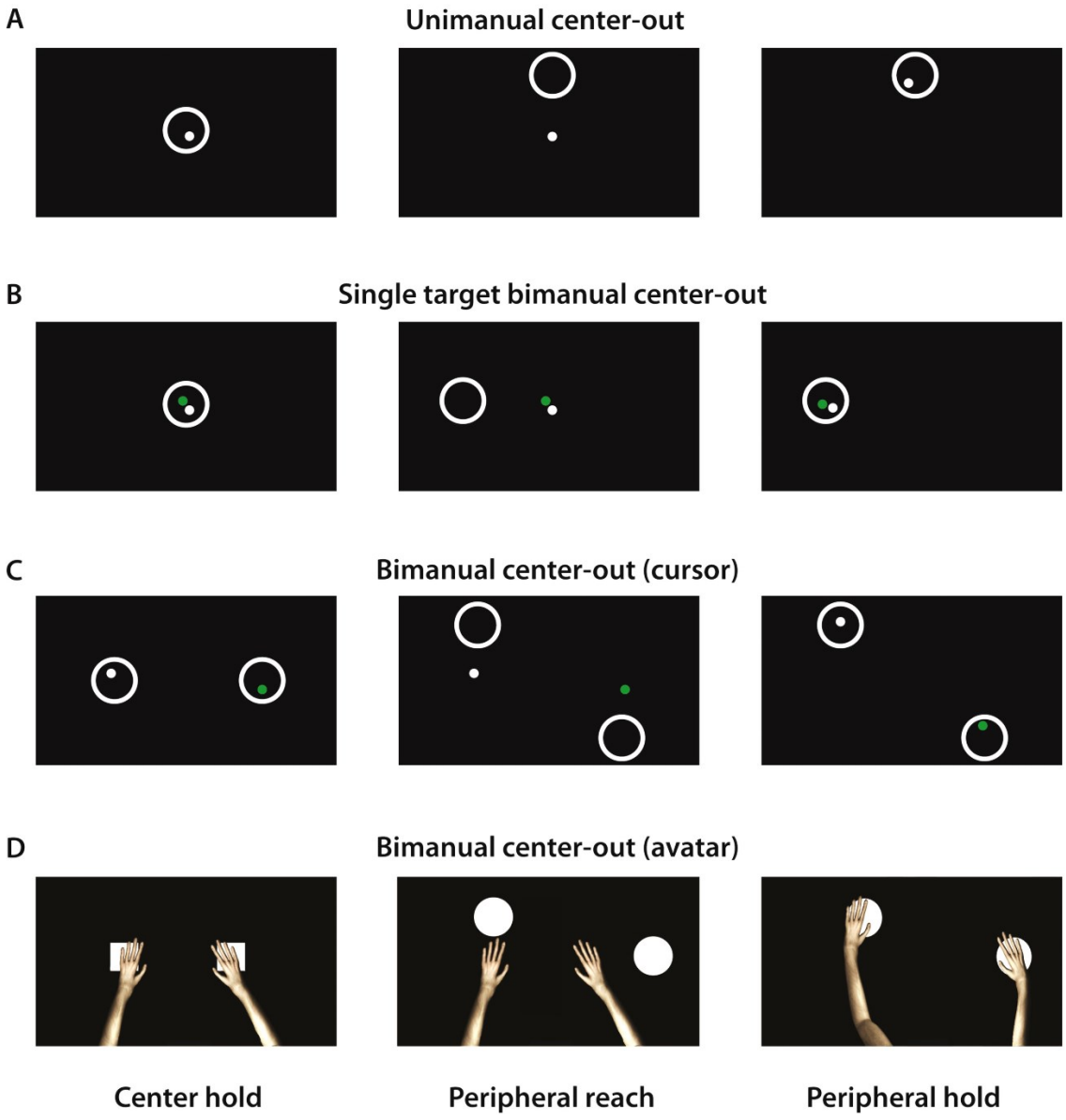

Figure 24: The four behavioral tasks used throughout training, from first to last. In each, there is a center hold step, a reach to peripheral target(s), and a peripheral target hold step. (A) Unimanual center-out using a cursor display. (B) Single target bimanual center-out with two cursors colored white (left joystick) and green (right joystick). (C) Bimanual center-out with two targets and a cursor display. (D) Same as (C) except the cursors are replaced with the arms/hands of the rhesus monkey avatar viewed from a first-person perspective. The center targets were changed to be filled white squares and the peripheral targets were changed to filled white circles.

and the right joystick cursor was green. The same steps (1)-(5) applied to the bimanual single-target task except both cursors needed to be in the center target (step (2)) or in the peripheral target in (step (4)). For example, if the peripheral target was to the left (Fig. 24B), both the right and left joysticks must be moved to the left into the peripheral target circle. Monkey C learned this task within 5 weeks of experimentation.

Lastly, monkey C learned the bimanual center-out task with two targets (Fig. 24C, left to right), which occurred over a span of approximately 6 months. The task design was based on a bimanual reach task used previously [76]. This differed from the single-target bimanual task in several ways. The left cursor was centered on the left half of the screen (left center point) and right cursor was centered on the right half of the screen (right center point). Similarly, there were two center targets which were also aligned on the left and right center points. The task became a duplicate of the unimanual version so that each arm would need to move to its center, hold, and move peripherally in its specified direction in the following steps:

(1) Right and left cursors must move to their corresponding center targets on the screen

(2) Both cursors must simultaneously remain inside the center targets for a random hold time (400-1000 ms)

(3) Center targets disappear and two peripheral targets appear: One is 0, 90, 180, or 270° relative to the left center point, one is 0, 90, 180, or 270° relative to the right center point

(4) The left cursor must move into the left peripheral target and the right cursor must move into the right peripheral target.

(5) Both peripheral targets must be entered and simultaneously held for 50 ms

(6) If steps (1)-(5) are completed within 10 seconds, the monkey receives reward

6.1.2 Introduction of rhesus monkey avatar during behavioral training

At this point, I introduced the rhesus monkey avatar as the end effector instead of the cursor. After a brief adjustment period of 2-3 weeks, the monkey re-learned bimanual center-out with the two avatar arms (Fig. 24D, left to right). In this design, the middle of the avatar hands represented the joystick position. If the middle of the avatar hand was inside the target circle, this was considered "in the target." The remainder of experiments used only the avatar display. For the next 3 months, I continued to train the monkey on the task in order to overtrain their performance, yielding highly stereotypical trajectories and fast, accurate trials. Some additional training was also due to a delay in the implantation surgery date.

A second rhesus monkey – monkey R (male, 7.2 kg) – was also trained in both unimanual and bimanual center-out, similar to monkey C. There was one key difference in the sequence, however. I was interested in the effect of training rhesus monkeys using the avatar arm end effector compared to training using the cursor end effector. The end effector was alternated from one day to the next between avatar and cursor, beginning with the first day of unimanual center-out training. This included 20 sessions to learn unimanual with its left arm, 15 sessions for unimanual right, and 20 for

bimanual. Alternating between avatar and cursor visual feedback enabled us to see the rate of learning of one mode compared to the other. The training sequence for monkey C could not provide this because the monkey was fully trained on the cursor end effector before the avatar was introduced in any experiment.

6.1.3 Paradigm for comparing the neural representations of unimanual and bimanual movements

After monkey C was implanted and recovered from surgery, both unimanual and bimanual experiments resumed. My goal was to study the differences between the neural representations of unimanual and bimanual movements. For the best comparison, I designed an experiment where all three movement types (unimanual left, unimanual right, and bimanual) were included within a single 60 minute experiment. The alternative would be to have different experiments on different days, but that would increase the likelihood that a given recorded neuron on one day goes away or is not the same neuron that is recorded on a different day. Furthermore, a neuron may change properties from one day to the next due to something completely unrelated to the experiment. The experiment proceeded in the following order:

(1) Bimanual center-out (150 trials)

(2) Unimanual left arm (150 trials)

(3) Unimanual right arm (150 trials)

(4) Bimanual center-out (continue until monkey stops working)

On the screen, the four stages of the experiment were made to be as similar as possible.

During (1) and (4), both arms appeared on their respective sides of the screen. During (2) and (3), only the working arm was shown to the monkey. Similarly, the door on the primate chair that allows the monkey to reach the joystick was closed for the non-working arm.

Two such experiments were conducted with monkey C for a total of 507 bimanual trials, 354 unimanual right trials, and 305 unimanual left trials. Monkey C was implanted approximately 6 months before these experiments with 768 electrodes implanted across both cortical hemispheres, as described in Section 5.1. In these sessions, 88-121 neurons were recorded from SMA (88-104 left hemisphere, 0-17 right hemisphere), 233-271 neurons were recorded from M1 (187-210 LH, 46-61 RH), 44-51 neurons were recorded from S1 (13-51 LH, 0-31 RH), and 29-47 neurons were recorded from PPC (0 LH, 29-47 RH).

6.2 Results

6.2.1 Comparison of cursor and avatar end effector during training

Monkey C was fully trained on the bimanual center-out task using cursor prior to any training with the avatar. In time, the monkey was able to reach similar, high levels of performance (>95% correct trials) with both end effectors. Comparing the two, however, is confounded by the fact that the monkey was fully trained on bimanual movements prior to avatar exposure. Monkey R was trained via alternating cursor and avatar experiments. To quantify the effect of end effector on behavioral performance for each monkey, I used two metrics: percentage of correct trials per session and the

percentage of attempted trials. The percent of attempted trials was calculated separately for each arm. I precisely defined an arm as "attempting a trial" if the corresponding joystick moved greater than 80% of the shortest distance between the center point and the target position. This metric gives an estimate of motivation and interest in the task, while percent correct gives an estimate of how well-learned the behavior is at a given time.

Monkey C scored higher in both percent correct trials and percent attempted trials for both arms during avatar experiments than cursor experiments ($p<0.05$, t-test). This is rather expected, given the confound of additional prior training before avatar experiments. For monkey R, the results were much more similar for the two end effectors, but with some subtle differences. During both right and left arm unimanual training, monkey R steadily improved in both performance metrics at approximately the same rate in both cursor and avatar paradigms (ANOVA, $p<0.01$). There was no significant effect of the visual display (cursor vs. avatar) during unimanual training, $p>0.05$, t-test). However, there was a subtle trend during bimanual training where avatar sessions have a higher attempted rate than cursor sessions (Fig. 25B-C). Looking at the two arms separately, the effect is significant for both the right arm ($p<0.05$, t-test). This is apparent when comparing the percent attempted for avatar session (red triangle) compared with the day-matched cursor session (blue circle). The avatar trials in nearly every session were attempted at a higher rate than cursor trials.

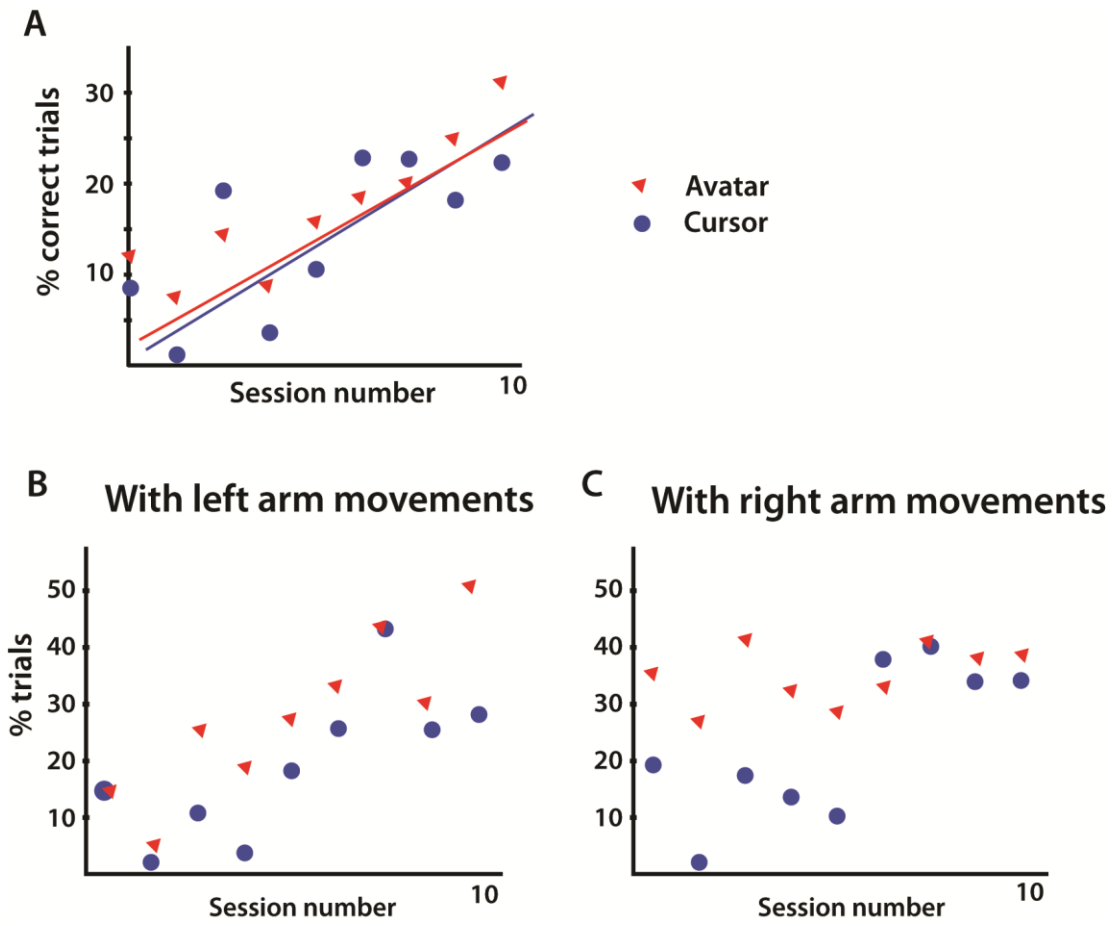

Figure 25: Comparison of bimanual behavioral training with cursor and avatar end effectors. (A) Percent of trials performed correctly during the first 10 sessions of the cursor-based (circles) or avatar-based (triangles) bimanual center-out. (B-C) Percent of total trials when the left (B) or right (C) arm reached greater that 80% of the distance from center to peripheral target. Experiments 1-10 in (A) are the same experiments 1-10 as in (B) and (C). From [242]. Reprinted with permission from AAAS.

6.2.2 Behavioral differences between unimanual and bimanual movements

Monkey C was trained to perform both unimanual and bimanual movements very accurately using joysticks (greater than 97% of the trials were correct, Fig. 26D). Reach trajectories for both were direct and performed in nearly the same length of time

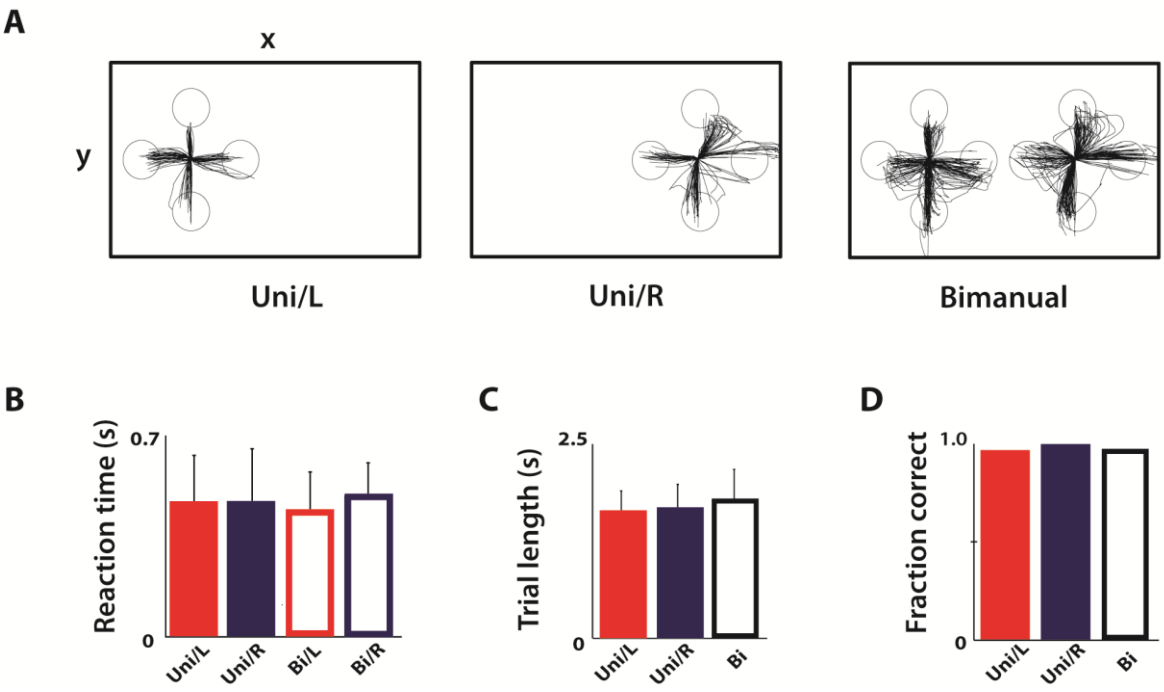

Figure 26: Behavioral results from bimanual and unimanual joystick control experiments. (A) Cursor trajectories for unimanual left, unimanual right, and bimanual trials shown as (x,y) position of the computer screen. (B) Reaction time of right and left arms during unimanual (filled bars) and bimanual (open bars) movements. (C) Comparison of trial length for unimanual left, right, and bimanual trials. (D) Comparison of fraction correct trials for each of the three trial types from a total of 354 right unimanual trials, 305 left unimanual trials, and 507 bimanual trials. All data indicates mean ± standard deviation. From [242]. Reprinted with permission from AAAS.

(Fig. 26C, $p>0.05$, ANOVA). Bimanual trajectories had somewhat more variation (compare Fig. 26A left, middle with Fig. 26A right), but this variation was still within the width of the target so it did not affect the trial outcome. There was no significant differences in reaction times of each arm between unimanual and bimanual ($p>0.05$, t-test, Fig. 26B). This establishes the minor, if any, differences between the behavior when only one arm moves compared to when both arms move simultaneously.

6.2.3 Neural modulation differences between unimanual and bimanual movements

The linear superposition hypothesis proposes that bimanual movements are simply the linear combination of two motor plans, one for each arm. At the behavioral level, I was unable to directly test this because only the motor output is observed. The motor plan is encoded in the neural modulations of motor-related cortical areas. To test this, we recorded from 434-450 neurons across M1 (233-271 neurons), S1 (44-51 neurons), SMA (88-121 neurons), and PPC (29-47 neurons) and in both hemispheres of monkey C (Fig. 27A).

Cortical recordings revealed widespread neuronal modulations that reflected movement timing and direction (Fig. 27B). Consistent with previous studies [76-78, 80], cortical activity from multiple cortical areas was different between unimanual and bimanual movements (Fig. 27B, 28-29). In motor areas M1 (Fig. 28) and SMA (Fig. 29), both individual units (Fig. 28A,C and Fig. 29A,C) and neuronal populations (Fig. 28B,D and Fig. 29B,D) alike exhibited directionally selective modulations during both unimanual and bimanual performance. M1 and SMA were selected for more comprehensive analysis due to more numerous recorded populations (187 and 104 neurons, respectively). For each configuration of the pair of targets, I characterized neuronal modulation as Δz – the difference between the movement epoch (from 150 to 600 ms after target appearance) firing rate and baseline firing rate, both expressed in normalized units (z-scores). Normalization to z-scores was applied to each unit's firing rate before any grouping or averaging of individual trials. Average modulations for all

target positions was quantified as absolute value of Δz averaged for all target positions, $\left|\overline{\Delta z}\right|$. Directional selectivity was measured as the standard deviation of Δz for different target positions $\sigma(\Delta z)$.

Looking at the left M1 neuron example (Fig. 28A, lower unimanual panels), there is a clear directional preferences for the right (contralateral) arm at angles 180° and to a lesser degree 270° during unimanual movements. The directional preference is less prominent for the left (ipsilateral) arm, with only 0° exhibiting a small stimulus-aligned response. Looking at the PETH during bimanual movements (upper 4x4 grid in Fig. 28A), it clear that the unimanual directional tuning does contribute but there is an additional amplification of activity across all left/right arm combinations. The 180° and 270° right arm columns (3rd and 4th columns in grid) do have a somewhat greater response than the 0° and 90° columns. The individual left/right combinations, however, do not simply reflect summed neural responses from the two single arms. This neuron is a particularly good example of this phenomenon because the ipsilateral arm has hardly any tuning, but evokes a positive shift in neural response when simultaneously engaged with the contralateral arm. This is clearly summarized by looking at the response amplitude (Δz) for each of the movement directions during unimanual and bimanual movements (Fig. 28C, Table 4). Furthermore, this was representative of what I observed across the entire population of left M1 neurons (Fig. 28B,D).

A second example of this bimanual tuning can be seen in SMA neurons (Fig. 29). Focusing again on a representative neuron (Fig. 29A,C), this effect is manifested in a

slightly different manner than in M1. The PETH response amplitude during unimanual movements is much lower in SMA than in M1 (compare unimanual panels in Fig. 28A,B with Fig. 29A,B). In the representative SMA neuron, the contralateral arm evokes a small response at 180° and the ipsilateral arm has an even smaller, broad representation of all directions except 0°. During bimanual movements (Fig. 29A, upper 4x4 grid), the pairwise combinations of left and right arms yield robust and pairwise unique neural responses. The strength of left/right combinations responses has little in common with the unimanual representation. For example, when both arms move at 90° there is a large response, despite the 90° direction being only minorly encoded during unimanual movements. The neural response in SMA is unique to the specific left/right direction pairwise combinations and not a linear byproduct of the two unimanual modulations. Similar to M1, the bimanual neural responses are higher in amplitude, both in the single cell and population examples (Figs. 28,29 C-D).

The transition from unimanual to bimanual movements (Table 4) induced several effects in M1 and SMA. First, I observed a prominent increase in $\left|\overline{\Delta z}\right|$ during bimanual movements by 76.7% and 34.6% for left M1 and right M1, respectively; and 35.8% and 37.9% for left and right SMA ($p<0.01$, t-test). M1 neurons exhibited clear preference for the contralateral rather than the ipsilateral arm during unimanual performance, both in terms of overall modulations (28.3% increase in $\left|\overline{\Delta z}\right|$ for contralateral vs. ipsilateral arm; $p<0.01$) and in terms of tuning depth (22.3% increase in

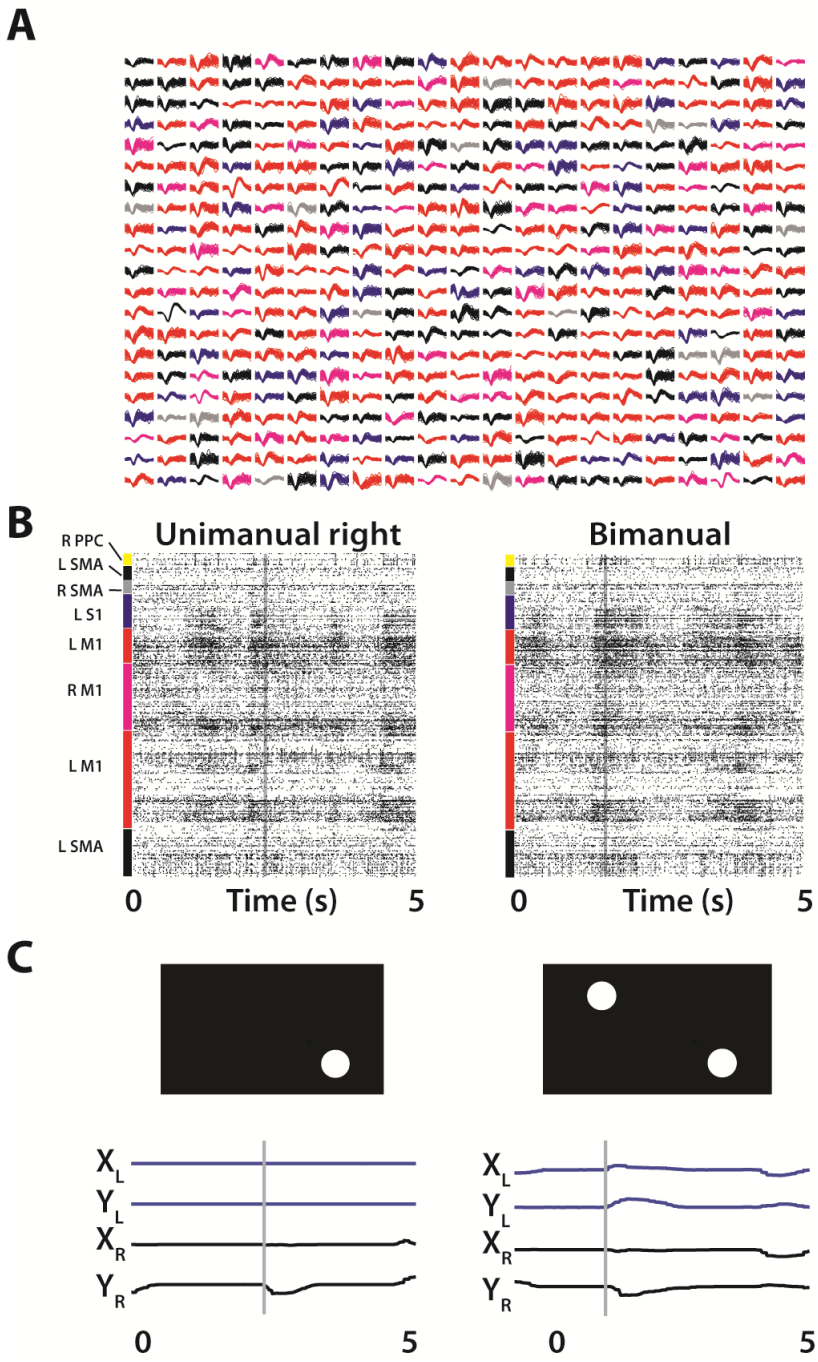

Figure 27: Large scale cortical recordings during unimanual and bimanual movements. (A) 441 sample waveforms from typical monkey C recording session with the color of the waveform indicating the recording site (see color column of (B). (B) Raster plot of a spike events from 438 neurons (y-axis) for a unimanual (left) and bimanual (right) trial. (C) Target location (top) and joystick traces (bottom) for the trial in (B). From [242]. Reprinted with permission from AAAS.

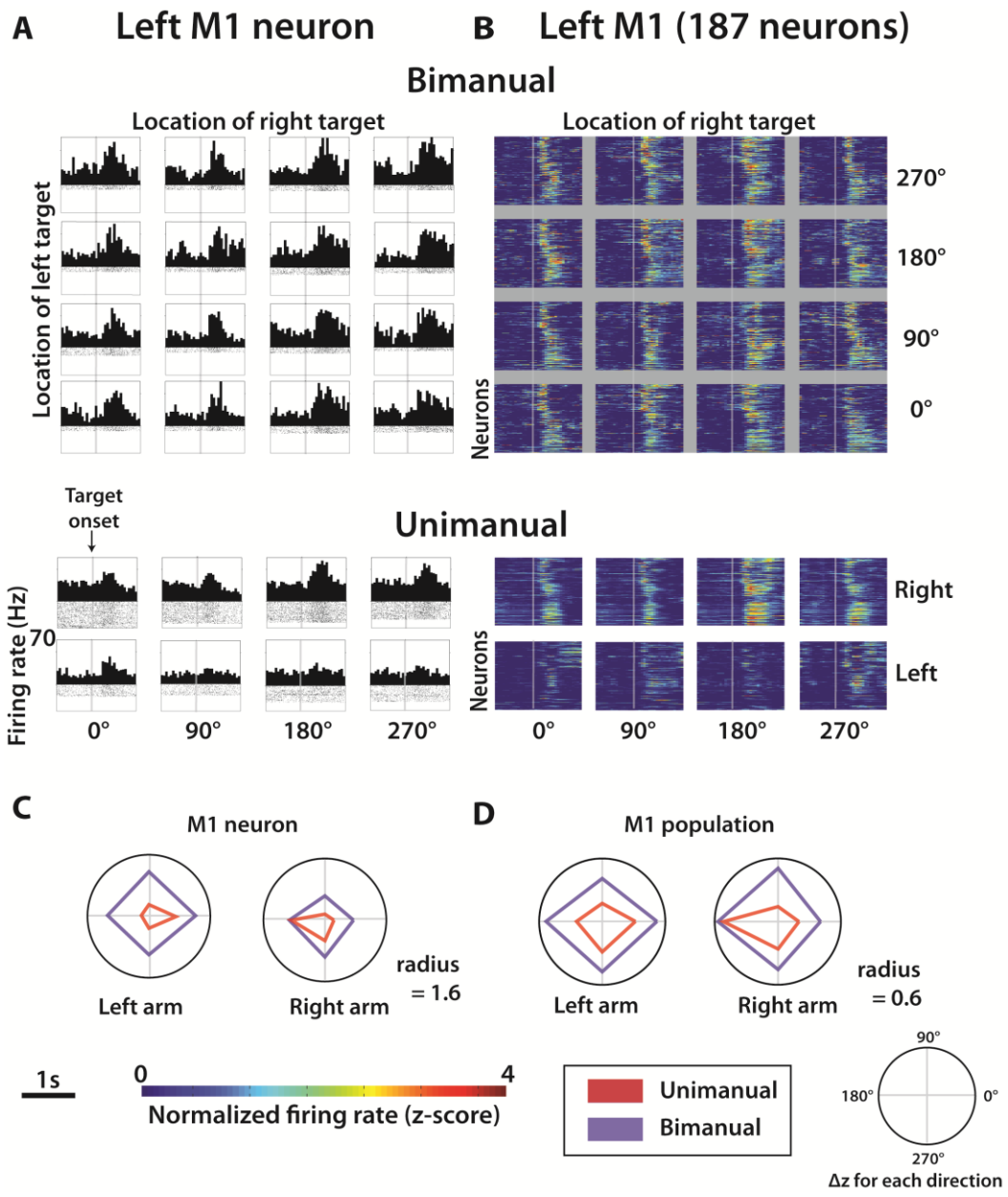

Figure 28: Modulations of M1 neurons during unimanual and bimanual movements. (A) Representative M1 neuron peri-event time histogram (PETH) aligned on target appearance (grey line) for each of the 16 left and right target combinations during bimanual movements. Below the 4x4 grid are corresponding PETHs for the same neuron during unimanual trial sin each of the four directions. (B) Same layout as (A) for the population of left M1 neurons. Each row of each color plot panel represents a single neuron and the pixel color is the normalized firing rate or z-score (color scale at bottom). (C-D) Δz for each of the four movement directions for unimanual (red) and bimanual (blue) trials for the left and right arms: for one M1 neuron (E), for a population of M1 neurons. From [242]. Reprinted with permission from AAAS.

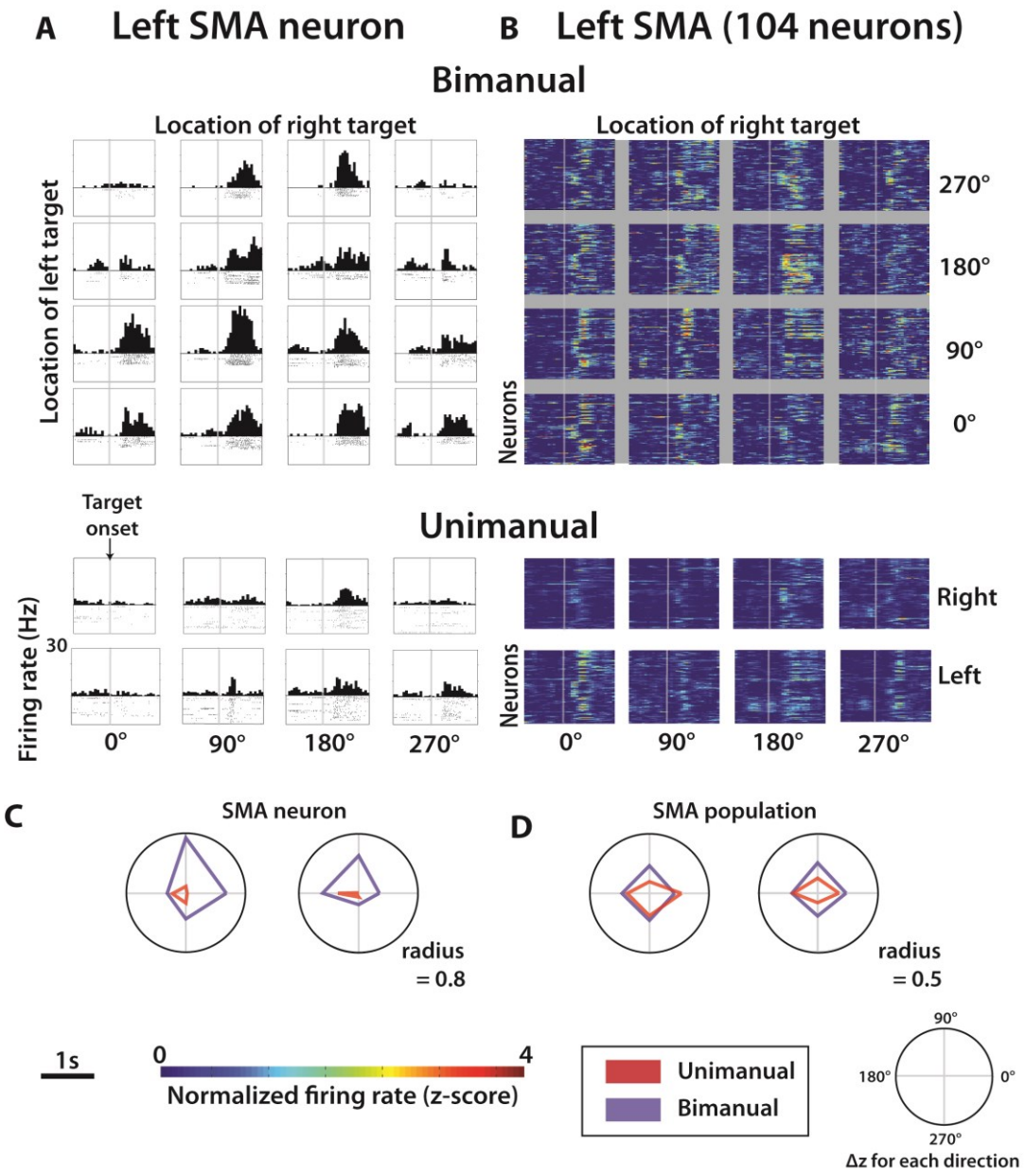

Figure 29: Modulations of SMA neurons during unimanual and bimanual movements. (A) Representative SMA neuron peri-event time histogram (PETH) aligned on target appearance (grey line) for each of the 16 left and right target combinations during bimanual movements. Below the 4x4 grid are corresponding PETHs for the same neuron during unimanual trials in each of the four directions. (B) Same layout as (A) for the population of left SMA neurons. Each row of each panel represents a single neuron and the color is the normalized firing rate or z-score (color scale at bottom). (C-D) Δz for each of the four movement directions for unimanual (red) and bimanual (blue) trials for the left and right arms: for one SMA neuron (E), for a population of SMA neurons. From [242]. Reprinted with permission from AAAS.

$\sigma(\Delta z)$. An opposite, ipsilateral preference was observed for SMA (19.1% decrease in $|\overline{\Delta z}|$, and 11.1% decrease in $\sigma(\Delta z)$; p<0.01). For both M1 and S1, directional tuning depth during the bimanual task was approximately equal for the left and right arm (left $\sigma(\Delta z)$: 0.08; right $\sigma(\Delta z)$: 0.09; p>0.01). Notably, SMA was the only area where more neurons were tuned to both arms after a transition from unimanual to bimanual movements (p<0.01) (Fig. 30A). In addition to changes in overall modulations and directional tuning depth, bimanual control resulted in changes in neuronal preferred directions (PDs), which shifted between the unimanual and bimanual conditions by 53.1±4.0° (mean ± s.e.m.) for the contralateral arm and 66.0±5.4° for the ipsilateral arm (Fig. 30B-C). A

Table 4: Unimanual and bimanual modulation differences by area. (Left data column) Mean response amplitude $\overline{\Delta z}$ for unimanual left, right, and bimanual trials shown separately for each area, with neurons count *n* for each area indicated next to name. (Right column) Modulation depth σ(Δz) for each arm during both unimanual and bimanual movements, again separated by cortical area. The modulation depth σ(Δz) for all directions of one arm ("Left"/"Right" columns) or all bimanual directional combinations ("All" column). From [242]. Reprinted with permission from AAAS.

			$\overline{\Delta z}$		σ<Δz>		
	n		Left	Right	Left	Right	All
L M1	187	U	0.16±0.01	0.20±0.01	0.11	0.13	-
		B	0.33±0.01		0.08	0.10	0.34
R M1	46	U	0.17±0.02	0.12±0.01	0.13	0.08	-
		B	0.19±0.01		0.08	0.09	0.12
L SMA	104	U	0.12±0.004	0.09±0.003	0.11	0.09	-
		B	0.14±0.003		0.08	0.07	0.13
R SMA	17	U	0.03±0.01	0.02±0.01	0.08	0.06	-
		B	0.03±0.01		0.05	0.06	0.06
L S1	51	U	-0.03±0.007	-0.01±0.005	0.13	0.09	-
		B	-0.02±0.003		0.06	0.06	0.10
L PPC	29	U	0.08±0.01	0.14±0.01	0.12	0.08	-
		B	0.13±0.01		0.11	0.06	0.15

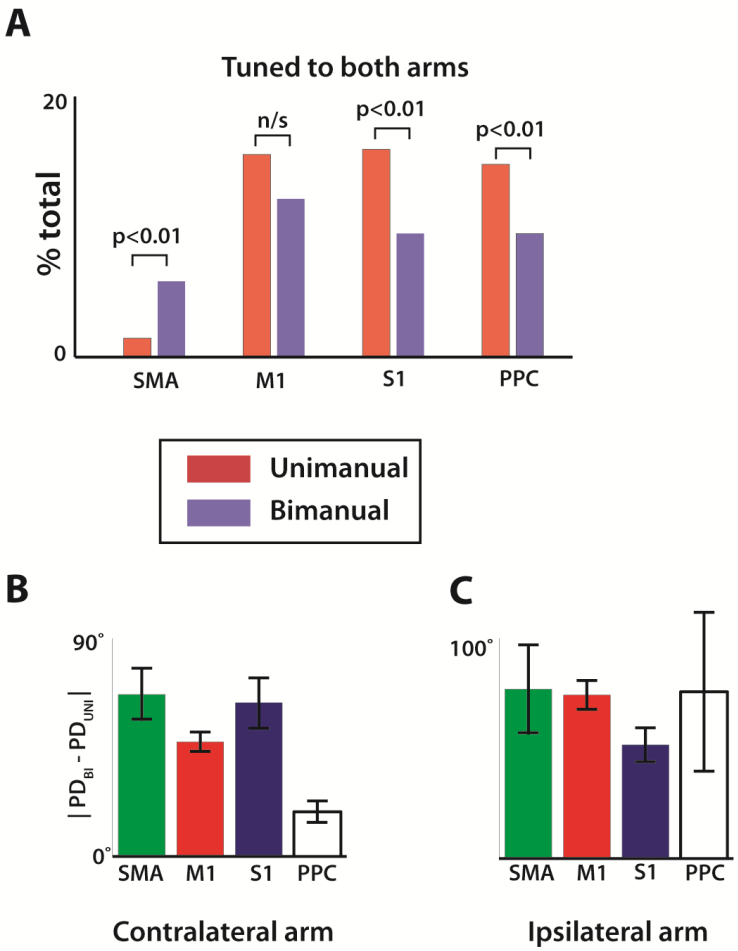

Figure 30: Directional tuning during bimanual versus unimanual movements. (A) Fraction of neurons in each cortical area which had significant tuning to both arms during unimanual (red) and bimanual (blue) trials, determined from regression. (B) The absolute value of the difference between preferred direction of the contralateral arm computed from bimanual trials and unimanual trials. Data shown separately for each cortical area. (C) Same analysis as (B) but showing the difference in preferred direction for the ipsilateral arm. All data are mean ± standard error. Analysis compiled from activity of 492 M1 neurons, 203 SMA neurons, 90 S1 neurons, and 61 PPC neurons. From [242]. Reprinted with permission from AAAS.

random shift in PD from unimanual to bimanual would indicate no relationship between the two and would give a mean PD shift, $|PD_{BI} - PD_{UNI}|$, that approaches 90°. Conversely, if the directional preference of an arm during bimanual movements could be directly obtained by knowing the unimanual PD, then $|PD_{BI} - PD_{UNI}|$ would be 0°.

The answer lies somewhere between 0° and 90°, suggesting some overlapping tuning but substantial differences that can be attributed to bimanual coordination. The PD shift also varied by area. For the contralateral arm (Fig. 30B), PPC had the least shift of 19.0°, then M1 with 48.6°, then S1 with 65.2°, and lastly SMA with 68.7°. For the ipsilateral arm (Fig. 30C), S1 had the smallest shift with 47.6° and the other three areas had mean shifts of approximately 70°.

6.3 Discussion

Even among these preliminary investigations, there were several key insights which guided the development of bimanual brain control of an avatar in VR. Early in training, it became clear that bimanual movements are an important increase in complexity from unimanual movements which must be accounted for throughout all aspects of the experiment. I observed with monkey R – a naïve monkey – that using an avatar end effector yielded increased participation earlier during the training sequence compared to a cursor end effector (Fig. 25). This result may at first seem obvious, given that the avatar display is much more realistic and this serves to engage the monkey more fully in the experiment. The logic, however, fails to account for the result that there was no significant benefit for avatar over cursor during unimanual training. Taken together, my result suggests a somewhat mixed conclusion: For simple tasks (e.g. unimanual center-out), a simple end effector is sufficient, but for more complex tasks (e.g. bimanual), a more realistic end effector system is significantly beneficial to the user. I speculate that the cause for this distinction has its roots in the spatial reference frames

used by the primate motor system. In upper limb control, arm-centric spatial reference frames play a pivotal role in goal-oriented movements [247, 248] and may provide a basis for the perception of body schema [249]. Even when movements were simply observed, sensorimotor [129] and premotor [249, 250] neurons in macaques have been shown to encode limb kinematics. Within the BMI context which this experiment is building towards, providing the subject with virtual arms, instead of cursor circles, could tap into the existing, arm-centric biological framework [247-251] and enhance the process of experience-dependent plasticity, which is believed to underlie the mechanism through which subjects learn to operate a BMI. These preliminary results in Fig. 25 suggest that this difference (cursor vs. avatar arms) is evident to macaques. Therefore it could be further exploited both in behavioral and brain-control research paradigms aimed at enhancing the user's experience as they learn to operate a BMI.

The bimanual joystick control tasks were also important results in neurobiological and BMI contexts. One of the main results – and key reason why bimanual BMI control is such a challenge – is that bimanual movements could not be described as a linear superposition of the representations of unimanual movements. Most clear in M1 and SMA brain regions (Fig. 28-29), but also evident in S1 and PPC (Fig. 30, Table 4), the activity of individual neurons and neuronal populations during bimanual tasks was not a weighted sum of unimanual patterns derived from data collected from right and left arms independently. These observations point to the existence of a separate, bimanual state of the network in which modulations represent

the movements of both arms simultaneously by way of a non-linear transformation of the separate neural tuning profiles of each arm (Fig. 28-29). At this point, I can only speculate about the function of this nonlinearity. From one moment to the next, the two arms need to be able to switch between unimanual and bimanual functionality. During unimanual control, it is important that the motor drive to the non-working arm is inhibited. Conversely, during two-arm behaviors, it becomes important that a motor program in one arm does not interfere with the other arm and does not evoke unwanted synergies in both arms, but rather permits a degree of independence. Nonlinear phenomena have been reported at the behavioral level in bimanual motor control studies which showed that motor systems can choose to favor stability (inter-limb coordination) over more unstable (inter-limb independence, linear) [252-254] motor programs in a task-dependent way. Because BMIs are driven by decoded neural activity, it becomes clear that there must be an adaptation to the decoding methods to account for this nonlinear phenomenon. A versatile BMI would ideally be capable of accurately decoding both unimanual and bimanual movements. This challenge motivated the framework for a generalized decoding model will be described more thoroughly in Chapters 9.

7. Passive observation of avatar arm movements as a tool to train a bimanual BMI for real-time decoding

Among the considerable list of challenges which stand between existing BMIs and clinically viable systems, establishing a training paradigm which removes the need for movements by the subject remains an important consideration. Early pre-clinical studies tended to ignore this challenge for a variety of reasons, including simplicity [114, 126]. Over the past ten years, however, work by several BMI groups have identified potential solutions which featured iteratively updating algorithms [116] or observation paradigms [111, 134, 242] which avoided the need for a subjects' own movements. In the most general case, a BMI paradigm will have three steps:

(1) Training: A period when the brain is expected to modulate its activity as it would during naturally enacted movements

(2) Model fitting: A neural decoding model is mathematically fit which relates the activity of individual neurons with specific motor parameters

(3) BMI execution: The neural decoder reads in the neural activity, decodes motor parameters, and uses the output signal to control an artificial device

In this chapter, I will focus on step (1). More specifically, I will utilize the recent developments in virtual reality to augment the realism of the end effector, as described in Chapter 6. Lastly, I will introduce an even more clinically relevant paradigm where the subject has no manual training on the task prior to passive observation experiments. The alternative is to use a subject who is highly trained to perform a specific movement.

Removing this prerequisite creates an opportunity for recently paralyzed patients to immediately begin training and regaining motor function with a BMI system.

7.1 Methods and experimental design

The same two rhesus monkeys from the joystick control experiments were used to evaluate the passive observation paradigm. Prior to the first experiment, monkey C completed a total of 24 months of training and experiments performing bimanual movements using both cursor and avatar end effectors. Monkey M had no prior training in bimanual joystick movements. Monkey M was highly trained to perform unimanual reaches with his left arm (Chapter 3 and 4 experiments) and had some experience with right arm movements several years earlier. Monkey M was also acclimated to the avatar end effector from previous experiments.

There were three types of passive observation experiments that both monkeys completed in the following sequence:

(1) Full passive observation – 3 sessions

(2) Passive observation + EMG – 1 session

(3) Passive observation + brain control 8-16 sessions

One slight variation was that monkey M began phase (3) immediately after phase (2), while monkey C had approximately 3.5 weeks off of experiments between (2) and (3).

During experiments, the monkeys were fully arm-restrained as described in Section 5.2.2. The eye movements were tracked and logged in real-time as described in Section 5.2.1. Neural and behavioral data collected was divided into "watching" and

"not watching" epochs based on the eye tracking data.

The experiment consisted of the monkey observing bimanual movements of rhesus monkey avatar arms (Section 5.3) from a first-person perspective. The avatar appeared on a display screen positioned approximately 40 cm in front of the monkey at eye level. The movements were automated and the monkey had no control over the virtual arms. The automated trajectories were produced using two different methods. Monkey C observed replayed arm movements from its own previous bimanual center-out joystick control session. Monkey M did not have prior joystick control sessions on this task and instead observed movements of the avatar limbs along ideal trajectories. These automated movements were enacted with a realistic distribution of reaction times and peak velocities, as well as acceleration profiles. I obtained the distribution of typical reaction times of monkey M for each arm from prior unimanual data. The automated passive observation movements were initiated after a reaction time drawn from a distribution with the same mean and variance as the monkey's own typical reaction time distribution. The same steps were taken to obtain realistic mean reach velocities from prior unimanual training. Acceleration and deceleration periods and the beginning and end of the reach were added to make the generated movement look natural and smooth. Passive observation trials followed the same task sequence as the bimanual center-out joystick control task. The monkey was rewarded when both avatar arms moved into and held their corresponding peripheral targets simultaneously. In addition to target-based rewards, a smaller juice reward quantity was dispensed at random intervals

between 2 and 8 seconds to encourage the monkey to look at the screen throughout the trial.

7.2 Results

7.2.1 Neural responses to passively observed movements

The simplest analysis regarding passively observed tuning by neurons was to look at peri-event time histograms (PETHs) aligned on target representation – the exact analysis performed for *actively* performed arm movements (Figs. 28,29). The event related "response", Δz, in this task would have a different interpretation. This is because the monkeys' own arms were not permitted to move. I observed a clear modulation of neural activity in the 200-600 ms window following target appearance in all recorded areas –M1, S1, SMA, and PPC (Fig. 31). This epoch of elevated neural activity is similar to the peri-movement activity observed in actively performed joystick movements (Fig. 28-29). Notably, this similarity was not immediately apparent. From the day 1 to day 3 of passive observation experiments, $\overline{\Delta z}$ in all four areas steadily increased (Fig. 31, 1-way ANOVA, $p<0.05$). This is likewise visualized in terms of the distribution of single neuron $\overline{\Delta z}$ for each of the first three days (Fig. 31C). On day 1, there is a cluster of single neuron $\overline{\Delta z}$ near 0, denoting that many neurons had essentially zero response to the target stimulus. On day 2 and 3, there is a clear rightward shift in the distribution of single neuron $\overline{\Delta z}$. Superimposed on the figure is the single neuron $\overline{\Delta z}$ for a typical joystick session. Similar to active movements, the recorded population

also responded more robustly in certain directions than others (Fig. 31A row 1 compared with row 2). I observed a very similar trend in the increase in $\overline{\Delta z}$ for both M1 and S1 in monkey M as well (Fig. 31B, lower).

A related question that stems from this finding is the following: how will this observation-based neural response persist across time? Put another way – can we identify and quantify neural plasticity as the brain develops an increased sense of control over the virtual arms? To address this, I analyzed data from a passive observation session exactly 30 days after the initial exposure to this paradigm. As noted earlier (Section 7.1), monkey C had no experiments during this day 3-30 window while monkey M had daily 1 hour brain control experiments during this window.

These follow-up experiments demonstrated that the neural modulations related to passively observed movements do persist for at least several weeks. For monkey C, the $\overline{\Delta z}$ distributions for M1, S1, and SMA were all significantly nonzero (2 sided t-test, $p<0.01$) while PPC $\overline{\Delta z}$ returned to zero in this span of time ($p>0.01$). The $\overline{\Delta z}$ magnitude was reduced relative to the day 3 magnitude, but remained very robust despite the over three week gap in experiments. For monkey M, the day 30 $\overline{\Delta z}$ measurements were even stronger than day 3 in both M1 and S1, suggesting that the neural representation continues to develop with daily experiments. These results provide a first demonstration of neural plasticity and the developing sense of agency of the virtual avatar arms. More specifically, the passively observed avatar movements viewed from a first-person perspective can evoke a long-lasting neural modulation in motor and

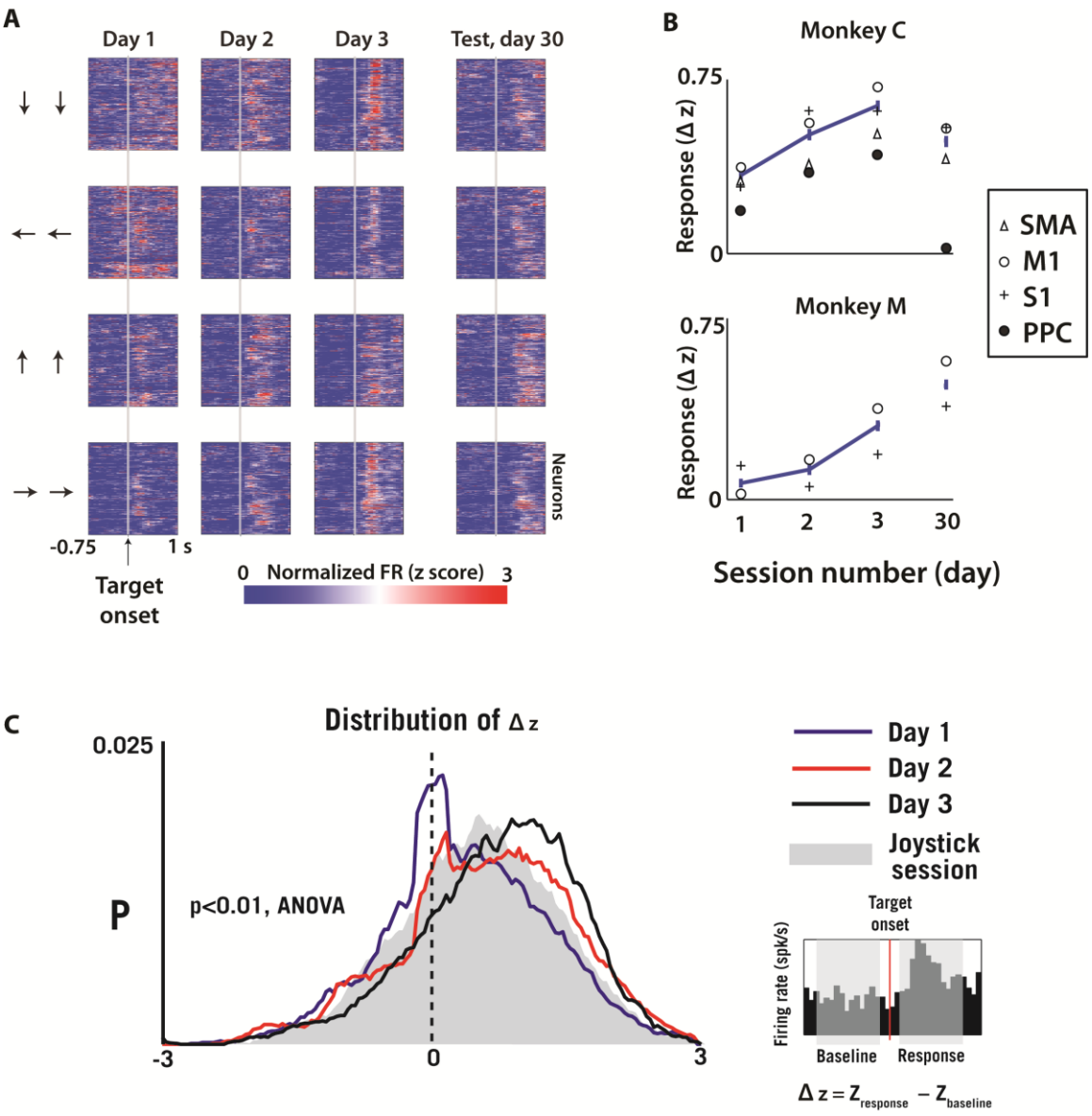

Figure 31: Plasticity during passive observation training. (A) PETHs during passive observations session with monkey C for the four parallel reach directions (rows) across days 1-3 and 30 relative to initial session. Within each of the 16 panels, rows are neurons, column are different times, and pixel color indicates normalized firing rate for each neuron. (B) Mean neural response (Δz relative to baseline) ± standard error (blue lines) on days 1-3 and 30 for both monkey C (top) and M (bottom). Shown separately are the means of each cortical area. (C) Distribution of monkey C $\overline{\Delta z}$ on each of the first 3 days of passive observation. Grey distribution was derived from joystick session. Inset: PETH showing "response" and "baseline" windows, and the computation for Δz. The $\overline{\Delta z}$ shift was significant, p<0.01 1-way ANOVA. From [242]. Reprinted with permission from AAAS.

sensory-related cortices.

7.2.2 Decoding passively observed movements

The next step was to more definitively show the neural representation of passively observed arm movements by employing the same neural decoding algorithms used for real-time brain control predictions. This is the logical progression from simply looking at the amplitude of stimulus-aligned neural activity. Neural activity that encodes motor parameters now takes on a *functional* role, rather than just responsive. To test the ability of populations of neurons to predict passively observed reaching movements, I performed an analysis offline which divided the experimental data into two segments: training (80%) and test (20%) data. I used a 5^{th} order unscented Kalman filter [150] to fit model parameters based on the training data and make predictions on the test data. The accuracy of the predictions was compared with the actual reach trajectories and quantified in terms of correlation coefficient, *r*.

Even within early passive observation sessions, there was clear motor encoding among the recorded neural populations. An example of the UKF predictions is shown in Fig. 32A. The predicted traces matched the actual traces for both left and right avatar arms (monkey C: r=0.46±0.05 for the left avatar arm versus r=0.12± 0.05 for the right; monkey M: r=0.47±0.03 versus r=0.23±0.02). These predictions did remain below that of joystick control predictions in Monkey C (Fig. 32B). Nevertheless, this result demonstrates a neural representation of bimanual arm movements during passively observed movements.

Next, several control experiments were conducted during passive observation (monkey C and M) and joystick control experiments (monkey C) to study the muscle activation patterns during active and passive tasks. I attached EMG electrodes to the monkey's left and right biceps, triceps, wrist flexor, and wrist extensor muscles for a total of eight EMG channels. During passive observation for both monkeys, the recorded EMG activity was very small and not directionally specific (Fig. 33A-B). The

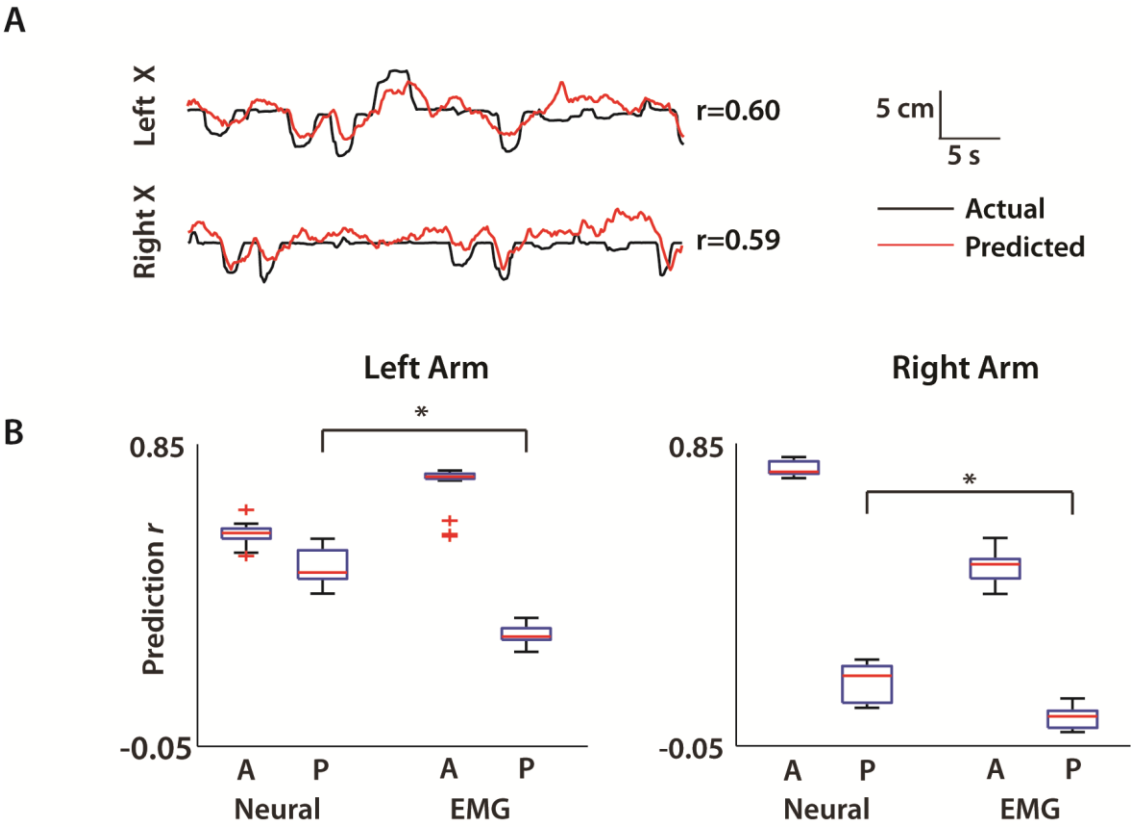

Figure 32: Decoded movements during passive observation paradigm (A) Actual (black) compared with predicted (red) trajectory for right and left arm X positions during a representative 25 s window. (B) Box plots showing distribution of prediction r for a typical active (A) joystick experiment or passive (P) observation experiments. Shown separately in each panel: Prediction r using neural activity ("Neural" columns) or using EMG activity ("EMG" columns). Two panels indicate prediction of left arm (left panel) and right arm (right panel). * indicates p<0.01 significance, t-test. From [242]. Reprinted with permission from AAAS.

small recorded EMG signals across the eight channels likely reflected adjustments in body position by the monkey for comfort or postural shifts. As a reference, I collected EMG signals from monkey C during bimanual joystick trials to show the movement-

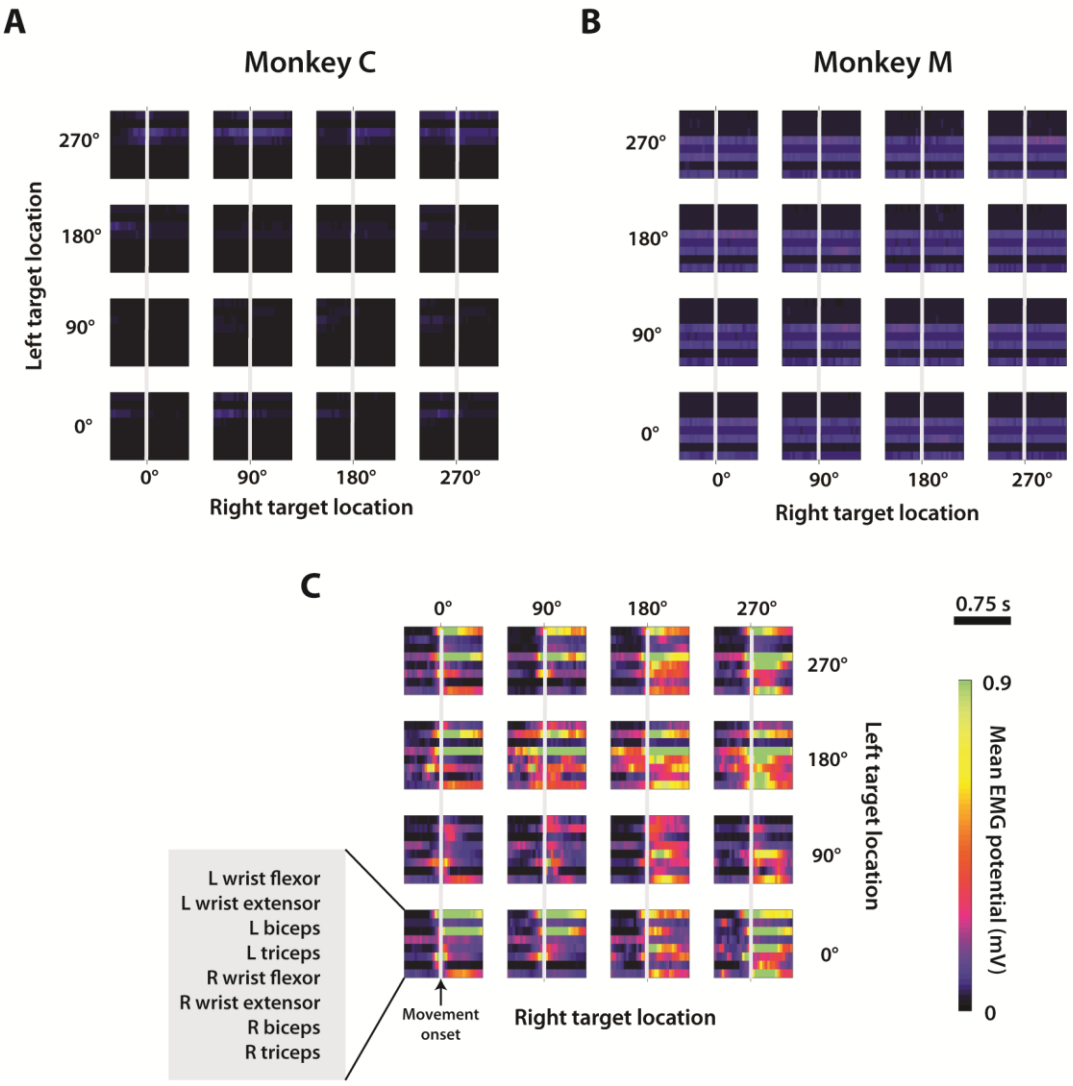

Figure 33: Arm EMGs during passive and active trials. (A) 4x4 plot of EMG signals vs. time for each of the 16 possible left/right target combinations during passive observation for monkey C. Within each panel, the 8 rows indicate 8 different muscles. Data is aligned on movement onset (white vertical band). Pixel color indicates amplitude of EMG signal in mV. (B) same as (A) but for monkey M. (C) Same layout as (A) but from active bimanual session where joysticks were used by both right and left arms. Color scale below (B). From [242]. Reprinted with permission from AAAS.

aligned EMG burst across all either 8 channels (Fig. 32C). Comparing the active with passive, there is a very clear difference. During passive experiments, the motor trajectory is encoded by neurons in the brain (Fig. 32), but this motor plan does not reach the relevant muscles in its body. Using the residual EMG signal during passive observation to predict arm trajectories yielded significantly lower prediction accuracy than by using neural activity (Fig. 32B, $p<0.01$, *t*-test) for both left and right arms. This further supports my earlier finding that neurons across M1, S1, SMA, and PPC encode movements of observed virtual arms and additionally demonstrates that this encoding can persist without movement-specific muscular activation

With the results from Fig. 32 showing neural representation of the movements of both arms during a bimanual reaching task, it would be reasonable to ask how exactly this is accomplished. The two options would be (1) simultaneous or (2) sequential

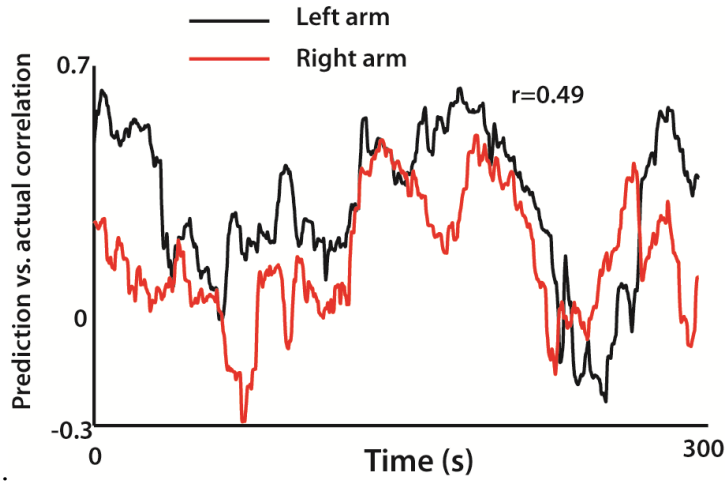

Figure 34: Temporal changes in prediction accuracy during passive observation. Prediction *r* for left (black) and right (red) arm x-position was computed using a sliding 30 second window. From [242]. Reprinted with permission from AAAS.

encoding of the two arms. Lacking a sophisticated gaze tracking system which can pinpoint the focus of the monkey's eye on the screen, I used a proxy for this measurement. To do so, I generated offline UKF predictions using a sliding window such that for a given moment in time, I could show how well each of the two arms was being represented by the neuronal ensemble. If each arm was predicted at the same moment, then there was a "bimanual encoding". If the monkey encoded primarily one, and secondarily the other, then this would become clear as well. Prior to this analysis, it was known that by computing kinematics predictions over an entire experiment (30-50 minutes), both arms were significantly represented by the brain (Fig. 32, $p<0.01$, t-test). It becomes clear from Fig. 34 that the encoding varies greatly in time and that quantifying prediction accuracy with a single number (Fig. 32) may not give the full picture. The single arm predictions fluctuated in time with *r* *r*anging from -0.29 to 0.64 (Fig. 34). The running accuracies for the two arms were weakly positively correlated between themselves (correlation coefficient of 0.25±0.12 for monkey C and 0.31±0.14 in monkey M, across all sessions; mean ± s.e.m.), likely reflecting drifts in overall attention to both arms. One could speculate in addition that attention was occasionally unevenly divided between the two avatar arms (e.g. negative correlation of running accuracies during the interval 155-200 s in Fig. 34), but this issue would need to be resolved using more precise eye tracking methods.

To obtain further evidence that cortical modulations during passive observation sessions reflected the goal of the bimanual task, I evaluated how cortical ensembles

represented the location of targets on each trial. Rather than decoding the moment to moment kinematics, this approach decodes the end goal of the movement from neural ensembles. I used a k-nearest neighbor (k-NN) classifier to extract target locations from cortical modulations (Fig. 35). k-NN is a non-parametric classification algorithm which searches nearest-neighbor data (from training data) within the feature space – in the case of neural predictions, this would be a space defined by binned firing rates of all the neurons. By searching for the *k*-nearest neighbors to the test data, the algorithm can be made more robust. The classifications of each "neighbor" are counted as votes towards the prediction of the unknown sample class. Neural activity was binned into a single 250 ms window during a specified epoch aligned on target onset. I then slid this window at 25 ms increments along the task interval from -0.5 to 0.75s and at each step, the k-NN model was fit with 75% of the session's trials and target location predictions were made on the remaining 25% of trials. Train and sample trials were randomly selected five-times and the resulting prediction performance in terms of fraction correct prediction was averaged.

To quantify cortical representation of each target – which potentially could be different for neurons from different hemispheres and/or areas – I used two classifiers, one for each target. Both target locations were clearly reflected by cortical ensembles, starting with the appearance of the targets and continuing throughout the trial (Fig. 35). The accuracy of each representation was measured as fraction correct. For consistency, data from day 3 (Fig. 32) of passive observation was used for both monkeys. Using k-

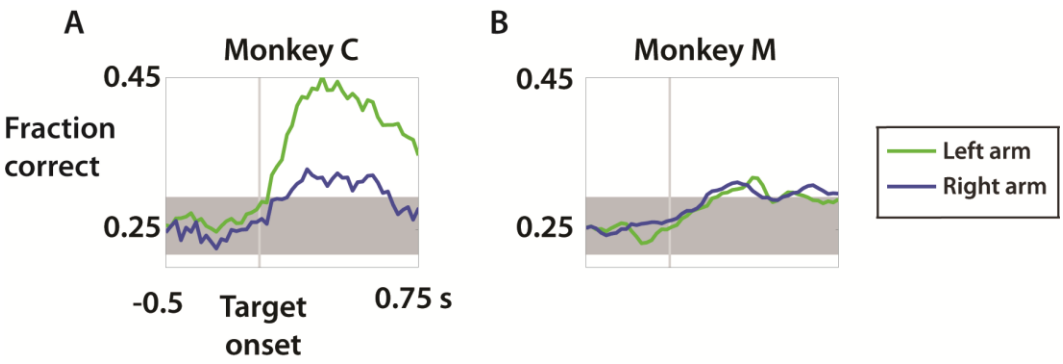

Figure 35: Timeline of neural representation of target locations for two monkeys. A 250 ms window of neural activity was moved at 25 ms steps across the task interval (X-axis) aligned on target onset (grey vertical bar). Y-axis values represent fraction correct prediction by the k-NN classifier for left (green) and right (blue) arms separately. Dark grey horizontal bar represents 95% CI of chance level classifier performance constructed using 1-proportion z-test with p_0 = 0.25. From [242]. Reprinted with permission from AAAS.

NN, the target location of the left arm (green line) was decoded more effectively than the right arm in monkey C which was consistent with the results from UKF decoding (Fig. 32B and 34). Despite this difference, both right and left target locations could be decoded from both monkeys at significant levels within the same epoch following target appearance. For monkey M, the neural representation of the two targets during was more subtle than for monkey C, however the classifier performance was above chance ($p<0.05$; 1-proportion z-test) in the same window as for monkey C. Even this small representation in monkey M was an important result. With no prior exposure to this task, a significant neural representation could be formed among M1 and S1 neurons, even on day 3 of training (Fig. 35). Neural representation of observed movements continued to develop for monkey M to the point that the encoding became even stronger in monkey M (Fig. 36B) than monkey C (Fig. 36A).

Continuing with this theme, it was important to look at how the neural

representation of the passively observed avatar arm movements changed over time. If this neural representation subsided after continued exposure, the VR paradigm would most likely have limited utility for BMI applications. To test this, I included both passive observation *only* experiments and passive observation + brain control experiments. For each day, I designated a 5 minute block of passive observation to be used for training the UKF model and the rest of the passive observation trials for test data. This allowed for head-to-head comparisons between the two types of experiments. I found that in both monkey C and monkey M, the neural representation persisted across several weeks of experiments (Fig. 36), although they followed different learning trajectories. For monkey C (Fig. 36A), the representation grew quickly and stabilized after around eight 60-minute sessions (spanning approximately 4 weeks). For monkey M

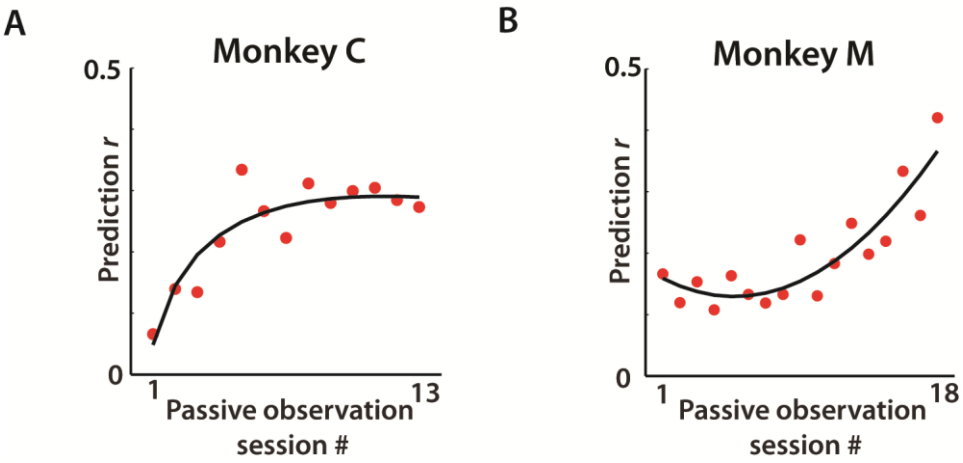

Figure 36: Cortical plasticity during passive observation experiments. For each session (red dot), the UKF prediction performance *r* was computed using training (5 minutes) and test data from passive observation trials. Data fit with logarithmic (A) or exponential (B) curves. From [242]. Reprinted with permission from AAAS.

(Fig. 36B), a small representation was present initially but developed more slowly. The most pronounced improvement to the neural representation in monkey M coincided with the late experiments during brain control learning (sessions 13-18 in Fig. 36B). Thus, the neural modulations during passive observation (Figs. 32-36) emerged with learning and persisted with continued experience.

7.3 Discussion

In these results, I have begun to demonstrate that employing a realistic avatar end effector, even when only observed passively, can evoke widespread neuronal plasticity and persistent neural responses not unlike that of naturally enacted movements. This is an important transition step between looking at purely the behavioral effect (Fig. 25) and fully implementing a passive observation paradigm into a BMI system. The trend towards BMIs which can be trained passively is apparent throughout the field. Several BMI groups have utilized movement-free paradigms as the tool to train the decoding model parameters, whether by asking subjects to imagine movements [134], observing cursor movements [135, 136] or observing robotic arm movements [111]. The latter [111] required a tetraplegic patient to imagine movements while observing pre-programmed trajectories. Over time, the computer assist was decreased giving way to cortical control. Notably, these studies were conducted in humans and methods such as "requesting the subject to imagine movements" were used.

Much BMI research is carried out in healthy nonhuman primates [116, 126, 195],

however, and such a request cannot be explicitly made. As a result, studies either train the decoding model on joystick movement data [126] or utilized algorithmic updates to refine the model as the monkey learns [116]. These pre-clinical studies can still provide valuable insights beyond simply BMI performance. For example, learning about the underlying principles (e.g. large-scale cortical plasticity) of passive observation training, as done in this study, is more easily accomplished in macaque models. Another byproduct of using nonhuman primate models was that the observation paradigm needed to be very realistic and intuitive in order to evoke an imagery response, because this could not be directly instructed to the animal.

Neural tuning to observed action has been reported previously, however there remains two distinct interpretations: (1) the brain generates congruent motor commands while observing the action [168, 255], or (2) the action is represented by mirror neurons [256-258]. Regarding the first interpretation, the strongest evidence comes from M1, an area that is not typically associated with mirror neuron phenomena [256, 257], c.f. [259]. In a study by the Hatsopoulos group, the neural modulations and preferred directions were congruent between observation and movement conditions in a unimanual task [255]. Existence of such neurons in M1 suggest that a movement is being covertly generated - but somehow inhibited downstream- during this congruence [260].

Mirror neurons are reported to exhibit congruence as well, but this congruence is most commonly associated with imitation [256, 258, 261]. Returning to the results from the present study, it remains unresolved what portion of the motor tuning is due to

imitation and what is due to a sense of agency of the virtual arms. That is, do the neurons develop stimulus-aligned activity (Fig. 31) and directional tuning (Figs. 31, 32, 35) as a byproduct of imitation learning? Learning in mirror neuron areas such as ventral premotor cortex has been proposed [168, 256, 258, 261] to play a key role in social learning and empathy. The interesting – and speculative – alternative would be that the motor modulations are not that of imitation or rehearsal but action [168]. This study also provides a new result showing that neural modulations exist during passive observation even when the action was unfamiliar (monkey M results). This remains an open question in motor neuroprosthetics and one which may impact training and end effector designs in coming years.

A second takeaway from these results was the stability of the neural representation across many sessions. It was not immediately known whether the neural representation of observed virtual arms would persist with time. One possibility was that the monkey would at some point realize the arms were externally controlled and begin to ignore their movements altogether. One way to mitigate the likelihood of this occurring was by interspersing the 7 minute passive observation epochs between 1 hour brain control experiments. That is, the subject was not explicitly made aware of which mode the experiment was in. This is most similar to the Tkach design [255] where the visual feedback was similar for both the enacted and automated trials. Without other long-term studies specifically quantifying the passive neural representation strength over time, the best comparisons are BMI studies featuring passive observation as tool for

training the BMI. In studies by Hochberg et al. [111], Ifft et al [242], and Wahnoun et al [135], a variation of the passive observation paradigm was able to effectively train the BMI decoder for up to 4, 5, and 6 weeks respectively. Most vividly, in the present study, I observed some of the most drastic improvement in the neural representation in monkey M (Fig. 36B) in parallel with the strongest improvements in BMI control (see next chapter). The two modes are certainly related and could be useful to:

(1) evoke an enhanced sense of agency during passive observation

which leads to

(2) improved fit of neural modulations to motor parameters

which leads to

(3) improved neural control of end effector

which leads to improvements in (1).

In summary, passive end effector observation was shown to have a clear neurophysiological manifestation which was stable over the course of several weeks. I speculate that this emerging neural representation is evidence that the monkeys are developing a sense of agency with the two virtual arms. It remains a possibility that supplementing passive experiments with active or neurally-controlled experiments could stabilize this representation over time.

8. A brain-machine interface for bimanual movements

The goal for which BMI technology has been developed should remain at the forefront of all design considerations. The motor goal of BMIs is full body mobility such that even a person suffering severe paralysis could walk, interact with the environment, and sustain a high quality of life. A survey of quadriplegic patients rated arm and hand function as the most desired mobility function [262]. Most early BMI studies have thus focused on reaching movements of a single cursor [94, 95, 150, 195], robot arm [111, 126, 134], or virtual arm [129]. Such research has been a valuable starting point, but much of the richness of primate movement complexity and coordination is a result of multi-limb control. Daily activities as simple as tying one's shoes, buttoning a shirt, or opening a jar require the spatiotemporal coordination of two limbs. Fortunately, the brain is skilled at these computations and even complex movements can be performed seamlessly.

The challenges of a bimanual BMI were anticipated and drove many of the advances described in Chapters 6-7. For example, unlike unimanual movements, bilateral movements require spatial and temporal coordination between limbs. This contributed to my hypothesis that larger samples of neurons must be simultaneously recorded from multiple, bilateral cortical areas in order to achieve similar levels of neuronal decoding accuracy as unimanual. A second hypothesis was that cortical plasticity, particularly in terms of cross-hemispheric synchronization, would be increased during bimanual BMI learning. Lastly, I sought to test my prediction that conjoint multi-limb models would outperform independent single-limb models due to

the nonlinearities of bimanual tuning evident both in my preliminary studies (Fig. 28-30, Table 1) and in studies by other groups [76, 80, 263].

The specific goal for this phase of experiments was to create a BMI that could simultaneously and accurately control two arms in a reaching task. As the control was improved over time, I continued to investigate several related questions about the underlying neural plasticity and muscle activation during brain control experiments.

8.1 Methods and experimental design

The bimanual BMI experiment was adapted from the similar joystick control and passive observation paradigms described in Sections 6.1 and 7.1. Two rhesus monkeys were implanted with multielectrode arrays prior to all experiments. Monkey C was implanted with 768 electrodes in bilateral M1, S1, SMA, PMd, and PPC as described in Section 5.1 and monkey M was implanted with 384 electrodes in bilateral M1 and S1 as described in Section 3.1. Neural signals were sorted using template matching algorithms within commercially available software (Plexon Inc., Dallas, TX). In monkey C, I simultaneously sampled (Fig. 27B) from SMA (73-110 units in the left hemisphere, 0-20 units in the right hemisphere; ranges for all experiments), M1 (176-218 LH, 45-62 RH), primary somatosensory cortex (S1) (9-64 LH, 0-34 RH), and posterior parietal cortex (PPC) (0-4 LH, 22-47 RH). In monkey M, I sampled from M1 (80-90 LH, 195-204 RH) and S1 (47-56 LH, 127-149 RH). The daily unit count neared 500 for each monkey, which constituted the highest number of simultaneously recorded units in non-human primates at the time of publication [264]. The high unit count for monkey M has

persisted for 54 months after the implantation surgery, and for monkey C has persisted for at least 25 months after the surgery (recordings are still continuing in both animals).

Both monkeys learned to operate a bimanual BMI without movement of their own arms ("BC without arms"), but through two different sequences. Monkey C began with approximately two years of joystick control training on a center-out task with one, and later with two, arms (Section 6.1.1). Following joystick control experiments, monkey C began brain control with arm movements ("BC with arms"). During BC with arms, experiments began with 5-7 minutes of bimanual center-out joystick control. This block of data was used to train the unscented Kalman filter (UKF) neural decoder (Section 2.2.3)[150]. After this, a UKF decoder with four output dimensions (X and Y position for both arms) controlled the position of the two avatar arms on the screen in real-time. The monkey's own arms were free to continue to move and manipulate the two joysticks, although the joysticks no longer had any control. Monkey C completed 24 sessions of BC with arms, concluding when I observed a consistent level of performance reaching greater than 75% correct trials. Next, four passive observation experiments were conducted in both monkey C and monkey M (Section 7.1). Monkey M had no previous experience with the bimanual task whatsoever. These passive observation sessions were important because they became the paradigm for training the UKF decoder at the beginning of all subsequent BC without arms experiments.

Both monkeys next began BC without arms. In a typical session, the fully arm-restrained monkey (Fig. 22) observed 5-7 minutes of automated bimanual center-out

movements towards circular targets. After this, the UKF model was fit and the mode of control was switched from the automated program to brain controlled movements. At no point were joysticks utilized in the BC without arms paradigm. This was important because the BMI control required no movements of one's own arms, not to train the model or during real-time control, thus making it the most viable solution for clinical implementations. The real-time brain control phase of BC without arms would continue for 30-40 minutes in each of the daily experiment sessions.

8.2 Results

8.2.1. Offline decoding of unimanual and bimanual movements

Before a real-time BMI to control two arms was tested, some offline analyses were performed to better understand the problem. From monkey C, there were many bimanual joystick control sessions which were a useful testbed for neural decoding analyses such as neuron dropping curves and optimization of decoder parameters (Chapter 9). The complexity of neuronal representations of bimanual movements became apparent from the neuron dropping curves (Fig. 37) [126, 195]. Neuronal dropping curves describe the deterioration of decoding accuracy as neurons are removed (dropped) from the population used for decoding. They are a useful analytical method for showing the effect of neural ensemble size on the ability to decode motor parameters, measured as correlation coefficient *r*. In the present study, this method clearly indicated that more neurons were needed to achieve the same decoding accuracy for each arm during the bimanual task than during the unimanual task (compare Fig.

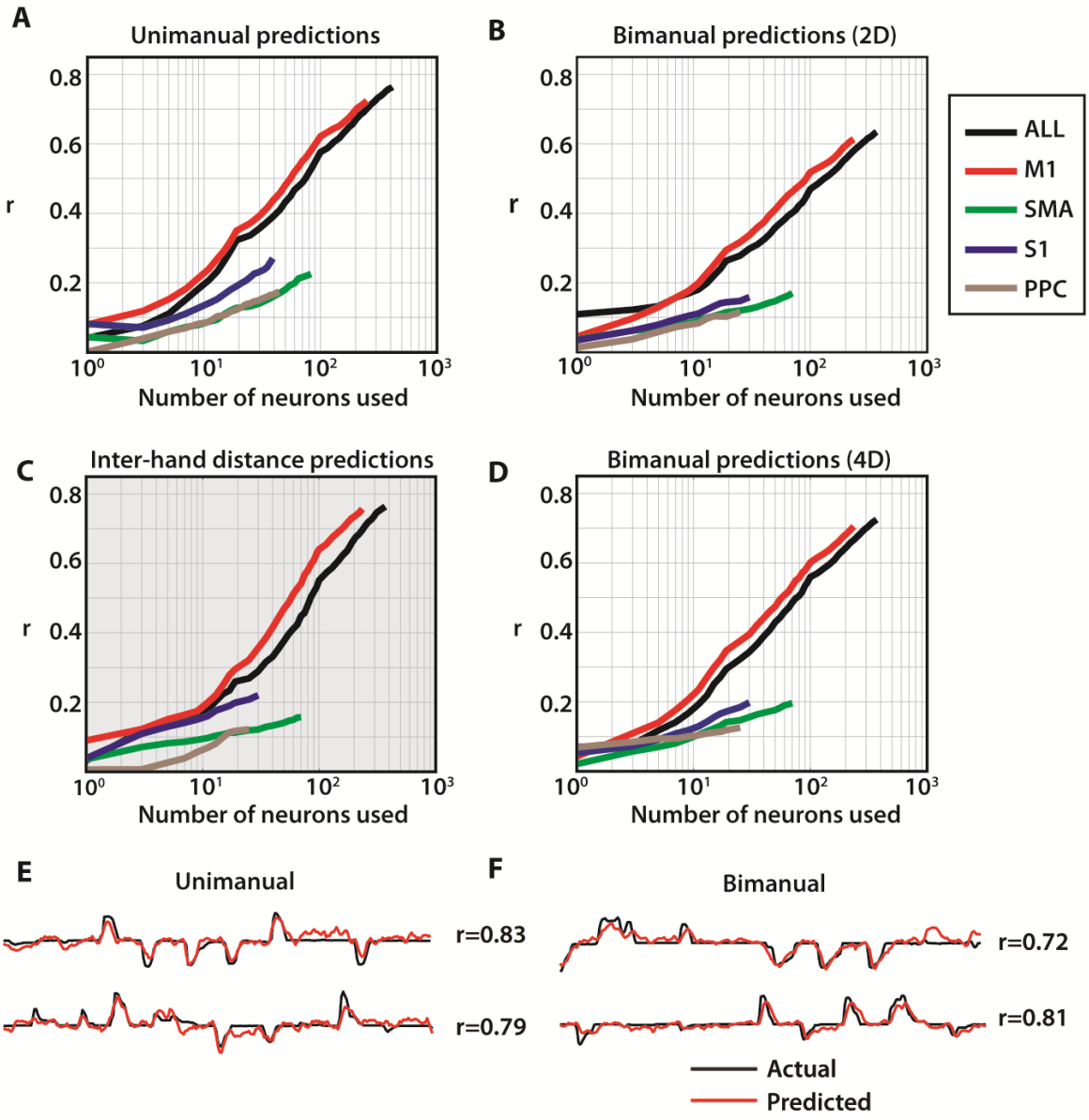

Figure 37: Neuron dropping curves for joystick control (A) Neuron dropping curves for unimanual joystick control,(B) bimanual joystick control using two 2D decoding models (C), inter-hand spacing, and (D), and bimanual joystick control using one 4D decoding model. Curves are shown separately for each area, indicated by color. (E-F) Offline predictions using 2D UKF for unimanual movements (E) and 4D UKF for bimanual movements (F). From [242]. Reprinted with permission from AAAS.

37A with Fig. 37B). For example, to achieve decoding accuracy of r = 0.5 with the 2D UKF, a mean of 80 neurons (drawn from the full population) were needed for

unimanual joystick control and 145 neurons from bimanual hand control, despite using the same 2D UKF for each hand. A 2D UKF model simply means that the X and Y position of each hand was predicted completely independently of the other arm. Alternatively, a 4D UKF conjointly models the two arms in a single model and makes no claim about independence. More information about parameters and modifications to the UKF will be discussed further in Chapter 9. The cleanest comparison between unimanual and bimanual complexity, however, is by using the same 2D model for each.

The decoding accuracy, quantified as *r*, was proportional to the logarithm of neuron count in each case (Fig. 37A-D). Additionally, bimanual movements required a longer time to train the UKF than unimanual movements (Fig. 38A). Furthermore, individual neurons more strongly contributed to the decoding of one of the arms when movements were unimanual, but more homogeneously represented each arm during bimanual movements (Fig. 38B,C). Both distributions were leftward shifted from the null distribution (Fig. 38D) collected from the same recording session but during periods without task execution ($p<0.05$ both right and left arms, Wilcoxon signed rank test). Greater bimanual prediction accuracy was obtained when the 2D UKF was trained on bimanual movements compared to the same model trained on unimanual movements of each arm separately (Fig. 38E, $p<0.01$). Similarly, training the UKF on bimanual movements yielded more accurate predictions for bimanual than for unimanual movements (Fig. 38F, $p<0.01$).

During bimanual joystick control, the position of the right and left arms was

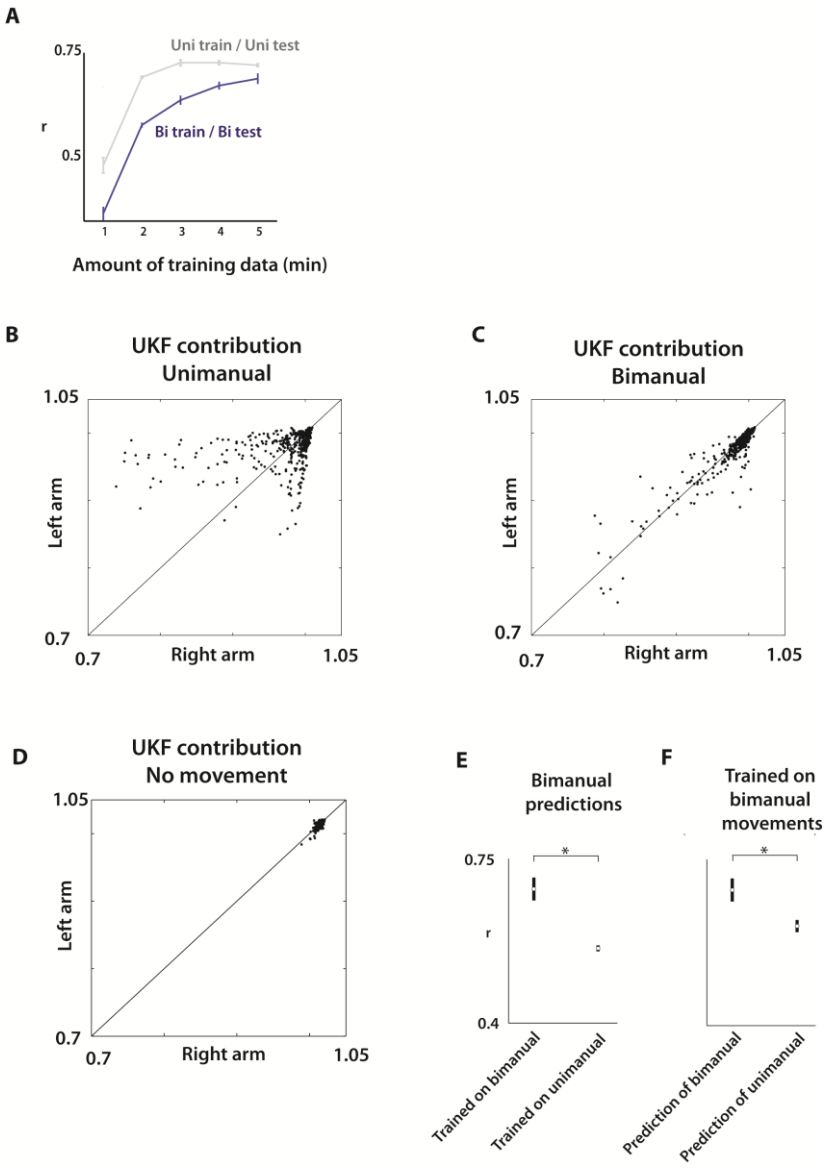

Figure 38: Decoding performance during joystick control. (A) Prediction r as a function of amount of training data for both unimanual (grey line) and bimanual movements (blue line). The decoding model for unimanual predictions was fit during unimanual trials and the model for bimanual predictions during bimanual trials. (B-D) Unscented Kalman filter noise variance terms fit on movements of left and right arms during unimanual (B), bimanual (C), and unattempted (D) trials of the same session. Values further below 1 indicate a stronger neural tuning to the predicted arm. Solid line drawn along y=x line, where both arms are represented equally. (E) Prediction of bimanual movements with training data drawn from bimanual or unimanual trials. (F) Prediction of bimanual or unimanual movements with a model trained on only bimanual trials. Data shown: mean±S.E.M. From [242]. Reprinted with permission from AAAS.

decoded from multi-area ensemble activity with high accuracy (r=0.85±0.02 and r=0.62±0.03, Fig. 37F, 38E-F). Looking at cortical areas separately, the best decoding was achieved with M1 neurons (n = 245; r = 0.73±0.03, average of two arm r values). A less numerous population of SMA neurons performed worse (n = 73; r = 0.22±0.02), but the contribution from SMA and other areas to the overall predictions was still evident from the rise of the entire ensemble dropping curve beyond the maximum M1 performance,as well as the steady rise of the individual area dropping curves (Fig. 37A,B,D). Moreover, when UKF predictions were run for individual neurons and all neurons were ranked by the accuracy of these predictions, many non-M1 neurons received high rankings. For example, of the 50 top ranked neurons, 27 (54%) were from M1, 16 (32%) from SMA, 4 (8%) from PPC, and 3 (6%) from S1. Therefore, even though M1 neurons contributed the greatest amount to kinematic predictions, non-M1 areas such as SMA, PPC, and S1 provided informative signals, as well. In addition to predictions of the coordinates of two hands, the distance between hands was represented with similar accuracy (Fig. 37C) when derived from the predictions of two hand positions made with the 4D UKF model.

In summary, analysis of bimanual joystick control data demonstrated some of the key challenges of bimanual movement decoding. First, the size of the recorded neuronal ensemble has a clear effect on decoding accuracy. Even with ensembles approaching 500 neurons, it was always advantageous to add more neurons. Interestingly, this was true both for M1 and non-M1 areas like S1, SMA, and PPC. Secondly, it was clear that the bimanual neural representation required more neurons to

reach the same level of decoding accuracy. This is not completely surprising, but it reinforces one of the biggest challenges that precludes BMIs for complex multi-joint movements – simply not having a large enough neuronal ensemble. Lastly, the unimanual and bimanual movement states appear to be represented differently by cortical populations, where the former evokes stronger encoding of one limb than the other and the latter is related to a more balanced representation of the those arms together. Together, these factors motivate the design and implementation of the real-time BMI for bimanual movements.

8.2.2 Real-time brain control of bimanual movements

The 4D UKF (Fig. 37) was chosen for real-time BMI experiments due to its ability to accurately decode bimanual kinematics in offline analyses (Figs. 32, 36-38). In addition, the 4D UKF had advantages over using two 2D models which will be discussed further in Chapter 9. Despite the strong decoder efficacy, switching from hand control (Fig. 26) to BC with arms resulted in a sharp drop in monkey C's performance level during initial sessions (Fig. 39A). However, over the next 24 sessions of BC with arms, monkey C's proficiency improved substantially in both bimanual task performance (i.e. percent of trials where both arms reached their targets within the maximal allowed trial duration; Fig. 39A) and individual arm performance (i.e. percent of trials where a single arm reached its correct target within the same duration; Fig. 39B). Additional improvement in performance was achieved after the decoder was upgraded from a 1st order UKF to a 5th order UKF (Figs. 39B). Changing from a 1st to 5th order

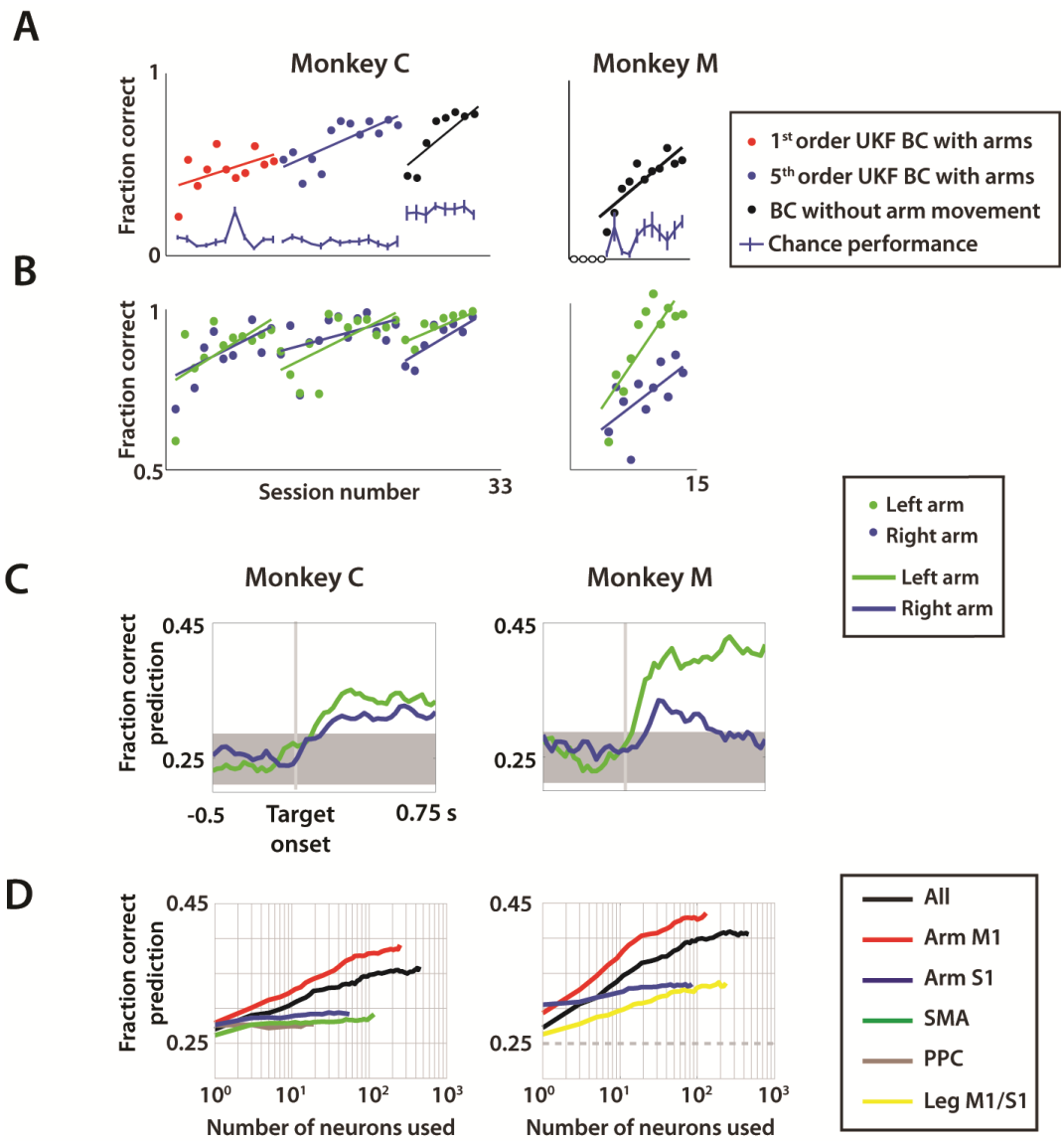

Figure 39: Brain control without arms. (A) Performance of monkey C (left) and monkey M (right) quantified as fraction correct trials during bimanual brain control experiments. Shown separately for monkey C are different decoding model parameter settings (red, blue markers) as well as BC without arms sessions (black, both monkeys). Sessions with less than 10 attempted trials were set to zero due to insufficient data (open circles). (B) Fraction of trials where the left arm (green circles) and right arm (blue circles) acquired their respective target during brain control. Linear fit for learning trends of each paradigm is shown in (A-B). (C) Fraction of correct predictions by k-NN of target location for each arm (blue/green) over the trial period during BC without arms in both monkey C (left column) and monkey M (right column). (D) Mean k-NN target prediction fraction correct from neuron dropping curves separated by cortical area for each monkey (same columns as E-F). UKF, unscented Kalman filter. From [242]. Reprinted with permission from AAAS.

provided a more detailed history of prior neuronal activity to be incorporated into the decoder. By the end of BC with arms training, a consistent level of performance exceeding 70% correct trials was achieved (Fig. 39A), including over 90% correct trials for each arm individually (Fig. 39B).

The next phase of experiments was BC without arms experiments, which were conducted in both monkeys. They were designed to match the practical needs of paralyzed patients who have to learn BMI control without being able to produce overt upper limb movements. Previously, to reach the same goal, single-effector BMI studies have employed a co-adaptive decoding model with iteratively updated tuning properties [116], and requested subjects to imagine movements [111, 134] or had them passively observe effector movements [135, 136]. In this study, a passive observation paradigm became the basis for how the BMI decoder was trained without requiring the monkeys to produce overt arm movements. For these experiments, the monkeys passively observed the movements of the avatar while its arms were gently restrained (Fig. 22).

After the UKF was trained on 5-7 minutes of passive observation, the mode of operation was switched to BC without arms for the remaining 25-45 min of the experiment. The monkeys controlled the avatar arms with modulations in their cortical activity while still fully arm-restrained. More specifically, the spiking activity from the neural ensemble was decoded by the UKF in real-time. The four outputs of the UKF were exactly the motor parameters used to move the avatar arms: X and Y position of

the each hand in 2D Cartesian space. Both monkeys rapidly improved the performance for each arm in the bimanual BC without arms task within 5-10 sessions (monkey C rising from 43% to 79%; monkey M from 15% to 62%; Fig. 39A, black circles). Similar to the passive observation pattern (Figs. 32B, 35), the performance accuracy for the left and right arms was unequal during the BC without arms task (monkey C: left 98.5%, right 94.4%; monkey M: left 96.4%, right 77.7%; average over last three BC without arms sessions). The first four BC without arms sessions for monkey M (open circles, Fig. 39A) contained fewer than 10 trials which met the minimum attention threshold and were counted as zero accuracy. To compute a chance performance level for each mode of control, I performed a shuffled-target analysis (Fig. 39A). Cursor trajectories of each trial were replayed with peripheral target locations drawn from a randomly shuffled set of target combinations. Correct performance was defined the same way as in online sessions, where both center and peripheral targets must be acquired within the 10 s timeout limit. Chance level performance derived from the shuffle test was very low for BC with arms data (less than 10% correct trials, Fig. 39A) and slightly higher but still far below monkey performance for BC without arms data (20-30% for monkey C, 10-20% for monkey M, Fig. 39A). For 20 out of the 21 BC without arms sessions, monkey performance was statistically greater than chance performance ($p<0.05$, *t*-test), the lone exception being the second session for monkey M.

Similar to the analyses on passive observation, I chose to perform a secondary analysis on the neural activity to predict target location from neural activity. This

analysis bypasses some of the confounds of using UKF decoder outputs to predict kinematic parameters, which themselves were a byproduct of the UKF model. Instead, I used a k-nearest neighbor (k-NN) classifier to extract target locations from cortical modulations (Fig. 39C, full description in Section 7.2.2). To quantify cortical representation of each target – which potentially could be different for neurons from different hemispheres and/or areas – I used two classifiers, one for each target. Both target locations were clearly reflected by cortical ensembles during BC without arms, starting with the appearance of the targets and continuing throughout the trial (Fig. 39C). The accuracy of each representation was measured as fraction correct. Using k-NN, the target location of the left arm was decoded more effectively than the right arm in both monkeys (Fig. 39C). This matches the behavioral results from Fig. 39B, which showed better BC without arms performance with the left hand of both monkeys as well. Despite this difference, both right and left target locations could be decoded at significant levels within the same epoch following target appearance. This dual representation persisted through the reaction time and movement epoch of a typical trial (Fig. 39C).

We next assessed the effect of the number of recorded neurons and relative contributions of cortical areas on k-NN decoding of target position. Similar to Fig. 39C, k-NN decoded left and right target locations during the BC without arms task. The mean prediction accuracy for both arms improved approximately linearly with the logarithm of neuronal ensemble size (e.g., for monkey M, M1 ensembles: fraction

correct=0.34 for n=5, fraction correct=0.37 for n=10, and fraction correct=0.43 for n=100, with chance level 0.25; Fig. 39D, right). This followed the same trend observed for prediction of arm kinematics (Fig. 37A-D). For monkey M, with microelectrodes implanted in both leg and arm M1 areas, the targets were better represented by neurons located in the arm area (fraction correct: 0.43±0.02, n=100) compared to the neurons in the leg area (fraction correct: 0.31±0.03, n=100; $p<0.01$). Neurons in the leg area of M1 did, however, contribute to predicting target location: a population of about 100 neurons in the leg area of M1 rivaled in accuracy 100 neurons located in the S1 arm region.

8.2.3 Muscle activity during bimanual BMI control

To provide clear evidence that the avatar movement control was a byproduct of neuronal modulations alone, I recorded EMG signals from the left and right arm during experiments. Similar to passive observation (Figs. 32-33), the muscle activity was greatly reduced in BMI control. More importantly, the small activity that was recorded did not contain information about the cursor position (Fig. 40). There were significant differences in the mutual information (MIn) between EMG and cursor position between the different experimental paradigms. For example, mean MIn was greater in joystick control than BC without arms for all four left arm muscles and reached significance in three of the four ($p<0.01$). Likewise, MIn was reduced in passive observation in three of four muscles as well ($p<0.01$). These provide an important control to show that the monkey was not simply moving its limbs to generate the neuronal modulations in motor-related cortex. Nevertheless, the modulations were able to represent the virtual

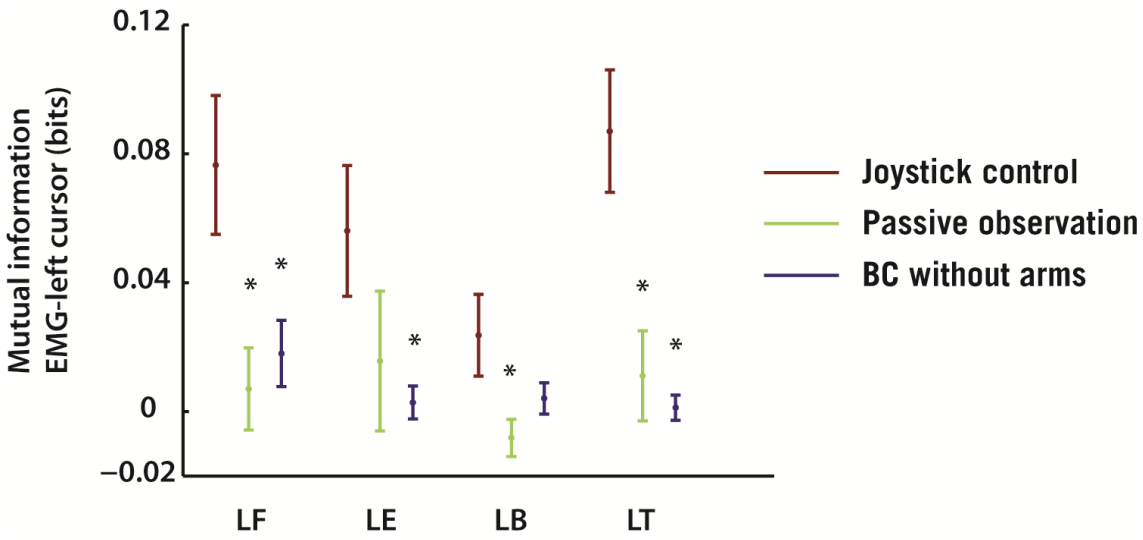

Figure 40: Relationship between muscle activity and cursor trajectories during experiments. Mutual information between cursor position and EMG signals from left forearm flexor (LF), left forearm extensor (LE), left biceps (LB), and left triceps (LT). Values shown are MI average for EMG-X position and EMG-Y position values. Three different experiment paradigms shown in different colors. Error bars denote mean ± s.e.m. * denotes p<0.01 difference from joystick control.

arms in all three conditions (joystick, passive observation, BC without arms).

An additional example of this result is shown in Figure 41. For a given successful trial where the left arm moves to the right and the right arm moves down (Fig. 41A), there were clear differences in forelimb muscle activation in the three paradigms (Fig. 41B). EMG signals during joystick control were higher amplitude and better encoded the left and right cursor positions (Fig. 41C) than either passive observation (Fig. 41D) or BC without arms (Fig. 41E). This was quantified by fitting cursor X and Y position as a multiple linear regression function of eight recorded EMG signals. Regression coefficients for each was computed and tested for significance ($p<0.01$). Coefficients reached higher amplitude during joystick control than passive observation or BC

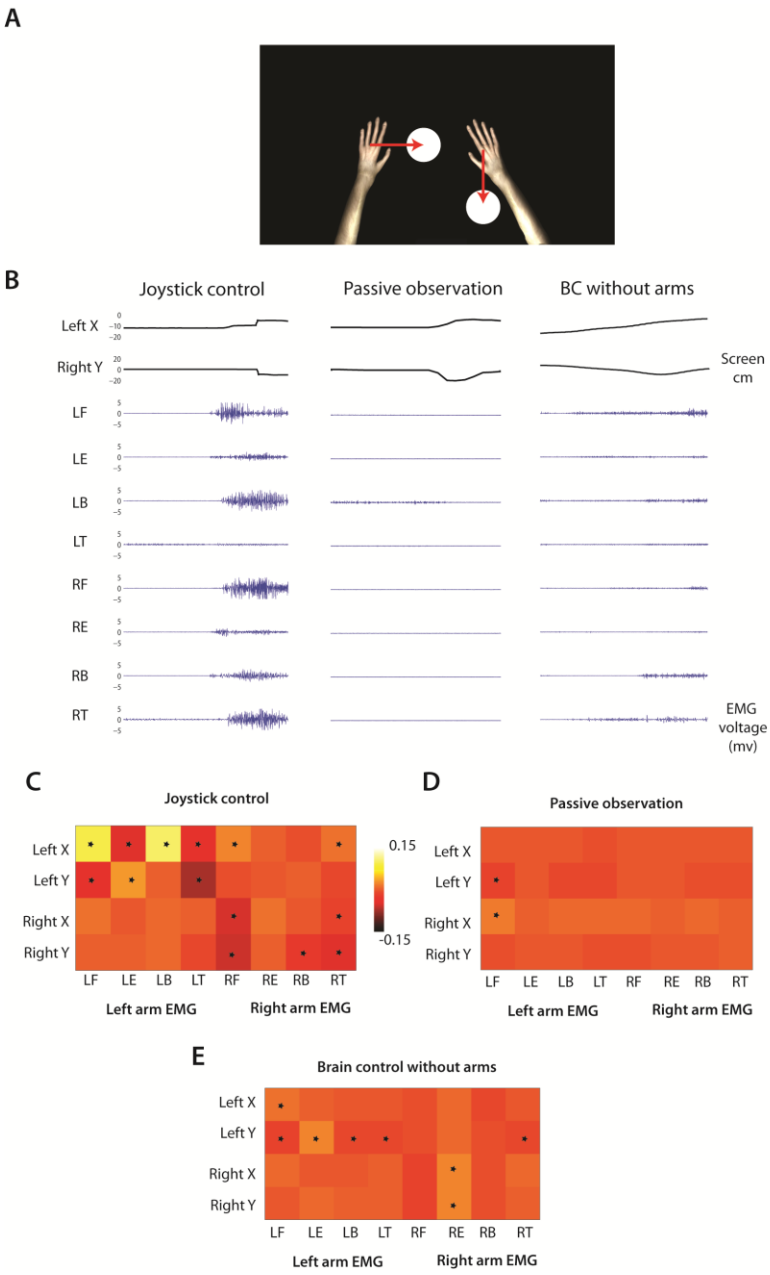

Figure 41: Differences in muscle activation during three experimental paradigms. For the same trial type, where the left arm moves rightward to the target and the right arm moves down (A), EMGs were recorded from eight forelimb muscles on Monkey C (B). Actual trajectories of the virtual arms shown in first two rows of (B). Using multiple linear regression, left and right cursor X and Y positions were fit as a function of EMG signals during active joystick control (C), passive observation (D), and brain control without arms (E). Regression coefficient amplitude shown by color and those reaching significance ($p<0.05$) denoted by black dot. LF-left flexor, LE-left extensor, LB-left biceps, LT-left triceps, RF-right flexor, RE-right extensor, RB-right biceps, RT-right triceps.

without arms, although the residual EMG signals during the latter two did reach significance in a few cases (black dots in Fig. 41D,E).

8.2.4. Neural plasticity during bimanual BMI learning

In parallel with each monkeys' learning of the BC without arms task, I observed plastic changes in the firing patterns of cortical ensembles. These changes were particularly clear in the functional reorganization of the cortical representation of the avatar during the passive observation task, which was measured at the beginning of each session of BC without arms, as reported earlier (Fig. 36). The decoding accuracy of passively observed avatar kinematics (measured as prediction *r*) was clearly enhanced as the BC without arms training progressed.

Furthermore, I observed a gradual reduction ($p<0.01$; ANOVA) in firing rate correlations amongst cortical neurons as animals were training in the BC without arms task (Fig. 42). During early BC without arms sessions, correlations between neurons were 1.7-2.2 times greater than during passive observation periods tested on the same day. Over the next few days, however, these cortical correlations decreased until they reached the same level as during passive observation ($p>0.01$, Fig. 42A). During this reduction, correlations between neurons from the same hemisphere (solid red line, Fig. 42B) and the same cortical area (solid blue line) remained higher than the correlations between neurons from different hemispheres or areas (dashed lines). An ANOVA test showed that both area and hemispheric relationships were factors related to the decrease in correlation ($p<0.01$). In both monkeys, there was a greater proportional decrease in

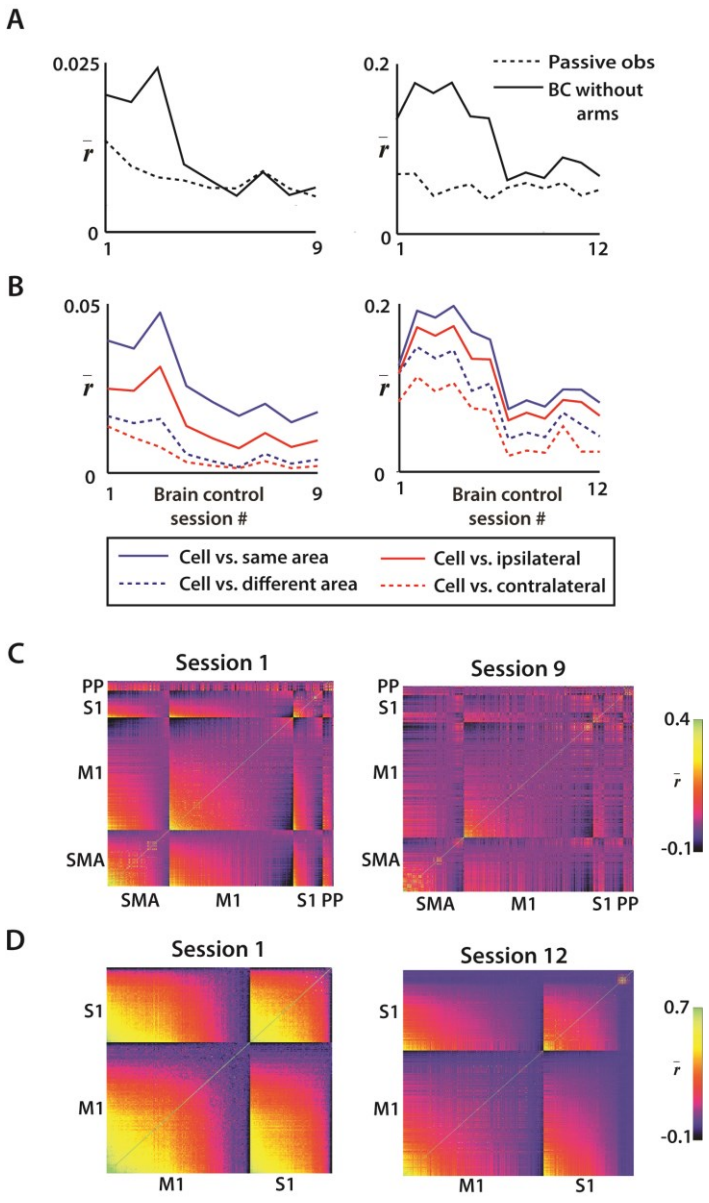

Figure 42: Cortical plasticity during passive observation and brain control without arm movement experiments. (A) Mean correlation r of neural firing among recorded neuronal populations throughout the passive observation and brain control without arm movement (BC without arms) epochs of training sessions. (B) Mean inter- and intra-hemispheric (red) and inter- and intra-area (blue) correlation $\bar{r}$ vs. session. (C) Neuron vs. neuron correlation indicated by pixel color for two monkeys on the first (left) and last (right) day of BC without arms training. Within each panel, neurons are sorted by cortical area and mean correlation strength. (D) Same as (C), except for monkey M. (A-B) Left column: monkey C, right column: monkey M. UKF, unscented Kalman filter; SMA, supplementary motor area; PP, posterior parietal cortex. From [242]. Reprinted with permission from AAAS.

cross-hemisphere correlation during BC without arms learning than within-hemisphere correlation (monkey C: 85.2% reduction across hemispheres vs. 54.0% within hemisphere; monkey M: 56.6% across hemispheres vs. 36.1% within hemisphere). Similarly, correlations between cortical areas (same hemisphere) decreased more than those within an area (monkey C: 76.6% reduction between cortical areas versus 54.0% within cortical area; monkey M: 53.7% reduction between cortical areas versus 29.9% within cortical area).

8.3 Discussion

The results from this study suggest that BMI technology can be applied to the challenging task of enabling bimanual control in subjects who do not produce overt arm movements. My work directly enhances the degree of sophistication of an upper limb BMIs by enabling simultaneous control of two arms. This was achieved by introducing a bimanual decoding/training paradigm – one that takes full advantage of large-scale simultaneous bi-hemispheric chronic cortical recordings of up to 500 neurons, a virtual reality training environment, an optimal bimanual decoding algorithm, and the recently discovered [128] phenomenon of visually-driven cross-modal cortical plasticity.

From earlier studies in the Nicolelis lab, we have argued that BMIs provide important insights into the physiological principles that govern the function of brain circuits [205]. In this context, my work tested whether these principles apply to bimanual motor control. To examine the role of neural ensembles for bimanual control, I utilized simultaneous, very large scale recordings from fronto-parietal cortical

ensembles [88, 205] and obtained extractions of bimanual motor parameters. Neuron dropping curves constructed from both manual control data (Fig. 37A-D) and real-time BC without arms data (Fig. 39D) indicate that the accuracy of neural decoding steadily and linearly improves with the logarithm of neuronal ensemble size. With a distributed multi-site recording approach, I demonstrated the representation of bimanual movements of several fronto-parietal cortical areas. This result is consistent with previous neurophysiological studies of bimanual motor control [73, 77, 78, 80, 263]. From the collected data, the M1 contribution to the decoding was the most substantial, which is likely due to a higher proportion of task related neurons. Supplementing the M1 ensemble (red line in Fig. 37A-D) with neuronal data from the other areas (black line) further improved the decoding. Furthermore, non-M1 areas such as PPC [265] and PMd [126, 157, 195] are known to be reliable sources for BMI decoding with an overlapping but often distinct role from M1 output [36, 266, 267]. This is especially true in an area such as SMA, which is known to be involved in bimanual coordination [73, 263].

These results support a highly distributed representation of bimanual movements by cortical ensembles, with individual neurons and neural populations representing both avatar arms simultaneously [73, 77, 263]. Most neurons recorded in this study contributed to the predictions of kinematics of each arm (Fig. 38B-D). Moreover, during online BMI control of bimanual movements such multiplexing of the kinematics of both arms by individual neurons became even more prominent (Fig. 38C).

Overall, my findings provide support for the notion that very large neuronal ensembles, not single neurons, may define the true physiological module underlying normal motor functionality [88, 129, 195, 205, 240]. This suggests that small cortical neuronal samples may be insufficiently informative to control complex motor behaviors using a BMI [115, 116, 268, 269], but BMIs with few neurons could be useful testbeds for experimentation with less challenging motor tasks. Although the study was not designed to test bimanual control with just a few neurons, I probed small ensembles indirectly by employing a neuron dropping analysis using a k-NN classifier to estimate the contribution of ensemble size to target representation during BC without arms (Fig. 37A-D). This analysis showed that large ensembles always performed better.

This study also provides new insights into the plasticity of cortical ensembles. Previously, we demonstrated that cortical ensembles can undergo substantial plasticity during learning of BMI tasks [195]. We even observed an emergence of visually evoked responses in S1 and M1 when attended to virtual avatar arms [128, 129]. Here, I observed improvements in performance as the monkeys enacted real-time BMI control of bimanual movements. These improvements were accompanied by a steady decline of correlated neural activity throughout the four recorded cortical areas and in both hemispheres (Fig. 42). Previous work [205, 270, 271] has identified that cortical modulations and inter-neuronal correlations initially increase during BMI operation, which have been suggested to serve a role in the initial learning of unfamiliar tasks. Additionally, we have reported a decrease in variance associated with neuronal

modulations during BC without arms learning [270]. Still, the potential function served by the decrease in neuronal correlations observed in this study and others [67, 272] remains to be fully understood. The most basic interpretation of this result is that correlated activity benefits early learning, but firing rate independence sustains later stages of the learning process when independent control of both arms is learned. Notably, changes were observed in a multitude of fronto-parietal structures across both cortical hemispheres.

Previous work from the Nicolelis lab reported elevated correlated activity between neurons [205] and increased neuronal modulations unrelated to movement kinematics [270] during early sessions of unimanual BC without arms. A similar change in neural correlations was reported in human EEG studies in which inter-hemispheric EEG coherence decreased during bimanual task-learning [67, 272]. Thus, the monkey data from this study indicate that inter-area and inter-hemispheric correlations may transiently increase during the initial learning phase and then decrease after subjects perfected bimanual motor behavior.

Overall, this study for the first time demonstrated that cortical large-scale recordings can enable bimanual BMI operation in primates – a type of operation that advanced clinical neural prostheses will employ in the future.

9. Decoding strategies for bimanual brain-machine interfaces

As more sophisticated BMI components continue to be developed, new strategies must be likewise designed to more efficiently extract information from the brain. With the vast majority of early BMI studies focused on single cursor or limb control, advances in BMI decoding were typically focused on this particular paradigm as well. There has been no shortage in the development of novel algorithms or decoding strategies customized for BMI implementation [143, 150, 273]. From my preliminary work on bimanual neurophysiology (Chapter 6), I discovered fundamental differences from unimanual movements in both behavior and cortical representation. This observation guided the final phase of my thesis work – to optimize neural decoding strategies specifically for bimanual movements.

I include this discussion after revealing the success of the bimanual BMI (Chapter 8) as a way to show its developmental steps more rigorously. Some of the key findings were implemented into the real-time BMI suite and some were not. Nevertheless, this analysis focuses on three questions: (1) which algorithm can decode bimanual movements most effectively, (2) which parameters or settings are optimal for this algorithm, and (3) can the decoding of upper limb movements include more paradigms by using a classify and predict two-stage switching model?

9.1 Algorithm for decoding bimanual movements

To decide upon the best neural decoding algorithm to use for bimanual BMI

control, I examined three of the most commonly used decoders for real-time control: the Kalman filter [110, 111, 143, 274], the Wiener filter [83, 114-116, 126], and the unscented Kalman filter (UKF) [129, 150, 169, 242]. All three have their advantages and disadvantages (Section 2.2), but are well established in single limb experiments. Linear decoders, such as the Kalman and Wiener filters, are associated with requiring less computational power such that real-time implementations could be realized. The Wiener filter has a straightforward formulation of kinematic output as a summation of neuronal spike counts scaled by their respective weights (Eq. 3 in Section 2.2.1). The Wiener filter is effective in low dof paradigms, but may show substantial jitter and noise. Furthermore, the algorithm lacks a probabilistic component that Bayesian models incorporate to more effectively capture naturalistic movements. The Kalman filter and UKF both feature recursive Bayesian inference in a two-step predict and update method (Eq. 4 in Section 2.2.2). The unscented transform and quadratic tuning model of the UKF enable this nonlinear Bayesian inference model to remain computationally light without sacrificing performance [150]. All three, however, have only been tested on-line with single limb experiments.

I first tested each algorithm on bimanual data with varying amounts of neural firing history (taps) to make the predictions (Fig. 43). I divided up bimanual center-out joystick control into training and test blocks. After computing predictions, I selected new training and test blocks using 10-fold cross-validation to generate distributions for each r value. The three algorithms were always trained and tested on the same data for

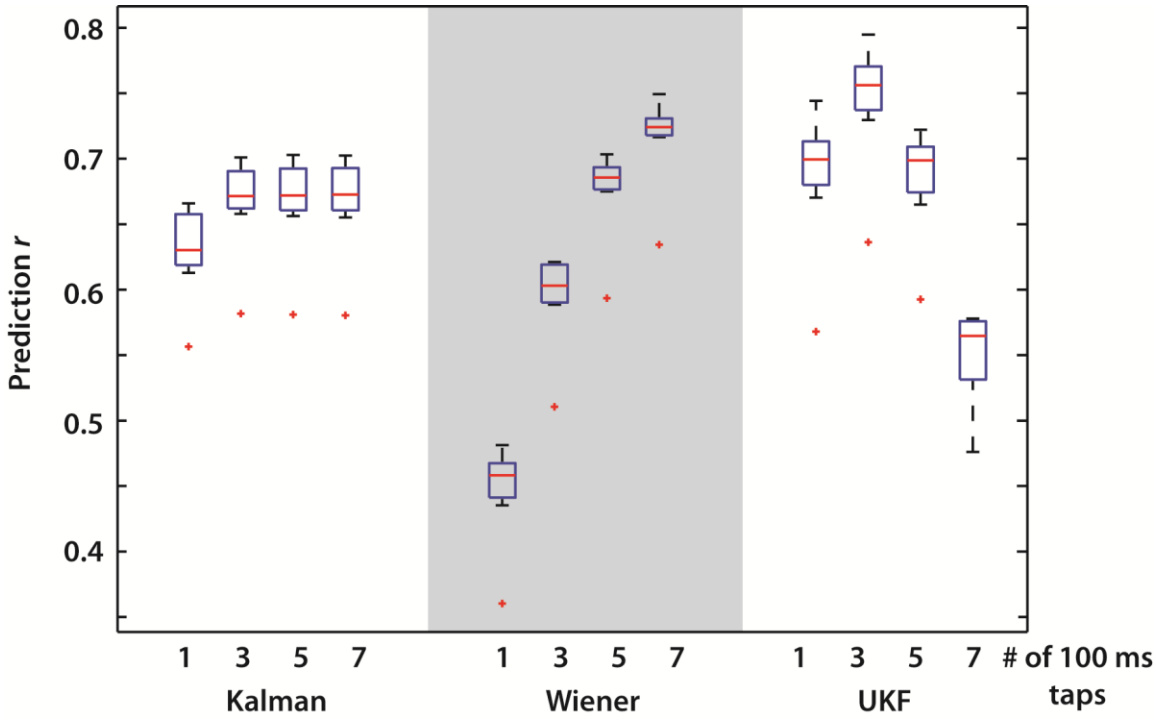

Figure 43: Comparison of different decoding algorithm and number of taps of neural activity used to make prediction of bimanual movements offline. For each of the three algorithms (Kalman filter, Wiener filter, unscented Kalman filter), bimanual X and Y positions were predicted and the separate r values averaged to yield a single r, and repeated to obtain a distribution. 1,3,5,or 7 taps of 100 ms of neural activity were used to make prediction.

accurate comparisons. In addition, I varied the "past taps" parameter of the decoder from 1-7 100ms bins of neural activity. Previous work has shown differing amounts of firing history are optimal in different types of movements, therefore it was important to identify the best setting for bimanual movement. For the UKF and Kalman filter, I included kinematics of both right and left arms. I refer to this as a conjoint model. The Wiener filter lacks a movement model and thus computes the two arms independently.

The strongest neural decoding performance was observed using the UKF with 3 past taps of neural activity (Figs. 43, 44). The 3 tap UKF decoding performance was stronger than all other UKF settings ($r=0.74\pm0.05$, $p<0.05$, ANOVA with post-hoc) and

Kalman filter settings ($p<0.05$). Decoding accuracy with the Wiener filter was highly dependent on the history of neural activity. With only a single past tap, the decoding accuracy was very low ($r=0.44\pm0.04$). With 7 taps, the Wiener filter decoding accuracy approximated that of the 3 tap UKF ($p>0.05$). This highlights a major distinction between the two models. The Wiener filter relies only on a linear combination of spike counts in a recent neural firing history. The other two, both probabilistic models, join this observation model with a statistical model of the two arms' movements. I found that both the Kalman filter and UKF require a smaller amount of history to reach their peak performance. Extending beyond 3 past taps actually hurts the UKF performance

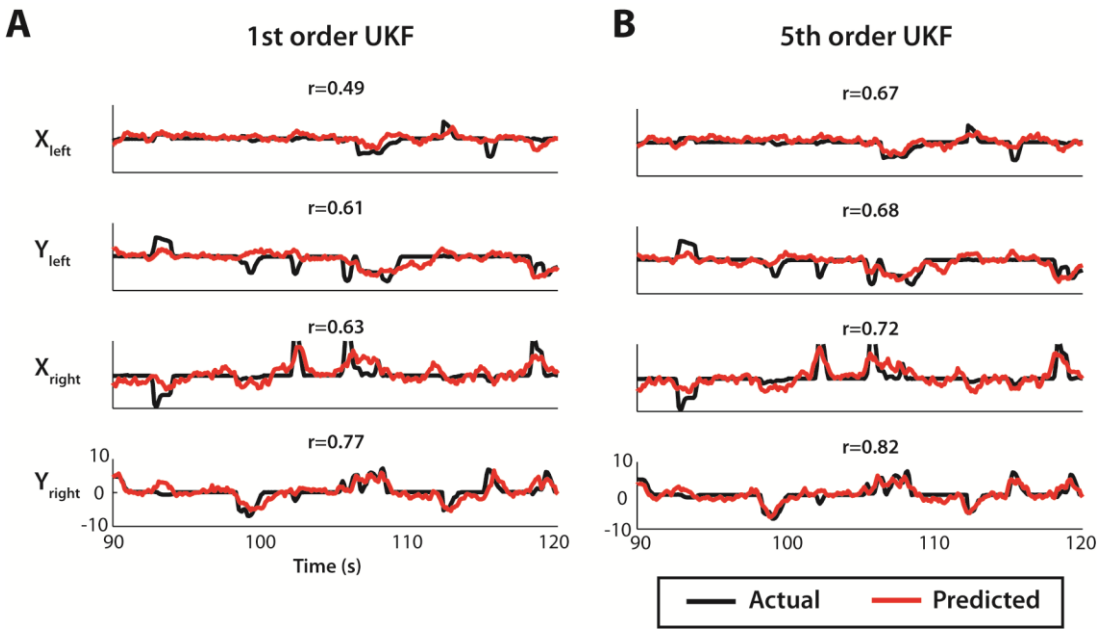

Figure 44: Comparison of 1st and 5th order unscented Kalman filters. (A) The X and Y cursor traces for left and right arms (black) were predicted with the 1st order UKF (red) and compared. The correlation between actual and predicted computed for each 30 second window as r. (B) Comparison of actual cursor traces and prediction using a 5th order UKF, with 3 past taps and 2 future taps of neural activity. From [242]. Reprinted with permission from AAAS.

substantially – a 7 tap UKF reduces the performance to r=0.55±0.04. Further comparing the decoder output (Fig. 44A compared with 44B) of a 1st order UKF (1 past tap) with a 5th order UKF (3 past taps, 2 future taps), it is clear the 5th order model captures the intricacies of movement more effectively. This distinction guided my decision to use a UKF with 3 past taps and 2 future taps (which are possible with the UKF's generative model) in real-time experiments as well (Chapter 8).

9.2 Conjoint representation of two arms in UKF model

I next analyzed the differences between using two UKF models, each with a 2D tuning function (and therefore, output), and using a single UKF with a 4D tuning function. I hypothesized that prediction accuracy could be improved by conjointly modeling the two arms. The 2D tuning model fit binned neural activity $y(t)$ as a function of single arm (x,y) position, velocity, and quadratic terms of both as in Eq. 16:

$$y(t) = \begin{bmatrix} b_1 & b_2 \end{bmatrix} \begin{bmatrix} pos_x(t) \\ pos_y(t) \end{bmatrix} + b_3 \sqrt{pos_x(t)^2 + pos_y(t)^2} + \begin{bmatrix} b_4 & b_5 \end{bmatrix} \begin{bmatrix} vel_x(t) \\ vel_y(t) \end{bmatrix} + b_3 \sqrt{vel_x(t)^2 + vel_y(t)^2} \quad (16)$$

For all bimanual experiments, a 4D extension was made to the quadratic tuning model of Eq. 16. More specifically, $y(t)$ was formulated as a function of bimanual (x,y) positions, velocities, and quadratic terms of each as in Eq. 17:

$$y(t) = \begin{bmatrix} b_1 & b_2 & b_3 & b_4 \end{bmatrix} \begin{bmatrix} pos_{xL}(t) \\ pos_{yL}(t) \\ pos_{xR}(t) \\ pos_{yR}(t) \end{bmatrix} + \begin{bmatrix} b_5 & b_6 \end{bmatrix} \begin{bmatrix} \sqrt{pos_{xL}(t)^2 + pos_{yL}(t)^2} \\ \sqrt{pos_{xR}(t)^2 + pos_{yR}(t)^2} \end{bmatrix} + \begin{bmatrix} b_7 & b_8 & b_9 & b_{10} \end{bmatrix} \begin{bmatrix} vel_{xL}(t) \\ vel_{yL}(t) \\ vel_{xR}(t) \\ vel_{yR}(t) \end{bmatrix} + \begin{bmatrix} b_{11} & b_{12} \end{bmatrix} \begin{bmatrix} \sqrt{vel_{xL}(t)^2 + vel_{yL}(t)^2} \\ \sqrt{vel_{xR}(t)^2 + vel_{yR}(t)^2} \end{bmatrix} \quad (17)$$

At each time step, a transition model is used to update the state (i.e. kinematics) prediction matrix P given information about the previous state, P_{t-1}, as shown in Eq. 18:

$$P_t = FP_{t-1}F^T + Q \quad (18)$$

where the F matrix (Table 5) is the linear component of the transition model and the Q matrix (Table 6) is the noise, which includes both random variations and any nonlinearities. These two matrices provide insight into my hypothesis that the right and left arms are not independently represented by the conjoint model. Note the highlighted values within each table – these represent the between-arm terms. The amplitude of these values is not trivial, and in many cases larger than certain within-arm terms. These models are fit purely on the left and right arm kinematics and therefore reflect subtle, but quantifiable linear and nonlinear relationships between arms. In other words, the movement covariance matrices F and Q indicate that the motion of one arm is predictive of the other arm. In the context of Eq. 18, this guarantees that the prediction of the state accounts for this between-arm covariation as well. The prediction step in the UKF gives a distribution, however, and is only the first step in the procedure.

Table 5: Linear movement model covariance matrix F from unscented Kalman filter. Upper-left 8x8 submatrix shows covariance terms from pairs of right and left arm kinematics. Rows/columns as labeled below. Highlighted cells represent values of between-arm covariation that is accounted for by a linear model

	LEFT X	LEFT Y	RIGHT X	RIGHT Y	LEFT VX	LEFT VY	RIGHT VX	RIGHT VY			
LEFT X	0.949	-0.001	0.006	0.002	0.136	-0.022	0.010	0.012	0	...	0
LEFT Y	0.000	0.939	0.005	0.005	0.003	0.159	-0.001	0.027	0	...	0
RIGHT X	-0.002	-0.003	0.905	0.019	-0.033	-0.009	0.188	-0.004	0	...	0
RIGHT Y	0.000	0.003	0.025	0.937	0.005	-0.030	0.011	0.172	0	...	0
LEFT VX	-0.193	-0.005	0.025	0.008	0.521	-0.086	0.037	0.047	0	...	0
LEFT VY	-0.001	-0.214	0.019	0.017	0.010	0.560	-0.002	0.095	0	...	0
RIGHT VX	-0.004	-0.008	-0.270	0.054	-0.094	-0.027	0.538	-0.013	0	...	0
RIGHT VY	0.000	0.012	0.090	-0.222	0.017	-0.106	0.040	0.612	0	...	0
	0	0	0	0	0	0	0	0	0	...	0
	⋮	⋮	⋮	⋮	⋮	⋮	⋮	⋮	⋮	⋱	0
	0	0	0	0	0	0	0	0	0	0	0

Table 6: Movement model noise covariance matrix Q from unscented Kalman filter, showing random variation and nonlinear components present. Upper-left 8x8 submatrix shows covariance terms from pairs of right and left arm kinematics. Rows/columns as labeled below. Highlighted cells represent values of between-arm covariation that is not accounted for by a linear model

	LEFT X	LEFT Y	RIGHT X	RIGHT Y	LEFT VX	LEFT VY	RIGHT VX	RIGHT VY			
LEFT X	0.046	-0.009	-0.010	0.005	0.176	-0.033	-0.028	0.019	0	...	0
LEFT Y	-0.009	0.053	-0.005	0.000	-0.036	0.187	-0.015	0.000	0	...	0
RIGHT X	-0.010	-0.005	0.079	-0.015	-0.037	-0.019	0.227	-0.053	0	...	0
RIGHT Y	0.005	0.000	-0.015	0.046	0.020	0.000	-0.042	0.166	0	...	0
LEFT VX	0.176	-0.036	-0.037	0.020	0.679	-0.128	-0.108	0.072	0	...	0
LEFT VY	-0.033	0.187	-0.019	0.000	-0.128	0.660	-0.054	-0.001	0	...	0
RIGHT VX	-0.028	-0.015	0.227	-0.042	-0.108	-0.054	0.654	-0.152	0	...	0
RIGHT VY	0.019	0.000	-0.053	0.166	0.072	-0.001	-0.152	0.594	0	...	0
	0	0	0	0	0	0	0	0	0	...	0
	⋮	⋮	⋮	⋮	⋮	⋮	⋮	⋮	⋮	⋱	0
	0	0	0	0	0	0	0	0	0	0	0

In the update step, this distribution incorporates the neural activity as well, which is referred to as the Kalman gain. Thus the 4D UKF conjointly models the two arms and uses the covariation terms throughout the predict and update procedures.

Applying the 4D model to data, I observed strong improvements to the decoding performance (Fig. 45). Recall that improved decoding using a 4D UKF was apparent in neuron dropping curves (Fig. 37D compared with Fig. 37B) as well. It should be noted that the behavioral covariation between the two arms is not a constant quantity, despite being modeled as such. It is task-specific and depends on how interrelated the two

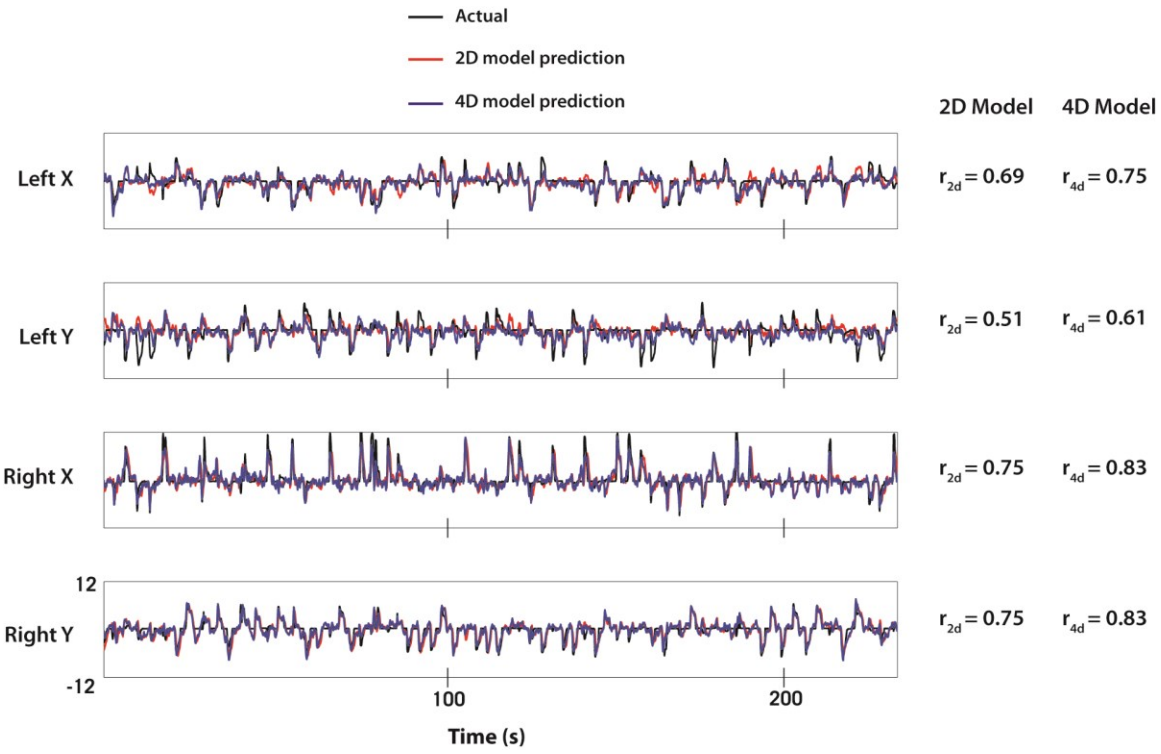

Figure 45: Comparison of 2D and 4D UKF prediction performance. Four rows: prediction of left arm x, left arm y, right arm x, and right arm y. Each panel shows actual trace (black) with 2D (red) and 4D UKF (blue) predictions superimposed. Prediction *r* for each model over the 225 s window is shown to right of panel. From [242]. Reprinted with permission from AAAS.

arms' movements need to be. By fitting and testing the data within the same task (bimanual center-out), however, this is a reasonable assumption.

9.3 A switching model for unimanual and bimanual BMI control

The success of the bimanual BMI stands as important progress towards the goal of a BMI capable of enacting a diverse repertoire of realistic upper limb movements. The logical progression is the question of generalizability [275]: how well can decoding strategies for one subset of movements generalize to enact accurate control of other subsets of movements? Alternatively, it may be beneficial to treat different movement states as unique conditions. With this consideration, the ideal BMI should be adaptable to varying behavioral states, especially states which are represented differently by the brain. Clear examples of this are unimanual and bimanual states. From neurophysiological analyses (Figs. 28-30, Table 4), it is clear that knowing only the contralateral/ipsilateral tuning during single arm movements is insufficient to predict bimanual kinematics. Shown here, and elsewhere [77, 80, 263], bimanual tuning by M1 and motor-related neurons is not the superposition of unimanual modulations, nor is it exclusively derived from contralateral hemisphere tuning. The mechanism behind bimanual neurophysiology may be poorly understood, but the manifestations of a separate bimanual state can be clearly observed. As such, I have designed a novel decoding strategy which exploits the different neurophysiological states that correspond to different behavioral states. I hypothesize that by identifying the behavioral state and switching to the appropriate decoder, I can obtain more accurate overall predictions.

9.3.1 Methods

To design a BMI capable of handling both unimanual and bimanual movements, I devised a two-stage classify and predict decoding technique (Fig. 46). In the first stage, the behavioral state is predicted as one of three possible states: unimanual left, unimanual right, and bimanual. For this prediction, I used a k-NN classifier [276] (description in Section 7.2.2). Depending on the predicted state, I would then use a different UKF model to predict kinematics. Three UKF models, each with different parameters sets, must be fit prior to online control. Every 100 ms, the k-NN model and all three UKF models generate a prediction. Although a subtle distinction in offline analyses, future online implementations may prefer to predict with the UKF only if

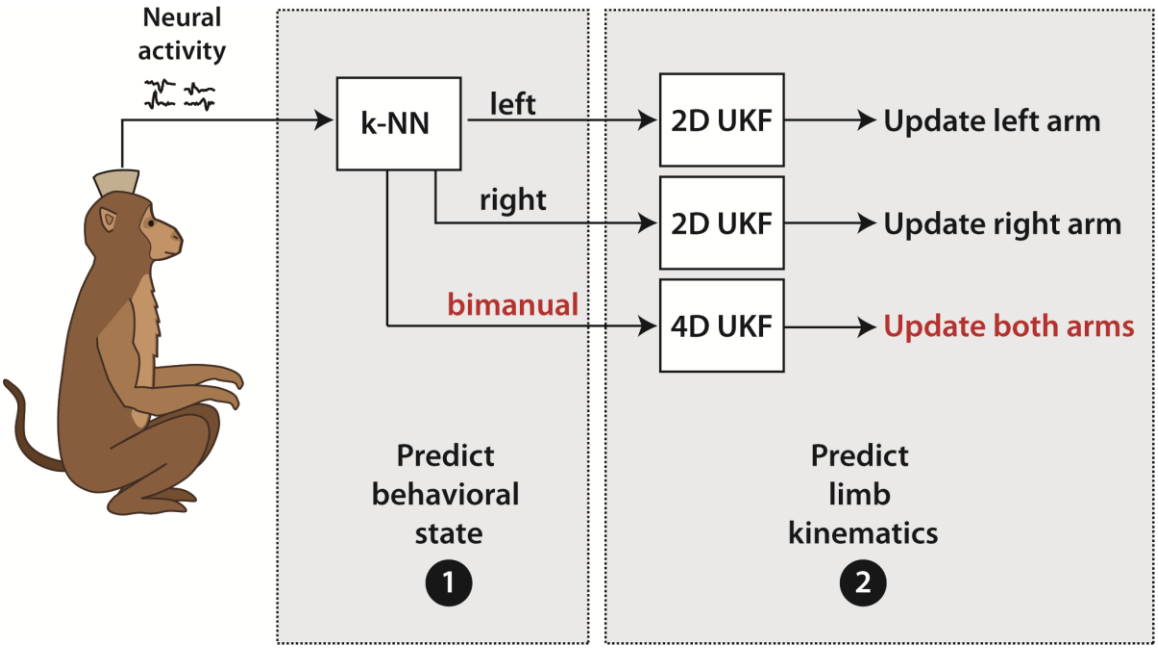

Figure 46: Two-stage classify and predict decoding strategy for unimanual and bimanual movements. The neural activity is first decoded to predict behavioral state using k-NN: left unimanual, right unimanual, or bimanual. The state prediction determines which UKF model is then used to predict kinematics from neural activity

selected by the k-NN classifier. The drawback of this design is that it sets up the two stages in a serial framework rather than in parallel, the latter of which can be preferable computationally.

Depending on the k-NN state classification (left/right/bimanual), the appropriate UKF model prediction is selected and used to update the arm or arms. If a unimanual state, the non-working arm is not moved from its position at the previous time step. This type of classify and predict, multi-stage model has been used previously by our lab for locomotion studies which classified forward and reverse walking states [240]. A multi-state decoding strategy for upper limb movement is perhaps even more important due to the moment-to-moment shifts in inter-arm coordination/independence.

9.3.2. Results

Data from the same unimanual/bimanual joystick control experiment as described in Section 6.3.3. were used for evaluating the two-stage switching model. To assess the efficacy of the first stage ("classify", Fig. 46), I analyzed how effectively the k-NN classifier could predict the behavioral state. Because the analysis was offline, I could compare the predicted behavioral state with the actual state at each 100 ms time step. Each of the three states could be predicted at highly significant rates ($p<0.01$, 2-proportion z-test, Fig. 47A). With a chance prediction level of 33%, left unimanual was predicted correctly at a rate of 74.79%, right unimanual at a rate of 71.75%, and bimanual at 85.43%. It is interesting to note that the bimanual state was predicted more accurately than either of the unimanual states even though it represents a "mixture" of left and

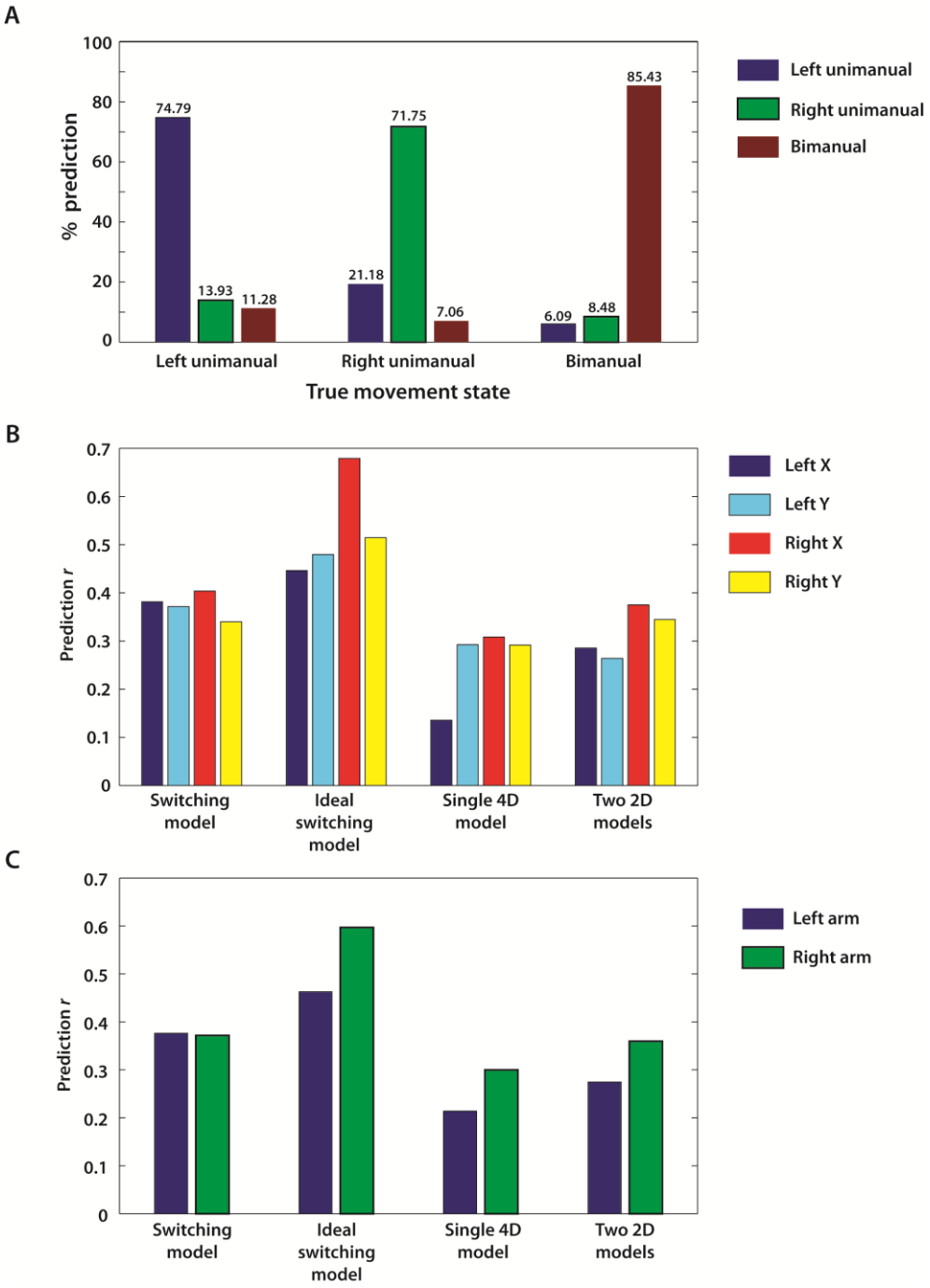

Figure 47: Performance of the switching model in prediction of movement state and kinematics. (A) Percent prediction for each of the three possible states when movement state was left unimanual (left cluster), right unimanual (middle), or bimanual (right). (B) UKF prediction *r* of the x and y position of each arm using four different decoding strategies: switching model, ideal switching model, single 4D model, and two 2D models. (C) Same as (B) but average *r* for X and Y shown.

right hemispheric commands. This further supports my earlier results that there are substantial differences in modulation between bimanual and unimanual movements at the cortical level. It was more likely that a left unimanual state was incorrectly predicted to be right unimanual (13.93%) than for a bimanual state to be incorrectly predicted to be only left (6.09%) or only right (8.48%). This confirms that the first of the two-stage classify and predict method can be a reliable tool to guide the UKF model selection step that follows.

Next, I compared the two-stage switching model with several alternatives: (1) an "ideal" switching model where the first stage was not predicted, but rather the actual behavioral state guided the UKF model selection step, (2) a single 4D UKF model, and (3) two 2D UKF models where each predicts one arm. The ideal switching model gives an upper bound estimate of switching model performance. Because it relies on knowledge of behavioral truth which is not available to a neural decoder, it is not a feasible design for real-time control. I found that the switching model outperformed both the 2D and 4D UKF implementations for both left arm ($r=0.37$ compared with $r=0.28$, $r=0.21$) and for right arm ($r=0.37$ compared with $r=0.36$, $r=0.30$). The ideal switching model (second cluster in Fig. 47B,C) outperformed all other models, including the actual switching model. Both left arm ($r=0.46$) and right arm ($r=0.60$) were strongly decoded by this approach. Even more vividly, the right arm X dimension was strongly predicted by the ideal switching model ($r=0.68$) but much more weakly by the other

three models (r=0.40, r=0.31, r=0.38 from left to right in Fig. 47B). This suggests that the second stage of the two-stage decoding paradigm is highly advantageous for improving predictions. The obvious drawback for using exclusively the 4D model is that it does not predict unimanual movements effectively (Fig. 38F) and likewise for 2D models tested on bimanual data (Fig. 38E). This is a byproduct of the 4D model being trained on bimanual data and the 2D models being trained on unimanual data. A switching model can bypass this problem by training on all three types of movements and using the context-appropriate model as needed.

9.4 Discussion

In this chapter, I have introduced several solutions towards creating improved decoding strategies for a bimanual BMI. First, I compared three of the most commonly used neural decoders in the field and applied them to decode bimanual movements. For each decoder, I tested several different amounts of neural firing history – from 100 ms to 700 ms. I found the strongest neural decoding could be obtained using an unscented Kalman filter with a 300 ms history of neural activity (three 100 ms taps). Next, I demonstrated the advantage of conjoint bimanual representation by a decoding model by comparing a 2D UKF with a 4D UKF. Lastly, I presented a solution for generalizing upper limb decoding by using a two-stage switching model featuring both a state classifier and a UKF decoder for limb kinematics. In doing so, I introduce a decoding framework that could handle the complex dynamics of two limb coordination and independence as a function of time. Although an early implementation, it builds off of

well-known neurophysiological observations to outperform models designed for solely one or two arms.

The comparison between different neural decoding algorithms is an important first step towards the design of an optimal decoding strategy. Certain algorithms may be optimal for certain movements, but not others. Since there has been no previous bimanual BMI, it was unknown how much could simply be inferred from unimanual findings. From a previous study with unimanual movements by Li et al [150], the UKF also outperformed the Kalman and Wiener filters. The Li et al study featured only 2D decoder output and the movements were slower, following a Lissajous curve in a continuously moving pursuit task. The Wiener filter used for comparison featured 10 past taps of 100 ms, an amount which I did not test in my analysis. Using a Wiener filter with ridge regression, as was used in my analysis, the decoding was very comparable to that of the Kalman filter. Another study [277] compared the Kalman filter, a linear method, with two nonlinear methods – General Regression Neural Network (GRNN) and Support Vector Regression (SVR). Both GFNN and SVR decoded M1 neural activity more effectively (in terms of correlation coefficient) and had lower root mean square error than the Kalman filter. It should be noted that an emerging trend in neural decoding algorithms is to feature feedback systems and adaptive updates [169, 246, 278]. I opted to perform the comparison using static models because adaptive update methods differ and could obscure the differences due the algorithm itself. Notwithstanding this confound, the static models described in the analysis do not

account for nonstationarities that are known to exist in neuronal movement encoding within motor-related cortices [279]. An optimal strategy may be to combine the nonlinear UKF decoder in an adaptive framework as described previously [169].

Related to the question of algorithm is the question of how much history of neural activity to use. Varying the number of 100 ms taps of past neural activity from 1 to 7 (for a total of 100 to 700 ms of neural firing history), there were substantial differences in decoding performance (Fig. 43). The Wiener filter always performed better with additional taps of neural activity, up to 7 taps (beyond this, improvement was negligible). This was not the case with the Kalman and UKF models, which differ fundamentally from the Wiener filter. Both the Kalman and UKF are probabilistic methods that make no assumption that the noise of the neurons is independent and of equal variance (unlike the Wiener filter). These two assumptions are flawed and are violated by real neural populations [143]. In addition, the Wiener filter requires more parameters to be fitted and therefore a greater amount of training data, increasing the risk of overfitting. From the results we also see that the Wiener filter performance depends on a more extensive history of neural activity, which could be detrimental in tasks with rapid movements and low autocorrelation terms at longer time lags. In addition to past taps, the UKF model allows for future taps by way of its generative model. This is facilitated by the observation model, or the neural tuning model, that estimates future neuronal rates from the estimated desired movement by way of the quadratic tuning function (Eqs. 16, 17) [150]. Together with the probabilistic methods

and reduced dependence on firing rate history, my analysis concludes that the UKF with 3 past taps and 2 future taps was the best algorithm and decoder settings among the three tested models for bimanual movements. This matches similar observations in single arm experiments where lower order (3-5th) UKF models were sufficient for online control [129].

Stemming from the offline analyses that a 4D UKF outperformed a 2D UKF, I successfully designed a BMI that controls movements of two limbs in real-time, utilizing neuronal ensemble data recorded from both cerebral hemispheres (Chapter 8). Developing decoding strategies that could accurately represent both arms' movements was a major unresolved question in BMI research prior to this investigation. I observed that not only did the conjoint modeling of two arms produce the strongest predictions, but the conjointly modeled arms could still be controlled independently during real-time BMI operation. The importance of bimanual movements in our everyday activities and specialized skills cannot be overstated [280]. Future clinical applications of BMIs aimed at restoring mobility in paralyzed patients will benefit greatly from the incorporation of multiple limbs. It still remains to be tested how well BMIs would control motor activities requiring precise inter-limb coordination. From this demonstration of BMI control of independent movements in two arms, it is clear that performance would benefit from the inclusion of large populations of neurons and multiple areas in both hemispheres.

The bimanual BMI study was also the first demonstration of four degrees of freedom (dof) decoded across two limbs. This is substantially different than, for

example, four dof control where all four dof are derived from a single arm [127]. In such designs, the dofs are often much more correlated with each other than when four dof come from two separate limbs. My results using the 4D UKF suggest that it is advantageous to adapt the neural tuning models for a higher dimensional output (kinematics) space rather than running independent models for separate joints or limbs.

A final question which I addressed was how to generalize the bimanual results for a broader set of movements. That is, what is the best strategy for decoding when the intended set of movements includes left arm movements, right arm movements, and bimanual movements? I proposed that these represent three distinct behavioral states and therefore three separate models should be used. As a result, there must be a mechanism to identify the state from cortical activity and switch between decoders. I found that a behavioral state was detectable with a simple classifier algorithm (Fig. 47A) and that a switching model could enhance decoding efficacy (Fig. 47B,C). This represents two key results. First, a framework for generalized BMI control of two arms. A decoding paradigm that only works in one subset of movements (i.e. bimanual) has limited utility. Rather, the decoding strategy should be flexible to handle shifts from bimanual control to single limb control as desired by the subject. This shift in intention relates to the second feature of a switching model – identification of higher order states. Hybrid BMIs featuring both kinematic and cognitive decoding have been proposed previously to augment motor BMI function with decoding higher-level processes such as decision making, forward estimation, executive function, and attention [63-65, 265, 281].

Often referred to as cognitive neural prosthetics (CNPs), such systems are typically proposed to sample from non-motor, cognitive areas such as area 5d [265] and the posterior reach [64], both within PPC. With the switching model described here, I propose that the information about the behavioral state can be decoded from the same areas where kinematics are encoded – M1, S1, and SMA in addition to PPC.

The most comparable design found in literature is a switching Kalman filter presented in several studies by Wu et al [274, 282]. This design, much like mine, featured multiple Kalman filter models. A key difference was that state transitions were described by Markov chains. Likewise, the states were modeled as "hidden states" which emerged from a Gaussian mixture model of firing rates, not actual behavioral states per se. A related design by Yu et al. [283] also utilized a probabilistic mixture of trajectory models rather than a single decoding model. These BMI implementations, in addition to the switching model presented in this chapter (Fig. 46), provide potential solutions for the challenge of generalizability by featuring the dynamic selection from an array of models.

I have addressed several important and unresolved challenges which preclude multi-limb or full body BMI systems. I first identified specific neural decoding algorithms and parameters that are optimized for extracting bimanual motor commands from neuronal ensembles. Furthermore, I demonstrated the advantage of a conjoint two-arm model over separate single-arm models. This result has a very practical application for future BMI designs: to reproduce complex body movements using BMI

control, the contributions of separate but functionally related muscle groups should be modeled jointly, not separately. Lastly, I joined with previous studies [240, 274, 282, 283] in showing that the best strategy for generalizing BMI function across the broadest range of movement types may be to utilize a switching model, allowing different neural decoders to uniquely represent different behavioral (Fig. 47)[240], cognitive, or "hidden" neurophysiological states [274, 283].

10. Conclusions and Broader Implications

Scientists study the world as it is
Engineers create the world that never has been

- Theodore von Kármán (1881 - 1963),
Aerospace engineer, physicist, mathematician

In presenting in the results of my thesis research, I intend to make a lasting and meaningful contribution towards the still new and evolving field of neuroengineering. It is a branch of engineering that Dr. Kármán and virtually all other scientists would have deemed unfathomable just 75 or even 50 years ago. It is the fusion of understanding complex, precisely evolved biological systems and the latest tools in computer science, electrical engineering, and virtual reality. I began each phase of my research process as a scientist, seeking an understanding of the language of the brain. As a biomedical engineer, studying the motor system of the brain gave me a template for how to decode and recreate natural movements with new advances in BMI technology. By merging the two disciplines, there exists an incredible opportunity to improve mobility and quality of life amongst patients with severe paralysis. With this new field, perhaps the quote from Dr. Kármán could be modified to read that "…neuroengineers recreate a world that has been irreversibly destroyed." Here, I will again review the discoveries, insights or advances which I have made in my thesis work. I will conclude with a broader discussion of the implications and remaining questions in the field.

10.1 Summary of contributions

1) **I discovered of the cortical representation of the speed-accuracy tradeoff during reaching movements known as Fitts' law**. I identified the effect of target size on neural firing profiles and demonstrated that task-relevant sensory parameters are encoded throughout primary sensorimotor cortex, both of which can be incorporated into BMI decoders to improve realism of upper limb movements

2) **I identified the neural correlates of motor plan transitions and the implications for brain-machine interface decoding**. I discovered that transiently considered, but cancelled, motor plans remain encoded by M1 and S1 populations. Despite this representation, neural decoders such as the linear discriminant analysis and the Wiener filter could reliably extract the intended movement.

3) **I scaled neural ensemble recordings and recording system to facilitate the largest number of simultaneously recorded single and multi-units in published literature.** This advance featured novel electrode designs, multisite surgical implantations, scaling and real-time networking of multiple acquisition systems, and efficient decoding algorithms capable of processing large streams of neuronal data in real-time.

4) **I successfully developed a clinically viable, movement-free training paradigm for brain-machine interfaces.** Using a realistic virtual reality avatar viewed from a first-person perspective, I found that subjects simply observing avatar movements could develop a neural representation of two virtual limbs by way of widespread neuronal

plasticity throughout M1, S1, SMA, and PPC. Furthermore, this paradigm enabled a naïve subject to bypass manual training and directly learn via bimanual BMI control.

5) **I developed the first successful bimanual brain-machine interface.** Through the convergence of large neuronal ensembles and plasticity, enhanced end effector realism, and a custom 4D decoding algorithm, a first-of-its-kind level of BMI control was reached. This represents the first time multiple limbs have been controlled simultaneously in a cortically-driven neuroprosthetic device.

6) **I improved neural decoding strategies for bimanual movements.** By testing several algorithms and parameter settings, I identified the model with the highest accuracy for bimanual decoding. I next proposed and tested a novel two-stage switching model that presents one potential solution for generalizing decoding for both one and two-limb BMI control.

10.2 Broader implications

The various discoveries and innovations presented in this thesis represent important milestones in the extraordinarily young field of brain-machine interfaces. The turn of the 21st century represented a shift in the way neuroscientists viewed severe paralysis and the subsequent motor rehabilitation. In the years that followed, crude brain-machine interfaces driven by only a few dozen neurons sparked our imaginations with both scientific successes and the realization of what seemed to be a science fiction fantasy. The challenge of recreating full motor and sensory function of the limbs and trunk with neuroengineering is formidable, however, and yet today we are still grasping

at such a minute subset of what the intact motor system is capable of. I suggest this context not to diminish early success, but as steadfast motivation to keep driving towards these science fiction-like ambitions.

The first two projects of my thesis work featured the in-depth study of M1 and S1 populations in primate brain during tasks which required various forms of decision making. A consistent theme from these two studies was to broaden the scope of involvement of such areas. Classical neuroscientists (and many BMI groups, interestingly) tended to compartmentalize the brain into different areas with unique specializations. A byproduct of this characterization was a very limited supposed role for M1. The results I present suggest a new role for M1, and to a lesser degree S1. M1/S1 cortex appears to multitask in my study of the cortical correlates of Fitts' law, encoding both the target information and information about the movement. In neurophysiological terms, this was evidence of a sensorimotor transformation. Decision making studies rarely associate M1 (or the visual equivalent, frontal eye field, in saccade studies) with evidence accumulation models. Similarly, the motor reprogramming task elucidated a decision making role of M1/S1 in reprogramming movements.

In a broad sense, these two studies provided strong evidence for an expanded role of primary sensorimotor cortex. Because BMIs often target these areas to extract movements, there are clear implications for BMI decoding. One could speculate on evolutionary reasons why the motor output structure of the brain (M1) would conserve upstream sensory or alternative motor plan information. Giving downstream structures

like M1 the ability to make, or change, a decision by crossing some decision threshold is a powerful way of bolstering certainty in movements while permitting rapid changes without requiring widespread cortical re-computation. Current models of change-of-decision [186] originally proposed to be in more cognitive areas, were found to exist in M1 as well. The most practical applications for the dual motor/cognitive encoding for BMIs are safety features. Slower firing rate onset in M1 was predictive of more precise and steady movements while steeper onset predicted more rapid movements, even at the expense of later switching to a different, more accurate, movement. There are unquestionably times that speed is important, even if mistakes are made. Other times, careful and accurate movements are favored. As BMIs continue to adapt features of the natural motor system, I expect that BMIs will include non-motor features that further aid in converging artificial limb control with that of the natural motor system.

The success of the bimanual brain-machine interface provides an optimistic outlook on the eventual goal of a full-body BMI system. The results bolster several of the prominent hypotheses in the current field. Expanding and diversifying the neuronal ensemble led to more accurately decoded movements. Utilizing a more realistic end effector led to more rapid learning during more complex tasks. The same decoding algorithms used for single limb control can be extended for multi-limb control by conjointly representing motor parameters of the two limbs in a single model. The most significant insight may come from the widespread plasticity during learning of both passive observation and bimanual BMI control.

These two plasticity results (Figs. 31, 36, and 42) are possibly even more surprising than the realization of a viable bimanual BMI. During passive observation experiments, I sampled from approximately 500 neurons across four cortical areas (M1, S1, SMA, and PPC) and observed a persistent, robust neural representation of these watched movements. It would perhaps seem more intuitive if the brain gradually ignored the virtual arms after continued exposure. Nonetheless, the stimulus-aligned responses persisted in all recorded areas (Fig. 31) and continued to encode information about the observed arm trajectories (Fig. 36). Having only sampled from a few hundred of the billions of neurons in the primate cortex, it is intriguing to consider how global this phenomenon may truly be. One could speculate that the subject felt "in control", even when the arms were not, as a result of the experimental design: interleaving brain-control sessions between passive observation sessions. This is an exciting possibility which again highlights how dynamic even a fully developed brain can be. One of the two subjects (monkey M) was naïve to the bimanual motor task – a task that took monkey C nearly six months to master. I introduced this monkey to the task by way of passive observation and eventually bimanual BMI control. The plasticity transformed neural modulations throughout the recorded ensemble, as it did in the first monkey, but not as rapidly. The plasticity in monkey M represents what we hope to be the learning trajectory of many human patients seeking rehabilitation following severe injury. Human patients seeking motor rehabilitation with BMIs are likely to face the same initial unfamiliarity that monkey M faced. The discovery that the brain is capable of such

strong and persistent adaptations reiterates the immense utility for this paradigm in future BMI implementations. Future observation paradigms could take this even further, with immersive virtual environments and tactile percepts via sensory cortex (S1) microstimulation.

Widespread neural plasticity also accompanied bimanual BMI learning, although this interpretation is less clear. The plasticity was manifested in terms of a steady decrease in cell-cell firing rate correlations extending from the first to the final day of BC without arms training. There have been some similar findings previously [67, 195, 225] which showed, as I did, that cross-hemispheric correlations decrease more than intra-hemispheric correlations. It seems likely that correlation between hemispheres is related to behavioral coordination [67, 284]. Bimanual motor control theorists still actively debate the locus and manifestation of this coordination. Certain control models propose very little cortical involvement [285], while others describe complex callosal inhibitory mechanisms [78]. Future work will need to clarify what the role of elevated correlations during the initial phase of learning. Whether the neural mechanisms relate to alternative behavioral strategies is unknown. The answer to such questions may provide key insights into the fundamentals of how exactly BMI operation is learned at the neural level.

Lastly, my thesis work developed strategies capable of decoding bimanual movements, including a generalized model which can adapt to enact single limb reaches as well. The first step was acknowledging that different types of behaviors are encoded

differently in the brain. One arm vs. two arms is one example. In real life movements, the flexibility to switch between movement types is much more valuable that the ability to do one subset of movements efficiently. Of course, simplified and repetitive laboratory experiments historically favor the latter. The idea to create a framework that generalizes across movement types was motivated by the optimism that eventually there will be a demand for versatile BMIs that can recreate realistic movements rather than BMIs with only a single functionality (i.e. reach with single arm). Arms, for example, serve many roles which extend far beyond anything tested in my thesis work. This includes critical roles in isometric contraction, locomotion, balance, posture and proprioception. Based on my results using a switching model with discrete states, I expect that different classes of movements will require different decoders. By observing the nonlinearities between highly comparable single and two-arm movements, it strengthens my belief that there is not a single, unified encoding of the brain. Rather, I suspect that lower order kinematic commands are subject to higher order states and potentially multiplex in a mechanism that is yet poorly understood.

10.3 Open questions

A full discussion of the "open questions" in BMIs could itself be a lengthy publication, however there tend to be several important themes to consider. First and foremost, it remains to be seen how brain-machine interfaces will impact clinical rehabilitation. Currently, the implanted clinical implementations are relatively simple, low-risk, and far from state-of-the-art. The technology is expensive and the surgery is

fully invasive. In future years, the cost and benefits for the users must be established in such a way that there is real opportunity to affect quality of life among the millions suffering from paralysis worldwide. There are different routes this may take. Small, portable BMI systems with wireless transmission seem to be a logical progression among patients seeking increased mobility. Alternatively, more robust systems with greater numbers of electrodes and decoded signal content could be preferable.

Secondly, will the goal be to restore prior function (arm or leg use) or to enhance existing rehabilitation tools (e.g. brain-controlled wheelchair)? If BMIs prove to be effective in applications of neuroprosthetics and rehabilitation, there will be a second wave of interest which could extend this technology towards personal augmentation in humans with no neuromotor deficits. That is, there may be the opportunity to *enhance* rather than simply rehabilitate a wide array of human capabilities. Such potential is already drawing interest in competitive realms such as military [286] and athletics [287]. The idea of enhancement immediately evokes questions of whether we, in a general sense, should be doing this. This is an example of how ethical concerns about BMIs will emerge whether or not they actually live up to their vast potential. At the very minimum, safety is a prominent concern which plagues invasive BMI systems. Approval processes for new devices are understandably slow and require extensive safety demonstrations. Preclinical studies in our lab have shown safe and stable implants for 4-6 years (and counting), but this number may need to improve prior to widespread use in humans. It remains to be determined how long after implantation

cortical implants must be deemed stable for intracortical BMIs to become more widely used. With many paralyzed patient candidates being quite young, BMIs must demonstrate safety on time scales of decades rather than just years.

With the advances over the past 15 years in brain-machine interfaces, the likelihood that this technology will become transformative in coming years is growing. With the onset of cardiac pacemaker technology 50 years ago, we have some precedent for how a previously unthinkable, highly invasive device could become widely used and successful. The brain is certainly more complex in many ways than the heart and these differences must be addressed. The extracted signals of the brains are the core of what makes BMIs run, yet they represent one's thoughts – the utmost private information that a human possesses. A code of ethics must be established as to limit the access to such data, especially with very large scale recordings. There is an interesting parallel between the dawn of the "big data" era and the emergence of large scale neural recording systems such as that in my thesis work. Commercially, big data analytics seek to mine huge sets of user data to identify patterns and guide strategies to better target consumers. It remains to be seen how human neural data sets will be protected or utilized commercially in future years.

Ethical, safety, and functionality debates aside, brain-machine interface technologies provide a unique opportunity for restoring mobility and sensation to severely paralyzed patients. With new advances come new questions and it will remain critical that neuroengineers pursue the scientific goals with a clear picture of the ethical

implications. At present, the exciting opportunity to significantly improve quality of life in paralyzed individuals is already becoming a reality. With multidisciplinary BMI laboratories growing in number and quality worldwide, it can only be speculated what could be possible just 5, 10, or 30 years into the future. It is at this seminal moment in the BMI field's early history that I submit the work in this thesis, in that it may contribute towards greater scientific knowledge and engineering achievements.

Appendix A: Analytical and statistical methods

A.1 Methods in data analysis

A.1.1. Peri-event time histograms (PETHs):

Modulations in cortical neuronal activity were analyzed using peri-event time histograms (PETHs). Spike timestamps for each neuron were first put into 50 ms bins and the activity of each neuron was normalized by subtracting the mean bin count and dividing by the standard deviation, which is statistically equivalent to the z-score. This normalization transforms the activity of each neuron to represent modulations as the fraction of overall modulations. Single neuron PETHs were computed in terms of firing rate (Hz), however population analysis utilized the normalized mean firing rate to facilitate comparison between neurons with different baseline firing rates. After the normalized mean firing rate was computed for each neuron, event-related modulations were analyzed by constructing PETHs. Movement-related modulations were computed as the difference between normalized mean firing rate during the typical movement epoch (150-600ms post-stimulus) and normalized mean firing rate during the baseline epoch (600-100ms pre-stimulus). This represents a difference in z-scores and is referred to as Δz in the analysis of this study. I computed Δz on a single trial basis and fit multiple linear regression models to compute parameters of directional tuning:

$$\Delta z = A * L_x + B * L_y + C * R_x + D * R_y \qquad (1)$$

where (L_x, L_y) and $\left(R_x, R_y\right)$ are (x,y) positions of the left and right targets on each trial.

Coefficients A, B, C, and D were fit for each neuron with regression. Preferred direction of each hand for each neuron was computed using vectors $(\vec{A},\vec{B})$ and $(\vec{C},\vec{D})$.

A second metric based on Δz was used to evaluate depth of directional tuning. A mean Δz was computed for each neuron, for each direction. Tuning depth was measured as the standard deviation of the mean Δz distribution across different directions. Overall movement-related modulations were estimated as the mean of Δz absolute value.

For comparisons between unimanual and bimanual modulation, all data was collected within the same session. The bimanual and unimanual PETHs shown in Figs. 28-29 represent neural activity normalized by the same mean and standard deviation of that single session. Within unimanual trials, Eq.1 was modified to only compute coefficients reflecting modulations of the working arm.

A.1.2 Sliding window discrete predictions

A discrete classifier was used to make predictions of target location from both passive observation and BC without arms sessions. I used either linear discriminant analysis (LDA) or a k-nearest neighbor (k-NN) model with k=5 for these predictions. LDA is a method used to classify data by identifying linear combinations of variables which best explain, or discriminate the data into multiple classes of objects or events. k-NN is a non-parametric classification algorithm which searches nearest-neighbor data (from training data) within the feature space – in the case of neural predictions, this would be a space defined by binned firing rates of all the neurons. By searching for the

k-nearest neighbors to the test data, the algorithm can be made more robust. The classifications of each "neighbor" are counted as votes towards the prediction of the unknown sample class. Neural activity was binned into a single 250ms window during a specified epoch aligned on target onset. I then slid this window at 25 ms increments along the task interval from -0.5 to 0.75s and at each step, the LDA or k-NN model was fit with 75% of the session's trials and target location predictions were made on the remaining 25% of trials. Train and sample trials were randomly selected five-times and the resulting prediction performance in terms of fraction correct prediction was averaged.

A.1.3. Offline predictions of neural activity

Right and left arm kinematics were decoded using an unscented Kalman filter (UKF) as described elsewhere [150]. The same model was used for both offline and online predictions with 3 past taps and 2 future taps of 100 ms binned neural activity. During the first 11 sessions of BC with arms, a 1st order UKF was used with only a single past tap of neural activity (Fig. 39A, red circles). Later BC with arms sessions and all BC without arms sessions employed the 5th order UKF. These settings were determined empirically by offline comparison (Figs. 43-44), as well as from previous studies in our lab [129]. Offline predictions were computed for both active and passive observation experiments in a similar way. Offline, I used 6 minutes of neural data collected during attempted trials (for joystick control) or while attending to the screen (passive observation) to fit the UKF tuning model. For unimanual offline analysis, the 2D tuning

model fit binned neural activity as *y(t)* a function of single arm (x,y) position, velocity, and quadratic terms of both as in Eq. 2:

$$y(t) = \begin{bmatrix} b_1 & b_2 \end{bmatrix} \begin{bmatrix} pos_x(t) \\ pos_y(t) \end{bmatrix} + b_3 \sqrt{pos_x(t)^2 + pos_y(t)^2} + \begin{bmatrix} b_4 & b_5 \end{bmatrix} \begin{bmatrix} vel_x(t) \\ vel_y(t) \end{bmatrix} + b_3 \sqrt{vel_x(t)^2 + vel_y(t)^2} \quad (2)$$

For bimanual experiments, both joystick control and passive observation, a 4D extension was made to the quadratic tuning model of Eq. 4. More specifically, *y(t)* was now formulated as a function of bimanual (x,y) positions, velocities, and quadratic terms of each as in Eq. 3:

$$y(t) = \begin{bmatrix} b_1 & b_2 & b_3 & b_4 \end{bmatrix} \begin{bmatrix} pos_{xL}(t) \\ pos_{yL}(t) \\ pos_{xR}(t) \\ pos_{yR}(t) \end{bmatrix} + \begin{bmatrix} b_5 & b_6 \end{bmatrix} \begin{bmatrix} \sqrt{pos_{xL}(t)^2 + pos_{yL}(t)^2} \\ \sqrt{pos_{xR}(t)^2 + pos_{yR}(t)^2} \end{bmatrix} + \begin{bmatrix} b_7 & b_8 & b_9 & b_{10} \end{bmatrix} \begin{bmatrix} vel_{xL}(t) \\ vel_{yL}(t) \\ vel_{xR}(t) \\ vel_{yR}(t) \end{bmatrix} + \begin{bmatrix} b_{11} & b_{12} \end{bmatrix} \begin{bmatrix} \sqrt{vel_{xL}(t)^2 + vel_{yL}(t)^2} \\ \sqrt{vel_{xR}(t)^2 + vel_{yR}(t)^2} \end{bmatrix} \quad (3)$$

I performed several preliminary analyses to optimize the amount of training data required for each model and generally found that 5-7 minutes was sufficient and beyond this yielded marginal improvements. Prediction performance was measured using correlation coefficient *r*. For each analysis, *r* was computed 5 times per data point and averaged, using a *k*-fold cross-validation technique. As such, I report prediction *r* as a distribution (mean±standard error) rather than a single point. I opted to use *r* as the metric for prediction accuracy due to its common usage in other BMI studies. Offline

predictions using EMG activity were performed using a similar procedure. Eight EMG voltage channels were each resampled at 10 Hz – the same rate as utilized for neural decoding. All other decoding steps and models (Eq. 3) were equivalent for the two methods.

A.1.4 Neuron dropping curves

In addition to computing *r* using all recorded neurons, I computed random neuron dropping curves to evaluate the functional effect of number of recorded neurons on offline prediction performance. This analysis was conducted separately for unimanual and bimanual conditions, although the amount of training data was enforced to be equal for both analyses. For each neuron dropping curve, the number of neurons was increased at fixed intervals. At each neuronal quantity, *n* randomly selected neurons were used to both train the model and make predictions of bimanual kinematics on a separate block of test data. This procedure was repeated 5 times at each step, each time a random subset of neurons was selected and a different block of the session was designated as training data in order to cross-validate the results. In addition, neuron dropping curves were computed both overall and by cortical area (Figs. 37A-D, 39D).

A.1.5. Neural correlation analyses

An additional neurophysiological analysis used during passive observation and brain control experiments was neuronal spike count correlation. Binned (25 ms bin size)

neuron activity patterns of single neurons of full experiments (not single trials, as in PETH analysis) were compared against the activity profiles of all other neurons in the population in a pairwise fashion. The comparison between neuron activity profiles was quantified as the Pearson's correlation coefficient *r* between equal length time series a and b as in Eq. 4:

$$r(a,b) = corr(a,b) = \frac{\sum_{i=1}^{n}(a_i - \bar{a})(b_i - \bar{b})}{\sqrt{\sum_{i=1}^{n}(a_i - \bar{a})^2}\sqrt{\sum_{i=1}^{n}(b_i - \bar{b})^2}} \quad (4)$$

where n is the length of a and b. Spike count correlation was quantified as the mean *r* of all pairwise comparisons, quantified as in Eq. 5:

$$\bar{r} = mean(\forall n_i \in \Psi, \forall n_j \in \Psi, corr(n_i, n_j)) \quad (5)$$

where Ψ is the ensemble of all recorded neurons and $corr(n_i, n_j)$ defined in Eq. 4. I extended this analysis to identify correlations within a cortical area (e.g. an M1 neuron correlated with another M1 neuron) as well as between areas (e.g. M1 neuron and SMA neuron) as well as intra-hemisphere vs. inter-hemisphere. Only cortical activity during periods of the session when the monkey was attending to the screen was used for spike count correlation comparisons.

A.2. Statistical analyses

Several statistical methods were used in this study to validate the results I obtained. I used a t-test (α=0.05) for parametric tests and the Wilcoxon signed rank test (α=0.05) or Wilcoxon rank sum test (α=0.05) for nonparametric tests when data was not

drawn from a normal distribution. Both 1-way and 2-way ANOVA tests (α=0.05) were utilized in the statistical analysis of correlated neural activity of Fig. 42. LDA or k-NN classifier performance was measured as fraction correct prediction. In this analysis, chance level performance was ¼. The 95% C.I. was constructed using the 1-proportion z-test (Eq. 6):

$$z = \frac{\hat{p} - p_0}{\sqrt{p_0(1-p_0)}}\sqrt{n} \qquad (6)$$

where n is the number of trials used for test data and $p_0 = 0.25$. Offline predictions of cursor X and Y position were compared with actual cursor positions using Pearson's product-moment correlation coefficient *r*. To generate a distribution of *r*, the prediction was repeated 5 times using the k-fold cross-validation technique, with each iteration using a different block of data for training and test data.

Appendix B: Algorithm for detection of movement onset (Matlab code)

```
function [mov_onset, do_not_use] = get_mvmtonset(trial_beg, timevect,
xprime, threshold)

% [MOV_ONSET, DO_NOT_USE] = GET_MVMTONSET(TRIAL_BEG, TIMEVECT, XPRIME,
THRESHOLD)

%  INPUTS:
%  trial_beg:  The beginning of the trial, or the first time you
%               want to start looking. Typically use target
%               appearance
%  timevect:   Vector of the times, during the trial, often
%              stored in trial(i).cursor(1,:)
%  xprime:     This is x' position where x' is the axis between
%               the center and the intended target. This requires
%               you to do a rotation matrix on x towards the
%               location of the target
%  threshold:  Parameter that determines how sensitive you want
%               to detection to be, the fraction of some parameter
%               that you want to trigger the identification of
%               movement. Recommended: 0.25
%  OUTPUTS:
%  mov_onset:  This is the time of movement onset
%  do_not_use: Flags the trial as being very unusual.  The methods of
                this algorithm were not able to easily detect the
                movement onset.
%  OVERVIEW:
%               Each function call, this list will be executed
%                sequentially until a satisfactory result is
%                 reached.
%          1) First simultaneous time where both vel and accel
%                suprathreshold
%          2) First time of velocity suprathreshold
%          3) First time of acceleration suprathreshold
%          4) First time of position suprathreshold
%          5) Identification as an unusable trial

dz_dt = diff(xprime);
D2z = diff(dz_dt);

B = findClosest(timevect, trial_beg);

first_t = true;
%FIRST CHECKS FOR SIMULTANEOUS THRESHOLD CROSSING FOR BOTH VELOCITY AND
ACCELERATION
for q=B:(length(xprime)-2)
    if (dz_dt(q)> threshold*max(dz_dt)) && (D2z(q) >
threshold*max(D2z)) && (first_t == true)
        mov_onset = timevect(1,q);
        first_t = false;
        do_not_use = false;
```

```
    end
end

if(first_t == true)
%IF FIRST OCCURANCE NOT FOUND, THEN LOOKS FOR FIRST INSTANCE OF
VELOCITY OVER SOME THRESHOLD
    for q=B:(length(xprime)-2)
        if (dz_dt(q)> threshold*max(dz_dt)) && (first_t == true)
            mov_onset = timevect(1,q);
            first_t = false;
            do_not_use = false;
        end
    end
end

if(first_t == true)
% IF NOT FOUND YET, IDENTIFIES MVMT ONSET AS THE TIME OF ACCELERATION
CROSSING SOME THRESHOLD
    for q=B:(length(xprime)-10)
        if (D2z(q)> threshold*max(D2z)) && (first_t == true)
            mov_onset = timevect(1,q);
            first_t = false;
            do_not_use = false;
        end
    end
end

if(first_t == true)
% IF STILL NOT FOUND, MOVEMENT ONSET THE TIME WHEN POSITION REACHES 10%
OF ITS FINAL AMPLITUDE
    for q=B:(length(xprime))
        if(xprime(q) > 0.1*max(xprime))&& (first_t == true)
            mov_onset = timevect(1,q);
            first_t = false;
            do_not_use = false;
        end
    end
end

if(first_t == true)
%IF NONE OF THE ABOVE METHODS WORK, JUST OUTPUTS DO_NOT_USE = TRUE
    do_not_use = true;
    mov_onset = trial_beg;
end
```

Appendix C: Switching model algorithm (Matlab code)

C.1 Main function

```
%% MAIN FUNCTION
% select epochs with both uni and bimanual trials

train_sz = 3000;  % 5 mins of training data for each
tbins = 3;        % Each 100 ms
group = [ones(3000,1); 2*ones(3000,1); 3*ones(3000,1)];

% Unimanual L
rz=1:length(v2_L);
tr_ixL = v2_L(rz(1:train_sz));        %selects training data
te_ixL = v2_L(rz(train_sz+1:end));    %selects test data
clear rz

% Unimanual R
rz=1:length(v2_R);
tr_ixR = v2_R(rz(1:train_sz));         %selects training data
te_ixR = v2_R(rz(train_sz+1:end));     %selects test data
clear rz

% BIMANUAL
st = 1;
rz = 1:length(v2_B);
tr_ixB = v2_B(rz(st:train_sz+st-1));
te_ixB = v2_B(rz([1:st-1 train_sz+st:length(v2_B)]));
clear rz

% BUILD MATRIX WITH TRAINING DATA
rw=1;
for i=[tr_ixL tr_ixR tr_ixB]
    training(rw,:) = mean(binned_spk(i-tbins+1:i,:));
    rw=rw+1;
end

% BUILD MATRIX FOR TEST (SAMPLE) DATA
rw=1;
for i=[te_ixL te_ixR te_ixB]
    sample(rw,:) = mean(binned_spk(i-tbins+1:i,:));
    rw=rw+1;
end

truth = [ones(length(te_ixL),1); 2*ones(length(te_ixR),1);
         3*ones(length(te_ixB),1)];

% CLASSIFY STEP
guesses = knnclassify(sample,training,group,3);  % k=3
true_states = truth;
guess_times = [te_ixL te_ixR te_ixB]; %"times" = time step number

FC = fc(guesses,truth);   % Fraction correct prediction of state
```

```
%% UKF setup step
FTAPS = 2;     % 2 future taps
PTAPS = 3;     % 3 past taps
MTAPS = 1;     % 1 movement tap

%% Population predictions
FRACT_FIT = 0.8;

% TRUE X, Y, VELOCITY X, VELOCITY Y
X=[xL(:,1:2) xR(:,1:2) xL(:,3:4) xR(:,3:4)];

XL_train = nan(size(xL));
XL_train(tr_ixL,:) = xL(tr_ixL,:);    % LEFT X AND Y

XR_train = nan(size(xR));
XR_train(tr_ixR,:) = xR(tr_ixR,:);    % RIGHT X AND Y

XB_train = nan(size(X));
XB_train(tr_ixB,:) = X(tr_ixB,:);     % BIMANUAL X AND Y

[v2, ind] = sort([te_ixL te_ixR te_ixB],'ascend');
truth = X(v2,:);

guesses_ordered = guesses(ind);
true_st_ordered = true_states(ind);

% 2D TUNING MODEL
f2=@(a,b) [a(1:2,:); sqrt(sum(a(1:2,:).^2)); a(3:4,:);
sqrt(sum(a(3:4,:).^2))];

% 4D TUNING MODEL
f4=@(a,b) [a(1:4,:);
    sqrt(sum(a(1:2,:).^2));
    sqrt(sum(a(3:4,:).^2));
    a(5:8,:);
    sqrt(sum(a(5:6,:).^2));
    sqrt(sum(a(7:8,:).^2))];

%FITTING UKF FOR EACH OF THREE BEHAVIORAL STATES
woutB = fit_ar_ukf_rrcv(XB_train, binned_spk, f4, [], FTAPS,
        PTAPS, MTAPS);
woutL = fit_ar_ukf_rrcv(XL_train, binned_spk, f2, [], FTAPS,
        PTAPS, MTAPS);
woutR = fit_ar_ukf_rrcv(XR_train, binned_spk, f2, [], FTAPS,
        PTAPS, MTAPS);

%PREDICTIONS
P = {woutL, woutR, woutB};

% Switching model
[pout, pout2] = ar_ukf_sm(binned_spk(v2,:),P,guesses_ordered,
true_st_ordered);
```

```
% Regular UKF models
pout_noswitch = ar_ukf(binned_spk(v2,:),woutB);
poutL_noswitch = ar_ukf(binned_spk(v2,:),woutL);
poutR_noswitch = ar_ukf(binned_spk(v2,:),woutR);
```

C.2 Function to coordinate switching protocol

```
function [predicted, predicted2]=ar_ukf_sm(y, params, mod_info,
mod_info_true)

% Unscented Kalman filter using any linear model with
%      autoregressive F in transition model
% The linear model can have arbitrary pre-processing

% y is neural data matrix (time x neurons)
% params are fit by the different AR UKF models
% mod info is the indicates the model to be used for each
%       row (time step) of y
% For every different number in mod_info, there will be a
      different model

nmods = length(params);

n = findDiffvals(mod_info);

if(n>nmods)
    error('More models requested than parameters provided')
elseif(n< nmods)
     warning('Not all models used. More params provided than
             needed')
end

PTAPS = params{1}.ptaps;

poutL = ar_ukf(y,params{1});
poutR = ar_ukf(y,params[288]);
poutB = ar_ukf(y,params{3});

%LEFT
x1pU = poutL(:,4*(PTAPS-1)+1);
y1pU = poutL(:,4*(PTAPS-1)+2);

%RIGHT
x2pU = poutR(:,4*(PTAPS-1)+1);
y2pU = poutR(:,4*(PTAPS-1)+2);

%BIMANUAL
x1pB = poutB(:,8*(PTAPS-1)+1);
y1pB = poutB(:,8*(PTAPS-1)+2);
x2pB = poutB(:,8*(PTAPS-1)+3);
y2pB = poutB(:,8*(PTAPS-1)+4);
```

```
test_len = rows(y);

predicted = zeros(test_len,4);
predicted2 = zeros(test_len,4);

for t=1:test_len
    gState = mod_info(t); % guessed state

    switch(gState)
        case(1) %LEFT
            predicted(t,1:2) = [x1pU(t) y1pU(t)];
            if(t>1)
                predicted(t,3:4) = predicted(t-1,3:4);
            else
                %leave at (0,0)
            end
        case(2) %RIGHT
            predicted(t,3:4) = [x2pU(t) y2pU(t)];
            if(t>1)
                predicted(t,1:2) = predicted(t-1,1:2);
            else
                %leave at (0,0)
            end
        case(3) %BIMANUAL
            predicted(t,1:4) = [x1pB(t) y1pB(t) x2pB(t) y2pB(t)];
    end

    if(nargin == 4) % a second model-reference is provided
        aState = mod_info_true(t); % actual state
        switch(aState)
            case(1) %LEFT
                predicted2(t,1:2) = [x1pU(t) y1pU(t)];
                if(t>1)
                    predicted2(t,3:4) = predicted2(t-1,3:4);
                else
                    %leave at (0,0)
                end
            case(2) %RIGHT
                predicted2(t,3:4) = [x2pU(t) y2pU(t)];
                if(t>1)
                    predicted2(t,1:2) = predicted2(t-1,1:2);
                else
                    %leave at (0,0)
                end
            case(3) %BIMANUAL
                predicted2(t,1:4) = [x1pB(t) y1pB(t) x2pB(t)
y2pB(t)];
        end
    end

end
```

Appendix D: Videos from bimanual BMI experiments

D.1 Screen capture of bimanual center out joystick control trials

Several trials of bimanual reaches using joysticks to control the two avatar arms are shown. From [242]. Reproduced with permission from AAAS.

D.2 Video of monkey performing bimanual joystick control trials using two joysticks

This video shows a side angle of the experimental setup where the arms of the monkey can be seen moving both joysticks in order to accurately control the avatar arms. Audible clicking sound is the juice reward dispensation following a correct trial. From [242]. Reproduced with permission from AAAS.

D.3 Video of monkey performing bimanual BC with arms

Similar to joystick control setup except that the movement of avatar arms now under control of neural decoder rather than joysticks. Monkey arms are unrestrained and visible in the video. Audible clicking sound is the juice reward dispensation following a correct trial. From [242]. Reproduced with permission from AAAS.

D.4 Screen capture of bimanual BC without arms

Several trials of bimanual reaches enacted under full brain control while both arms are fully restrained in the experimental setup. From [242]. Reproduced with permission from AAAS.

References

1. Kaas, J.H., *Evolution of somatosensory and motor cortex in primates.* Anat Rec A Discov Mol Cell Evol Biol, 2004. **281**(1): p. 1148-56.

2. DeVivo, M.J., *Causes and costs of spinal cord injury in the United States.* Spinal Cord, 1997. **35**(12): p. 809-13.

3. Bergman, H., et al., *Physiological aspects of information processing in the basal ganglia of normal and parkinsonian primates.* Trends Neurosci, 1998. **21**(1): p. 32-8.

4. Bastian, A.J., et al., *Cerebellar ataxia: abnormal control of interaction torques across multiple joints.* J Neurophysiol, 1996. **76**(1): p. 492-509.

5. Fu, Q.G., et al., *Temporal encoding of movement kinematics in the discharge of primate primary motor and premotor neurons.* J Neurophysiol, 1995. **73**(2): p. 836-54.

6. Georgopoulos, A.P., A.B. Schwartz, and R.E. Kettner, *Neuronal population coding of movement direction.* Science, 1986. **233**(4771): p. 1416-9.

7. Evarts, E.V., *Activity of pyramidal tract neurons during postural fixation.* J Neurophysiol, 1969. **32**(3): p. 375-85.

8. Kalaska, J.F. and D.J. Crammond, *Cerebral cortical mechanisms of reaching movements.* Science, 1992. **255**(5051): p. 1517-23.

9. Fritsch, G. and E. Hitzig, *Über die elektrische Erregbarkeit des Grosshirns.* Arch Anat Physiol Med Wiss., 1870. **1870**: p. 300-332.

10. Fritsch, G. and E. Hitzig, *The electrical excitability of the cerebrum, in Neurosurgical Classic XII, translated by Wilkins RH.* Journal of Neurosurgery, 1963. **20**: p. 904-916.

11. Scott, S.H., *The role of primary motor cortex in goal-directed movements: insights from neurophysiological studies on non-human primates.* Curr Opin Neurobiol, 2003. **13**(6): p. 671-7.

12. Kurtzer, I. and S.H. Scott, *A multi-level approach to understanding upper limb function.* Prog Brain Res, 2007. **165**: p. 347-62.

13. Scott, S.H., *Inconvenient truths about neural processing in primary motor cortex.* J Physiol, 2008. **586**(5): p. 1217-24.

14. Donoghue, J.P. and J.N. Sanes, *Motor areas of the cerebral cortex.* J Clin Neurophysiol, 1994. **11**(4): p. 382-96.

15. Crammond, D.J. and J.F. Kalaska, *Modulation of preparatory neuronal activity in dorsal premotor cortex due to stimulus-response compatibility.* J Neurophysiol, 1994. **71**(3): p. 1281-4.

16. Romo, R. and W. Schultz, *Neuronal activity preceding self-initiated or externally timed arm movements in area 6 of monkey cortex.* Exp Brain Res, 1987. **67**(3): p. 656-62.

17. Georgopoulos, A.P., *Cortical mechanisms subserving reaching.* Ciba Found Symp, 1987. **132**: p. 125-41.

18. Hoshi, E., K. Shima, and J. Tanji, *Task-dependent selectivity of movement-related neuronal activity in the primate prefrontal cortex.* J Neurophysiol, 1998. **80**(6): p. 3392-7.

19. Kandel, E.R., J.H. Schwartz, and T.M. Jessell, *Principles of neural science*. 4th ed. 2000, New York: McGraw-Hill, Health Professions Division. xli, 1414 p.

20. Jones, E.G., et al., *Cells of origin and terminal distribution of corticostriatal fibers arising in the sensory-motor cortex of monkeys.* J Comp Neurol, 1977. **173**(1): p. 53-80.

21. Kultas-Ilinsky, K., E. Sivan-Loukianova, and I.A. Ilinsky, *Reevaluation of the primary motor cortex connections with the thalamus in primates.* J Comp Neurol, 2003. **457**(2): p. 133-58.

22. Li, X.G., S.L. Florence, and J.H. Kaas, *Areal distributions of cortical neurons projecting to different levels of the caudal brain stem and spinal cord in rats.* Somatosens Mot Res, 1990. **7**(3): p. 315-35.

23. Lebedev, M.A. and S.P. Wise, *Tuning for the orientation of spatial attention in dorsal premotor cortex.* Eur J Neurosci, 2001. **13**(5): p. 1002-8.

24. Lebedev, M.A. and S.P. Wise, *Insights into seeing and grasping: distinguishing the neural correlates of perception and action.* Behav Cogn Neurosci Rev, 2002. **1**(2): p. 108-29.

25. Kaufman, M.T., et al., *Roles of monkey premotor neuron classes in movement preparation and execution.* J Neurophysiol, 2010. **104**(2): p. 799-810.

26. Kettner, R.E., J.K. Marcario, and M.C. Clark-Phelps, *Control of remembered reaching sequences in monkey. I. Activity during movement in motor and premotor cortex.* Exp Brain Res, 1996. **112**(3): p. 335-46.

27. Kettner, R.E., J.K. Marcario, and N.L. Port, *Control of remembered reaching sequences in monkey. II. Storage and preparation before movement in motor and premotor cortex.* Exp Brain Res, 1996. **112**(3): p. 347-58.

28. Cisek, P. and J.F. Kalaska, *Neural correlates of reaching decisions in dorsal premotor cortex: specification of multiple direction choices and final selection of action.* Neuron, 2005. **45**(5): p. 801-14.

29. Hanakawa, T., *Rostral premotor cortex as a gateway between motor and cognitive networks.* Neurosci Res, 2011. **70**(2): p. 144-54.

30. Wise, S.P., G. di Pellegrino, and D. Boussaoud, *The premotor cortex and nonstandard sensorimotor mapping.* Can J Physiol Pharmacol, 1996. **74**(4): p. 469-82.

31. Nakayama, Y., et al., *Transformation of a virtual action plan into a motor plan in the premotor cortex.* J Neurosci, 2008. **28**(41): p. 10287-97.

32. Tanji, J. and K. Shima, *Role for supplementary motor area cells in planning several movements ahead.* Nature, 1994. **371**(6496): p. 413-6.

33. Hoffstaedter, F., et al., *The "What" and "When" of Self-Initiated Movements.* Cereb Cortex, 2012.

34. Tankus, A., et al., *Encoding of speed and direction of movement in the human supplementary motor area.* J Neurosurg, 2009. **110**(6): p. 1304-16.

35. Dum, R.P. and P.L. Strick, *The origin of corticospinal projections from the premotor areas in the frontal lobe.* J Neurosci, 1991. **11**(3): p. 667-89.

36. Scherberger, H. and R.A. Andersen, *Target selection signals for arm reaching in the posterior parietal cortex.* J Neurosci, 2007. **27**(8): p. 2001-12.

37. Cui, H. and R.A. Andersen, *Posterior parietal cortex encodes autonomously selected motor plans.* Neuron, 2007. **56**(3): p. 552-9.

38. Kalaska, J.F., *From intention to action: motor cortex and the control of reaching movements.* Adv Exp Med Biol, 2009. **629**: p. 139-78.

39. Lacquaniti, F., *Central representations of human limb movement as revealed by studies of drawing and handwriting.* Trends Neurosci, 1989. **12**(8): p. 287-91.

40. Sergio, L.E., C. Hamel-Paquet, and J.F. Kalaska, *Motor cortex neural correlates of output kinematics and kinetics during isometric-force and arm-reaching tasks.* J Neurophysiol, 2005. **94**(4): p. 2353-78.

41. Boline, J. and J. Ashe, *On the relations between single cell activity in the motor cortex and the direction and magnitude of three-dimensional dynamic isometric force.* Exp Brain Res, 2005. **167**(2): p. 148-59.

42. Xing, J. and R.A. Andersen, *Models of the posterior parietal cortex which perform multimodal integration and represent space in several coordinate frames.* J Cogn Neurosci, 2000. **12**(4): p. 601-14.

43. Feldman, A.G., *Once more on the equilibrium-point hypothesis (lambda model) for motor control.* J Mot Behav, 1986. **18**(1): p. 17-54.

44. Adamovich, S.V., M.F. Levin, and A.G. Feldman, *Central modifications of reflex parameters may underlie the fastest arm movements.* J Neurophysiol, 1997. **77**(3): p. 1460-9.

45. Levin, M.F. and A.G. Feldman, *The role of stretch reflex threshold regulation in normal and impaired motor control.* Brain Res, 1994. **657**(1-2): p. 23-30.

46. Bernshteĭn, N.A., *The co-ordination and regulation of movements*. 1st English ed. 1967, Oxford, New York,: Pergamon Press. xii, 196 p.

47. Latash, M.L., et al., *Postural synergies and their development.* Neural Plast, 2005. **12**(2-3): p. 119-30; discussion 263-72.

48. Tresch, M.C. and A. Jarc, *The case for and against muscle synergies.* Curr Opin Neurobiol, 2009. **19**(6): p. 601-7.

49. Ting, L.H. and J.M. Macpherson, *A limited set of muscle synergies for force control during a postural task.* J Neurophysiol, 2005. **93**(1): p. 609-13.

50. d'Avella, A., P. Saltiel, and E. Bizzi, *Combinations of muscle synergies in the construction of a natural motor behavior.* Nat Neurosci, 2003. **6**(3): p. 300-8.

51. d'Avella, A. and E. Bizzi, *Shared and specific muscle synergies in natural motor behaviors.* Proc Natl Acad Sci U S A, 2005. **102**(8): p. 3076-81.

52. Latash, M.L. and J.G. Anson, *Synergies in health and disease: relations to adaptive changes in motor coordination.* Phys Ther, 2006. **86**(8): p. 1151-60.

53. Scholz, J.P. and G. Schoner, *The uncontrolled manifold concept: identifying control variables for a functional task.* Exp Brain Res, 1999. **126**(3): p. 289-306.

54. Georgopoulos, A.P., et al., *On the relations between the direction of two-dimensional arm movements and cell discharge in primate motor cortex.* J Neurosci, 1982. **2**(11): p. 1527-37.

55. Ashe, J. and A.P. Georgopoulos, *Movement parameters and neural activity in motor cortex and area 5.* Cereb Cortex, 1994. **4**(6): p. 590-600.

56. Moran, D.W. and A.B. Schwartz, *Motor cortical representation of speed and direction during reaching.* J Neurophysiol, 1999. **82**(5): p. 2676-92.

57. Roitman, J.D. and M.N. Shadlen, *Response of neurons in the lateral intraparietal area during a combined visual discrimination reaction time task.* J Neurosci, 2002. **22**(21): p. 9475-89.

58. Churchland, A.K., R. Kiani, and M.N. Shadlen, *Decision-making with multiple alternatives.* Nat Neurosci, 2008. **11**(6): p. 693-702.

59. Pardo-Vazquez, J.L., V. Leboran, and C. Acuna, *Neural correlates of decisions and their outcomes in the ventral premotor cortex.* J Neurosci, 2008. **28**(47): p. 12396-408.

60. Andersen, R.A., et al., *Corticocortical connections of anatomically and physiologically defined subdivisions within the inferior parietal lobule.* J Comp Neurol, 1990. **296**(1): p. 65-113.

61. Blatt, G.J., R.A. Andersen, and G.R. Stoner, *Visual receptive field organization and cortico-cortical connections of the lateral intraparietal area (area LIP) in the macaque.* J Comp Neurol, 1990. **299**(4): p. 421-45.

62. Pesaran, B., M.J. Nelson, and R.A. Andersen, *Free choice activates a decision circuit between frontal and parietal cortex.* Nature, 2008. **453**(7193): p. 406-9.

63. Andersen, R.A., E.J. Hwang, and G.H. Mulliken, *Cognitive neural prosthetics.* Annu Rev Psychol, 2010. **61**: p. 169-90, C1-3.

64. Musallam, S., et al., *Cognitive control signals for neural prosthetics.* Science, 2004. **305**(5681): p. 258-62.

65. Andersen, R.A., et al., *Cognitive neural prosthetics.* Trends Cogn Sci, 2004. **8**(11): p. 486-93.

66. Vega-Gonzalez, A., B.J. Bain, and M.H. Granat, *Measuring continuous real-world upper-limb activity.* Conf Proc IEEE Eng Med Biol Soc, 2005. **4**: p. 3542-5.

67. Gerloff, C. and F.G. Andres, *Bimanual coordination and interhemispheric interaction.* Acta Psychol (Amst), 2002. **110**(2-3): p. 161-86.

68. Geffen, G.M., D.L. Jones, and L.B. Geffen, *Interhemispheric control of manual motor activity.* Behav Brain Res, 1994. **64**(1-2): p. 131-40.

69. Jeeves, M.A., P.H. Silver, and I. Jacobson, *Bimanual co-ordination in callosal agenesis and partial commissurotomy.* Neuropsychologia, 1988. **26**(6): p. 833-50.

70. Tuller, B. and J.A. Kelso, *Environmentally-specified patterns of movement coordination in normal and split-brain subjects.* Exp Brain Res, 1989. **75**(2): p. 306-16.

71. Grillner, S., *Neurobiological bases of rhythmic motor acts in vertebrates.* Science, 1985. **228**(4696): p. 143-9.

72. Donchin, O., S.C. de Oliveira, and E. Vaadia, *Who tells one hand what the other is doing: the neurophysiology of bimanual movements.* Neuron, 1999. **23**(1): p. 15-8.

73. Tanji, J., K. Okano, and K.C. Sato, *Neuronal activity in cortical motor areas related to ipsilateral, contralateral, and bilateral digit movements of the monkey.* J Neurophysiol, 1988. **60**(1): p. 325-43.

74. Viviani, P., et al., *Hemispheric asymmetries and bimanual asynchrony in left- and right-handers.* Exp Brain Res, 1998. **120**(4): p. 531-6.

75. Lang, W., et al., *Negative cortical DC shifts preceding and accompanying simultaneous and sequential finger movements.* Exp Brain Res, 1988. **71**(3): p. 579-87.

76. Donchin, O., et al., *Single-unit activity related to bimanual arm movements in the primary and supplementary motor cortices.* J Neurophysiol, 2002. **88**(6): p. 3498-517.

77. Donchin, O., et al., *Primary motor cortex is involved in bimanual coordination.* Nature, 1998. **395**(6699): p. 274-8.

78. Rokni, U., et al., *Cortical representation of bimanual movements.* J Neurosci, 2003. **23**(37): p. 11577-86.

79. Gribova, A., et al., *Timing of bimanual movements in human and non-human primates in relation to neuronal activity in primary motor cortex and supplementary motor area.* Exp Brain Res, 2002. **146**(3): p. 322-35.

80. Steinberg, O., et al., *Neuronal populations in primary motor cortex encode bimanual arm movements.* Eur J Neurosci, 2002. **15**(8): p. 1371-80.

81. Rouiller, E.M., et al., *Transcallosal connections of the distal forelimb representations of the primary and supplementary motor cortical areas in macaque monkeys.* Exp Brain Res, 1994. **102**(2): p. 227-43.

82. Liu, J., et al., *Origins of callosal projections to the supplementary motor area (SMA): a direct comparison between pre-SMA and SMA-proper in macaque monkeys.* J Comp Neurol, 2002. **443**(1): p. 71-85.

83. Ganguly, K., et al., *Cortical representation of ipsilateral arm movements in monkey and man.* J Neurosci, 2009. **29**(41): p. 12948-56.

84. Paddock, C. (2009) *Paralysis affects more Americans than previously thought*. Medical news today.

85. Dobkin, B.H. and L.A. Havton, *Basic advances and new avenues in therapy of spinal cord injury.* Annu Rev Med, 2004. **55**: p. 255-82.

86. Fouad, K. and K. Pearson, *Restoring walking after spinal cord injury.* Prog Neurobiol, 2004. **73**(2): p. 107-26.

87. Lebedev, M.A. and M.A. Nicolelis, *Toward a whole-body neuroprosthetic.* Prog Brain Res, 2011. **194**: p. 47-60.

88. Lebedev, M.A. and M.A. Nicolelis, *Brain-machine interfaces: past, present and future.* Trends Neurosci, 2006. **29**(9): p. 536-46.

89. Green, A.M. and J.F. Kalaska, *Learning to move machines with the mind.* Trends Neurosci, 2011. **34**(2): p. 61-75.

90. McFarland, D.J., et al., *The P300-based brain-computer interface (BCI): effects of stimulus rate.* Clin Neurophysiol, 2011. **122**(4): p. 731-7.

91. Leuthardt, E.C., et al., *A brain-computer interface using electrocorticographic signals in humans.* J Neural Eng, 2004. **1**(2): p. 63-71.

92. Nicolelis, M.A., et al., *Chronic, multisite, multielectrode recordings in macaque monkeys.* Proc Natl Acad Sci U S A, 2003. **100**(19): p. 11041-6.

93. Mak, J.N., et al., *EEG correlates of P300-based brain-computer interface (BCI) performance in people with amyotrophic lateral sclerosis.* J Neural Eng, 2012. **9**(2): p. 026014.

94. Long, J., et al., *Target selection with hybrid feature for BCI-based 2-D cursor control.* IEEE Trans Biomed Eng, 2012. **59**(1): p. 132-40.

95. Li, Y., et al., *A hybrid BCI system for 2-D asynchronous cursor control.* Conf Proc IEEE Eng Med Biol Soc, 2010. **2010**: p. 4205-8.

96. Kubler, A., et al., *A brain-computer interface controlled auditory event-related potential (p300) spelling system for locked-in patients.* Ann N Y Acad Sci, 2009. **1157**: p. 90-100.

97. Farwell, L.A. and E. Donchin, *Talking off the top of your head: toward a mental prosthesis utilizing event-related brain potentials.* Electroencephalogr Clin Neurophysiol, 1988. **70**(6): p. 510-23.

98. Miller, K.J., *Broadband spectral change: evidence for a macroscale correlate of population firing rate?* J Neurosci, 2010. **30**(19): p. 6477-9.

99. Felton, E.A., et al., *Electrocorticographically controlled brain-computer interfaces using motor and sensory imagery in patients with temporary subdural electrode implants. Report of four cases.* J Neurosurg, 2007. **106**(3): p. 495-500.

100. Chao, Z.C., Y. Nagasaka, and N. Fujii, *Long-term asynchronous decoding of arm motion using electrocorticographic signals in monkeys.* Front Neuroeng, 2010. **3**: p. 3.

101. Mountcastle, V.B., *Modality and topographic properties of single neurons of cat's somatic sensory cortex.* J Neurophysiol, 1957. **20**(4): p. 408-34.

102. Rall, W., *Electrophysiology of a dendritic neuron model.* Biophys J, 1962. **2**(2 Pt 2): p. 145-67.

103. Fetz, E.E., *Operant conditioning of cortical unit activity.* Science, 1969. **163**(3870): p. 955-8.

104. Fetz, E.E. and M.A. Baker, *Operantly conditioned patterns on precentral unit activity and correlated responses in adjacent cells and contralateral muscles.* J Neurophysiol, 1973. **36**(2): p. 179-204.

105. Fetz, E.E. and D.V. Finocchio, *Operant conditioning of isolated activity in specific muscles and precentral cells.* Brain Res, 1972. **40**(1): p. 19-23.

106. Fetz, E.E. and D.V. Finocchio, *Operant conditioning of specific patterns of neural and muscular activity.* Science, 1971. **174**(4007): p. 431-5.

107. Schmidt, E.M., *Single neuron recording from motor cortex as a possible source of signals for control of external devices.* Ann Biomed Eng, 1980. **8**(4-6): p. 339-49.

108. Jones, K.E., P.K. Campbell, and R.A. Normann, *A glass/silicon composite intracortical electrode array.* Ann Biomed Eng, 1992. **20**(4): p. 423-37.

109. Nordhausen, C.T., P.J. Rousche, and R.A. Normann, *Optimizing recording capabilities of the Utah Intracortical Electrode Array.* Brain Res, 1994. **637**(1-2): p. 27-36.

110. Bansal, A.K., et al., *Decoding 3D reach and grasp from hybrid signals in motor and premotor cortices: spikes, multiunit activity, and local field potentials.* J Neurophysiol, 2012. **107**(5): p. 1337-55.

111. Hochberg, L.R., et al., *Reach and grasp by people with tetraplegia using a neurally controlled robotic arm.* Nature, 2012. **485**(7398): p. 372-5.

112. Nicolelis, M.A., et al., *Sensorimotor encoding by synchronous neural ensemble activity at multiple levels of the somatosensory system.* Science, 1995. **268**(5215): p. 1353-8.

113. Chapin, J.K., et al., *Real-time control of a robot arm using simultaneously recorded neurons in the motor cortex.* Nat Neurosci, 1999. **2**(7): p. 664-70.

114. Wessberg, J., et al., *Real-time prediction of hand trajectory by ensembles of cortical neurons in primates.* Nature, 2000. **408**(6810): p. 361-5.

115. Serruya, M.D., et al., *Instant neural control of a movement signal.* Nature, 2002. **416**(6877): p. 141-2.

116. Taylor, D.M., S.I. Tillery, and A.B. Schwartz, *Direct cortical control of 3D neuroprosthetic devices.* Science, 2002. **296**(5574): p. 1829-32.

117. Vetter, R.J., et al., *Chronic neural recording using silicon-substrate microelectrode arrays implanted in cerebral cortex.* IEEE Trans Biomed Eng, 2004. **51**(6): p. 896-904.

118. Oliveira, L.M.O. and D. Dimitrov, *Surgical Techniques for Chronic Implantation of Microwire Arrays in Rodents and Primates*, in *Methods for Neural Ensemble Recordings*, M.A.L. Nicolelis, Editor. 2008: Boca Raton (FL).

119. Bjornsson, C.S., et al., *Effects of insertion conditions on tissue strain and vascular damage during neuroprosthetic device insertion.* J Neural Eng, 2006. **3**(3): p. 196-207.

120. Polikov, V.S., P.A. Tresco, and W.M. Reichert, *Response of brain tissue to chronically implanted neural electrodes.* J Neurosci Methods, 2005. **148**(1): p. 1-18.

121. Landis, D.M., *The early reactions of non-neuronal cells to brain injury.* Annu Rev Neurosci, 1994. **17**: p. 133-51.

122. Kipke, D.R., et al., *Silicon-substrate intracortical microelectrode arrays for long-term recording of neuronal spike activity in cerebral cortex.* IEEE Trans Neural Syst Rehabil Eng, 2003. **11**(2): p. 151-5.

123. Bai, Q. and K.D. Wise, *Single-unit neural recording with active microelectrode arrays.* IEEE Trans Biomed Eng, 2001. **48**(8): p. 911-20.

124. Cui, X., et al., *Surface modification of neural recording electrodes with conducting polymer/biomolecule blends.* J Biomed Mater Res, 2001. **56**(2): p. 261-72.

125. Biryukova, E.V., et al., *Kinematics of human arm reconstructed from spatial tracking system recordings.* J Biomech, 2000. **33**(8): p. 985-95.

126. Carmena, J.M., et al., *Learning to control a brain-machine interface for reaching and grasping by primates.* PLoS Biol, 2003. **1**(2): p. E42.

127. Velliste, M., et al., *Cortical control of a prosthetic arm for self-feeding.* Nature, 2008. **453**(7198): p. 1098-101.

128. Shokur, S., et al., *Expanding the primate body schema in sensorimotor cortex by virtual touches of an avatar.* Proc Natl Acad Sci U S A, 2013. **110**(37): p. 15121-6.

129. O'Doherty, J.E., et al., *Active tactile exploration using a brain-machine-brain interface.* Nature, 2011. **479**(7372): p. 228-31.

130. Gallagher, I.I., *Philosophical conceptions of the self: implications for cognitive science.* Trends Cogn Sci, 2000. **4**(1): p. 14-21.

131. Nahab, F.B., et al., *The neural processes underlying self-agency.* Cereb Cortex, 2011. **21**(1): p. 48-55.

132. Costantini, M. and P. Haggard, *The rubber hand illusion: sensitivity and reference frame for body ownership.* Conscious Cogn, 2007. **16**(2): p. 229-40.

133. Traynelis, S.F. and F. Jaramillo, *Getting the most out of noise in the central nervous system.* Trends Neurosci, 1998. **21**(4): p. 137-45.

134. Hochberg, L.R., et al., *Neuronal ensemble control of prosthetic devices by a human with tetraplegia.* Nature, 2006. **442**(7099): p. 164-71.

135. Wahnoun, R., J. He, and S.I. Helms Tillery, *Selection and parameterization of cortical neurons for neuroprosthetic control.* J Neural Eng, 2006. **3**(2): p. 162-71.

136. Kim, S.P., et al., *Point-and-click cursor control with an intracortical neural interface system by humans with tetraplegia.* IEEE Trans Neural Syst Rehabil Eng, 2011. **19**(2): p. 193-203.

137. Kennedy, P.R., et al., *Direct control of a computer from the human central nervous system.* IEEE Trans Rehabil Eng, 2000. **8**(2): p. 198-202.

138. Wiener, N., *Extrapolation, interpolation, and smoothing of stationary time series, with engineering applications*. 1949, Cambridge: Technology Press of the Massachusetts Institute of Technology. ix, 163 p.

139. Haykin, S.S., *Adaptive filter theory*. 4th ed. 2002, Upper Saddle River, N.J.: Prentice Hall. xvi, 920 p.

140. Kim, S.P., et al., *A comparison of optimal MIMO linear and nonlinear models for brain-machine interfaces.* J Neural Eng, 2006. **3**(2): p. 145-61.

141. Bashashati, A., et al., *A survey of signal processing algorithms in brain-computer interfaces based on electrical brain signals.* J Neural Eng, 2007. **4**(2): p. R32-57.

142. Kalman, R.E., *A New Approach to Linear Filtering and Prediction Problems.* Trans. ASME, Journal of Basic Engineering, 1960. **82**: p. 35-45.

143. Wu, W., et al., *Bayesian population decoding of motor cortical activity using a Kalman filter.* Neural Comput, 2006. **18**(1): p. 80-118.

144. Wu, W., et al., *Closed-loop neural control of cursor motion using a Kalman filter.* Conf Proc IEEE Eng Med Biol Soc, 2004. **6**: p. 4126-9.

145. Koyama, S., et al., *Comparison of brain-computer interface decoding algorithms in open-loop and closed-loop control.* J Comput Neurosci, 2010. **29**(1-2): p. 73-87.

146. Brockwell, A.E., A.L. Rojas, and R.E. Kass, *Recursive bayesian decoding of motor cortical signals by particle filtering.* J Neurophysiol, 2004. **91**(4): p. 1899-907.

147. Gao, Y.B.M., et al., *Statistical encoding model for a primary motor cortical brain-machine interface*, in *Advances in Neural Information Processing*. 2002, MIT Press: Cambridge, MA.

148. Kim, S.P., et al., *Divide-and-conquer approach for brain machine interfaces: nonlinear mixture of competitive linear models.* Neural Netw, 2003. **16**(5-6): p. 865-71.

149. Sanchez, J.C., et al., *Simultaneus prediction of four kinematic variables for a brain-machine interface using a single recurrent neural network.* Conf Proc IEEE Eng Med Biol Soc, 2004. **7**: p. 5321-4.

150. Li, Z., et al., *Unscented Kalman filter for brain-machine interfaces.* PLoS One, 2009. **4**(7): p. e6243.

151. Shoham, S., et al., *Statistical encoding model for a primary motor cortical brain-machine interface.* IEEE Trans Biomed Eng, 2005. **52**(7): p. 1312-22.

152. Doucet, A., S. Godsill, and C. Andrieu, *On sequential Monte Carlo sampling methods for Bayesian filtering.* Statistics and Computing, 2000. **10**: p. 197-208.

153. Eden, U., et al., *Reconstruction of hand movement trajectories from a dynamic ensemble of spiking motor cortical neurons.* Conf Proc IEEE Eng Med Biol Soc, 2004. **6**: p. 4017-20.

154. Eden, U.T., et al., *Dynamic analysis of neural encoding by point process adaptive filtering.* Neural Comput, 2004. **16**(5): p. 971-98.

155. Truccolo, W., L.R. Hochberg, and J.P. Donoghue, *Collective dynamics in human and monkey sensorimotor cortex: predicting single neuron spikes.* Nat Neurosci, 2010. **13**(1): p. 105-11.

156. Saleh, M., et al., *Encoding of coordinated grasp trajectories in primary motor cortex.* J Neurosci, 2010. **30**(50): p. 17079-90.

157. Hatsopoulos, N., J. Joshi, and J.G. O'Leary, *Decoding continuous and discrete motor behaviors using motor and premotor cortical ensembles.* J Neurophysiol, 2004. **92**(2): p. 1165-74.

158. Sussillo, D., et al., *A recurrent neural network for closed-loop intracortical brain-machine interface decoders.* J Neural Eng, 2012. **9**(2): p. 026027.

159. Jaeger, H. and H. Haas, *Harnessing nonlinearity: predicting chaotic systems and saving energy in wireless communication.* Science, 2004. **304**(5667): p. 78-80.

160. Xu, K., et al., *Local-learning-based neuron selection for grasping gesture prediction in motor brain machine interfaces.* J Neural Eng, 2013. **10**(2): p. 026008.

161. Tankus, A., I. Fried, and S. Shoham, *Sparse decoding of multiple spike trains for brain-machine interfaces.* J Neural Eng, 2012. **9**(5): p. 054001.

162. Liao, Y., et al., *Mutual information analysis on non-stationary neuron importance for brain machine interfaces.* Conf Proc IEEE Eng Med Biol Soc, 2012. **2012**: p. 2748-51.

163. Wang, Y. and J.C. Principe, *Tracking the non-stationary neuron tuning by dual Kalman filter for brain machine interfaces decoding.* Conf Proc IEEE Eng Med Biol Soc, 2008. **2008**: p. 1720-3.

164. Matlack, C., C. Moritz, and H. Chizeck, *Applying best practices from digital control systems to BMI implementation.* Conf Proc IEEE Eng Med Biol Soc, 2012. **2012**: p. 1699-702.

165. Julier, S.J. and J.K. Uhlmann, *A new extension of the Kalman filter to nonlinear systems.* Signal Processing, Sensor Fusion, and Target Recognition Vi, 1997. **3068**: p. 182-193.

166. Wan, E.A. and R. van der Merwe, *The unscented Kalman Filter for nonlinear estimation.* Ieee 2000 Adaptive Systems for Signal Processing, Communications, and Control Symposium - Proceedings, 2000: p. 153-158.

167. Cisek, P. and J.F. Kalaska, *Neural correlates of mental rehearsal in dorsal premotor cortex.* Nature, 2004. **431**(7011): p. 993-6.

168. Dushanova, J. and J. Donoghue, *Neurons in primary motor cortex engaged during action observation.* Eur J Neurosci, 2010. **31**(2): p. 386-98.

169. Li, Z., et al., *Adaptive decoding for brain-machine interfaces through Bayesian parameter updates.* Neural Comput, 2011. **23**(12): p. 3162-204.

170. Fitts, P.M., *The information capacity of the human motor system in controlling the amplitude of movement.* J Exp Psychol, 1954. **47**(6): p. 381-91.

171. Fitts, P.M. and J.R. Peterson, *Information Capacity of Discrete Motor Responses.* J Exp Psychol, 1964. **67**: p. 103-12.

172. Shannon, C.E. and W. Weaver, *The Mathematical Theory of Communication*. 1949, Urbana, IL: University of Illinois Press.

173. Gillan, D.J., et al., *How should Fitts' Law be applied to human-computer interaction?* Interact Comput, 1992. **4**(3): p. 291-313.

174. Felton, E.A., et al., *Evaluation of a modified Fitts law brain-computer interface target acquisition task in able and motor disabled individuals.* J Neural Eng, 2009. **6**(5): p. 056002.

175. Ifft, P.J., M.A. Lebedev, and M.A. Nicolelis, *Cortical correlates of fitts' law.* Front Integr Neurosci, 2011. **5**: p. 85.

176. Bohan, M., et al., *Effects of target height and width on 2D pointing movement duration and kinematics.* Motor Control, 2003. **7**(3): p. 278-89.

177. Awiszus, F., *Spike train analysis.* J Neurosci Methods, 1997. **74**(2): p. 155-66.

178. Grandvalet, Y., *Least absolute shrinkage is equivalent to quadratic penalization*. Perspectives in Neural Computing, ed. L. Niklasson, M. Boden, and T. Ziemske. 1998, Berlin: Springer Verlag.

179. Card, S.K., W.K. English, and B.J. Burr, *Evaluation of Mouse, Rate-Controlled Isometric Joystick, Step Keys, and Text Keys for Text Selection on a Crt.* Ergonomics, 1978. **21**(8): p. 601-613.

180. Munro, H., et al., *The effect of distance on reaction time in aiming movements.* Exp Brain Res, 2007. **183**(2): p. 249-57.

181. Boyd, L.A., et al., *Manipulating time-to-plan alters patterns of brain activation during the Fitts' task.* Exp Brain Res, 2009. **194**(4): p. 527-39.

182. Plamondon, R. and A.M. Alimi, *Speed/accuracy trade-offs in target-directed movements.* Behav Brain Sci, 1997. **20**(2): p. 279-303; discussion 303-49.

183. Juras, G., K. Slomka, and M. Latash, *Violations of Fitts' law in a ballistic task.* J Mot Behav, 2009. **41**(6): p. 525-8.

184. Gold, J.I. and M.N. Shadlen, *The neural basis of decision making.* Annu Rev Neurosci, 2007. **30**: p. 535-74.

185. Pearson, J. and M.L. Platt, *Confidence and corrections: how we make and un-make up our minds.* Neuron, 2009. **63**(6): p. 724-6.

186. Resulaj, A., et al., *Changes of mind in decision-making.* Nature, 2009. **461**(7261): p. 263-6.

187. Lebedev, M.A., J.E. O'Doherty, and M.A. Nicolelis, *Decoding of temporal intervals from cortical ensemble activity.* J Neurophysiol, 2008. **99**(1): p. 166-86.

188. Soso, M.J. and E.E. Fetz, *Responses of identified cells in postcentral cortex of awake monkeys during comparable active and passive joint movements*. J Neurophysiol, 1980. **43**(4): p. 1090-110.

189. Lebedev, M.A., J.M. Denton, and R.J. Nelson, *Vibration-entrained and premovement activity in monkey primary somatosensory cortex.* J Neurophysiol, 1994. **72**(4): p. 1654-73.

190. Thaler, L. and M.A. Goodale, *Neural substrates of visual spatial coding and visual feedback control for hand movements in allocentric and target-directed tasks.* Front Hum Neurosci, 2011. **5**: p. 92.

191. Lee, I.H. and J.A. Assad, *Putaminal activity for simple reactions or self-timed movements.* J Neurophysiol, 2003. **89**(5): p. 2528-37.

192. Shen, L. and G.E. Alexander, *Neural correlates of a spatial sensory-to-motor transformation in primary motor cortex.* J Neurophysiol, 1997. **77**(3): p. 1171-94.

193. Zhang, J., et al., *Dynamics of single neuron activity in monkey primary motor cortex related to sensorimotor transformation.* J Neurosci, 1997. **17**(6): p. 2227-46.

194. Hernandez, A., et al., *Decoding a perceptual decision process across cortex.* Neuron, 2010. **66**(2): p. 300-14.

195. Lebedev, M.A., et al., *Cortical ensemble adaptation to represent velocity of an artificial actuator controlled by a brain-machine interface.* J Neurosci, 2005. **25**(19): p. 4681-93.

196. Todorov, E. and M.I. Jordan, *Optimal feedback control as a theory of motor coordination.* Nat Neurosci, 2002. **5**(11): p. 1226-35.

197. Gardner, E.P. and R.M. Costanzo, *Properties of kinesthetic neurons in somatosensory cortex of awake monkeys.* Brain Res, 1981. **214**(2): p. 301-19.

198. Nelson, R.J., B.N. Smith, and V.D. Douglas, *Relationships between sensory responsiveness and premovement activity of quickly adapting neurons in areas 3b and 1 of monkey primary somatosensory cortex.* Exp Brain Res, 1991. **84**(1): p. 75-90.

199. Liu, Y., J.M. Denton, and R.J. Nelson, *Neuronal activity in primary motor cortex differs when monkeys perform somatosensory and visually guided wrist movements.* Exp Brain Res, 2005. **167**(4): p. 571-86.

200. Wise, S.P., et al., *Premotor and parietal cortex: corticocortical connectivity and combinatorial computations.* Annu Rev Neurosci, 1997. **20**: p. 25-42.

201. Alexander, G.E. and M.D. Crutcher, *Neural representations of the target (goal) of visually guided arm movements in three motor areas of the monkey.* J Neurophysiol, 1990. **64**(1): p. 164-78.

202. Opris, I., M. Lebedev, and R.J. Nelson, *Motor Planning under Unpredictable Reward: Modulations of Movement Vigor and Primate Striatum Activity.* Front Neurosci, 2011. **5**: p. 61.

203. Moritz, C.T., S.I. Perlmutter, and E.E. Fetz, *Direct control of paralysed muscles by cortical neurons.* Nature, 2008. **456**(7222): p. 639-42.

204. Lebedev, M.A., et al., *Future developments in brain-machine interface research.* Clinics (Sao Paulo), 2011. **66 Suppl 1**: p. 25-32.

205. Nicolelis, M.A. and M.A. Lebedev, *Principles of neural ensemble physiology underlying the operation of brain-machine interfaces.* Nat Rev Neurosci, 2009. **10**(7): p. 530-40.

206. Gilja, V., et al., *Challenges and opportunities for next-generation intracortically based neural prostheses.* IEEE Trans Biomed Eng, 2011. **58**(7): p. 1891-9.

207. Simeral, J.D., et al., *Neural control of cursor trajectory and click by a human with tetraplegia 1000 days after implant of an intracortical microelectrode array.* J Neural Eng, 2011. **8**(2): p. 025027.

208. MacKenzie, S., *Fitts' law as a research and design tool in human-computer interaction.* Human Computer Interaction, 1992. **7**(91-139).

209. MacKenzie, S., T. Kauppinen, and M. Silfverberg, *Accuracy measures for evaluating computer pointing devices.* Proceedings of the ACM Conference on Human Factors in Computer Systems - CHI 2001, New York, 2001: p. 9-16.

210. Ifft, P.J., M.A. Lebedev, and M.A. Nicolelis, *Reprogramming movements: extraction of motor intentions from cortical ensemble activity when movement goals change.* Front Neuroeng, 2012. **5**: p. 16.

211. Chen, X., K.W. Scangos, and V. Stuphorn, *Supplementary motor area exerts proactive and reactive control of arm movements.* J Neurosci, 2010. **30**(44): p. 14657-75.

212. Vickers, D. and P. Smith, *Accumulator and random-walk models of psychophysical discrimination: a counter-evaluation.* Perception, 1985. **14**(4): p. 471-97.

213. Georgopoulos, A.P., J.F. Kalaska, and J.T. Massey, *Spatial trajectories and reaction times of aimed movements: effects of practice, uncertainty, and change in target location.* J Neurophysiol, 1981. **46**(4): p. 725-43.

214. Georgopoulos, A.P., et al., *Interruption of motor cortical discharge subserving aimed arm movements.* Exp Brain Res, 1983. **49**(3): p. 327-40.

215. Kertzman, C., et al., *The role of posterior parietal cortex in visually guided reaching movements in humans.* Exp Brain Res, 1997. **114**(1): p. 170-83.

216. Baumann, M.A., M.C. Fluet, and H. Scherberger, *Context-specific grasp movement representation in the macaque anterior intraparietal area.* J Neurosci, 2009. **29**(20): p. 6436-48.

217. Lebedev, M.A. and S.P. Wise, *Oscillations in the premotor cortex: single-unit activity from awake, behaving monkeys.* Exp Brain Res, 2000. **130**(2): p. 195-215.

218. Cisek, P. and J.F. Kalaska, *Simultaneous encoding of multiple potential reach directions in dorsal premotor cortex.* J Neurophysiol, 2002. **87**(2): p. 1149-54.

219. Genovesio, A., et al., *Prefrontal cortex activity related to abstract response strategies.* Neuron, 2005. **47**(2): p. 307-20.

220. Tanji, J., *Sequential organization of multiple movements: involvement of cortical motor areas.* Annu Rev Neurosci, 2001. **24**: p. 631-51.

221. Hanes, D.P. and J.D. Schall, *Neural control of voluntary movement initiation.* Science, 1996. **274**(5286): p. 427-30.

222. Wong-Lin, K., et al., *Optimal performance in a countermanding saccade task.* Brain Res, 2010. **1318**: p. 178-87.

223. Snyder, L.H., A.P. Batista, and R.A. Andersen, *Change in motor plan, without a change in the spatial locus of attention, modulates activity in posterior parietal cortex.* J Neurophysiol, 1998. **79**(5): p. 2814-9.

224. Jackson, A. and E.E. Fetz, *Interfacing with the computational brain.* IEEE Trans Neural Syst Rehabil Eng, 2011. **19**(5): p. 534-41.

225. Zacksenhouse, M. and S. Nemets, *Strategies for Neural Ensemble Data Analysis for Brain-Machine Interface (BMI) Applications.* 2008.

226. Pesaran, B., S. Musallam, and R.A. Andersen, *Cognitive neural prosthetics.* Curr Biol, 2006. **16**(3): p. R77-80.

227. Santhanam, G., et al., *A high-performance brain-computer interface.* Nature, 2006. **442**(7099): p. 195-8.

228. Hwang, E.J. and R.A. Andersen, *Brain control of movement execution onset using local field potentials in posterior parietal cortex.* J Neurosci, 2009. **29**(45): p. 14363-70.

229. Hasegawa, R.P., Y.T. Hasegawa, and M.A. Segraves, *Single trial-based prediction of a go/no-go decision in monkey superior colliculus.* Neural Netw, 2006. **19**(8): p. 1223-32.

230. Hasegawa, R.P., Y.T. Hasegawa, and M.A. Segraves, *Neural mind reading of multi-dimensional decisions by monkey mid-brain activity.* Neural Netw, 2009. **22**(9): p. 1247-56.

231. Hanes, D.P. and J.D. Schall, *Countermanding saccades in macaque.* Vis Neurosci, 1995. **12**(5): p. 929-37.

232. Pare, M. and D.P. Hanes, *Controlled movement processing: superior colliculus activity associated with countermanded saccades.* J Neurosci, 2003. **23**(16): p. 6480-9.

233. Scangos, K.W. and V. Stuphorn, *Medial frontal cortex motivates but does not control movement initiation in the countermanding task.* J Neurosci, 2010. **30**(5): p. 1968-82.

234. Mirabella, G., P. Pani, and S. Ferraina, *Neural correlates of cognitive control of reaching movements in the dorsal premotor cortex of rhesus monkeys.* J Neurophysiol, 2011. **106**(3): p. 1454-66.

235. Nicolelis, M.A., *Actions from thoughts.* Nature, 2001. **409**(6818): p. 403-7.

236. Basar, K., et al., *Nucleus accumbens and impulsivity.* Prog Neurobiol, 2010. **92**(4): p. 533-57.

237. Kim, S. and D. Lee, *Prefrontal cortex and impulsive decision making.* Biol Psychiatry, 2011. **69**(12): p. 1140-6.

238. Miller, E.K., *The prefrontal cortex and cognitive control.* Nat Rev Neurosci, 2000. **1**(1): p. 59-65.

239. Krawczyk, D.C., *Contributions of the prefrontal cortex to the neural basis of human decision making.* Neurosci Biobehav Rev, 2002. **26**(6): p. 631-64.

240. Fitzsimmons, N.A., et al., *Extracting kinematic parameters for monkey bipedal walking from cortical neuronal ensemble activity.* Front Integr Neurosci, 2009. **3**: p. 3.

241. Collinger, J.L., et al., *High-performance neuroprosthetic control by an individual with tetraplegia.* Lancet, 2013. **381**(9866): p. 557-64.

242. Ifft, P.J., et al., *A brain-machine interface enables bimanual arm movements in monkeys.* Sci Transl Med, 2013. **5**(210): p. 210ra154.

243. Schwarz, D., et al., *Chronic Wireless Recordings of Very Large Scale Brain Activity in Freely Moving Rhesus Monkeys.* Nature Methods, 2013. **(in review)**.

244. Kimmel, D.L., D. Mammo, and W.T. Newsome, *Tracking the eye non-invasively: simultaneous comparison of the scleral search coil and optical tracking techniques in the macaque monkey.* Front Behav Neurosci, 2012. **6**: p. 49.

245. Kalal, Z., K. Mikolajczyk, and J. Matas, *Tracking-Learning-Detection.* IEEE Trans Pattern Anal Mach Intell, 2011.

246. Cunningham, J.P., et al., *A closed-loop human simulator for investigating the role of feedback control in brain-machine interfaces.* J Neurophysiol, 2011. **105**(4): p. 1932-49.

247. Colby, C.L., *Action-oriented spatial reference frames in cortex.* Neuron, 1998. **20**(1): p. 15-24.

248. Rizzolatti, G., et al., *The space around us.* Science, 1997. **277**(5323): p. 190-1.

249. Graziano, M.S., *Where is my arm? The relative role of vision and proprioception in the neuronal representation of limb position.* Proc Natl Acad Sci U S A, 1999. **96**(18): p. 10418-21.

250. Ochiai, T., H. Mushiake, and J. Tanji, *Effects of image motion in the dorsal premotor cortex during planning of an arm movement.* J Neurophysiol, 2002. **88**(4): p. 2167-71.

251. Graziano, M.S. and C.G. Gross, *A bimodal map of space: somatosensory receptive fields in the macaque putamen with corresponding visual receptive fields.* Exp Brain Res, 1993. **97**(1): p. 96-109.

252. Saha, D.J. and P. Morasso, *Stabilization strategies for unstable dynamics.* PLoS One, 2012. **7**(1): p. e30301.

253. Peper, C.E. and R.G. Carson, *Bimanual coordination between isometric contractions and rhythmic movements: an asymmetric coupling.* Exp Brain Res, 1999. **129**(3): p. 417-32.

254. Ridderikhoff, A., C.L. Peper, and P.J. Beek, *Unraveling interlimb interactions underlying bimanual coordination.* J Neurophysiol, 2005. **94**(5): p. 3112-25.

255. Tkach, D., J. Reimer, and N.G. Hatsopoulos, *Congruent activity during action and action observation in motor cortex.* J Neurosci, 2007. **27**(48): p. 13241-50.

256. Rizzolatti, G., L. Fogassi, and V. Gallese, *Neurophysiological mechanisms underlying the understanding and imitation of action.* Nat Rev Neurosci, 2001. **2**(9): p. 661-70.

257. Rizzolatti, G., et al., *Premotor cortex and the recognition of motor actions.* Brain Res Cogn Brain Res, 1996. **3**(2): p. 131-41.

258. Rizzolatti, G. and L. Craighero, *The mirror-neuron system.* Annu Rev Neurosci, 2004. **27**: p. 169-92.

259. Nishitani, N. and R. Hari, *Temporal dynamics of cortical representation for action.* Proc Natl Acad Sci U S A, 2000. **97**(2): p. 913-8.

260. Hickok, G., *Eight problems for the mirror neuron theory of action understanding in monkeys and humans.* J Cogn Neurosci, 2009. **21**(7): p. 1229-43.

261. Rizzolatti, G., *The mirror mechanism in monkeys and humans.* Neurosci Res, 2008. **61**: p. S1-S1.

262. Anderson, K.D., *Targeting recovery: priorities of the spinal cord-injured population.* J Neurotrauma, 2004. **21**(10): p. 1371-83.

263. Kazennikov, O., et al., *Neural activity of supplementary and primary motor areas in monkeys and its relation to bimanual and unimanual movement sequences.* Neuroscience, 1999. **89**(3): p. 661-74.

264. Stevenson, I.H. and K.P. Kording, *How advances in neural recording affect data analysis.* Nat Neurosci, 2011. **14**(2): p. 139-42.

265. Hauschild, M., et al., *Cognitive signals for brain-machine interfaces in posterior parietal cortex include continuous 3D trajectory commands.* Proc Natl Acad Sci U S A, 2012. **109**(42): p. 17075-80.

266. Santucci, D.M., et al., *Frontal and parietal cortical ensembles predict single-trial muscle activity during reaching movements in primates.* Eur J Neurosci, 2005. **22**(6): p. 1529-40.

267. Requin, J., J.C. Lecas, and N. Vitton, *A comparison of preparation-related neuronal activity changes in the prefrontal, premotor, primary motor and posterior parietal areas of the monkey cortex: preliminary results.* Neurosci Lett, 1990. **111**(1-2): p. 151-6.

268. Tillery, S.I. and D.M. Taylor, *Signal acquisition and analysis for cortical control of neuroprosthetics.* Curr Opin Neurobiol, 2004. **14**(6): p. 758-62.

269. Georgopoulos, A.P., R.E. Kettner, and A.B. Schwartz, *Primate motor cortex and free arm movements to visual targets in three-dimensional space. II. Coding of the direction of movement by a neuronal population.* J Neurosci, 1988. **8**(8): p. 2928-37.

270. Zacksenhouse, M., et al., *Cortical modulations increase in early sessions with brain-machine interface.* PLoS One, 2007. **2**(7): p. e619.

271. Olson, B. and J. Si, *Evidence of a mechanism of neural adaptation in the closed loop control of directions.* International Journal of Intelligent Computing and Cybernetics, 2008. **3**(1): p. 5-23.

272. Andres, F.G., et al., *Functional coupling of human cortical sensorimotor areas during bimanual skill acquisition.* Brain, 1999. **122 (Pt 5)**: p. 855-70.

273. Dethier, J., et al., *Design and validation of a real-time spiking-neural-network decoder for brain-machine interfaces.* J Neural Eng, 2013. **10**(3): p. 036008.

274. Wu, W., et al., *Modeling and decoding motor cortical activity using a switching Kalman filter.* IEEE Trans Biomed Eng, 2004. **51**(6): p. 933-42.

275. Rouse, A.G., et al., *A chronic generalized bi-directional brain-machine interface.* J Neural Eng, 2011. **8**(3): p. 036018.

276. Cover, T.M. and P.E. Hart, *Nearest neighbor pattern classification.* IEEE Trans. Inform. Theory, IT, 1967. **13**(1): p. 21-27.

277. Xu, K., et al., *Comparisons between linear and nonlinear methods for decoding motor cortical activities of monkey.* Conf Proc IEEE Eng Med Biol Soc, 2011. **2011**: p. 4207-10.

278. Shanechi, M.M., et al., *Feedback-controlled parallel point process filter for estimation of goal-directed movements from neural signals.* IEEE Trans Neural Syst Rehabil Eng, 2013. **21**(1): p. 129-40.

279. Homer, M., et al., *Adaptive Offset Correction for Intracortical Brain Computer Interfaces.* IEEE Trans Neural Syst Rehabil Eng, 2013.

280. Swinnen, S.P. and N. Wenderoth, *Two hands, one brain: cognitive neuroscience of bimanual skill.* Trends Cogn Sci, 2004. **8**(1): p. 18-25.

281. Tankus, A., I. Fried, and S. Shoham, *Cognitive-motor brain-machine interfaces.* J Physiol Paris, 2013.

282. Wu, W., et al., *A Switching Kalman Filter Model for the Motor Cortical Coding of Hand Motion.* Proceedings of the 25th Annual International Conference of the IEEE EMBS, 2003. **3**: p. 2083-2086.

283. Yu, B.M., et al., *Mixture of trajectory models for neural decoding of goal-directed movements.* J Neurophysiol, 2007. **97**(5): p. 3763-80.

284. Cardoso de Oliveira, S., *The neuronal basis of bimanual coordination: recent neurophysiological evidence and functional models.* Acta Psychol (Amst), 2002. **110**(2-3): p. 139-59.

285. Swinnen, S.P., et al., *Interlimb coordination deficits in patients with Parkinson's disease during the production of two-joint oscillations in the sagittal plane.* Mov Disord, 1997. **12**(6): p. 958-68.

286. Koebler, J. *Scientists Warn of Ethical Battle Concerning Military Mind Control*. 2012 27 January, 2014]; Available from: http://www.usnews.com/news/articles/2012/03/20/scientists-warn-of-ethical-battle-concerning-military-mind-control.

287. Sherlin, L.H., N.C. Larson, and R.M. Sherlin, *Developing a Performance Brain Training approach for baseball: a process analysis with descriptive data.* Appl Psychophysiol Biofeedback, 2013. **38**(1): p. 29-44.

288. Abazov, V.M., et al., *Direct search for charged higgs bosons in decays of top quarks.* Phys Rev Lett, 2002. **88**(15): p. 151803.

Biography

Peter Ifft, son of Mark and Michelle and brother of Andrea Ifft, was born in St. Paul, Minnesota on June 17, 1988. The Ifft family moved several times including to southern California and Oregon before settling in Rockford, Illinois in 1998 where Peter completed middle and high school. From a young age, Peter was equally driven in both academic pursuits and athletics, particularly in baseball. His passion for science began through a combination of science fair projects and inspiring teachers in grade school.

Peter graduated high school and received a college athletic scholarship for baseball at University of Illinois at Chicago at the age of 16. He studied bioengineering, engaged in research work, and achieved athletic success in the four years at UIC before graduating with a bachelor's degree in May, 2009 as valedictorian. As an undergraduate, he was involved in BMES, Tau Beta Pi, and Alpha Eta Mu Beta societies, was the 3-time UIC Scholar-Athlete of the Year, and received the Coleman Medal of Honor for his commitment to excellence on and off the field in addition to many other awards.

In fall of 2009, Peter began the PhD program in biomedical engineering at Duke University. He has six publications: *Future developments in brain-machine interface research* (2011), *Active tactile exploration using a brain-machine-brain interface* (2011). *Cortical correlates of Ftts' law* (2011), *Reprogramming movements: extraction of motor intentions from cortical ensemble activity when movement goals change* (2012), *A brain-machine interface enables bimanual arm movements in monkeys* (2013), including one publication as an undergraduate researcher: *Rapid prototyping for neuroscience and neural engineering* (2008).